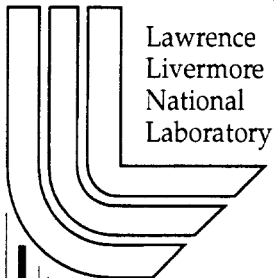# Geostatistical Analysis of Spatial Variability of Mineral Abundance and K_d in Frenchman Flat, NTS, Alluvium

Steven F. Carle, Mavrik Zavarin, and Gayle A. Pawloski

November 1, 2002

U.S. Department of Energy

Lawrence
Livermore
National
Laboratory

DISCLAIMER

This report has been reproduced directly from the best available copy.

Available electronically at http://www.doc.gov/bridge

Available for a processing fee to U.S. Department of Energy
And its contractors in paper from
U.S. Department of Energy
Office of Scientific and Technical Information
P.O. Box 62
Oak Ridge, TN 37831-0062
Telephone: (865) 576-8401
Facsimile: (865) 576-5728
E-mail: reports@adonis.osti.gov

Available for the sale to the public from
U.S. Department of Commerce
National Technical Information Service
5285 Port Royal Road
Springfield, VA 22161
Telephone: (800) 553-6847
Facsimile: (703) 605-6900
E-mail: orders@ntis.fedworld.gov
Online ordering: http://www.ntis.gov/ordering.htm

OR

Lawrence Livermore National Laboratory
Technical Information Department's Digital Library
http://www.llnl.gov/tid/Library.html

Geostatistical Analysis of
Spatial Variability of Mineral Abundance and
K_d in Frenchman Flat, NTS, Alluvium

Steven F. Carle, Mavrik Zavarin, and Gayle A. Pawloski

Lawrence Livermore National Laboratory
Livermore, California

CONTENTS

LIST OF FIGURES

LIST OF TABLES

1 Introduction

LLNL hydrologic source term modeling at the Cambric site (Pawloski et al., 2000) showed that retardation of radionuclide transport is sensitive to the distribution and amount of radionuclide sorbing minerals. While all mineralogic information available near the Cambric site was used in these early simulations (11 mineral abundance analyses from UE-5n and 9 from RNM-1), these older data sets were qualitative in nature, with detection limits too high to accurately measure many of the important radionuclide sorbing minerals (e.g. iron oxide). Also, the sparse nature of the mineral abundance data permitted only a hypothetical description of the spatial distribution of radionuclide sorbing minerals. Yet, the modeling results predicted that the spatial distribution of sorbing minerals would strongly affect radionuclide transport. Clearly, additional data are needed to improve understanding of mineral abundances and their spatial distributions if model predictions in Frenchman Flat are to be defensible.

This report evaluates new high-resolution quantitative X-Ray Diffraction (XRD) data on mineral distributions and their abundances from core samples recently collected from drill hole ER-5-4. The total of 94 samples from ER-5-4 were collected at various spacings to enable evaluation of spatial variability at a variety of spatial scales as small as 0.3 meters and up to hundreds of meters. Additional XRD analyses obtained from drillholes UE-5n, ER-5-3, and U-11g-1 are used to augment evaluation of vertical spatial variability and permit some evaluation of lateral spatial variability. A total of 163 samples are evaluated.

Recently, Los Alamos National Laboratory (LANL) and IT Corporation provided a detailed analysis of lithology and mineral distribution based on XRD, X-Ray Fluorescence (XRF), Scanning Electron Microscopy (SEM), petrography, and electron microprobe data from ER-5-4 as well as several other drill holes (Warren et al., 2002). These results provide the foundation for our geostatistical analysis of the XRD data. The origin of the XRD data and procedures used to obtain it are described in Chapter 2. The remainder of this report analyzes the spatial variability of the XRD data using geostatistical techniques. An important goal is to develop acceptable models of heterogeneity of mineral abundances and distribution coefficient (K_d) that can be incorporated into reactive transport modeling at hydrologic source term (HST) and Corrective Action Unit (CAU) scales.

Before spatial variability can be quantitatively characterized using variograms and stochastic simulation algorithms, the frequency distributions and spatial variability of the data must be examined for deviations from the normality and stationarity assumptions employed in geostatistics. This preliminary data analysis is described in Chapter 3. While the emphasis of our statistical analysis is placed on radionuclide sorbing minerals included in a mechanistic sorption model (iron oxide, smectite, calcite, zeolite, and mica/illite), data regarding other primary and secondary minerals are also evaluated. This is done to

- evaluate whether statistically significant correlations can be made between radionuclide sorbing and non-sorbing minerals (Section 3.4), and

- compare our mineralogic interpretations and geostatistical analyses of spatial variability of sorbing mineral abundance with the alluvial layering interpretations by Warren et al. (2002) (Section 3.5).

Because the mineralogic spatial variability is in part attributed to geology, consideration of geologic processes such as alluvial layering described by Warren et al. (2002) needs to be integrated into the geostatistical analysis.

This report also evaluates the mineral abundance data from the perspective of modeling radionuclide transport using particle tracking. In Chapter 4, the XRD data are converted to distribution coefficients (K_d) based on a mechanistic sorption model developed at LLNL (Zavarin and Bruton, 2000a; 2000b; Zavarin et al., 2002).[1] Frequency distributions and depth profiles of K_d are evaluated for a variety of radionuclides.

Chapter 5 conducts variogram analyses on both mineral abundance and K_d data. The mineral abundance data are categorized into "mineralization zones," where mineral abundance appears uniform in mean and variance, or, statistically "stationary" as described in Chapter 3. Within the mineralization zones, all of the sorbing and non-sorbing minerals except for hematite exhibit mostly random spatial variation. Spatial continuity of K_d is evident in variogram analyses and is primarily associated with variations in mineral abundance between different mineralization zones. Variogram models for K_d are developed for both vertical and lateral directions.

Chapter 6 employs the results of the analyses of spatial variability in the previous chapters to develop methods for simulating the spatial variability of mineral abundances and K_d. One approach is based on the concept of "chemofacies," where alluvial zones or layers have relatively uniform mean values of sorbing minerals. The three-dimensional geometry of the chemofacies are partly associated with the alluvial layers interpreted by Warren et al. (2002). The other approach employs the geostatistical concept of random fields and is applicable to K_d only. For most radionuclides, spatial variation of K_d throughout large portions of Frenchman Flat could be realistically simulated by Gaussian random fields. The exceptions are radionuclides such as Ca and Sr that are very sensitive to clinoptilolite abundance, which varies significantly between central and northern Frenchman Flat. Alternatively, a hybrid zonal and random field approach is demonstrated for generation of random fields of K_d for Ca and Sr.

Chapter 7 summarizes the interpretations and conclusions of the report. Chapter 8 provides references.

---

[1] Linking a mechanistic sorption model to a K_d model was described in a recent report (Zavarin, 2002).

Figure 1.1 provides a diagram illustrating the approaches taken in analyzing spatial variability of sorbing mineral abundances and K_d in Frenchman Flat, given the available data. The top of the figure illustrates hypothetical depth profiles of the mineral abundances. Based on interpretation of zonal variations of mean mineral abundances, mineralization zones are identified as indicated by the colored regions. The alluvial layering interpretation by Warren et al. (2002), which is based on a more comprehensive geologic interpretation, shows some similarities and differences compared to mineralization zones in defining unit boundaries. The K_d random field approach, shown at left, treats K_d as a random variable throughout Frenchman Flat alluvium, independent of mineralization zone. Based on the component additivity approach, K_ds are generated for each radionuclide (middle left), spatial variability of K_d within Frenchman Flat is modeled with variograms (bottom left), and stochastic random fields based on Gaussian random fields are be developed (bottom middle).

In the chemofacies approach, variogram analysis is applied to assess spatial variability within mineralization zones (middle right). In this application, only hematite exhibited measurable spatial correlation within a mineralization zone, with a vertical range of spatial correlation of about 5 m. Therefore, the spatial variation of mineral abundances and K_d within mineralization zones is, for practical purposes, entirely attributed to random variation. Therefore, zones which have relatively constant zonal mean abundances of sorbing minerals — chemofacies — will also have relatively constant K_ds. Because the chemofacies are related to the alluvial layering interpretation by Warren et al. (2002), three-dimensional models of sorbing mineral abundance or K_d could be developed using the geometric framework of alluvial layering (not shown).
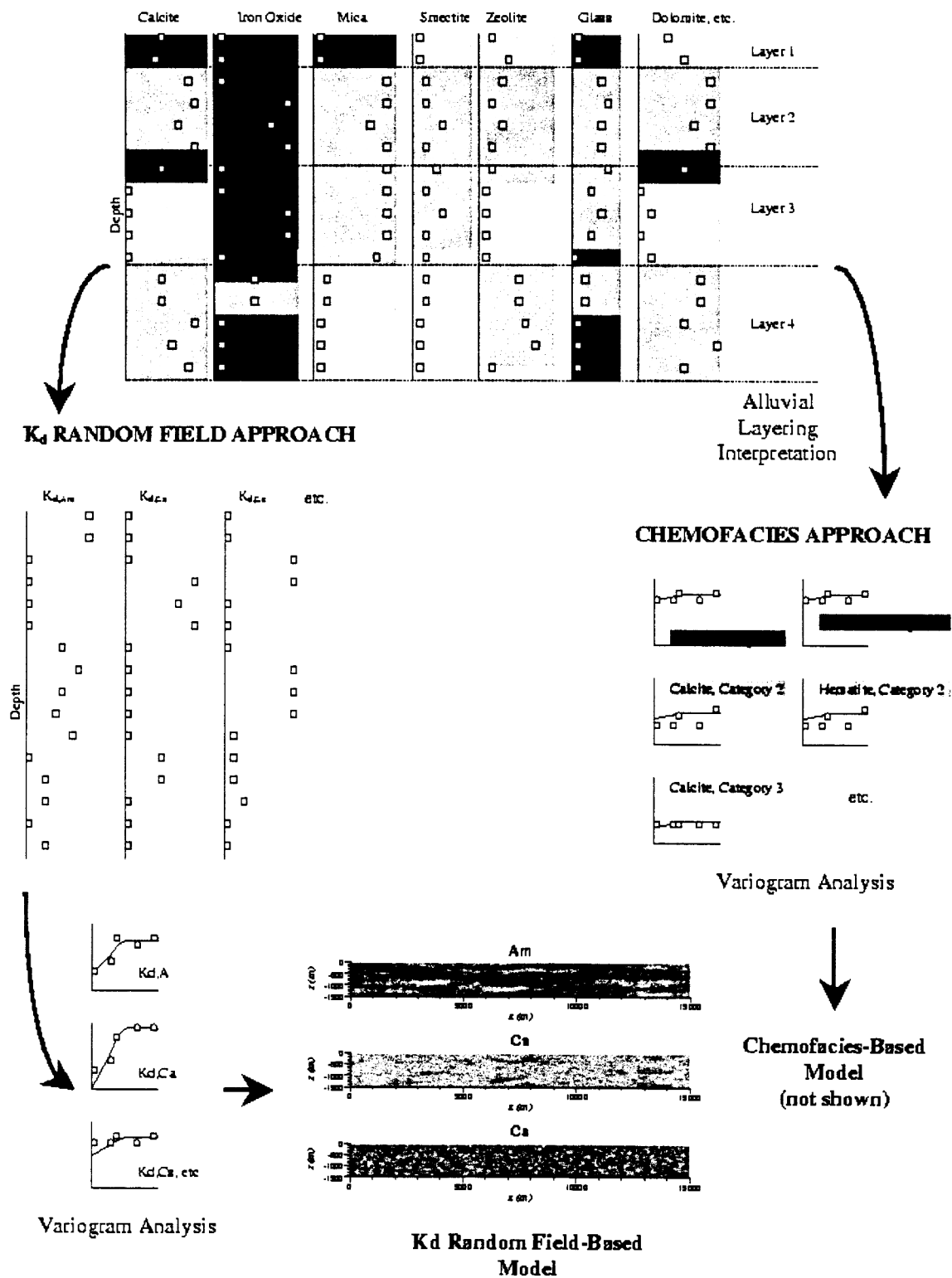
Figure 1.1 Diagram illustrating K_d random field and chemofacies approaches to addressing spatial variability of mineral abundances and K_d in the context of modeling reactive transport of radionuclides in Frenchman Flat.

2 Mineral Abundance Data Included in the Geostatistical Analysis

The geostatistical evaluation of mineral distribution in Frenchman Flat alluvium is based on recent quantitative X-Ray Diffraction (XRD) data collected on alluvium from four wells: ER-5-4, ER-5-3, UE-5n, and U-11g-1 (Figure 2.1). Sampling of well ER-5-4 was performed for the specific purpose of evaluating spatial variability of mineral abundance, with sampling intervals ranging from 0.3 to 10 meters and spanning nearly 1000 meters (Figure 2.2). Sampling intervals were chosen to enable evaluation of both small and large scale mineral spatial variability. Samples from well UE-5n were included in our analysis to evaluate lateral variability (UE-5n is located 477 meters from ER-5-4). UE-5n alluvium samples were collected in 1976 and stored at the NTS; small sub-samples were taken for quantitative XRD analysis. Samples from wells ER-5-3 and U-11g-1 were also included in our analysis to compare mineralogies of northern and central Frenchman Flat. Samples from ER-5-3 were collected as part of the UGTA program in FY01. U-11g-1 core was collected in 1971 and stored at the NTS; small subsamples were taken for quantitative XRD.

The quantitative XRD data discussed in this report were collected at Los Alamos National Laboratory and analyzed using the computer code FULLPAT (Chipera and Bish, 2001). Detailed descriptions of the data are reported in Warren et al. (2002) and will not be repeated here. While older XRD data exist for wells UE-5n, U-11g-1, and several other wells in Frenchman Flat, they were not included in our analysis. There are several issues that make inclusion of older XRD data problematic. First, many of the older data sets report mineral abundances for only a select number of minerals. Second, detection limits of the older data sets were, in all cases, much higher. Third, as pointed out in Warren et al. (2002), the data analysis methodology used to analyze older data sets was less rigorous, resulting in inconsistencies between recent quantitative XRD and older "qualitative" XRD data (see Warren et al., 2002 discussion of UE-5n data). To simplify the statistical interpretation of XRD data, we relied solely on recent quantitative XRD data reported in Warren et al. (2002).

It is important to distinguish the difference in approach used here and in Warren et al. (2002). In our analysis, we rely solely on the geostatistical evaluation of mineralogic abundance data based on recent quantitative XRD analyses. The interpretation of alluvial layering by Warren et al. (2002) was based on a combination of XRD, x-ray fluorescence (XRF), scanning electron microscopy (SEM), electron microprobe, and petrographic analyses, as well as historical data. Our statistical analysis is focused on sorbing minerals included in our mechanistic sorption model (iron oxide, smectite, illite/mica, zeolite, and calcite). Our approach should, therefore, be distinguished from that of Warren et al. (2002) in that it is not focused on alluvial layering but is, instead, focused on spatial variability of sorbing mineral abundances from the perspective of conducting simulations of reactive transport. Nevertheless, the interpretations of alluvial layers and sorbing mineral abundances share much in common, as will be discussed in various sections of this report.

In this report, we did not directly integrate the three component model described in Warren et al. (2002) into our analysis of spatial variability of mineral abundances. The three component

model (i.e. division of alluvium into crystals (phenocrysts), lithics/pyroclasts, and reactive matrix) and an index of reactive mineral accessibility were used in Warren et al. (2002) to assess whether reactive minerals may not be accessible to fluids and, thus, not contribute to radionuclide sorption. While these data were not included directly in our model, the information provided regarding sorbing mineral accessibility is consistent with recent mechanistic sorption model validation experiments (Zavarin et al., 2002). In these validation experiments, it was found that iron oxide reactivity is much lower than predicted based on batch single mineral laboratory studies. The information provided in Warren et al. (2002) suggests that the reduced reactivity can be understood based on the three component model and reactive mineral accessibility. The iron oxide (referred to in XRD data tables as hematite) abundance reported in quantitative XRD analyses, in reality, includes magnetite, maghemite, limonite (goethite), hematite, and hydrous ferric oxide minerals. Warren et al. (2002) found that the majority of the iron oxide (from petrographic analyses) occur as altered magnetite phenocrysts within the matrix and the lithics. The size of the magnetite phenocrysts, based on petrographic thin sections (see Figure 36 of Warren et al. (2002)), suggests that the surface area of these iron oxides will be quite low (calculated to be ~0.02 m^2/g based on simple cubic mineral particle assumption). This fraction of iron oxide should not contribute significantly to radionuclide retardation simply because the reactive surface area is too small to be significant (particularly in light of the low iron oxide mineral abundances of this alluvium). Thus, the dominant fraction of iron oxide would not be expected to contribute significantly to radionuclide retardation. Based on the petrographic analyses, the most accessible and high surface area iron oxide fraction (limonite in the matrix component) comprises only 3.5% of the total iron oxide. This is in general agreement with SEM-based evaluation of iron oxide accessibility. This is also in general agreement with our mechanistic sorption model validation experiments which suggested that the *average* iron oxide surface area must be in the range of 0.2 m^2/g, a surface area much lower than that observed for synthetic high surface area iron oxides (e.g. 50 m^2/g for goethite). By using the adjusted low reactive surface area of iron oxides, we are indirectly accounting for the complex iron oxide mineralogy suggested in Warren et al. (2002).
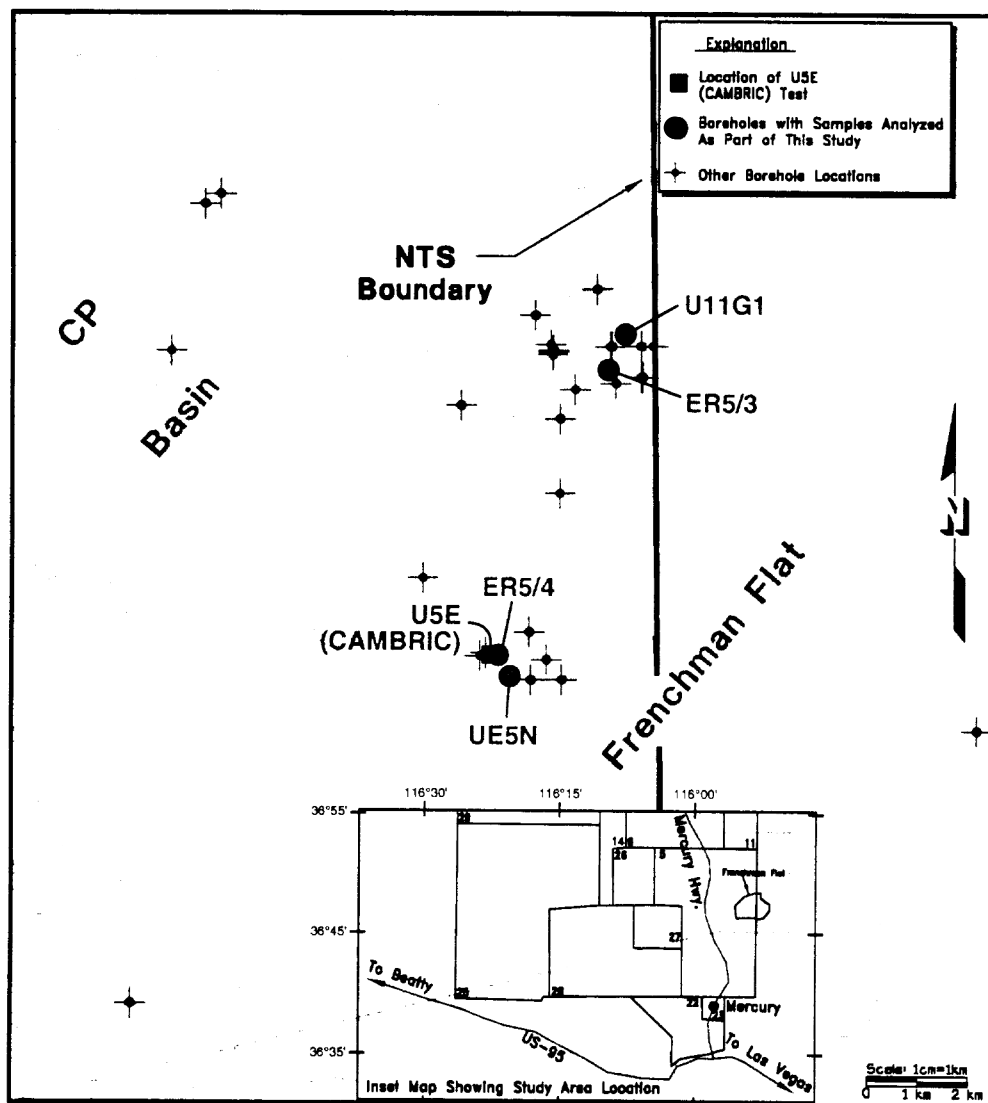
Figure 2.1. Location of drillholes UE-5n, ER-5-4, U-11g-1, and ER-5-3 from which mineralogic abundance data were retrieved. UE-5n and ER-5-4 are located in central Frenchman Flat while U-11g-1 and ER-5-3 are located in northern Frenchman Flat. Figure from Warren et al. (2002).
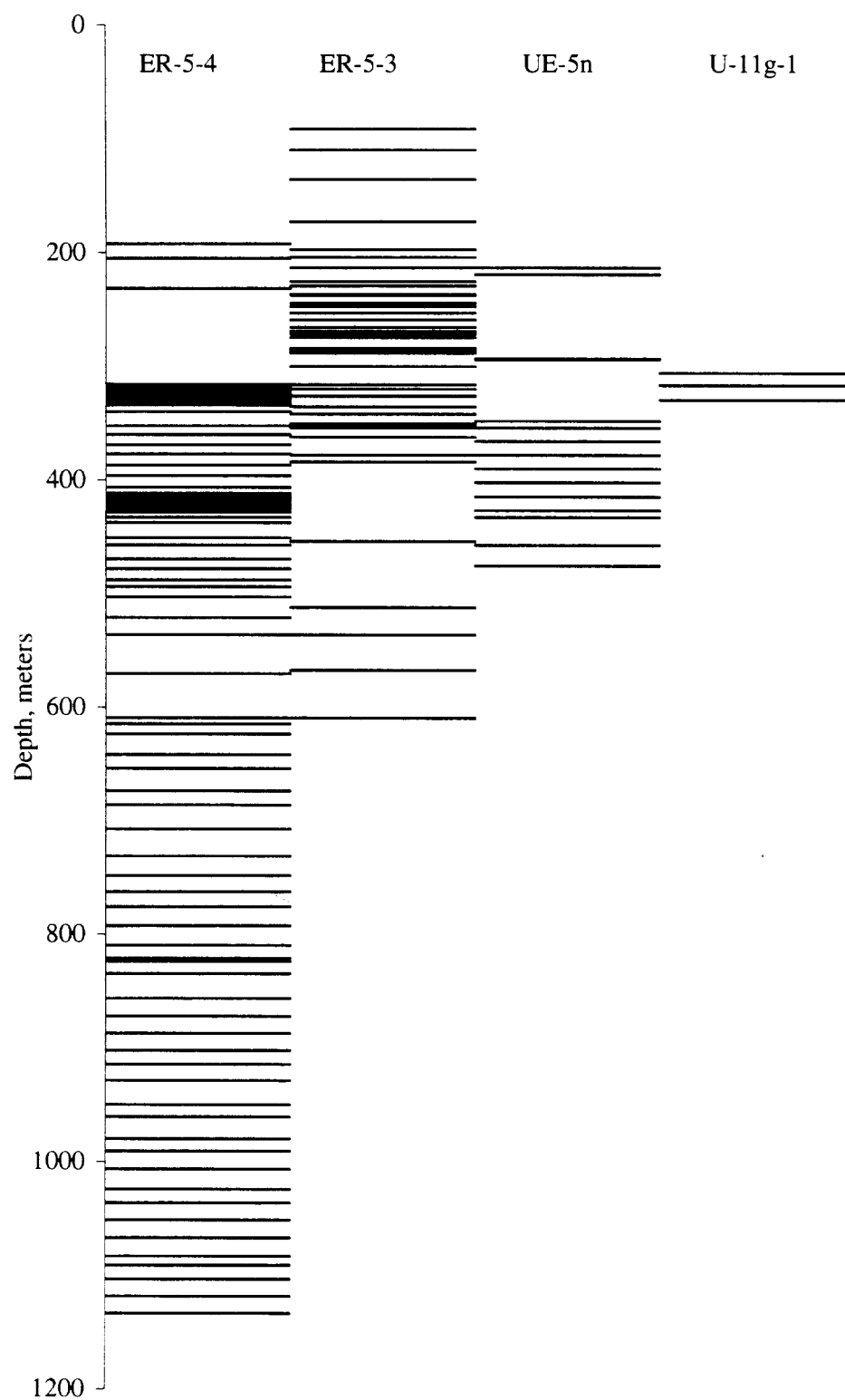
Figure 2.2 Comparison of XRD data sample depths for wells ER-5-4, ER-5-3, UE-5n, and U-11g-1.

3 Preliminary Data Interpretation

The overall goal of this study is to understand and characterize the spatial variation of sorbing minerals in Frenchman Flat alluvium, with consideration for the potential impact on reactive transport of radionuclides.[2] To achieve this goal requires an effort to ensure that plausible statistical models are used to characterize the spatial variation of minerals. The statistical models must also be plausible from a geological perspective. The spatial variation of mineral abundance cannot be entirely attributed to random processes. Geologic processes such as alluvial fan progradation, commingling, provenance (origin and source of the rock), and in-situ alteration dictate the spatial distribution of minerals. Nonetheless, analysis of spatial variation of mineral abundance with respect to random variable concepts will be useful for modeling field-scale transport.

In this chapter, we interpret the XRD data on mineral abundances from drillholes ER-5-4, ER-5-3, UE-5n, and U-11g-1 in Frenchman Flat using univariate and bivariate statistics as a preliminary step to performing geostatistical analysis of spatial variability of mineral abundances and K_d (see Chapters 5 and 6). The purpose of the preliminary data interpretation is to understand the statistical characteristics of the data that will affect variogram analysis discussed in Chapter 5. Before variogram analysis can begin, the topics of "stationarity" and normality must be addressed.

Geostatistical analyses typically employ the concepts of statistical stationarity of the mean or variance and normality in the frequency distribution. For clarification, stationarity means that the statistical properties (such as the mean and variance) of a random variable (such as mineral abundance) do not vary in space (within the region of interest). From a geological perspective, a geologic attribute could be considered statistically stationary if its mean value and degree of fluctuation is uniform through the region of interest. For example, the mean and variance of particle size could be assumed stationary in a poorly-sorted layer, but non stationary in a fining-upward layer. Stationarity of the mean or "first-order stationarity" occurs if the local mean does not depend on location (e.g., vertical position in a layer). Second-order stationarity occurs if both the mean and spatial covariance do not depend on location. In geostatistics, another form of stationarity called "intrinsic stationarity" is often assumed, where the local mean can vary smoothly in space but the variance remains stationary. The concept of intrinsic stationarity is useful in applications where the data exhibit fluctuations about a trend.

A normal (Gaussian) frequency distribution is usually assumed in a geostatistical analysis, not only because the normal distribution is a common model for random processes, but because the normal distribution is characterized entirely by the mean and variance (no third or higher order statistics are needed). Successful application of geostatistical techniques greatly depends on the appropriateness of the stationarity and normality assumptions. Therefore, it is good practice to carefully examine the data for nonstationarity in the mean (e.g., trends) and variance (e.g., spatial variations in the degree of fluctuation) and deviation from normality before carrying out the

---

[2] In this report, we define sorbing minerals based on the surface complexation/ion exchange model developed for near-field hydrologic source term modeling. In this model, sorbing minerals include: iron oxide, smectite, illite/mica, zeolite (clinoptilolite), and calcite. While other minerals may, in fact, sorb radionuclides, we use the term "sorbing minerals" strictly to refer to five minerals included in our sorption model.

variogram analysis. Otherwise, the variogram analysis may produce spurious results that introduce artifacts or mask out valuable information in the data.

Twenty-one different minerals were identified in the high-quality XRD data for drillholes ER-5-4, ER-5-3, UE-5n, and U-11g-1 in Frenchman Flat (Warren et al., 2002). We present these data in several different formats to address several opening questions about mineralogic spatial variation:

- Do the mineral abundances vary with depth and location in Frenchman Flat?

- How much of the spatial variation can be characterized by random processes, and how much of the spatial variation must be attributed to ordered geologic processes?

- Do the sorbing mineral abundances show significant correlation with non-sorbing minerals?

To address the first question, we plot the abundance of each mineral (mass percent based on XRD) on a log scale versus depth. These plots can be used to evaluate whether spatial variation of mineral abundances is in part related to random or "micro-scale" variability, and in part related to geological conditions, such as distinct zones or "layers" (Section 3.1). To address the second question, data are plotted as histograms and normal probabilities on both linear and log scales (Section 3.2). The frequency distributions (histograms) and normal probability plots call attention to different zones or layers — the non-random components of variation (Section 3.3). Finally, to address the third question, scatterplots are used to examine correlation between abundances of different minerals (Section 3.4). Statistical tests are used to determine whether correlations are significant between abundances of the sorbing minerals and different sorbing or non-sorbing minerals.

The combined interpretation of the mineral abundance versus depth, the linearly and logarithmically-scaled frequency distributions and normal probabilities, and the mineral abundance correlations are used to identify zones where the mean abundances of individual minerals appear stationary. Within these zones, the variogram analysis can be performed with more confidence because first-order stationarity and normality assumptions are appropriate. The identification of statistically stationary mineralogic zones is related to the geological interpretation of alluvial layers identified by Warren et al. (2002). However, it is important to distinguish the difference in approach used here and in Warren et al. (2002). In our interpretations, we rely solely on the statistical evaluation of mineralogic abundance data based on the XRD analyses. The interpretation of alluvial layering of Warren et al. (2002) was based on a combination of XRD, x-ray fluorescence (XRF), scanning electron microscopy (SEM), electron microprobe, and petrographic analyses. Because our statistical analysis was focused on sorbing minerals included in our mechanistic sorption model (iron oxide, smectite, illite/mica, zeolite, and calcite), our interpretation of layering is biased towards these minerals. Our approach should, therefore, be distinguished from that of Warren et al. (2002) in that it is not focused on alluvial layering but is, instead, focused on zones within the alluvial section that are of direct relevance to reactive transport, which we refer to as "mineralization zones." Nevertheless, the interpretations of alluvial layering and mineralization zones share much in common, as will be discussed later in Section 3.5.

3.1 Mineral Abundance vs. Depth

Figures 3.1 to 3.4 show plots of mineral abundance (mass percent based on XRD) on a log scale versus depth. The log scale is useful for spanning the nearly three orders of magnitude range in measured abundance of different minerals. The log scale is particularly useful for comparing low abundance minerals, such as hematite, to high abundance minerals, such as smectite, on the same plot. Because there are 21 different minerals observed in 4 different drillholes, the plots of mass percent versus depth are divided into groups of minerals as well as by drillhole. Each figure represents a different drillhole. In each figure, the minerals included in the mechanistic sorption model (calcite, hematite, mica, smectite, and clinoptilolite (a zeolite)) are plotted in the upper left;[3] dolomite, kaolinite, glass, analcime (a zeolite), and mordenite (a zeolite) are plotted in the upper right; feldspars, including orthoclase (low-T feldspar) and sanidine (high-T feldspar) K-feldspars and albite, bytownite, and anorthite[4] plagioclase feldspars are plotted in the lower left; opal, quartz, tridymite, hornblende, and clinopyroxene are plotted in the lower right.

Figure 3.1 shows the mineral abundance data for ER-5-4. This data set includes 94 samples obtained over a range of depth from about 192 to 1134 m. This is the most extensive and detailed mineralogic data set for any drillhole in Frenchman Flat. Data spacing is variable, typically from about 0.3 m (1 ft) to about 15 m (50 ft). The variable data spacing promotes examination of the vertical variability at a range of scales given a limited number of samples. Mineral abundances range from 0.1 to over 80 mass percent. The lower detection limit is, at best, 0.1 mass percent, depending on the mineral. Detailed information regarding the XRD analysis can be found in Warren et al. (2002). Mineral abundances below the detection limit are not shown on the depth plots. For example, clinopyroxene was not detected in any samples from ER-5-4 and was, therefore, not plotted. Dolomite is detected sporadically — where not plotted, the dolomite abundance was below the detection limit of 0.1 %.

Upon close examination of the mineral abundance data for ER-5-4, it appears that the mineral percentages typically exhibit smaller scale variability superposed on a larger-scale variability. The smaller scale variability is evident by a "cloud" or "scatter" of mineral percentages where data are closely spaced. The smaller scale variability generally occurs over scales less than the smallest data spacing of 0.3 m (or 1 ft). As a result, a structured pattern of small-scale spatial variability is generally not evident in the data. From a transport modeling perspective at CAU or HST scales, the small-scale variability in the mineralogy will be more practically addressed by use of effective properties rather than explicit of point values (see Chapter 6).

The larger (subregional) scale variability appears to occur in zones. In a zone, the means and variances of one or more minerals are different than in surrounding zones. For example, in the depth range of about 315 to 340 m, clinoptilolite and cristobalite show large differences in both mean and variance compared to their mineral abundances above and below. The clinoptilolite percentage is relatively high, while the cristobalite percentage is relatively low. Also with respect to depths above and below that zone, kaolinite is largely absent, opal is sporadically present, and some minerals, such as smectite and bytownite, appear to have larger variances but

---

[3] The mechanistic sorption model is discussed in Chapter 4.

[4] Only one sample contained anorthite (Ca-plagioclase). Generally, plagioclase was divided into albite (Na-plagioclase) and bytownite ($Na_{0.3-0.1}Ca_x$-plagioclase).

similar means. Another distinctive zone occurs between depths of about 700 and 780 m, where mean values of calcite and dolomite are relatively high, clinoptilolite is moderately high, orthoclase and bytownite feldspars are relatively low, and hornblende is not detected. A complete interpretation of mineralization zones for all drillholes is discussed in Section 3.3.

Figure 3.2 shows the mineral abundance data for drillhole UE-5n, which is located 477 m SSE of drillhole ER-5-4. Comparison of mineralogic data from drillholes ER-5-4 and UE-5n offers an opportunity to examine lateral continuity of the mineral abundances. The XRD data for UE-5n span a range of depth from about 210 to 475 m. The zonal mean values of the mineralogic abundances in drillholes ER-5-4 and UE-5n appear to correlate very closely in this depth range. Mineral abundances between depths of about 344 and 379 m in drillhole UE-5n appear to correlate with the distinctive zone in drillhole ER-5-4 between the 315 and 340 m depth range noted above. Most obviously in this zone, the clinoptilolite abundance is elevated, and the cristobalite abundance is diminished. Kaolinite is not present. This example clearly shows that certain zones of mineral abundance may be recognized and correlated laterally to different drillholes in southern Frenchman Flat over scales of hundreds of meters, as indicated by Warren et al. (2002) for alluvial layers.

Figure 3.3 shows the mineral abundance data for ER-5-3, which is located in northern Frenchman Flat 5855 m NNE of ER-5-4. The mineral abundance data in ER-5-3 span depths between about 90 and 610 m. It is expected that the provenance of alluvium will exhibit differences between central and northern Frenchman Flat. Warren et al. (2002) point out that alluvium from ER-5-4 and UE-5n is vitric and chemically resembles the Wahmonie Formation, but also shows some influence from other prominent lithologies proximal to Frenchman Flat. Alluvium from ER-5-3 and U-11g-1 chemically resembles regional ash flow tuffs and is predominantly zeolitic rather than vitric. The differences are evident by comparison of mineral abundances in ER-5-4 and ER-5-3 (Figures 3.1 and 3.3). Among the sorbing minerals, ER-5-3 exhibits several differences with respect to ER-5-4 over a similar depth range:

- larger abundances of clinoptilolite,

- slightly lower abundances of mica at greater depth,

- <0.1 mass percent hematite below about 460 m depth,

- more extensive zones of high calcite abundance, and

- slightly lower smectite abundance at greater depths.

Overall, the depth profiles of sorbing mineral abundances are clearly different between drillholes ER-5-3 and ER-5-4. In addition, no obvious correlation of zonal mean mineral abundances is evident, as will be discussed later in this chapter.

The depth profiles of non-sorbing mineral abundances are also very different between ER-5-3 and ER-5-4. For example:

- No dolomite appears in ER-5-3 (below detection limit), although it occasionally appears in ER-5-4.

- Kaolinite is generally present to a depth of 1000 m (except for the 315 to 340 m depth range) in ER-5-4, but only to a depth of about 390 m in ER-5-3 (except for the 180 to 270 m depth range).

- Glass is abundant in ER-5-4 and sporadic in ER-5-3.

- Cristobalite abundance is consistently lower in ER-5-3 below a depth of about 220 m.

- The zeolites analcime and mordenite appear occasionally in ER-5-3, but not in ER-5-4.

- Orthoclase (low-T K-feldspar) abundance is consistently lower in ER-5-3 below a depth of about 230 m.

- Bytownite (plagioclase) abundance is typically lower in ER-5-3.

- Opal is rare in ER-5-4, but generally ubiquitous in ER-5-3 below a depth of about 200 m.

- The quartz fraction is usually higher in ER-5-3.

- Tridymite is absent below a depth of about 200 m in ER-5-3 and below a depth of about 700 m in ER-5-4 (except for the 315 to 340 m interval).

Interestingly, sanidine (high-T K-feldspar) and albite (Na-plagioclase) abundances exhibit similar decreases below similar depths of about 230-310 m.

Figure 3.4 shows mineral abundance data for U-11g-1, located 720 m NNE of ER-5-3. Mean zonal abundances appear to correlate between U-11g-1 and ER-5-3 at similar depths, suggesting that zones with similar abundances of minerals or alluvial layers defined by Warren et al. (2002) may be laterally extensive over scales of hundreds of meters in the northern Frenchman Flat area. However, due to the limited XRD data for U-11g-1, this correlation is not verified at all depths.
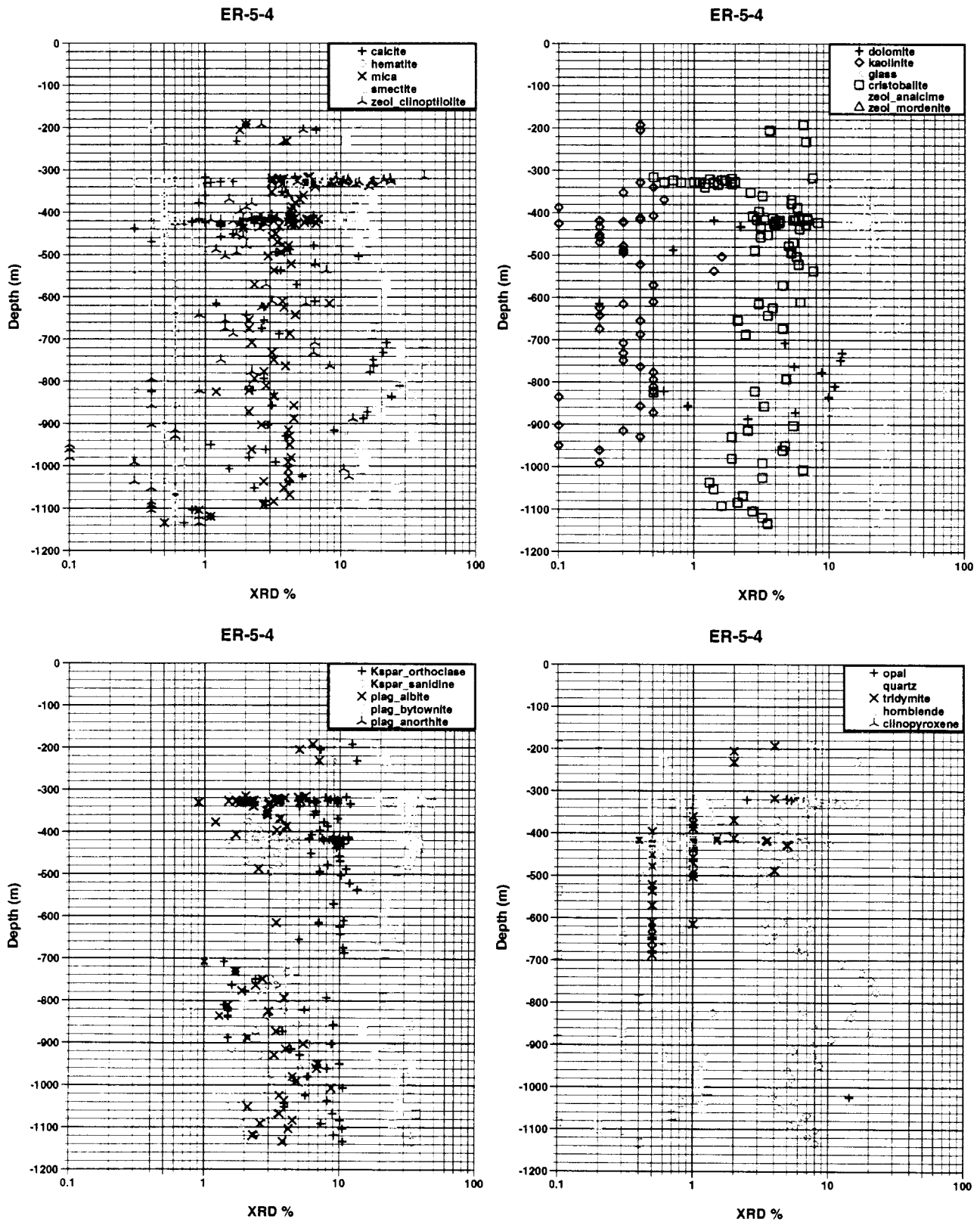
Figure 3.1 Mineral abundance data from ER-5-4 obtained by XRD analysis. Depth relative to ground surface. Data from Warren et al. (2002).

3-6
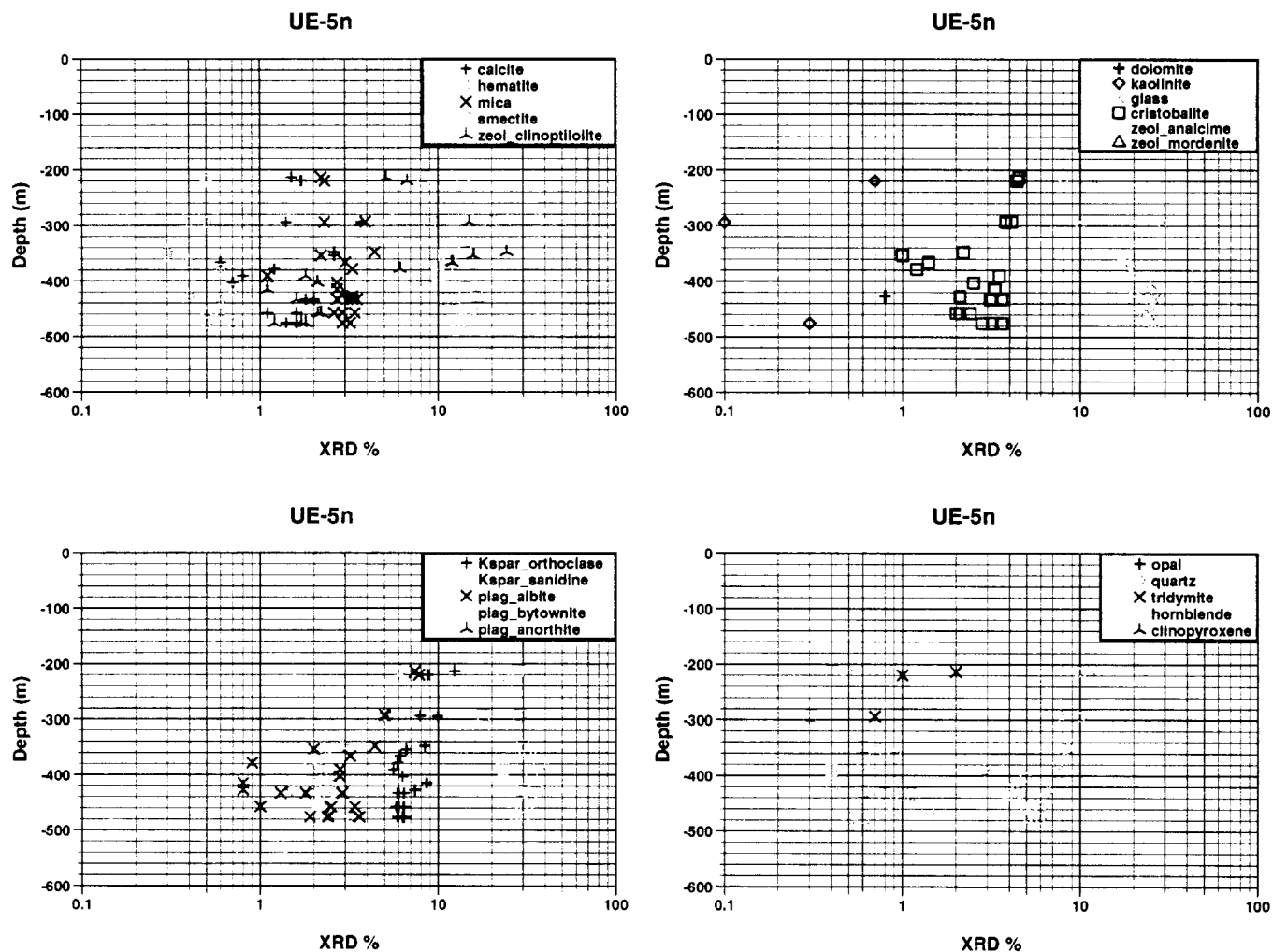
Figure 3.2 Mineral abundance data from UE-5n obtained by XRD analysis. Depth relative to ground surface. Data from Warren et al. (2002).
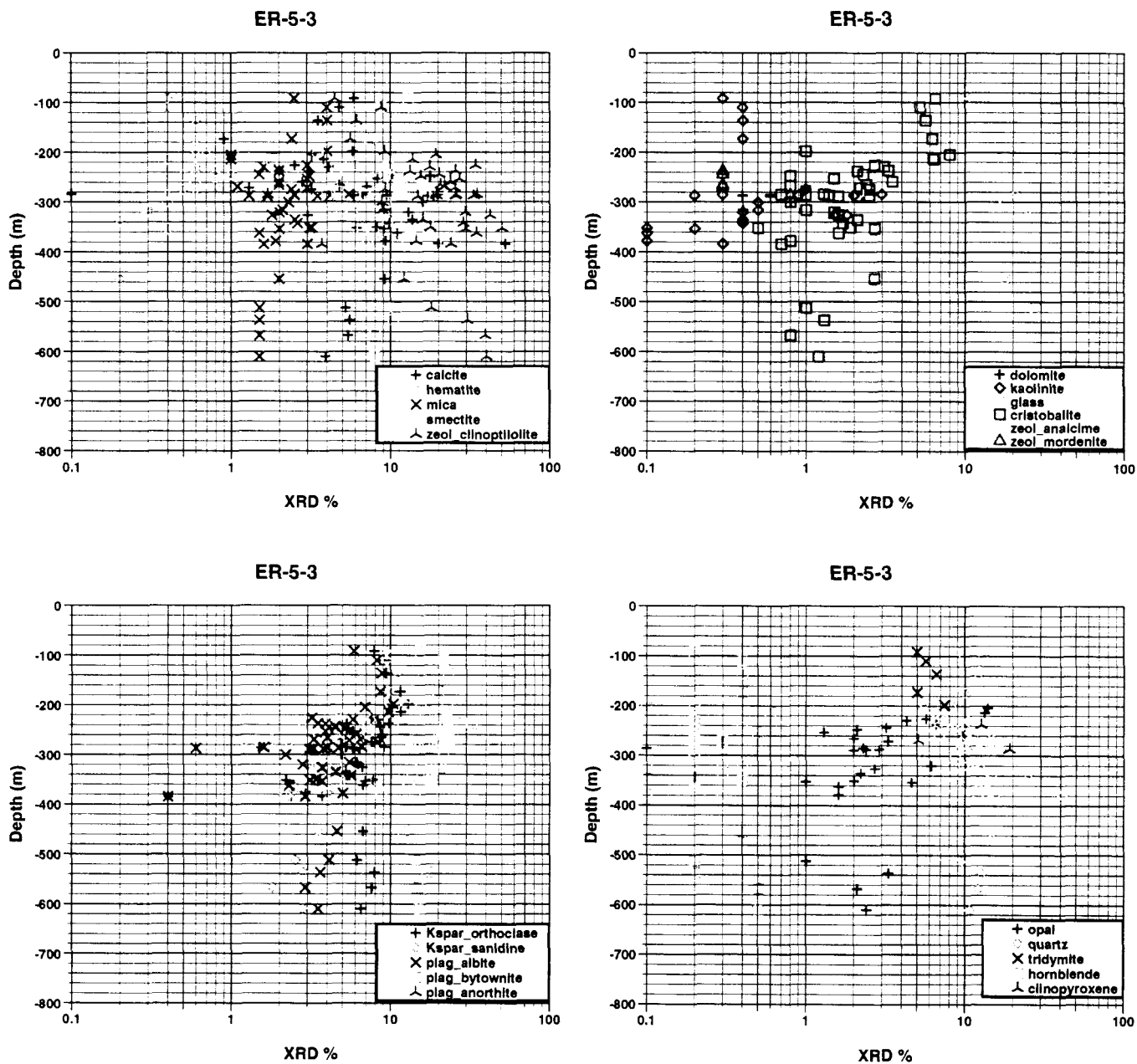
Figure 3.3 Mineral abundance data from ER-5-3 obtained by XRD analysis. Depth relative to ground surface. Data from Warren et al. (2002).
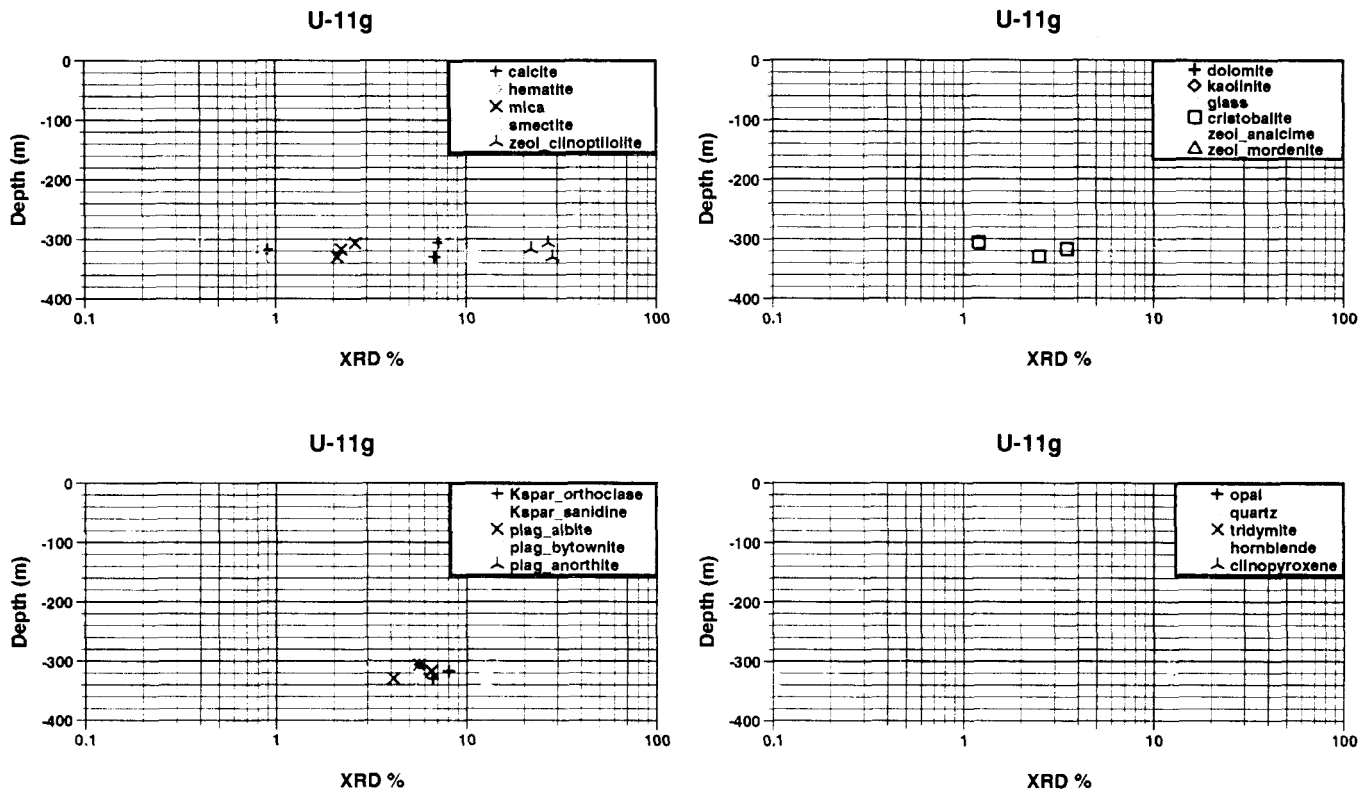
Figure 3.4 Mineral abundance data from drillhole U-11g-1 obtained by XRD analysis. Depth relative to ground surface. Data from Warren et al. (2002).

3.2 Univariate Statistics

Univariate statistics are functions of one variable, such as mineral percentage. A bivariate statistic is a function of two variables, such as mineral percentage at one location and mineral percentage at another location (e.g. spatial correlation or variogram) or mineral percentage of two different minerals at the same location (e.g., correlation).

Typical univariate statistics of interest are mean, variance, and median as well as the entire frequency distribution (histogram). This section examines the frequency distributions of the mineral abundances to help identify and distinguish "zones" having consistent mean and random variability of mineral abundances. Based on our preliminary interpretation of the mineral fraction data versus depth (section 3.1), the major non-random cause of spatial variability of mineral abundances appears to be zonal. The zonal variation is primarily attributed to differences in provenance of alluvial layers (Warren et al., 2002).

Both histograms and normal probability plots will be used to examine the frequency distributions. Normal probability plots provide means for examining the frequency distribution relative to a normal (Gaussian) distribution. If the frequency distribution of the data is normal, the data will plot as a straight line on the normal probability plot. An important reason for examining the histograms and probability plots is to identify sub-populations within the data that

appear to correspond to distinct zones. Data having different sub-populations with different means and variances may show distinct peaks on the histograms and segmented lines of different slope on the normal probability plot. The histograms and normal probability plots are scaled both linearly and logarithmically to examine the shape of the frequency distributions. In some cases either the linear or logarithmic (log) scale is more useful, so both are shown for all minerals. The log scale is particularly useful for minerals that exhibit a large range in abundance, such as calcite and clinoptilolite.

3.2.1 Histograms

Histograms are useful for examining the variation of mineral abundance in several ways:

- to illustrate the range of mineral abundances,

- to illustrate the most frequent mineral abundances,

- to examine the shape of the distribution compared to a normal or log-normal distribution, and

- to examine the possibility of bi-modal or multi-modal distributions indicating two or at least three distinct sub-populations, respectively, within the frequency distribution.

Histograms are presented both on a linear and logarithmic scale. For some minerals, linearly scaled histograms have large right-skewness, indicating that the frequency distributions are better viewed with a log scale. Right skewness in the linearly scaled histogram tends to occur for minerals that have a large range in mineral abundance, such as calcite and clinoptilolite.

The histograms are presented along with several univariate statistics — mean, standard deviation, coefficient of variation, minimum and maximum, median (50th percentile), and lower and upper quartiles (25th and 75th percentiles) — at upper right. The coefficient of variation is the mean divided by the standard deviation, which measures the degree of spread in the distribution. A coefficient of variation of 1.0 or greater indicates either a relatively large range of values, a large skewness, or a bi- or multi-modal distribution. Comparison of the mean to the median also indicates skewness; if the median is significantly less than the mean, the distribution is skewed right.

3.2.1.1 Linearly Scaled Histograms

Figures 3.5 to 3.8 show histograms of mineral abundance (mass percentage based on XRD data) on a linear scale for all 21 minerals from ER-5-3, ER-5-4, UE-5n, and U-11g-1. Some distinct sub-populations within the frequency distributions are readily recognized. Some of the distributions are bi- or multi-modal. Often, the mineral abundance for many samples is below the detection limit (mineral abundances reported as below the detection limit were included as 0% in the summary statistics and histograms). For example, the left-most peak on hematite histogram indicates that a large number of samples contained iron oxide abundances below the

detection limit. The frequency scale (y-axis) on the histogram for hematite indicates that the hematite is below the detection limit in about 19% of the data. The histograms, in conjunction with the depth versus mineral abundance plots (Figures 3.1 to 3.4), indicate several other minerals with abundance frequently below the detection limit — dolomite, kaolinite, analcime, mordenite, clinopyroxene, glass, cristobalite, opal, tridymite, sanidine, albite, and anorthite. Other minerals — mica, smectite, quartz, hornblende, orthoclase, and bytownite — are ubiquitous or rarely observed to be below the detection limit.

Because of the strong right-skewness of the frequency distributions for calcite and clinoptilolite, it is difficult to determine from the linearly scaled histograms whether a significant proportion of the XRD percentages for calcite and clinoptilolite are below the detection limit. For calcite and clinoptilolite, a log-scale histogram (see Figure 3.9) better displays the frequency distribution, particularly for much of the data having low XRD percentages.

Only two of the linearly scaled histograms obviously reveal multi-modal frequency distributions — orthoclase and bytownite — having three and four apparently distinct peaks, respectively. Distinct peaks for orthoclase are centered at about 2, 6, and 9 mass percent, and for bytownite at about 1.5, 15, 21, and 33 mass percent. Most of the histograms show right skewness, indicating that the frequency distributions may be closer to log-normal than normal. If the frequency distribution is multi-modal, the question of skewness within the entire frequency distribution is not directly applicable. Several of the minerals — dolomite, kaolinite, analcime, mordenite, clinopyroxene, opal, tridymite, and anorthite — have zero median values, indicating that for the majority of the samples these mineral abundances are below XRD detection limits (~0.1 mass percent). Table 3.1 summarizes the univariate statistical analysis of the linearly scaled mineral abundance histograms. In identifying the number of modes or "peaks" in the frequency distributions, the " +" symbol is used to indicate "greater than or equal to."

Table 3.1 Summarized interpretation of univariate statistics of the linearly scaled mineral abundance histograms.

Mineral	Mean (mass %)	σ (%)	σ/mean	Median (mass %)	Skewness	# of modes
Calcite	5.11	6.64	1.30	2.70	Right	1+
Hematite	0.44	0.27	0.61	0.50	?	2
Mica	3.44	1.71	0.50	3.20	None	1
Smectite	13.81	7.54	0.54	12.20	Right	1
Clinoptilolite	9.90	11.01	1.11	4.10	Right	1+
Dolomite	0.52	2.01	3.88	0.00	?	2+
Kaolinite	0.21	0.38	1.80	0.00	?	2+
Analcime	0.01	0.18	12.73	0.00	?	2
Mordenite	0.02	0.14	6.50	0.00	?	2
Clinopyroxene	0.23	1.83	8.07	0.00	?	2
Glass	13.11	12.18	0.93	15.00	?	2
Cristobalite	2.88	1.95	0.68	2.50	Right	2+
Opal	0.89	2.38	2.67	0.00	?	2+
Quartz	8.42	4.94	0.59	7.50	Right	1+
Tridymite	0.56	1.27	2.28	0.00	?	2+
Hornblende	0.57	0.40	0.71	0.50	Right	1+
Orthoclase	7.34	2.71	0.37	7.40	?	3+
Sanidine	3.26	2.25	0.69	2.80	?	2+
Albite	2.95	2.37	0.80	2.90	?	2
Bytownite	24.88	9.56	0.38	26.10	?	4
Anorthite	0.01	0.12	12.73	0.00	?	2
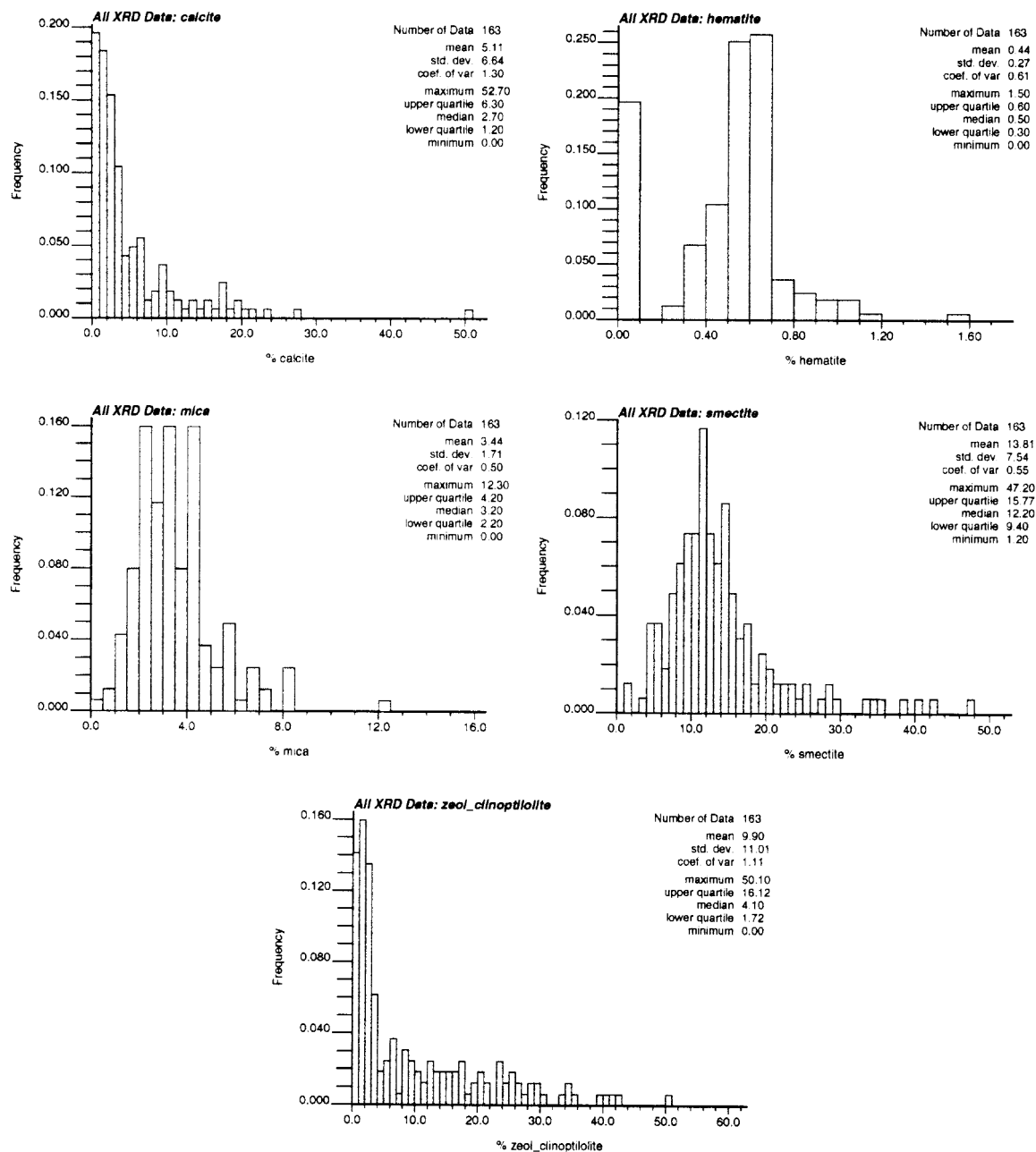
Figure 3.5 Linearly scaled histograms of calcite, hematite, mica, smectite, and clinoptilolite abundances for XRD data from ER-5-4, ER-5-3, UE-5n, and U-11g-1. Mineral abundances reported as below the detection limit were included as 0% in these histograms. Data from Warren et al. (2002).

All XRD Data: dolomite

Number of Data	163
mean	0.52
std. dev.	2.01
coef. of var	3.88
maximum	12.40
upper quartile	0.00
median	0.00
lower quartile	0.00
minimum	0.00

All XRD Data: kaolinite

Number of Data	163
mean	0.21
std. dev.	0.38
coef. of var	1.80
maximum	3.00
upper quartile	0.30
median	0.00
lower quartile	0.00
minimum	0.00

All XRD Data: zeol_analcime

Number of Data	163
mean	0.01
std. dev.	0.18
coef. of var	12.73
maximum	2.30
upper quartile	0.00
median	0.00
lower quartile	0.00
minimum	0.00

All XRD Data: zeol_mordenite

Number of Data	163
mean	0.02
std. dev.	0.14
coef. of var	6.50
maximum	1.50
upper quartile	0.00
median	0.00
lower quartile	0.00
minimum	0.00

All XRD Data: clinopyroxene

Number of Data	163
mean	0.23
std. dev.	1.83
coef. of var	8.07
maximum	19.20
upper quartile	0.00
median	0.00
lower quartile	0.00
minimum	0.00

Figure 3.6 Linearly scaled histograms of dolomite, kaolinite, analcime, mordenite, and clinopyroxene abundances for XRD data from ER-5-4, ER-5-3, UE-5n, and U-11g-1. Mineral abundances reported as below the detection limit were included as 0% in these histograms. Data from Warren et al. (2002).
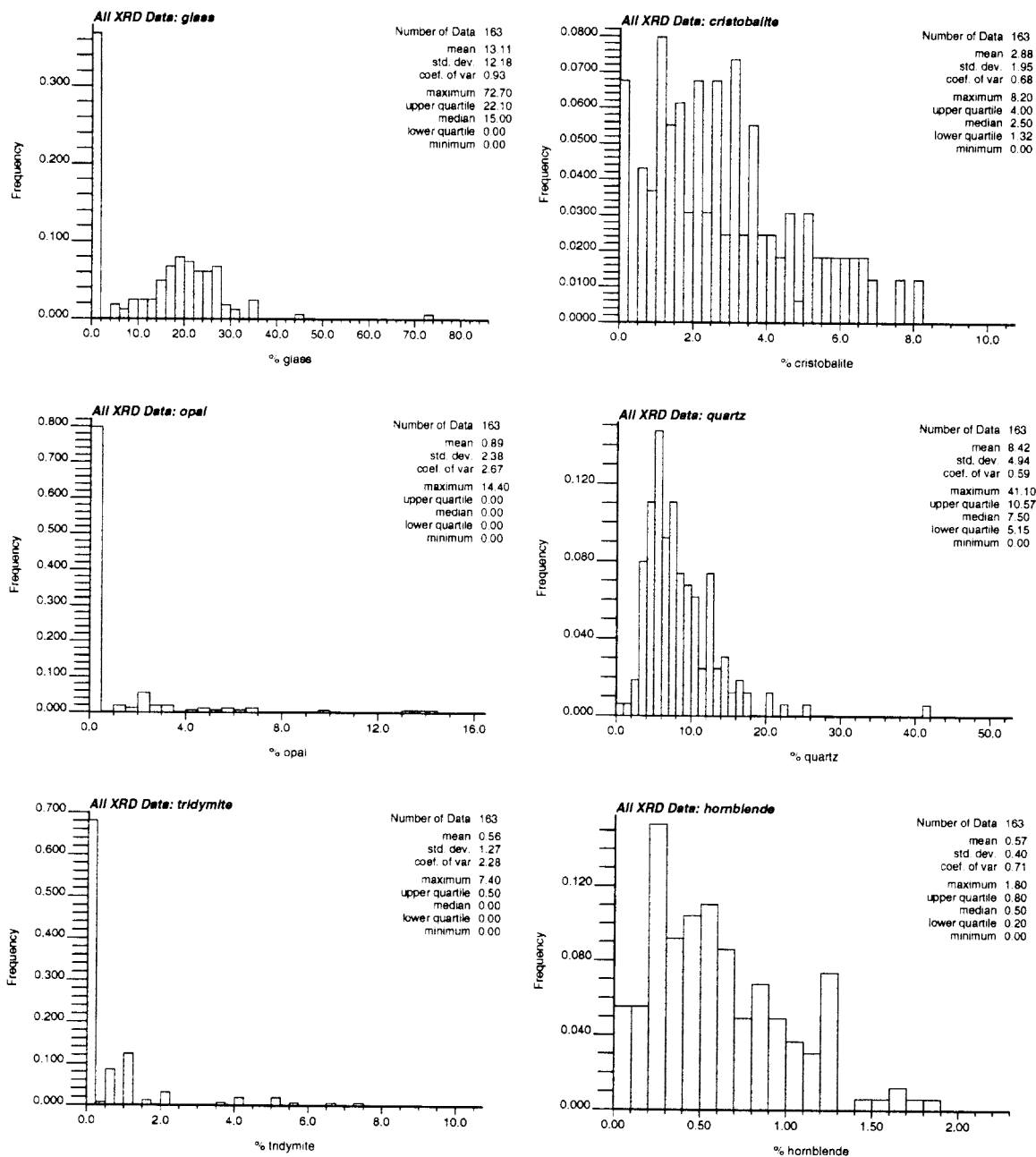
Figure 3.7 Linearly scaled histograms of glass, cristobalite, opal, quartz, and tridymite, and hornblende abundances for XRD data from ER-5-4, ER-5-3, UE-5n, and U-11g-1. Mineral abundances reported as below the detection limit were included as 0% in these histograms. Data from Warren et al. (2002).

All XRD Data: feld_Kspar_orthoclase

Number of Data	163
mean	7.34
std. dev.	2.71
coef. of var	0.37
maximum	13.40
upper quartile	9.37
median	7.40
lower quartile	5.80
minimum	0.40

Frequency axis: 0.000, 0.020, 0.040, 0.060, 0.080, 0.100
X-axis: 0.0, 4.0, 8.0, 12.0, 16.0
% feld_Kspar_orthoclase

All XRD Data: feld_Kspar_sanidine

Number of Data	163
mean	3.26
std. dev.	2.25
coef. of var	0.69
maximum	12.30
upper quartile	3.97
median	2.80
lower quartile	2.10
minimum	0.00

Frequency axis: 0.000, 0.040, 0.080, 0.120, 0.160
X-axis: 0.0, 4.0, 8.0, 12.0, 16.0
% feld_Kspar_sanidine

All XRD Data: feld_plag_albite

Number of Data	163
mean	2.95
std. dev.	2.37
coef. of var	0.80
maximum	10.40
upper quartile	4.10
median	2.90
lower quartile	0.90
minimum	0.00

Frequency axis: 0.000, 0.050, 0.100, 0.150, 0.200
X-axis: 0.0, 4.0, 8.0, 12.0, 16.0
% feld_plag_albite

All XRD Data: feld_plag_bytownite

Number of Data	163
mean	24.88
std. dev.	9.56
coef. of var	0.38
maximum	47.10
upper quartile	32.25
median	26.10
lower quartile	18.22
minimum	1.00

Frequency axis: 0.0000, 0.0100, 0.0200, 0.0300, 0.0400, 0.0500, 0.0600
X-axis: 0.0, 10.0, 20.0, 30.0, 40.0, 50.0
% feld_plag_bytownite

All XRD Data: feld_plag_anorthite

Number of Data	163
mean	0.01
std. dev.	0.12
coef. of var	12.73
maximum	1.60
upper quartile	0.00
median	0.00
lower quartile	0.00
minimum	0.00

Frequency axis: 0.00, 0.20, 0.40, 0.60, 0.80, 1.00
X-axis: 0.00, 0.50, 1.00, 1.50, 2.00
% feld_plag_anorthite

Figure 3.8 Linearly scaled histograms of orthoclase, sanidine, albite, bytownite, and anorthite, and hornblende abundances for XRD data from ER-5-4, ER-5-3, UE-5n, and U-11g-1. Mineral abundances reported as below the detection limit were included as 0% in these histograms. Data from Warren et al. (2002).

3.2.1.2 Log-Scaled Histograms

Figures 3.9-3.12 show log-scaled histograms for the 21 minerals reported in the XRD analysis. The log scaling is useful because:

- It helps span the wide variation in mineral abundances (up to 3 orders of magnitude).

- The mineral abundances within zones or alluvial layers tend to be log-normally distributed.

- Portions of the frequency distribution that fall below the detection limit are more clearly identified.

For most minerals, distinct sub-populations within the frequency distributions are more readily recognized on the log scale. Peaks in the frequency distribution corresponding to values with mineral abundances at or below the detection limit of the XRD analysis are more easily identified. Distinct sample populations at or below the detection limit are clearly evident in calcite and clinoptilolite histograms in Figure 3.9, which were not obvious with linear scaling in Figure 3.5. Bi- or multi-modal distributions are more apparent on the log scale. For example, the calcite and clinoptilolite frequency distributions appear to be composed of three or more sub-populations in addition to the one at or below the detection limit. The frequency distributions for glass, cristobalite, and albite appear to contain two sub-populations in addition to the sub-population at or below the detection limit. Orthoclase and bytownite appear to contain two or more sub-populations with the log scale. In the case of orthoclase and bytownite, which have very low coefficients of variation of 0.37 and 0.38, respectively, the linear scaling is actually more revealing.

The log-scaled frequency distributions generally show less skewness. In sub-populations for data above detection limits, nearly symmetric, bell-shaped distributions are evident for hematite, mica, smectite, quartz. In addition, the frequency distributions within bi- or multi-modal distributions appear more symmetric, particularly for calcite, hematite, clinoptilolite, glass, cristobalite, orthoclase, sanidine, and albite. Overall, the mineral abundance frequency distributions are better characterized as uni-, bi-, or multi-modal log normal distributions rather than uni-, bi- or multi-modal normal distributions. Therefore, if variability of mineralization is to be considered in a modeling effort, assumptions of log-normal distributions within different zones will be more plausible and justifiable for most minerals. Nonetheless, it is useful to examine the frequency distributions with both linear and logarithmic scaling, mainly because some minerals have narrow ranges of variability and some minerals have wide ranges of variability.

Table 3.2 summarizes interpretation of the univariate statistics for the log-scaled histograms. In Table 3.2, the units are scaled to logarithm of abundance as a fraction instead of percentage to better accommodate log units. The mean, standard deviation, coefficient and median are based only on data values above the detection limit of 0.1%. The coefficient of variation is not shown

because it is not a viable statistic for logarithmic values. The percentage of values above the XRD detection limit for each mineral are also given.

Compared to the univariate statistics for the linearly scaled histograms, the log-scaled histograms exhibit consistently smaller variances and skewness. The reduction in variance is attributed not only to the $\log_{10}$ units, but also the exclusion of the data below detection limits and reduction in skewness.

Table 3.2 Summarized interpretation of univariate statistics for log-scaled mineral abundance histograms.[1]

Mineral	Mean Log Mass Fraction	σ	Median	Skewness	% above detection limit	# of modes
Calcite	-1.48	0.46	-1.51	Small	89	1+
Hematite	-2.29	0.13	-2.30	Small	79	2
Mica	-1.50	0.21	-1.49	Small	98	1
Smectite	-0.92	0.23	-0.91	Small	100	1
Clinoptilolite	-1.32	0.61	-1.32	Small	98	3+
Dolomite	-1.77	0.56	-2.05	?	14	2+
Kaolinite	-2.48	0.30	-2.52	Small	47	2+
Analcime	-1.64	0.0	-1.64	?	0.6	2
Mordenite	-2.33	0.28	-2.52	?	3.7	2
Clinopyroxene	-0.97	0.25	-0.90	?	1.9	2
Glass	-0.72	0.19	-0.69	Small	63	2
Cristobalite	-1.58	0.29	-1.55	Small	90	2+
Opal	-1.55	0.46	-2.00	Small	21	2
Quartz	-1.13	0.22	-1.12	Small	99	1+
Tridymite	-1.87	0.44	-1.82	Small	20	3
Hornblende	-2.34	0.31	-2.30	Small	0.71	2+
Orthoclase	-1.18	0.23	-1.13	Small	100	3+
Sanidine	-1.50	0.21	-1.53	Small	91	2+
Albite	-1.48	0.25	-1.46	Small	77	2
Bytownite	-0.65	0.25	-0.58	Small	99	4
Anorthite	-1.80	0.0	-1.80	?	0.6	2

[1] Note that values reported as below detection limit were not included in log-scaled summary statistics.
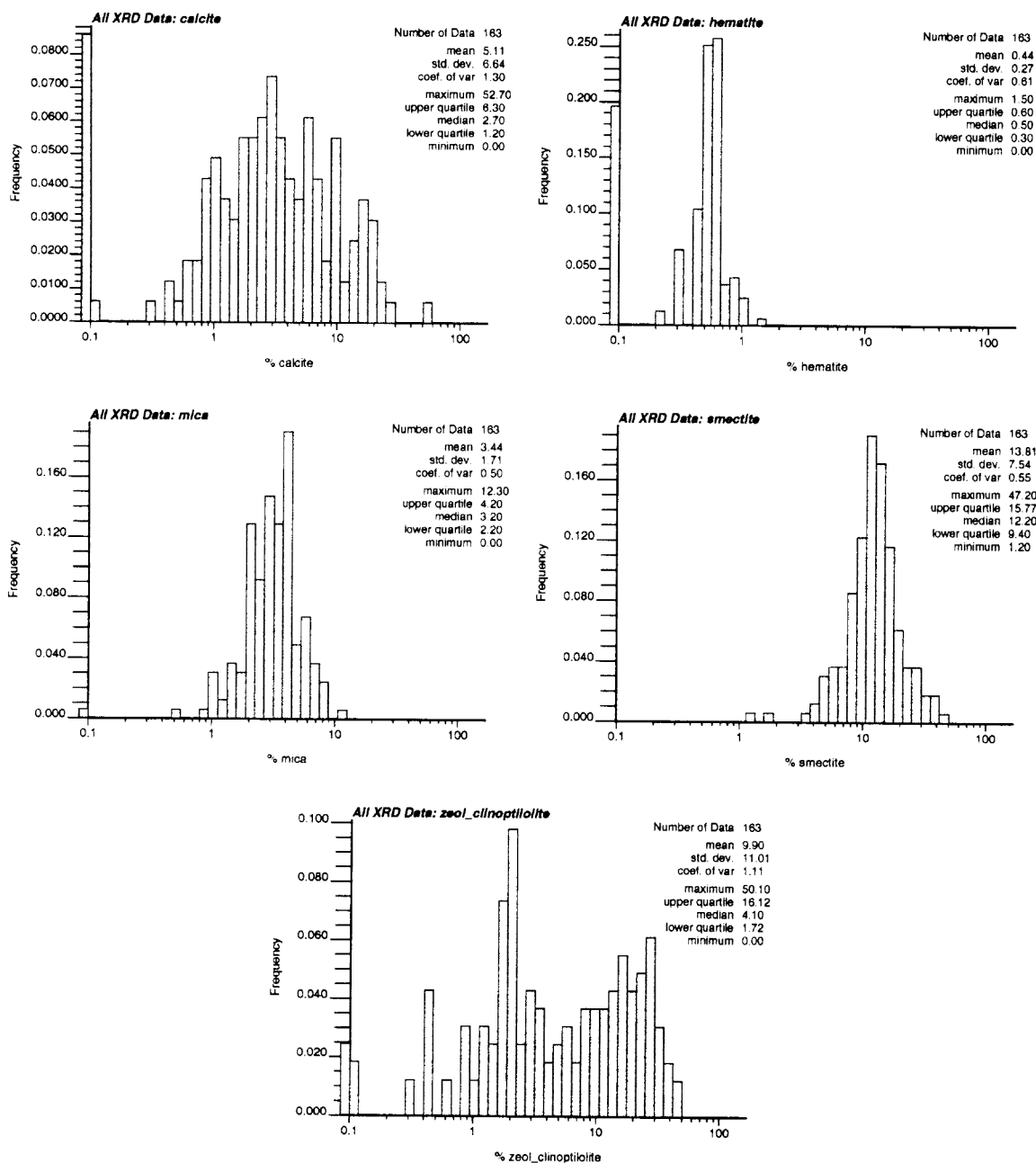
Figure 3.9 Log-scaled histograms of calcite, hematite, mica, smectite, and clinoptilolite abundances for XRD data from ER-5-4, ER-5-3, UE-5n, and U-11g-1. Mineral abundances reported as below the detection limit were plotted to the left of the 0.1% value. Data from Warren et al. (2002).

All XRD Data: dolomite

Frequency

0.800
0.700
0.600
0.500
0.400
0.300
0.200
0.100
0.000

0.1   1   10   100

% dolomite

Number of Data 163
mean 0.52
std. dev. 2.01
coef. of var 3.88
maximum 12.40
upper quartile 0.00
median 0.00
lower quartile 0.00
minimum 0.00

All XRD Data: kaolinite

Frequency

0.500
0.400
0.300
0.200
0.100
0.000

0.1   1   10   100

% kaolinite

Number of Data 163
mean 0.21
std. dev. 0.38
coef. of var 1.80
maximum 3.00
upper quartile 0.30
median 0.00
lower quartile 0.00
minimum 0.00

All XRD Data: zeol_analcime

Frequency

1.00
0.80
0.60
0.40
0.20
0.00

0.1   1   10   100

% zeol_analcime

Number of Data 163
mean 0.01
std. dev. 0.18
coef. of var 12.73
maximum 2.30
upper quartile 0.00
median 0.00
lower quartile 0.00
minimum 0.00

All XRD Data: zeol_mordenite

Frequency

0.80
0.60
0.40
0.20
0.00

0.1   1   10   100

% zeol_mordenite

Number of Data 163
mean 0.02
std. dev. 0.14
coef. of var 8.50
maximum 1.50
upper quartile 0.00
median 0.00
lower quartile 0.00
minimum 0.00

All XRD Data: clinopyroxene

Frequency

1.00
0.80
0.60
0.40
0.20
0.00

0.1   1   10   100

% clinopyroxene

Number of Data 163
mean 0.23
std. dev. 1.83
coef. of var 8.07
maximum 19.20
upper quartile 0.00
median 0.00
lower quartile 0.00
minimum 0.00

Figure 3.10 Log-scaled histograms of dolomite, kaolinite, analcime, mordenite, and clinopyroxene abundances for XRD data from drillholes ER-5-4, ER-5-3, UE-5n, and U-11g-1. Mineral abundances reported as below the detection limit were plotted to the left of the 0.1% value. Data from Warren et al. (2002).
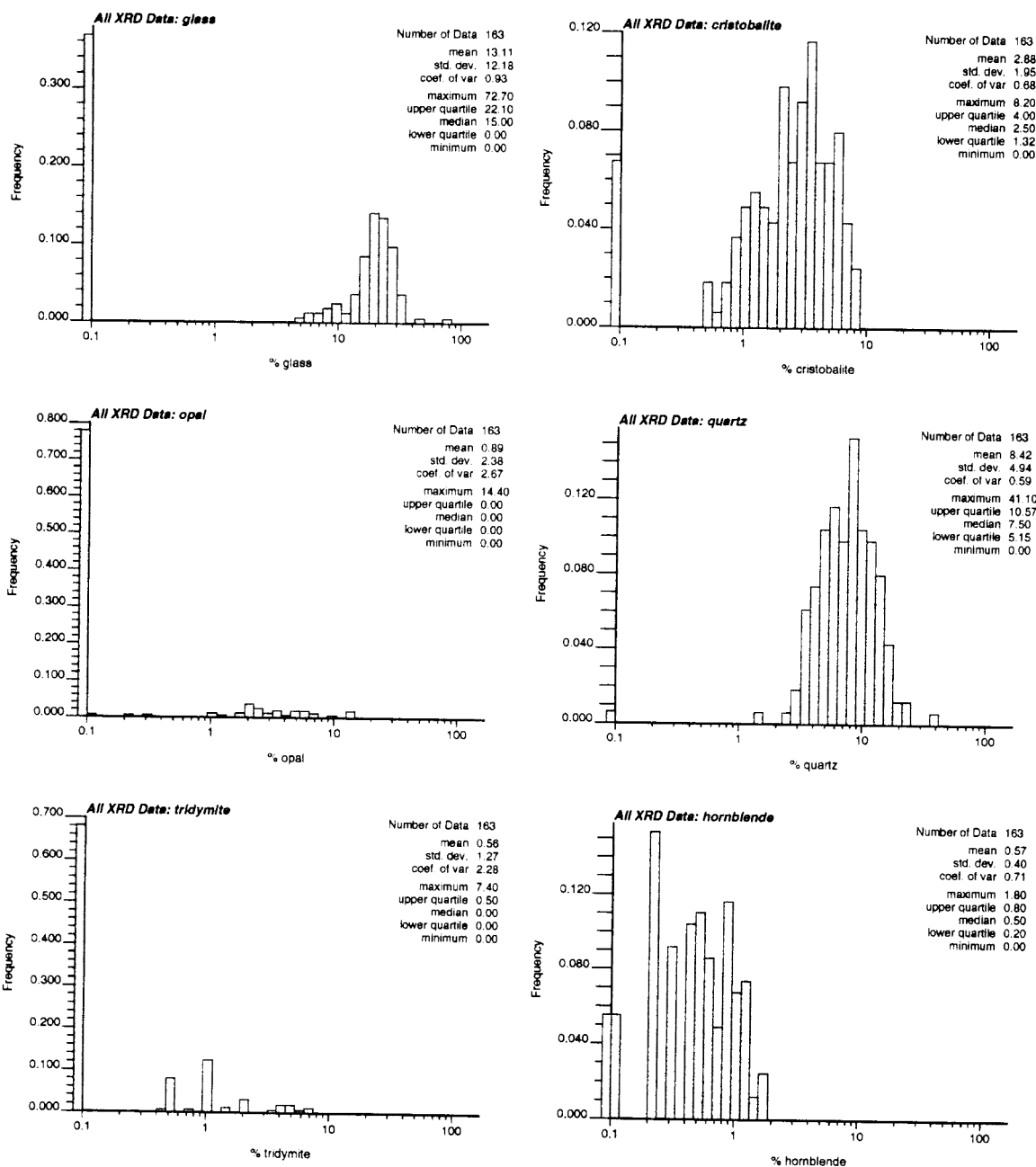
Figure 3.11 Log-scaled histograms of glass, cristobalite, opal, quartz, tridymite, and hornblende abundances for XRD data from drillholes ER-5-4, ER-5-3, UE-5n, and U-11g-1. Mineral abundances reported as below the detection limit were plotted to the left of the 0.1% value. Data from Warren et al. (2002).

3-21
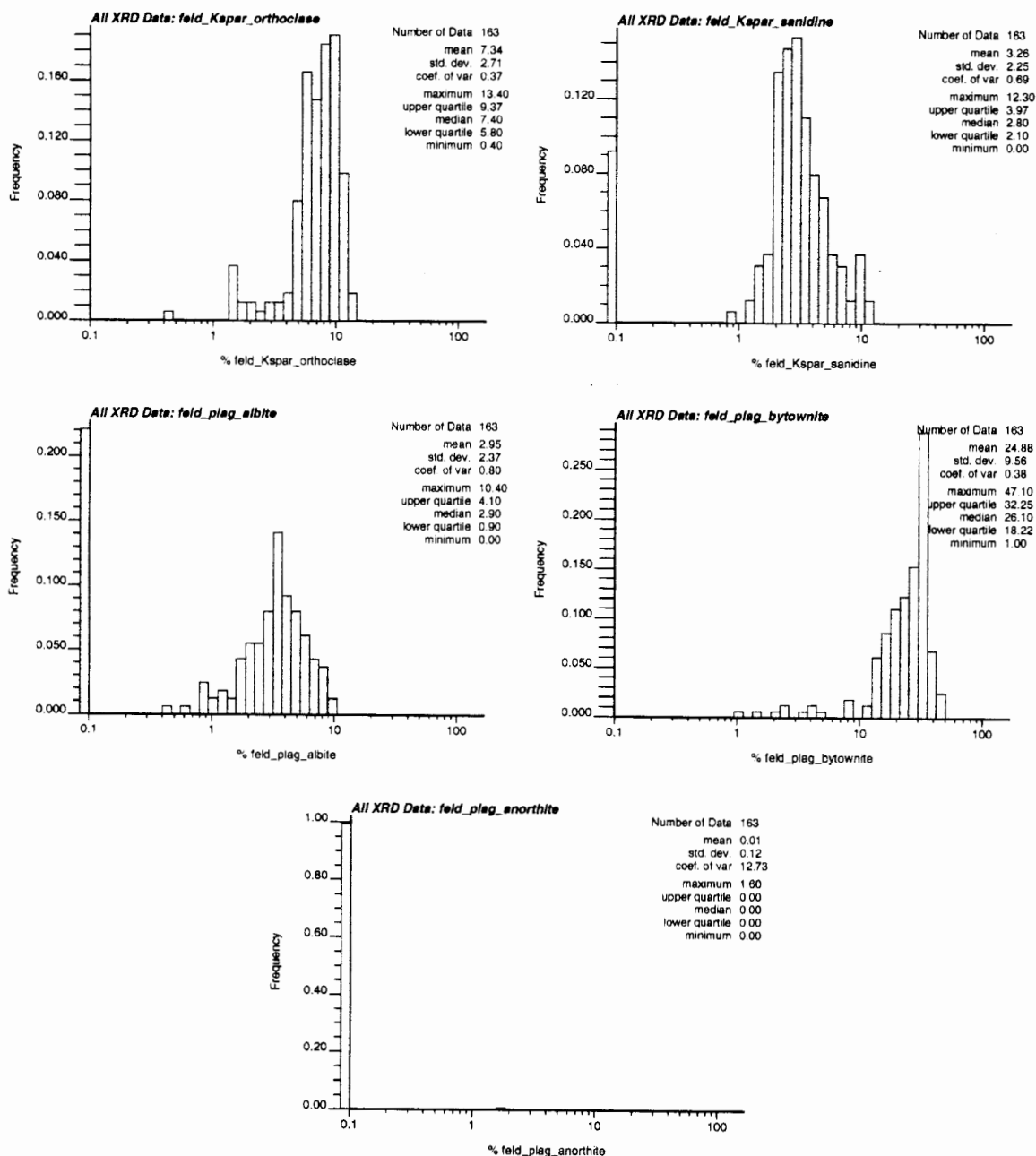
Figure 3.12 Log-scaled histograms of orthoclase, sanidine, albite, bytownite, and anorthite, and hornblende abundances for XRD data from drillholes ER-5-4, ER-5-3, UE-5n, and U-11g-1. Mineral abundances reported as below the detection limit were plotted to the left of the 0.1% value. Data from Warren et al. (2002).

3.2.2 Normal Probability Plots

Normal probability plots are used to compare a frequency distribution with a normal (Gaussian) distribution. In a normal probability plot, the cumulative probability of the data is plotted on a customized cumulative probability scale on the Y axis versus the data value on the X axis, which may be linearly or logarithmically scaled. If the frequency distribution is normal, the cumulative probability curve will plot along a straight line. Multiple sub-populations of normally-distributed data may be evident from multiple linear segments.

Both linear and log scaling are useful for analyzing the mineral abundance data on a probability plot. The linear scale may be more appropriate for minerals that exhibit small coefficients of variation for the range of samples analyzed, such as mica. The linear scale is also useful in accounting for mineral abundances reported as below the detection limit (plotted as 0 mass percent here); on a log scale, these values cannot be plotted. Also, the linear scale can be more revealing for analyzing the portion of the frequency distribution having larger values, which is compressed by the log scale. The log scale is usually more appropriate for data that are log-normally distributed or have a wide range of values. Also, the log scale can be more revealing for portions of the frequency distribution having smaller values.

Interpretation of the probability plot is not always straightforward. The cumulative probability plot may appear more curved than linear. This may be attributed to a non-normal distribution. Depending on the shape of the frequency distribution of sub-populations within the data, either the logarithmic or linear scale may yield a more linear cumulative distribution. The appearance of distinct linear segments indicates multiple sub-populations. The points where change in slope occur indicate possible cutoff values for dividing the data in sub-populations. Data near the tails (the extreme low and high values of the distribution) are usually undersampled, and thus may appear scattered. In general, undue attention should not be paid to the data tails.

3.2.2.1 Linearly Scaled Normal Probability Plots

Figures 3.13 to 3.16 show linearly scaled probability plots for the 21 minerals. The horizontal scales are linearly scaled in units of percent. The range of each horizontal scale is customized to the mineral because of the large differences in magnitude and range of mineral abundance for different minerals.

The interpretation of the probability plots is mainly concerned with identifying portions of the cumulative probability curve that indicate sub-populations within the data. For example, in the probability plot for smectite shown in Figure 3.13, two linear segments are evident, with a break in slope at about 16% smectite. Using the probability plot, the interpretation could be made that smectite generally falls into two sub-populations where a 16% cutoff value provides a good indication of whether a datum is more likely in a sub-population or zone of higher or lower smectite abundance.

Another important feature of the probability plot is the portion of the data that is below the detection limit. This appears as a vertical segment of cumulative probabilities on the far left of

the probability plot. For example, in Figure 3.13 the cumulative distribution function for hematite begins at the lower left by rising vertically to about 19%, which represents the portion of data where hematite abundances are below the detection limit. An important question is whether data which plot below the detection limit may actually represent the extreme low values of the frequency distribution of a sub-population of data entirely above the detection limit. This issue may be addressed by examining how the portions of the probability plot for data above and below the detection limit merge together. If a significant change in slope can be observed which is not a result of scatter in the tail, it is likely that much of the data below the detection limit represents a separate sub-population of very small or zero values. Hematite, for example, appears to exhibit a separate sub-population for values below 0.1 % because an abrupt slope change is seen in the cumulative probability between values of hematite abundance above and below 0.1%. On the other hand, no abrupt slope change is seen for mica abundance above and below 0.1%. The data for mica that fall below the detection limit probably represent extremely low values (tails) in a sub-population that falls mostly above the detection limit. Other minerals besides hematite that appear to exhibit sub-populations with very small or zero value abundances are calcite, clinoptilolite, dolomite, kaolinite, analcime, mordenite, clinopyroxene, glass, cristobalite, opal, tridymite, sanidine, albite, and anorthite. Other minerals besides mica that appear to be ubiquitous (where XRD zero values probably represent extremely low values in the frequency distribution) are smectite, quartz, hornblende, orthoclase, and bytownite.
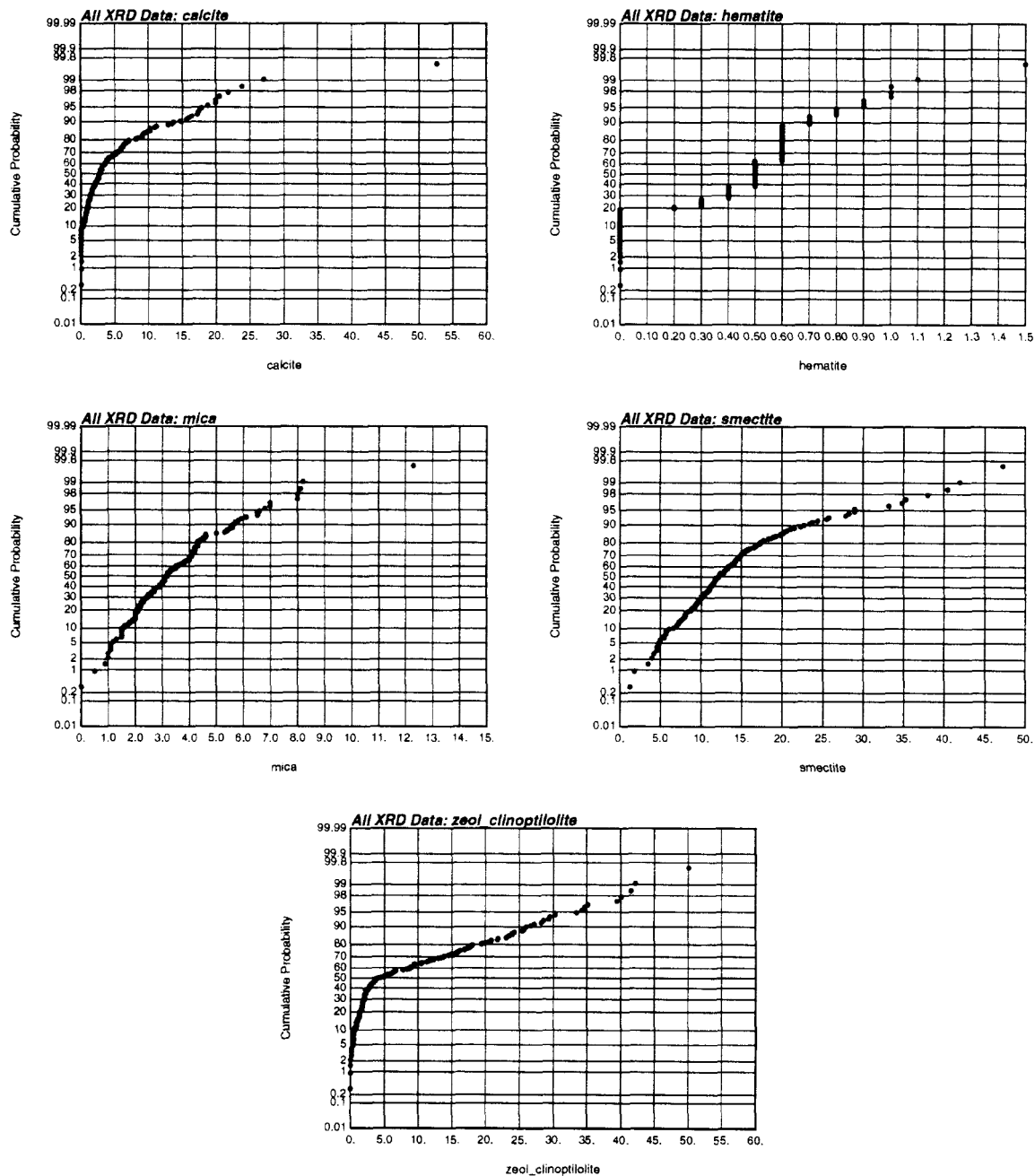
Figure 3.13 Linearly scaled probability plots of cumulative abundance of sorbing minerals calcite, hematite, mica, smectite, and clinoptilolite clinopyroxene detected by XRD analysis in ER-5-3, ER-5-4, UE-5n, and U-11g-1.
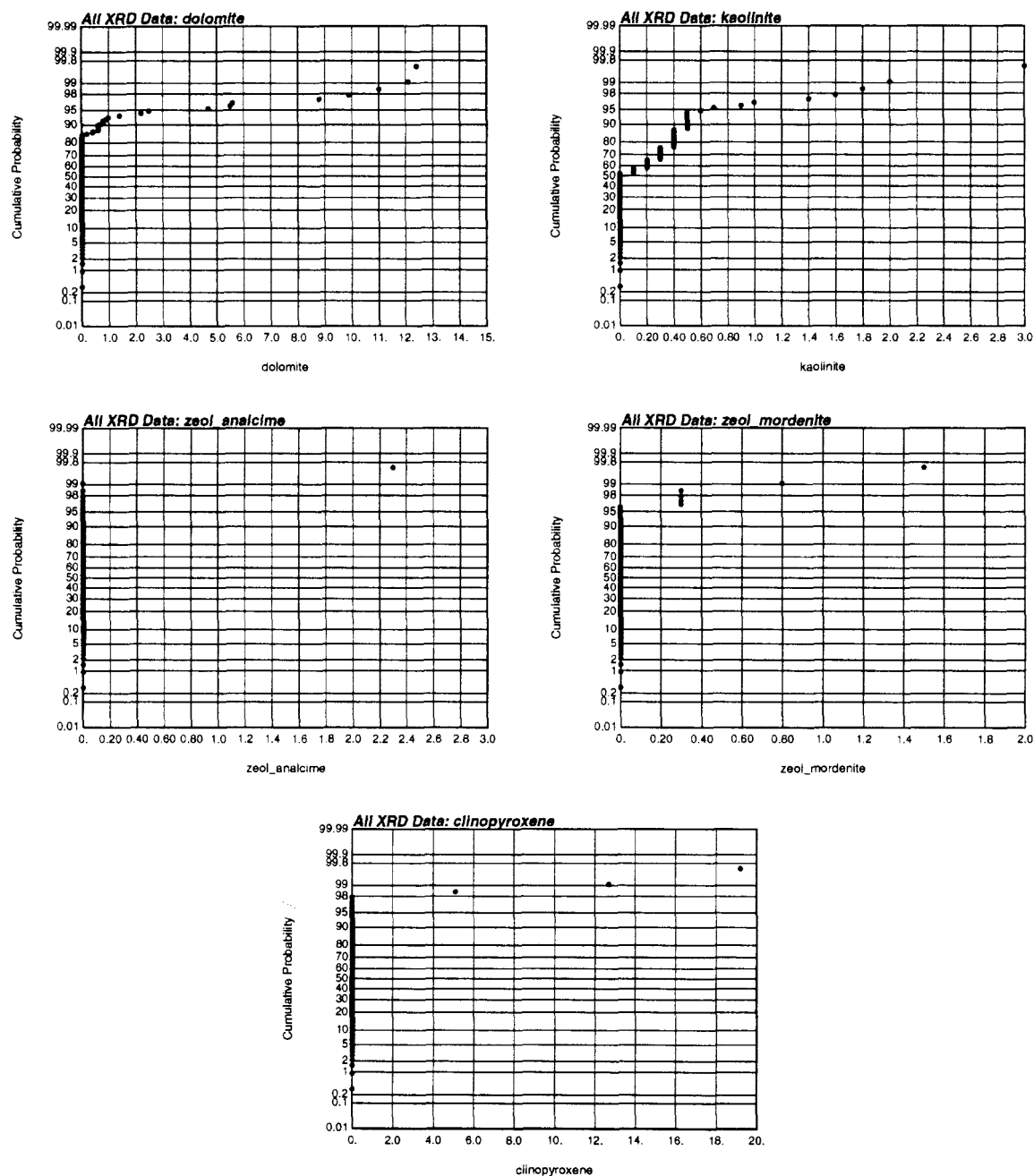
Figure 3.14 Linearly scaled probability plots of cumulative abundance of non-sorbing minerals dolomite, kaolinite, analcime, mordenite, and clinopyroxene detected by XRD analysis in ER-5-3, ER-5-4, UE-5n, and U-11g-1.
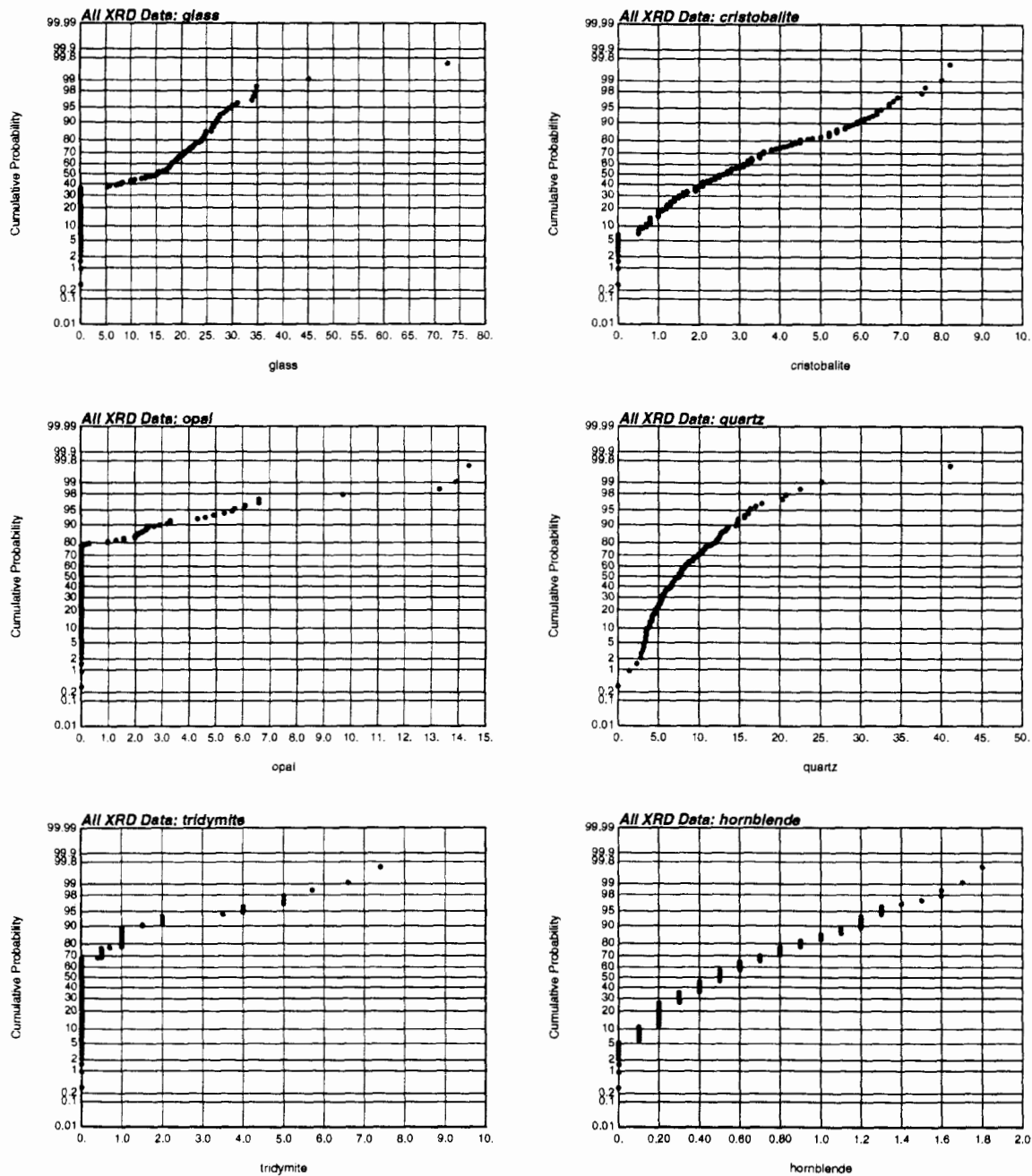
Figure 3.15 Linearly scaled probability plots of cumulative abundance of the non-sorbing minerals glass, cristobalite, opal, quartz, tridymite, and hornblende detected by XRD analysis in ER-5-3, ER-5-4, UE-5n, and U-11g-1.
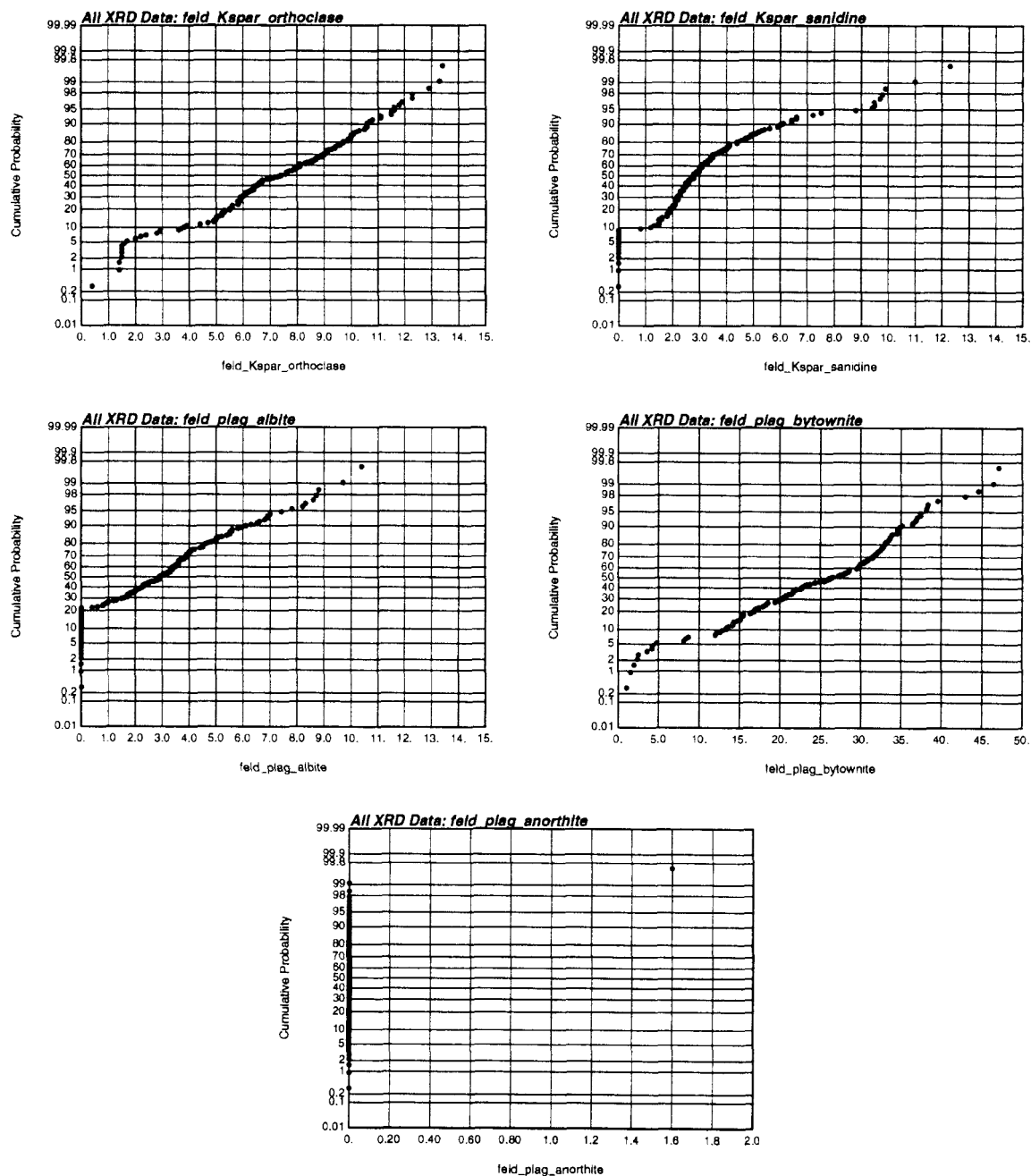
Figure 3.16 Linearly scaled probability plots of cumulative abundance of the non-sorbing minerals orthoclase, sanidine, albite, bytownite, anorthite detected by XRD analysis in ER-5-3, ER-5-4, UE-5n, and U-11g-1.

3.2.2.2 Log-Scaled Normal Probability Plots

Figures 3.17 to 3.20 show log-scaled normal probability plots of mineral abundance. Considering that the frequency distribution of most of the sub-populations appear approximately log-normal, a log-scaled probability plot should, in general, more clearly reveal separate sub-populations compared to the linearly scaled probability plot. This is particularly true for calcite and clinoptilolite, which have large ranges of mineral abundance. However, for other minerals similar interpretations can be made from both the linearly and log-scaled probability plots. The main exception is for identifying sub-populations with zero values (below the detection limit) — in this case the linear scale is more revealing.
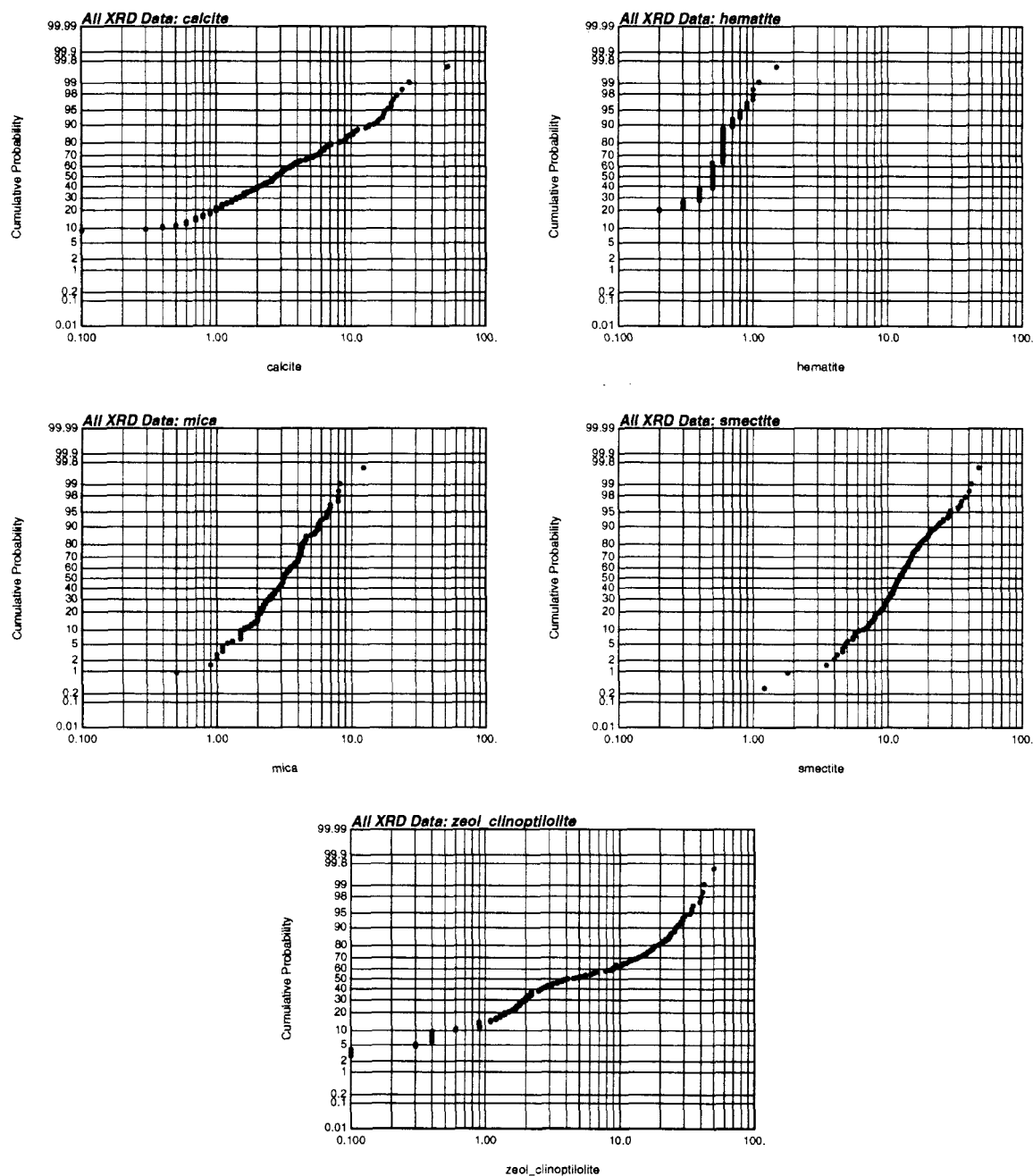
Figure 3.17 Log-scaled probability plots of cumulative abundance of sorbing minerals calcite, hematite, mica, smectite, and clinoptilolite clinopyroxene detected by XRD analysis in drill drillholes ER-5-3, ER-5-4, UE-5n, and U-11g-1.
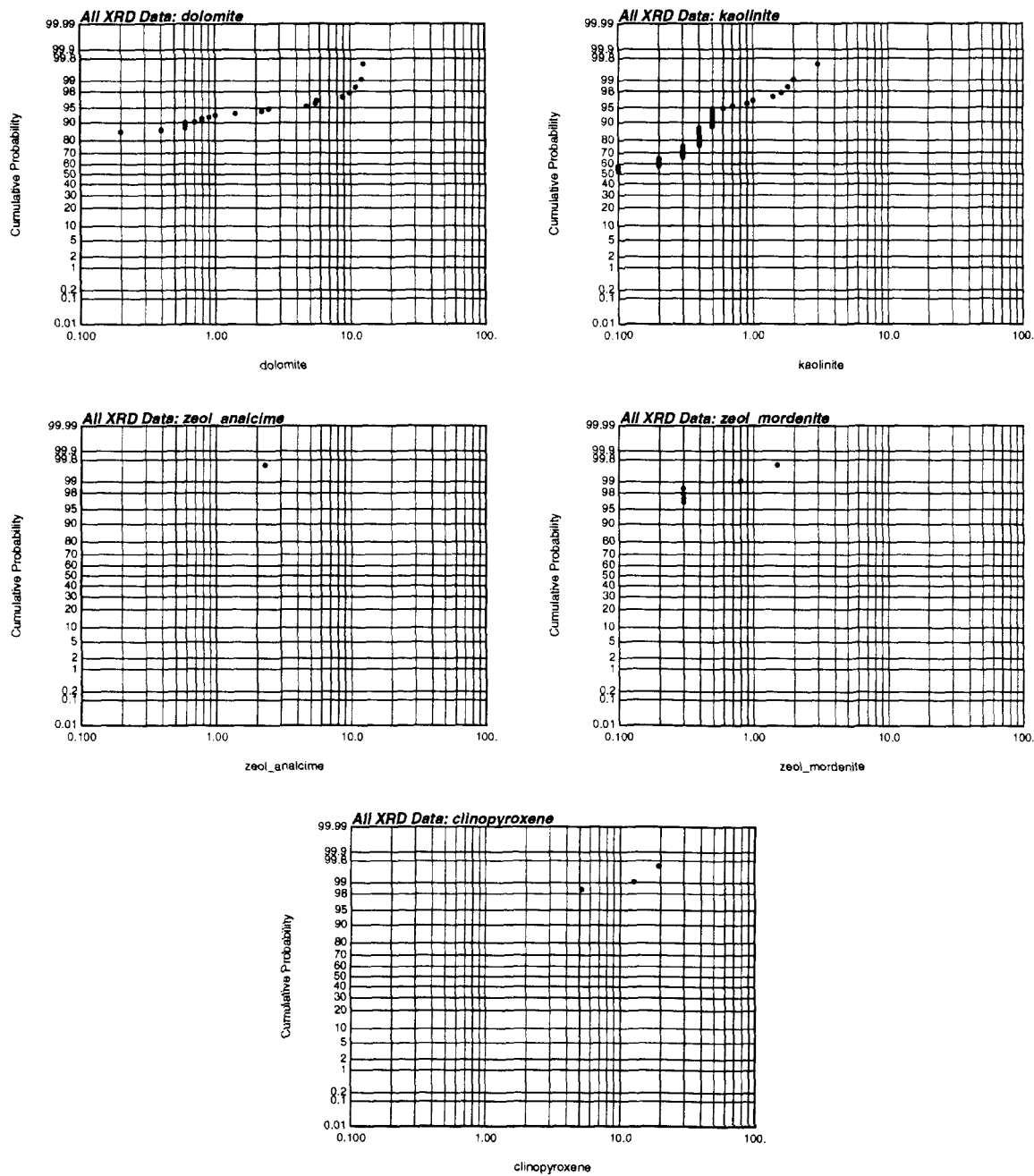
Figure 3.18 Log-scaled probability plots of cumulative abundance of non-sorbing minerals dolomite, kaolinite, analcime, mordenite, and clinopyroxene detected by XRD analysis in drill drillholes ER-5-3, ER-5-4, UE-5n, and U-11g-1.
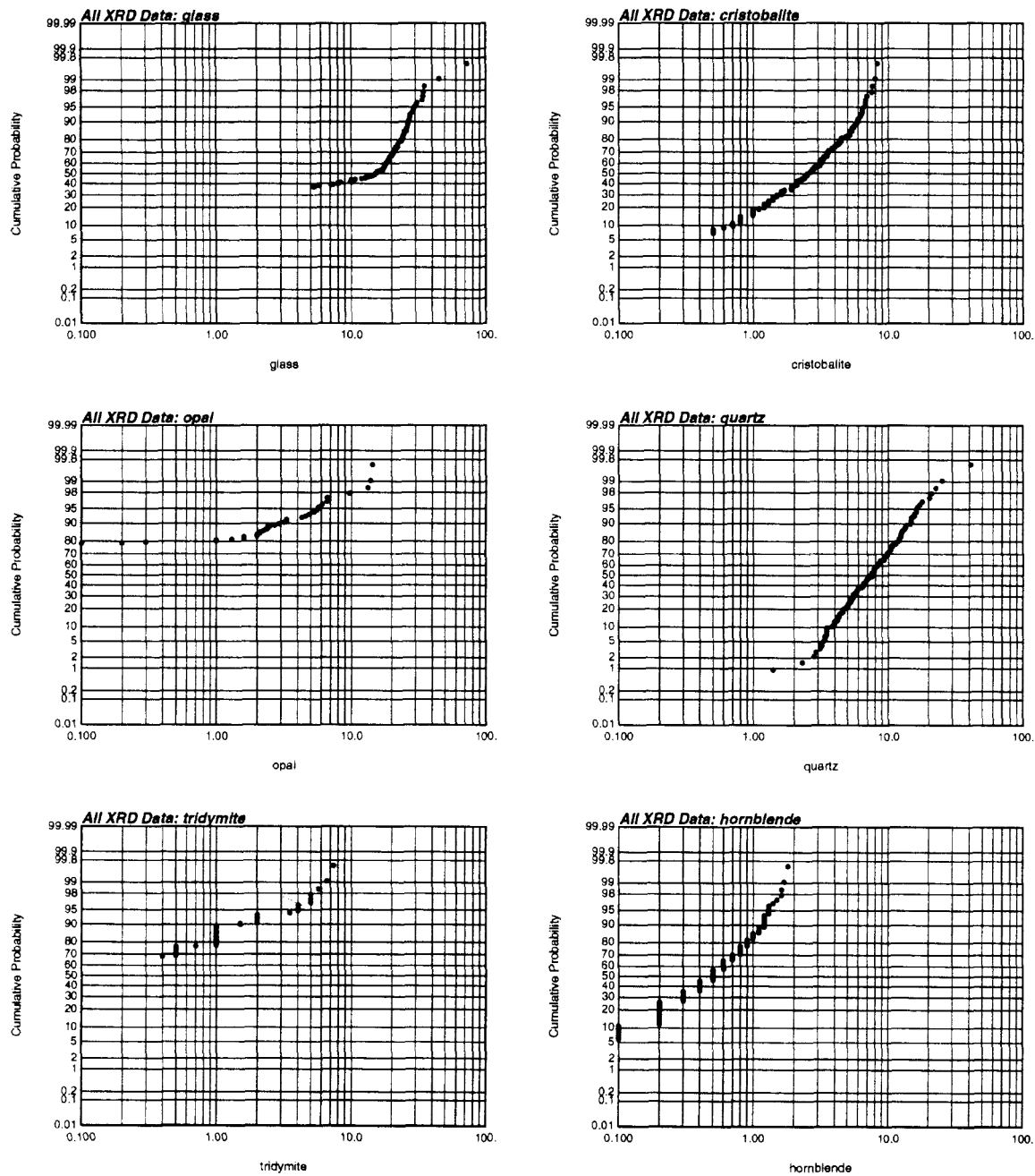
Figure 3.19 Log-scaled probability plots of cumulative abundance of the non-sorbing minerals glass, cristobalite, opal, quartz, tridymite, and hornblende detected by XRD analysis in drill drillholes ER-5-3, ER-5-4, UE-5n, and U-11g-1.
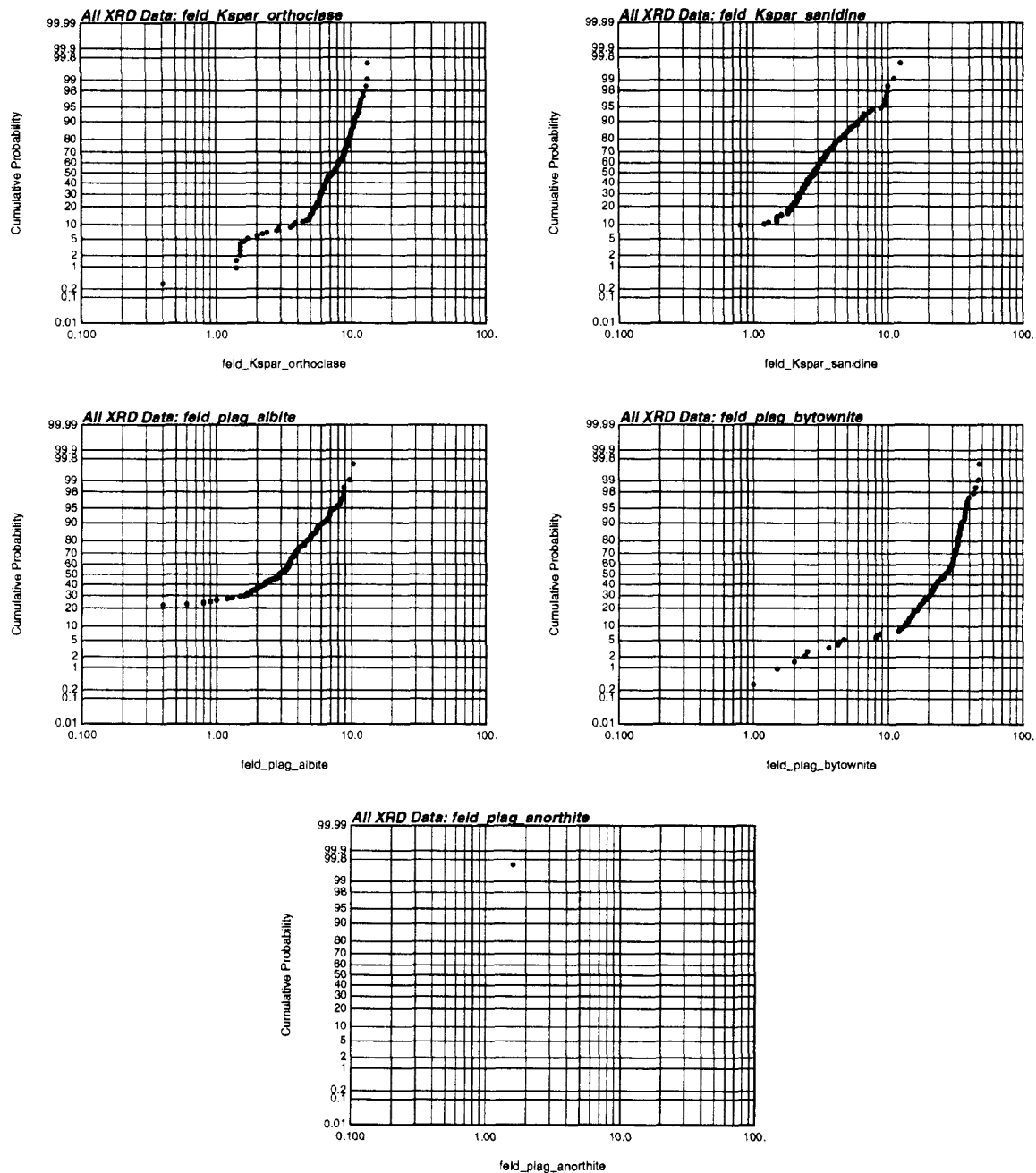
Figure 3.20 Log-scaled probability plots of cumulative abundance of the non-sorbing minerals orthoclase, sanidine, albite, bytownite, anorthite detected by XRD analysis in drill drillholes ER-5-3, ER-5-4, UE-5n, and U-11g-1.

3.2.2.3 Interpretation of Normal Probability Plots

Table 3.3 summarizes the interpretation of both the linear and log-scaled probability plots. Based on the normal probability plots with linear and log scales, the number of sub-populations and their approximate cutoff values (bounds for different sub-populations) are identified. For some minerals — calcite, mica, smectite, clinoptilolite, cristobalite, tridymite, hornblende, orthoclase, albite, and bytownite — different nonzero cutoff values are identified in the linearly and log-scaled probability plots. The differences may occur because some sub-populations in the mineral abundances are not widely separated (for which linear scaling is more effective) or because the mineral abundance has a wide range of variation (for which the log scaling is more effective). For example, a bi-modal distribution is more evident for mica using linear scaling. For quartz, the frequency distribution appears uni-modal with log scaling, but is difficult to interpret with linear scaling. For other minerals — hematite, dolomite, analcime, mordenite, clinopyroxene, glass, opal, sanidine, and anorthite — the interpretation of the mineral fraction of sub-population cutoffs is generally the same for either linear or log scaling.

The right column in Table 3.3 gives the total number of sub-populations and respective cutoff values inferred from both linearly and log-scaled probability plots. These interpretations of the univariate statistics are intended to provide some guidance for interpreting the raw mineral abundance data with respect to zones (or alluvial layers) having similar statistical properties. In interpreting zones, the cutoff values do not have to be honored within each zone because there may be overlap between the frequency distributions of different sub-populations of each mineral. In the next section, zones are identified in the plots of mineral abundance versus depth shown in Figures 3.1 to 3.4. The cutoff values identified in this section were used to help distinguish zones of similar mineral abundance.

Table 3.3 Summarized interpretation of linearly and logarithmically scaled normal probability plots, with number of sub-populations and estimated cutoffs (in mass %) given.

Mineral	Sub-Populations: Cutoffs Linear Scaling	Sub-Populations: Cutoffs Log Scaling	Sub-Populations: Cutoffs Total
Calcite	3: 0.0, 4.0	2: 16.0	4: 0.0, 4.0, 16.0
Hematite	2: 0.0	1	2: 0.0
Mica	2: 4.5	1	2: 4.5
Smectite	2: 16.0	3: 8.0, 16.0	3: 8.0, 16.0
Clinoptilolite	3: 0.0, 3.0	4: 1.5, 3.0, 22.0	5: 0.0, 1.5, 3.0, 22.0
Dolomite	2: 0.0	1	2: 0.0
Kaolinite	3: 0.0, 0.60?	1	3: 0.0 0.60?
Analcime	2: 0.0	1	2: 0.0
Mordenite	2: 0.0	1	2: 0.0
Clinopyroxene	2: 0.0	1	2: 0.0
Glass	3: 0.0, 17.0	2: 17.0	3: 0.0, 17.0
Cristobalite	3: 0.0, 3.8	2: 5.0	4: 0.0, 3.8, 5.0
Opal	2: 0.0	1	2: 0.0
Quartz	?	1	1
Tridymite	2: 0.0	2: 4.5	3: 0.0, 4.5
Hornblende	2: 0.5	2: 1.1	3: 0.5, 1.1
Orthoclase	1?	2: 4.8	2: 4.8
Sanidine	2: 3.5	2: 3.5	2: 3.5
Albite	3: 0.0, 4.0	2: 3.0	4: 0.0, 3.0, 4.0
Bytownite	2: 29.0	3: 11.0, 29.0	3: 11.0, 29.0
Anorthite	2: 0.0	1	2: 0.0

3.3 Mineralization Zones

In our geostatistical interpretation of the mineral abundance data for ER-5-3, ER-5-4, UE-5n, and U-11g-1, a "mineralization zone" is defined as a vertical interval where the mineral abundance data appear to fall within a sub-population characterized by a mean and variance. The purpose of identifying the zones is to separate out the spatial variation of the mineral abundances attributed to random processes from those related to geologic processes, such as differences in provenance.

For this study, the identification of the zones is in part quantitative — based on identifying sub-populations and cutoff values as described the previous section — and part subjective. The subjective aspect involves study of the mineral abundance versus depth profiles (Figures 3.1 to 3.4) with consideration of the geologic processes involved. As indicated by Warren et al. (2002), distinct alluvial layers can be identified from a combined interpretation of the mineralogic, chemical, and lithologic data in ER-5-4 and UE-5n. These different alluvial layers have different provenance. With that in mind, the alluvial layers should be evident where shifts in mean mineral abundances occur (assuming the distribution of mean mineral abundances is indicative of provenance).[5] Therefore, if the sub-populations of a mineral have overlapping frequency distributions (e.g., smectite), the interpretations of zonal mean abundances for that mineral need to be interpreted in the context of zonal means for other minerals. In other words, the mineral abundance data for each mineral cannot be interpreted independently of all other minerals. Unfortunately, it is not straightforward to perform a fully quantitative and simultaneous interpretation of the spatial interrelationships, interdependencies, and geological tendencies of all the mineralization zones. As mentioned earlier, the methodology used here is distinctly different from the methods used in Warren et al. (2002). Here, we rely solely on quantitative XRD data. The alluvial layering interpretation used in Warren et al. (2002) relies on XRD along with SEM, XRF, microprobe and petrographic analyses. It should also be recognized that identification and interpretation of mineralogical zones based on an alluvial layering model may be complicated by diagenesis that may not conform to stratigraphic boundaries. While the data used to assign layering is different, our data analysis is, in general consistent with that of Warren et al. (2002). Section 3.5 provides comparison of these two interpretations.

Table 3.4 presents our interpretation of the number of distinct mineralization zones and zonal mean abundances for drillholes ER-5-4, UE-5n, ER-5-3, and U-11g-1 based on our statistical analysis of the univariate data and interpretation of the mineral vs. depth profiles. The number of zones may include a zone composed exclusively of mineral abundance below the detection limit, which is indicated by a zonal mean abundance of 0.0 (e.g., for calcite, hematite, dolomite, kaolinite, analcime, mordenite, clinopyroxene, glass, cristobalite, opal, tridymite, sanidine, albite, and anorthite.)

---

[5] This, of course, does not need to be the case. For example, it is possible that mean mineral abundances for two alluvial layers would be identical. However, a textural or petrographic analysis might show an obvious distinction between the two layers.

Table 3.4 Number of mineralization zones and zonal mean abundances interpreted from XRD data from ER-5-4, UE-5n, ER-5-3, and U-11g-1.

Mineral	# of Zones	Zone mean abundance (%)
Calcite	4	0.0, 2.8, 8.9, 20.6
Hematite	2	0.0, 0.55
Mica	3	1.45, 3.2, 6.7
Smectite	3	4.5, 12.4, 28
Clinoptilolite	4	0.36, 2.1, 5.9, 21
Dolomite	3	0.0, 0.89, 8.8
Kaolinite	2	0.0, 0.42
Analcime	2	0.0, 2.30
Mordenite	2	0.0, 0.58
Clinopyroxene	2	0.0, 12.3
Glass	3	0.0, 8.3, 23
Cristobalite	3	0.0, 1.61, 4.3
Opal	2	0.0, 3.6
Quartz	2	5.2, 11.7
Tridymite	3	0.0, 0.78, 3.6
Hornblende	3	0.0, 0.28, 0.87
Orthoclase	2	3.9, 8.3
Sanidine	4	0.0, 2.8, 5.9, 9.6
Albite	4	0.0, 2.9, 6.1, 8.8
Bytownite	4	3.5, 14.4, 22, 32
Anorthite	2	0.0, 1.60

Depth profiles of the zonal mean abundances are useful for identifying zones or "layers" that could be expected to have similar radionuclide sorbing properties. The raw mineral abundance data are more difficult to interpret because of the scatter related to random processes. Figures 3.21 to 3.24 show the same plots of mineral abundance versus depth for ER-5-4, UE-5n, ER-5-3, and U-11g-1 as shown in Figures 3.1 to 3.4, but with profiles of zonal mean abundance superposed. Note that because of the log scale, the zonal mean values of 0.0 are plotted at a value of 0.1% (the detection limit). Depth intervals where the zonal mean abundance is constant indicate continuous intervals of similar mineral abundance. For example, in ER-5-4 the zone mean abundances of all minerals is relatively stable between the depths of about 500 to 700 m. Below a depth of 700 m, the zonal mean abundances of several minerals — calcite, dolomite, cristobalite, glass, orthoclase, albite, bytownite, sanidine, quartz, tridymite, and hornblende show an abrupt change. This represents a clear transition in the mineralogy of the alluvium, which are identified as distinct alluvial layers by Warren et al. (2002).

In other depth intervals, the zonal mean abundances of several minerals appear to fluctuate rapidly with depth. For example, in the depth interval between 780 to 900 m in drillhole ER-5-4,

the zone mean abundances of nearly all minerals appear to fluctuate rapidly with depth. On closer inspection, the fluctuation appears to occur between values of zonal mean abundances from alluvium above 780 m depth and below 900 m depth. This would indicate that changes in alluvial composition occur in the 780 to 900 m depth interval. In this interval, it appears that at least two different types of alluvial sediment are interfingering.

In ER-5-3, zonal mean abundances appear relatively uniform above a depth of 200 m and below a depth of 400 m. Between the depths of about 220 to 400 m there is much fluctuation in the zonal mean abundances. For some minerals — hematite, mica, albite, sanidine, and bytownite — the fluctuation occurs primarily between zonal mean abundances above 220 and below 400 m. For other minerals — calcite and the rare minerals mordenite, anorthite, and clinopyroxene — relatively high zonal mean abundances are observed between the 220 to 400 m depth. Smectite shows fluctuations to relatively lower zonal mean abundances between 220 to 400 m depth. Clinoptilolite and opal show consistently higher zonal mean abundances below 220 m depth. Tridymite is conspicuously absent below 220 m depth. Overall, the mineralogy could be divided into three major layers in ER-5-3 based on the 220 and 400 m depths. The variation in mineral abundances within the depths between 220 and 400 m appears to be related, in part, to interfingering of alluvial sediments with the different provenances of the layers above 220 m and below the 400 m. It may also suggest possible in-situ alteration, though the interpretation of alteration is better suited to the comprehensive lithologic and petrographic characterization performed by Warren et al. (2002).

The zonal mean abundances appear to correlate very closely between nearby drillholes — ER-5-4 and UE-5n in central Frenchman Flat and ER-5-3 and U-11g-1 in northern Frenchman Flat. The composition of mineralization zones or alluvial layers appears to persist laterally over the scale of hundreds of meters, but not across the scale of 5 to 10 km between the southern and northern testing areas of Frenchman Flat basin.
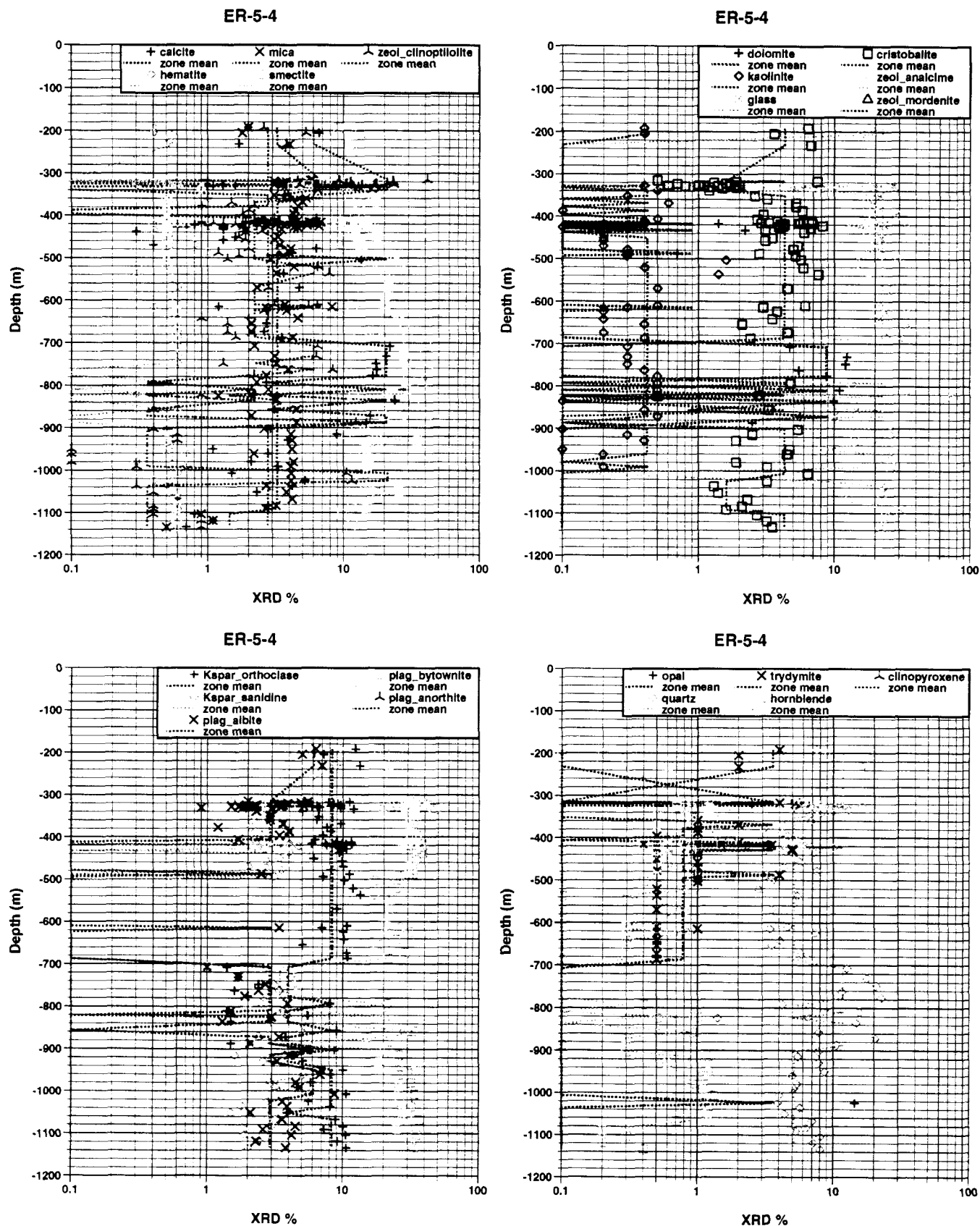
Figure 3.21 Mineral abundance data from ER-5-4, with zonal mean abundances superposed.
Data from Warren et al. (2002).
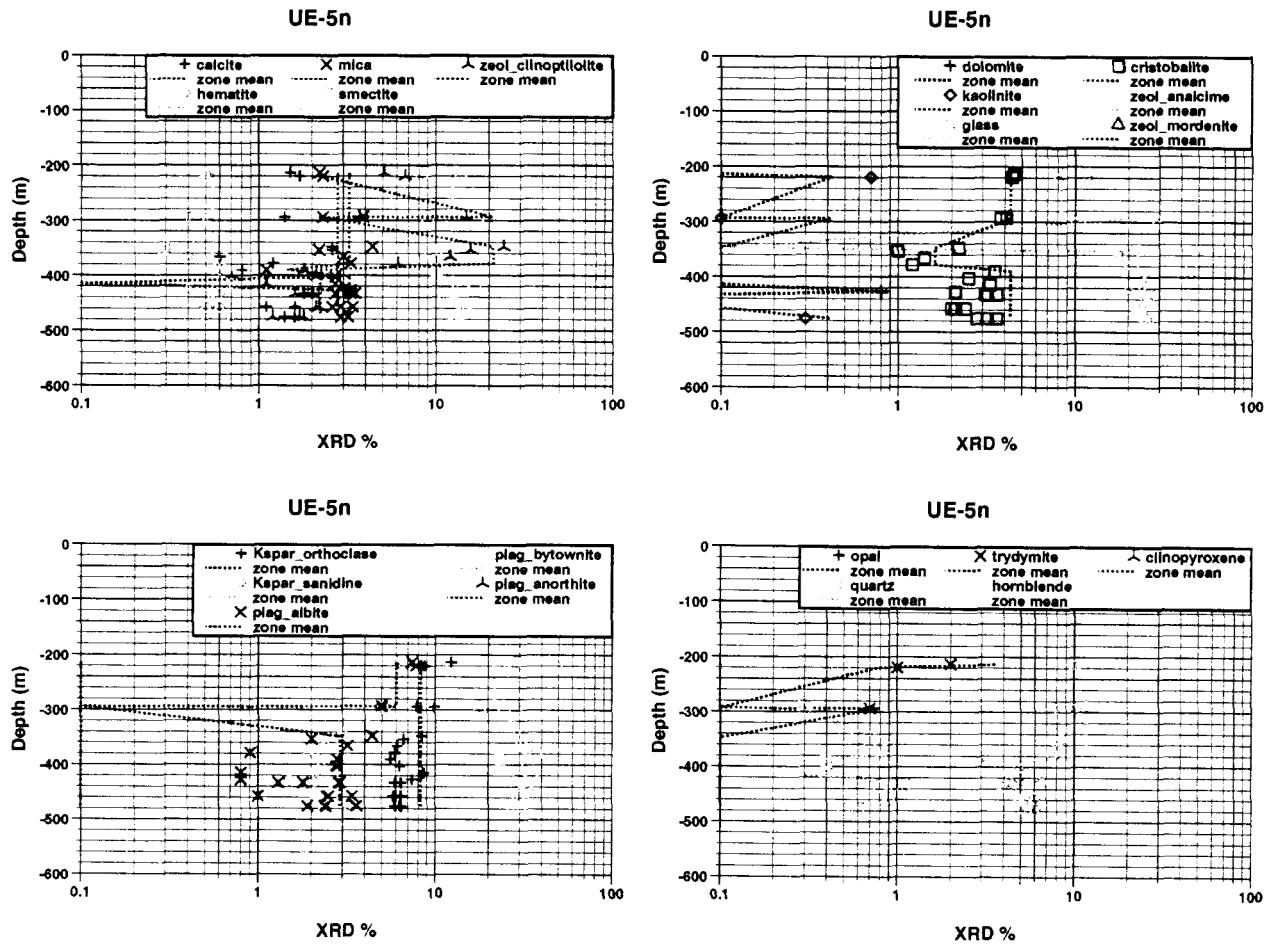
Figure 3.22 Mineral abundance data from UE-5n, with zonal mean abundances superposed. Data from Warren et al. (2002).
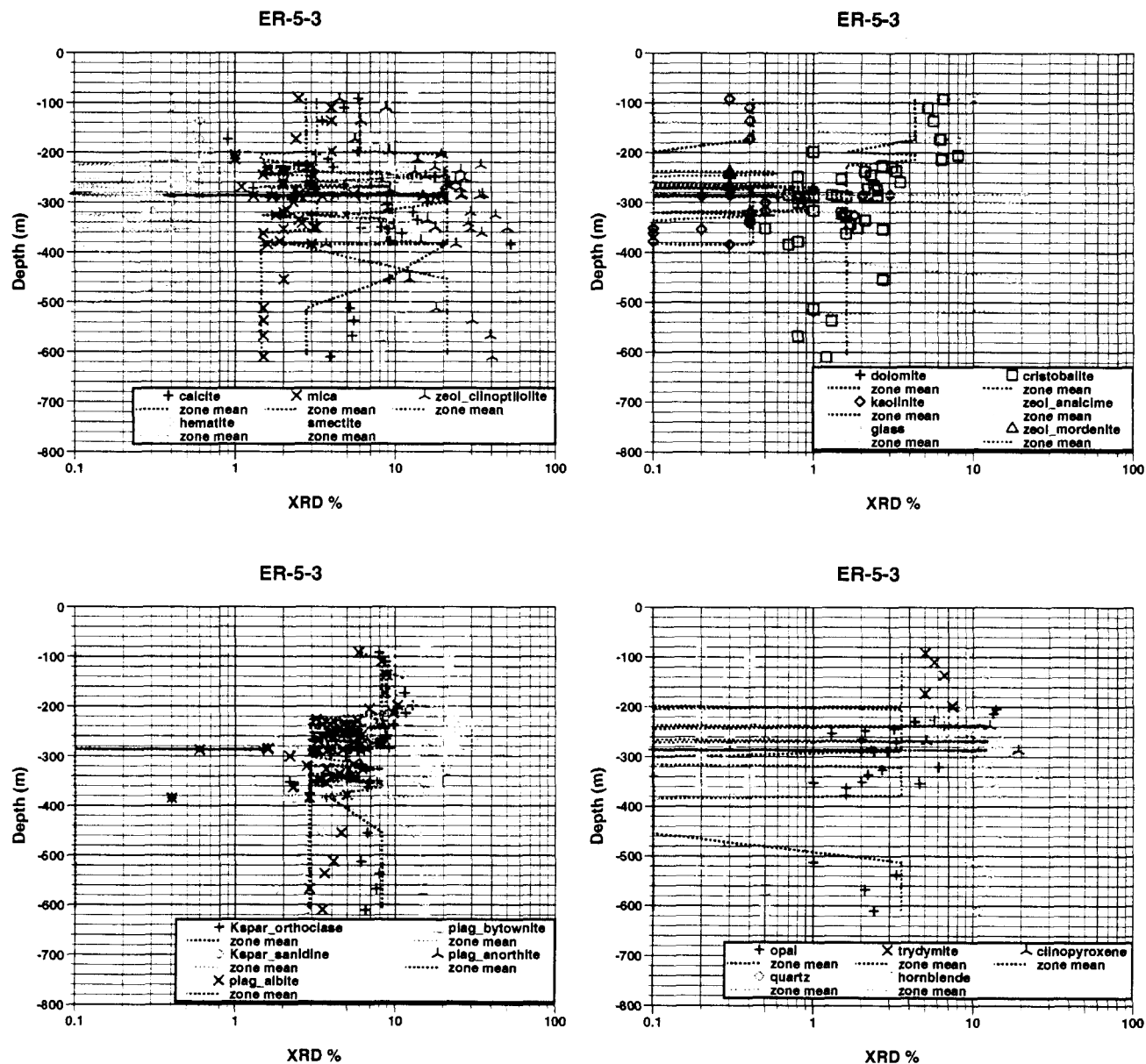
Figure 3.23 Mineral abundance data from ER-5-3, with zonal mean abundances superposed. Data from Warren et al. (2002).

U-11g

Legend:
+ calcite / zone mean
hematite / zone mean
X mica / zone mean
smectite / zone mean
人 zeol_clinoptilolite / zone mean

Depth (m): 0, -100, -200, -300, -400
XRD %: 0.1, 1, 10, 100

U-11g

Legend:
+ dolomite / zone mean
◇ kaolinite / zone mean
glass / zone mean
☐ cristobalite / zone mean
zeol_analcime / zone mean
△ zeol_mordenite / zone mean

Depth (m): 0, -100, -200, -300, -400
XRD %: 0.1, 1, 10, 100

U-11g

Legend:
+ Kspar_orthoclase / zone mean
Kspar_sanidine / zone mean
X plag_albite / zone mean
plag_bytownite / zone mean
人 plag_anorthite / zone mean

Depth (m): 0, -100, -200, -300, -400
XRD %: 0.1, 1, 10, 100

U-11g

Legend:
+ opal / zone mean
quartz / zone mean
X trydymite / zone mean
hornblende / zone mean
人 clinopyroxene / zone mean

Depth (m): 0, -100, -200, -300, -400
XRD %: 0.1, 1, 10, 100

Figure 3.24 Mineral abundance data from drillhole U-11g-1, with zonal mean abundances superposed. Data from Warren et al. (2002).

3.4 Correlations between Sorbing and Non-Sorbing Minerals

Considering that the spatial distribution of calcite, hematite, mica, smectite, and clinoptilolite (defined as the sorbing minerals in this report) are of primary interest in application to reactive transport modeling, three important questions may arise:

- Does spatial cross-correlation between different sorbing minerals exist, such that the abundances of some sorbing minerals are dependent on the abundances of other sorbing minerals?

- Does spatial cross-correlation between sorbing and non-sorbing minerals exist, such that the abundances of some non-sorbing minerals are indicative of the abundances of sorbing minerals?

- Might the correlation of abundances of different minerals be interpreted to indicate the origin of the mineral abundances — whether by deposition or in-situ mineralization (alteration)?

This section addresses these questions by statistical analysis of the bivariate correlation between abundances of sorbing and other sorbing or non-sorbing minerals at the same location.

If the abundance of one mineral at a particular location does not depend on the abundance of another mineral at that same location, the bivariate correlation of abundances of two minerals at the same location should not differ significantly from zero. A complete evaluation of spatial cross-correlation of mineral abundances for different minerals would require examining the bivariate correlation for data from different (instead of the same) locations, which is beyond the scope of this report. Spatial auto-correlation correlation of mineral abundances is examined in Chapter 5 using variogram analyses.

The question of the origin of mineral distribution is critical to development of conceptual models for addressing spatial variability of mineral abundance. For example, if mineral abundance can be entirely related to provenance and alluvial fan deposition, then a depositionally-based model, such as described by the alluvial layers identified by Warren et al. (2002), may provide an accurate and geologically plausible conceptual model for describing much of the spatial variation of minerals. If, however, diagenetic processes are involved, other considerations such as the role of the thermal, hydrologic, and climatic history of the basin may need to be integrated into development of the conceptual model.

One way to address these questions is to examine the correlation of mineral abundances of different minerals. If the mineral abundances of two minerals are significantly correlated (negatively or positively) then the abundance of one mineral contains information on the abundance of the other. If the mineral abundances of two minerals are not significantly correlated, then the mineral abundance of one mineral is, in effect, statistically independent of the other.

Correlation of the mineral abundances of two minerals, $f_{1,i}$ and $f_{2,i}$, for $i=1,...,N$ data is measured by the correlation coefficient ρ defined by:

$$\rho = \frac{\sum_{i=1}^{N}\left(f_{1,i} - \overline{f}_1\right)\left(f_{2,i} - \overline{f}_2\right)}{\sqrt{\sum_{i=1}^{N}\left(f_{1,i} - \overline{f}_1\right)^2 \sum_{i=1}^{N}\left(f_{2,i} - \overline{f}_2\right)^2}}$$

where $\overline{f}_{1,i}$ and $\overline{f}_{2,i}$ are the mean values of the mineral fraction of minerals 1 and 2, respectively.

The statistical analysis of correlation greatly depends on the assumption that the joint probability distribution is a binormal (two-dimensional Gaussian) distribution. In practice, a scatterplot is used to display the joint probability distribution, where the axes are scaled by the magnitude of the values of the two variables. If the joint probability distribution is binormal, the points on the scatterplot will look like an oval cloud with increasing density toward the center. If the data are positively correlated, the cloud will be elongated in a direction with positive slope. If the data are uncorrelated ($\rho = 0$), the cloud in the scatterplot will either have no elongation or the elongation will be in the vertical or horizontal direction. If the data are negatively correlated, the cloud will be elongated in a direction with negative slope. For perfect correlation of -1.0 or $+1.0$, the cloud will appear as a line. Non-binormal joint probability distributions may be caused by non-Gaussian probability distributions. Multiple sub-populations may appear as several fairly distinct clouds in the scatterplot. We examined the correlation of both the mineral abundances and $\log_{10}$ transformed mineral abundances. The $\log_{10}$ transformation consistently exhibited a closer approximation to a binormal distribution.

Alternatively, "rank correlation" can be used as a robust detector of correlation, particularly for non-Gaussian probability distributions. Rank correlation, r, is defined by

$$r = \frac{\sum_{i=1}^{N}\left(R_{1,i} - \overline{R}_1\right)\left(R_{2,i} - \overline{R}_2\right)}{\sqrt{\sum_{i=1}^{N}\left(R_{1,i} - \overline{R}_1\right)^2 \sum_{i=1}^{N}\left(R_{2,i} - \overline{R}_2\right)^2}}$$

where $R_{1,i}$ and $R_{2,i}$ are the rank of datum i for variables 1 and 2, respectively. Rank correlation provides a measure of the relative rank or order of the two variables that is insensitive to the shape of the frequency distribution of either variable. Rank correlation measures the tendency for extreme values of two variables to occur in tandem.

When evaluating the correlation of two variables, it is good practice to evaluate both ρ and r. It is possible that ρ may appear significant as a result of outliers or deviation from a binormal

distribution. The rank correlation provides a second test; if ρ is significant and unaffected by deviations from a binormal distribution, then r should also be significant.

Significance of ρ can be tested by evaluating the Student's distribution, $A(t,v)$, where

$$t = \rho \sqrt{\frac{N-2}{1-\rho^2}} ,$$

N is number of data, and $v = (N-2)$ degrees of freedom. For this study, $A(t,v)$ was evaluated using the FORTRAN function "betai" from Numerical Recipes (Press et al., 1992). The value of $1-A(t,v)$ is the significance level at which the hypothesis that correlation is actually zero is disproved. In this application, the significance level represents an estimate of the probability that the correlation could actually be zero, given the uncertainty of the data. If $1-A(t,v)$ is greater or equal to the significance level, ρ is not significantly different than zero. Typically, a significance level of 0.05 is assumed. The significance of r can be tested in a similar manner, where r is substituted for ρ.

The final goal of this section is to determine which sorbing and non-sorbing minerals exhibit significant correlation with the sorbing minerals. The test for "significance" in this study requires passing of four tests:

- The absolute value of the correlation, ρ, must be greater than or equal to 0.250.

- The significance level of the correlation, ρ, for $\Pr\{\rho = 0\}$ must be less than or equal to 0.05

- The absolute value of rank correlation, r, must be greater than or equal to 0.250.

- The significance level of the rank correlation, r, for $\Pr\{r=0\}$ must be less than or equal to 0.05

Figures 3.25 to 3.39 show the scatterplots of the mineral abundance data. The $\log_{10}$ fractions of the dependent variables, the sorbing minerals — calcite, hematite, mica, smectite, and clinoptilolite — are scaled on the Y axis, and the $\log_{10}$ fractions of the independent variable, whether a sorbing or non-sorbing mineral, are scaled on the X axis. A list of important statistics are given on the right of each scatterplot, including:

- number of data evaluated and plotted (above the detection limit),

- number trimmed (below the detection limit),

- the mean and standard deviation of the X and Y variables in $\log_{10}$ units,

- the correlation and its significance level (probability that the correlation equals 0.0),

- the rank correlation and its significance level (probability that the rank correlation equals 0.0).

Tables 3.5 to 3.9 summarize the statistics (based on $\log_{10}$ mineral abundance) used to evaluate the significance of correlation between sorbing minerals and other sorbing or non-sorbing minerals.

Table 3.5 Correlation statistics used to determine magnitude and significance of correlation between calcite and other sorbing or non-sorbing minerals.

Mineral Pair		ρ	$Pr(\rho=0)$	r	$Pr(r=0)$	Significant Correlation?
Y variable	X variable					
Calcite	Hematite	-0.240	0.008	-0.190	0.038	No
Calcite	Mica	-0.068	0.408	-0.155	0.060	No
Calcite	Smectite	0.129	0.118	0.079	0.340	No
Calcite	Clinoptilolite	0.264	0.001	0.317	0.000	Yes
Calcite	Dolomite	0.563	0.003	0.537	0.007	Yes
Calcite	Kaolinite	0.153	0.195	0.255	0.028	No
Calcite	Glass	-0.139	0.176	-0.063	0.541	No
Calcite	Cristobalite	-0.308	0.000	-0.333	0.000	Yes
Calcite	Opal	-0.271	0.135	-0.463	0.006	No
Calcite	Quartz	0.471	0.000	0.464	0.000	Yes
Calcite	Tridymite	0.035	0.810	-0.013	0.928	No
Calcite	Hornblende	-0.333	0.000	-0.373	0.000	Yes
Calcite	Orthoclase	-0.506	0.000	-0.434	0.000	Yes
Calcite	Sanidine	0.021	0.812	0.041	0.638	No
Calcite	Albite	-0.194	0.039	-0.129	0.175	No
Calcite	Bytownite	-0.642	0.000	-0.706	0.000	Yes

Table 3.6 Correlation statistics used to determine magnitude and significance of correlation between hematite and other sorbing or non-sorbing minerals.

Mineral Pair						Significant
Y variable	X Variable	ρ	$Pr(\rho=0)$	r	$Pr(r=0)$	Correlation?
Hematite	Calcite	-0.240	0.008	-0.190	0.110	No
Hematite	Mica	-0.040	0.651	0.012	0.888	No
Hematite	Smectite	0.042	0.631	0.121	0.170	No
Hematite	Clinoptilolite	-0.158	0.073	-0.137	0.123	No
Hematite	Dolomite	0.381	0.184	0.495	0.072	No
Hematite	Kaolinite	0.117	0.182	0.270	0.002	No
Hematite	Glass	-0.060	0.554	0.222	0.027	No
Hematite	Cristobalite	0.175	0.049	0.189	0.033	No
Hematite	Opal	0.045	0.882	0.002	0.994	No
Hematite	Quartz	-0.226	0.010	-0.096	0.279	No
Hematite	Tridymite	0.208	0.139	-0.001	0.993	No
Hematite	Hornblende	0.024	0.790	0.016	0.856	No
Hematite	Orthoclase	0.117	0.182	0.270	0.002	No
Hematite	Sanidine	0.013	0.886	0.066	0.479	No
Hematite	Albite	0.018	0.865	0.077	0.458	No
Hematite	Bytownite	0.142	0.106	0.230	0.008	No

Table 3.7 Correlation statistics used to determine magnitude and significance of correlation between mica and other sorbing or non-sorbing minerals.

Mineral Pair						Significant
Y variable	X variable	ρ	$Pr(\rho=0)$	r	$Pr(r=0)$	Correlation?
Mica	Calcite	-0.068	0.408	-0.151	0.065	No
Mica	Hematite	-0.040	0.651	-0.081	0.351	No
Mica	Smectite	0.193	0.014	0.164	0.038	No
Mica	Clinoptilolite	-0.116	0.144	-0.205	0.010	No
Mica	Dolomite	0.000	0.998	0.051	0.812	No
Mica	Kaolinite	0.025	0.829	-0.056	0.626	No
Mica	Glass	-0.143	0.150	-0.131	0.188	No
Mica	Cristobalite	0.020	0.809	0.072	0.375	No
Mica	Opal	-0.052	0.763	0.011	0.948	No
Mica	Quartz	-0.258	0.001	-0.347	0.000	Yes
Mica	Tridymite	-0.08	0.900	0.052	0.715	No
Mica	Hornblende	0.469	0.000	0.511	0.000	Yes
Mica	Orthoclase	0.062	0.431	0.103	0.191	No
Mica	Sanidine	-0.115	0.164	-0.135	0.103	No
Mica	Albite	-0.170	0.056	-0.191	0.032	No
Mica	Bytownite	0.253	0.001	0.428	0.000	Yes

Table 3.8 Correlation statistics used to determine magnitude and significance of correlation between smectite and other sorbing or non-sorbing minerals.

| Mineral Pair | | | | | | Significant |
Y variable	X Variable	ρ	Pr(ρ=0)	r	Pr(r=0)	Correlation?
Smectite	Calcite	0.129	0.118	0.076	0.355	No
Smectite	Hematite	0.042	0.631	0.094	0.283	No
Smectite	Mica	0.193	0.014	0.166	0.035	No
Smectite	Clinoptilolite	-0.395	0.000	-0.443	0.000	Yes
Smectite	Dolomite	0.794	0.000	0.807	0.000	Yes
Smectite	Kaolinite	0.150	0.191	0.231	0.042	No
Smectite	Glass	0.014	0.886	-0.052	0.604	No
Smectite	Cristobalite	0.072	0.382	0.141	0.083	No
Smectite	Opal	-0.494	0.002	-0.503	0.002	Yes
Smectite	Quartz	-0.094	0.235	-0.190	0.016	No
Smectite	Tridymite	-0.590	0.000	-0.531	0.000	Yes
Smectite	Hornblende	0.152	0.060	0.140	0.083	No
Smectite	Orthoclase	-0.404	0.000	-0.223	0.004	No
Smectite	Sanidine	-0.282	0.000	-0.175	0.034	No
Smectite	Albite	-0.344	0.000	-0.274	0.002	Yes
Smectite	Bytownite	-0.318	0.000	0.064	0.417	No

Table 3.9 Correlation statistics used to determine magnitude and significance of correlation between clinoptilolite and other sorbing or non-sorbing minerals.

| Mineral Pair | | | | | | Significant |
Y variable	X Variable	ρ	Pr(ρ=0)	r	Pr(r=0)	Correlation?
Clinoptilolite	Calcite	0.264	0.001	0.317	0.000	Yes
Clinoptilolite	Hematite	-0.158	0.073	-0.177	0.045	No
Clinoptilolite	Mica	-0.116	0.144	-0.206	0.009	No
Clinoptilolite	Smectite	-0.395	0.000	-0.447	0.000	Yes
Clinoptilolite	Dolomite	-0.303	0.162	-0.401	0.058	No
Clinoptilolite	Kaolinite	0.144	0.214	0.198	0.087	No
Clinoptilolite	Glass	-0.388	0.000	-0.340	0.000	Yes
Clinoptilolite	Cristobalite	-0.449	0.000	-0.468	0.000	Yes
Clinoptilolite	Opal	-0.072	0.677	-0.080	0.643	No
Clinoptilolite	Quartz	0.492	0.000	0.567	0.000	Yes
Clinoptilolite	Tridymite	0.342	0.013	0.248	0.077	No
Clinoptilolite	Hornblende	-0.313	0.000	-0.312	0.000	Yes
Clinoptilolite	Orthoclase	-0.103	0.196	-0.182	0.022	No
Clinoptilolite	Sanidine	0.106	0.206	0.132	0.114	No
Clinoptilolite	Albite	0.086	0.347	0.118	0.193	No
Clinoptilolite	Bytownite	-0.212	0.007	-0.381	0.000	No

Table 3.10 summarizes the type of correlation — exactly positive (1), not significant (0), positive (+), or negative (-) — between sorbing minerals and other sorbing or non-sorbing minerals. The autocorrelations (correlations between the same mineral) are exactly +1.0. Based on Table 3.10, several conclusions on the correlation of mineral abundances can be made:

- Only one sorbing mineral, clinoptilolite, shows significant correlation with other sorbing minerals — calcite (positive) and smectite (negative).

- The sorbing mineral hematite is not significantly correlated with any other minerals, either sorbing or non-sorbing.

- Of the non-sorbing minerals that are sufficiently abundant to test for correlation, only two, kaolinite and sanidine, show no significant correlation with any sorbing minerals.

- None of the non-sorbing minerals show significant correlation with all sorbing minerals.

- Two non-sorbing minerals show significant correlation with the same three sorbing minerals — quartz and hornblende (to calcite, mica, and clinoptilolite). Four non-sorbing minerals show significant correlation with two sorbing minerals — dolomite (to calcite and smectite), cristobalite (to calcite and clinoptilolite), and bytownite (to calcite and mica). Four non-sorbing minerals show significant correlation to one sorbing mineral — glass (to clinoptilolite), tridymite (to smectite), orthoclase (to calcite), and albite (to smectite).

For some of these correlations, a geologic and/or geochemical significance can be applied. For example, the negative correlation between calcite and bytownite suggests that calcite may have formed as a result of weathering of the Ca-rich plagioclase. However, these correlations between minerals are rather subtle, are difficult to explain based solely on XRD information, and therefore, benefit when evaluated in conjunction with other supportive evidence. Furthermore, lithologic characterization of alluvium from the ER-5-4 central Frenchman Flat well in Warren et al. (2002) suggests that secondary minerals are not formed in-situ but are instead a part of the original mineralogy of the sediments. Thus, geochemical interpretation of sediment alteration history at this location reflects the alteration history of the alluvium-forming precursor and not in-situ post-depositional alteration processes. Lithologic data for northern Frenchman Flat wells (primarily ER-5-3) is limited but suggests possible in-situ secondary alteration. The complex history of the sediments and their alteration can best be deciphered using a combination of lithologic and petrographic, XRD, SEM, XRF, and microprobe analyses. The results presented here suggest that correlations between minerals exist but the correlations cannot be rigorously interpreted without a combination of XRD and other techniques.

Table 3.10 Summary of types of correlation — exactly positive (1), not significant (blank), positive (+), and negative (-) — between sorbing minerals and sorbing or non-sorbing minerals.

Mineral	Type of Correlation with sorbing minerals:					Any Significant Correlation?
	Calcite	Hematite	Mica	Smectite	Clinoptilolite	
Calcite	1				+	Yes
Hematite		1				No
Mica			1			No
Smectite				1	-	Yes
Clinoptilolite	+			-	1	Yes
Dolomite	+			+		Yes
Kaolinite						No
Glass					-	Yes
Cristobalite	-				-	Yes
Opal				-		Yes
Quartz	+		-		+	Yes
Tridymite				-		Yes
Hornblende	-		+		-	Yes
Orthoclase	-					Yes
Sanidine						No
Albite				-		Yes
Bytownite	-		+			Yes

calcite vs. hematite

Number of data 119
Number plotted 119
Number trimmed 44

log10(X Variable): mean -0.286
std. dev. 0.135

log10(Y Variable): mean 0.426
std. dev. 0.399

correlation -0.240
Pr[correlation=0] 0.008

rank correlation -0.190
Pr[rank correlation=0] 0.038

calcite vs. mica

Number of data 149
Number plotted 149
Number trimmed 14

log10(X Variable): mean 0.477
std. dev. 0.216

log10(Y Variable): mean 0.511
std. dev. 0.463

correlation -0.068
Pr[correlation=0] 0.408

rank correlation -0.155
Pr[rank correlation=0] 0.060

calcite vs. smectite

Number of data 149
Number plotted 149
Number trimmed 14

log10(X Variable): mean 1.088
std. dev. 0.232

log10(Y Variable): mean 0.511
std. dev. 0.463

correlation 0.129
Pr[correlation=0] 0.118

rank correlation 0.079
Pr[rank correlation=0] 0.340

calcite vs. zeol_clinoptilolite

Number of data 146
Number plotted 146
Number trimmed 17

log10(X Variable): mean 0.657
std. dev. 0.615

log10(Y Variable): mean 0.517
std. dev. 0.454

correlation 0.264
Pr[correlation=0] 0.001

rank correlation 0.317
Pr[rank correlation=0] 0.000

Figure 3.25 Scatterplots evaluating bivariate correlation between calcite and the sorbing minerals hematite, mica, smectite, and clinoptilolite.
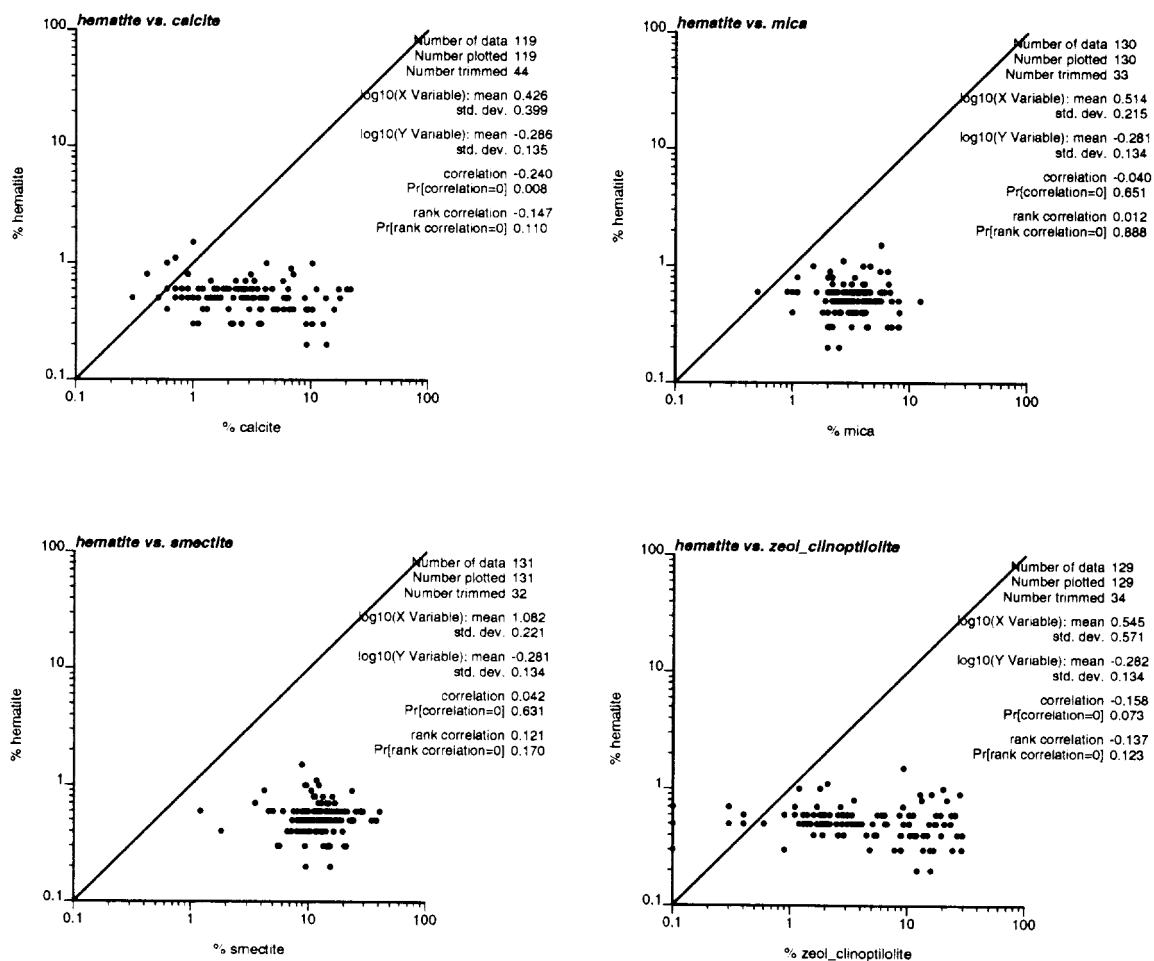
Figure 3.26 Scatterplots evaluating bivariate correlation between hematite and the sorbing minerals calcite, mica, smectite, and clinoptilolite.
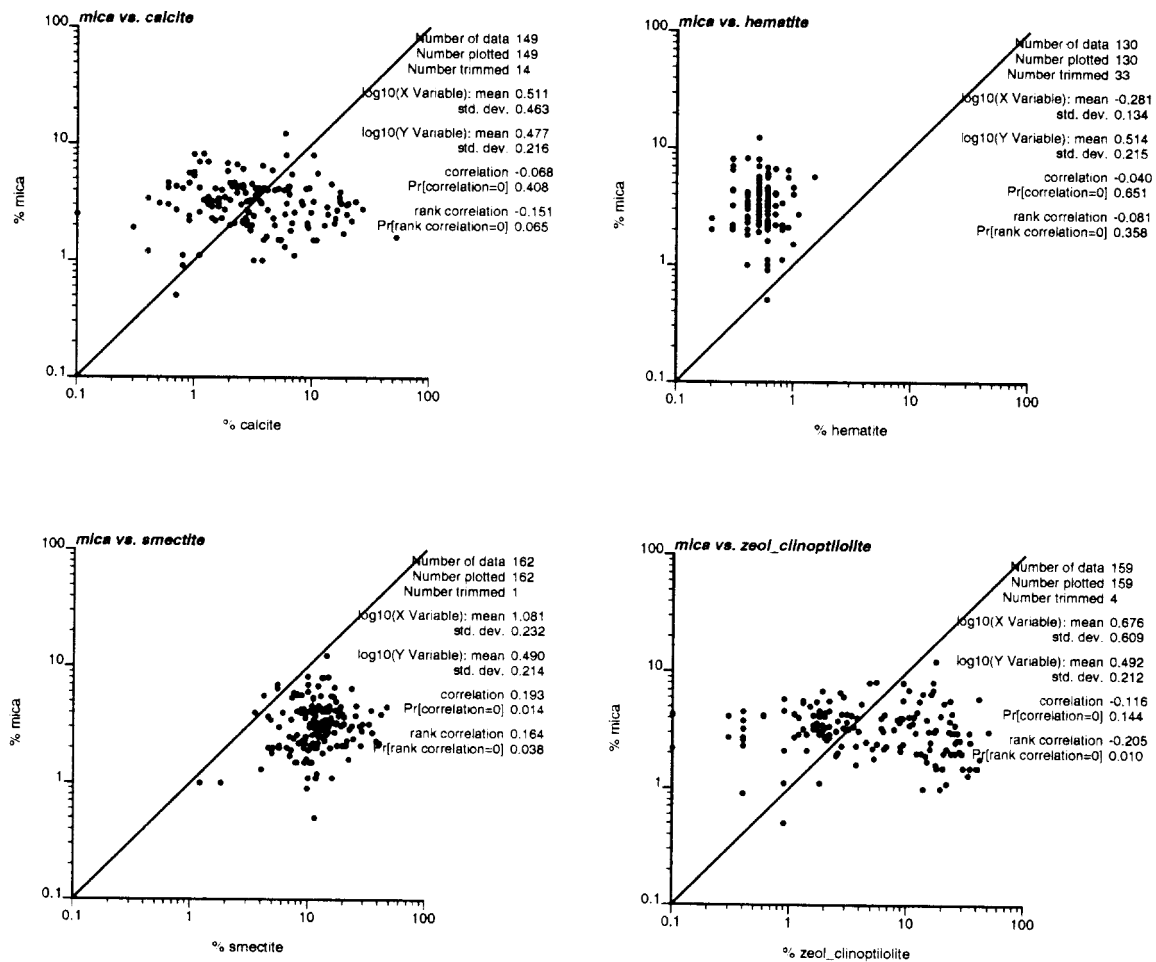
Figure 3.27 Scatterplots evaluating bivariate correlation between mica and the sorbing minerals calcite, hematite, smectite, and clinoptilolite.
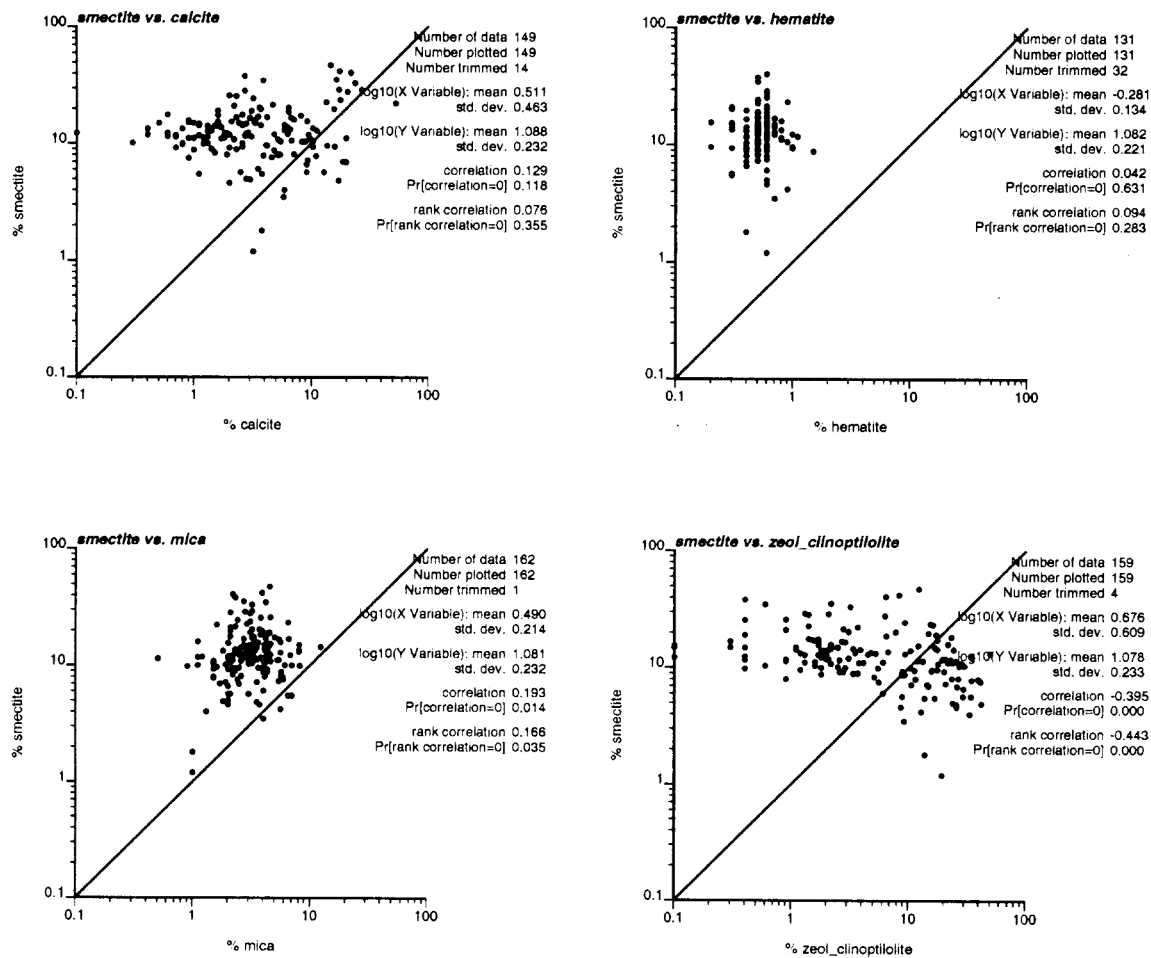
Figure 3.28 Scatterplots evaluating bivariate correlation between smectite and the sorbing minerals calcite, hematite, mica, and clinoptilolite.
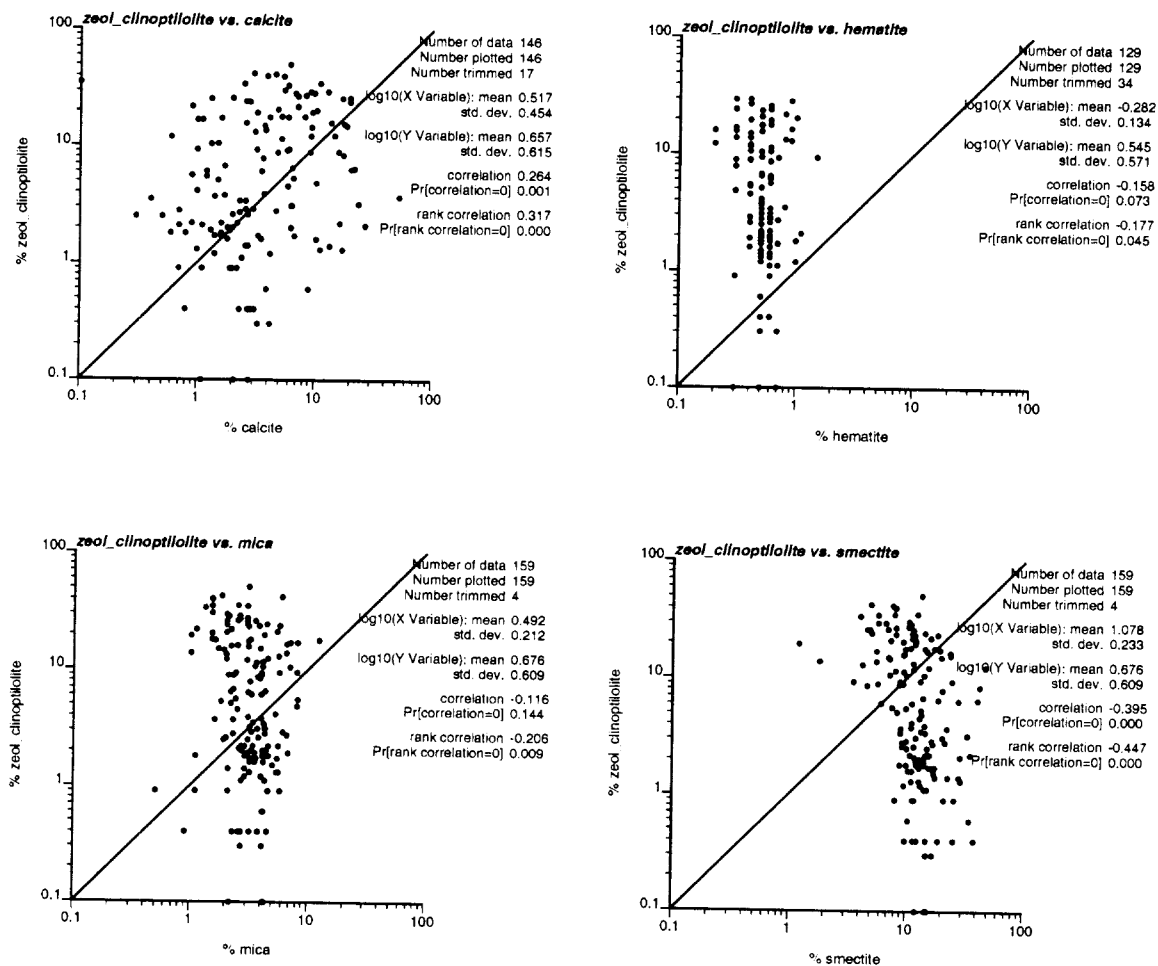
Figure 3.29 Scatterplots evaluating bivariate correlation between clinoptilolite and the sorbing minerals calcite, hematite, mica, and smectite.

calcite vs. dolomite

Number of data 24
Number plotted 24
Number trimmed 139

log10(X Variable): mean 0.217
std. dev. 0.546

log10(Y Variable): mean 0.969
std. dev. 0.399

correlation 0.563
Pr[correlation=0] 0.003

rank correlation 0.537
Pr[rank correlation=0] 0.007

% calcite / % dolomite

calcite vs. kaolinite

Number of data 74
Number plotted 74
Number trimmed 89

log10(X Variable): mean -0.482
std. dev. 0.287

log10(Y Variable): mean 0.660
std. dev. 0.416

correlation 0.153
Pr[correlation=0] 0.195

rank correlation 0.255
Pr[rank correlation=0] 0.028

% calcite / % kaolinite

calcite vs. glass

Number of data 97
Number plotted 97
Number trimmed 66

log10(X Variable): mean 1.287
std. dev. 0.179

log10(Y Variable): mean 0.357
std. dev. 0.383

correlation -0.139
Pr[correlation=0] 0.176

rank correlation -0.063
Pr[rank correlation=0] 0.541

% calcite / % glass

calcite vs. cristobalite

Number of data 139
Number plotted 139
Number trimmed 24

log10(X Variable): mean 0.413
std. dev. 0.291

log10(Y Variable): mean 0.452
std. dev. 0.421

correlation -0.308
Pr[correlation=0] 0.000

rank correlation -0.333
Pr[rank correlation=0] 0.000

% calcite / % cristobalite

calcite vs. opal

Number of data 32
Number plotted 32
Number trimmed 131

log10(X Variable): mean 0.393
std. dev. 0.477

log10(Y Variable): mean 0.733
std. dev. 0.428

correlation -0.271
Pr[correlation=0] 0.135

rank correlation -0.463
Pr[rank correlation=0] 0.008

% calcite / % opal

calcite vs. quartz

Number of data 149
Number plotted 149
Number trimmed 14

log10(X Variable): mean 0.867
std. dev. 0.227

log10(Y Variable): mean 0.511
std. dev. 0.463

correlation 0.471
Pr[correlation=0] 0.000

rank correlation 0.464
Pr[rank correlation=0] 0.000

% calcite / % quartz

Figure 3.30 Scatterplots evaluating bivariate correlation between calcite and the non-sorbing minerals dolomite, kaolinite, glass, cristobalite, opal, and quartz.

Figure 3.31 Scatterplots evaluating bivariate correlation between calcite and the non-sorbing minerals tridymite, hornblende, orthoclase, sanidine, albite, and bytownite.

hematite vs. dolomite

Number of data	14
Number plotted	14
Number trimmed	149
log10(X Variable): mean	0.100
std. dev.	0.508
log10(Y Variable): mean	-0.303
std. dev.	0.149
correlation	0.381
Pr[correlation=0]	0.184
rank correlation	0.495
Pr[rank correlation=0]	0.072

hematite vs. kaolinite

Number of data	64
Number plotted	64
Number trimmed	99
log10(X Variable): mean	-0.471
std. dev.	0.262
log10(Y Variable): mean	-0.301
std. dev.	0.121
correlation	-0.227
Pr[correlation=0]	0.071
rank correlation	-0.246
Pr[rank correlation=0]	0.050

hematite vs. glass

Number of data	99
Number plotted	99
Number trimmed	64
log10(X Variable): mean	1.275
std. dev.	0.179
log10(Y Variable): mean	-0.286
std. dev.	0.123
correlation	-0.060
Pr[correlation=0]	0.554
rank correlation	0.222
Pr[rank correlation=0]	0.027

hematite vs. cristobalite

Number of data	127
Number plotted	127
Number trimmed	36
log10(X Variable): mean	0.461
std. dev.	0.265
log10(Y Variable): mean	-0.283
std. dev.	0.135
correlation	0.175
Pr[correlation=0]	0.049
rank correlation	0.189
Pr[rank correlation=0]	0.033

hematite vs. opal

Number of data	14
Number plotted	14
Number trimmed	149
log10(X Variable): mean	0.679
std. dev.	0.423
log10(Y Variable): mean	-0.316
std. dev.	0.159
correlation	0.045
Pr[correlation=0]	0.882
rank correlation	0.002
Pr[rank correlation=0]	0.994

hematite vs. quartz

Number of data	130
Number plotted	130
Number trimmed	33
log10(X Variable): mean	0.821
std. dev.	0.196
log10(Y Variable): mean	-0.281
std. dev.	0.134
correlation	-0.226
Pr[correlation=0]	0.010
rank correlation	-0.096
Pr[rank correlation=0]	0.279

Figure 3.32 Scatterplots evaluating bivariate correlation between hematite and the non-sorbing minerals dolomite, kaolinite, glass, cristobalite, opal, and quartz.

3-58

hematite vs. tridymite

100

Number of data 52
Number plotted 52
Number trimmed 111

log10(X Variable): mean 0.082
std. dev. 0.350

log10(Y Variable): mean -0.264
std. dev. 0.111

correlation 0.208
Pr[correlation=0] 0.139

rank correlation -0.001
Pr[rank correlation=0] 0.993

10

% hematite

1

0.1

0.1   1   10   100

% tridymite

hematite vs. hornblende

100

Number of data 127
Number plotted 127
Number trimmed 36

log10(X Variable): mean -0.276
std. dev. 0.302

log10(Y Variable): mean -0.283
std. dev. 0.135

correlation 0.024
Pr[correlation=0] 0.790

rank correlation 0.016
Pr[rank correlation=0] 0.856

10

% hematite

1

0.1

0.1   1   10   100

% hornblende

hematite vs. feld_Kspar_orthoclase

100

Number of data 131
Number plotted 131
Number trimmed 32

log10(X Variable): mean 0.870
std. dev. 0.170

log10(Y Variable): mean -0.281
std. dev. 0.134

correlation 0.117
Pr[correlation=0] 0.182

rank correlation 0.270
Pr[rank correlation=0] 0.002

10

% hematite

1

0.1

0.1   1   10   100

% feld_Kspar_orthoclase

hematite vs. feld_Kspar_sanidine

100

Number of data 116
Number plotted 116
Number trimmed 47

log10(X Variable): mean 0.520
std. dev. 0.215

log10(Y Variable): mean -0.284
std. dev. 0.136

correlation 0.013
Pr[correlation=0] 0.886

rank correlation 0.066
Pr[rank correlation=0] 0.479

10

% hematite

1

0.1

0.1   1   10   100

% feld_Kspar_sanidine

hematite vs. feld_plag_albite

100

Number of data 95
Number plotted 95
Number trimmed 68

log10(X Variable): mean 0.523
std. dev. 0.267

log10(Y Variable): mean -0.286
std. dev. 0.145

correlation 0.018
Pr[correlation=0] 0.865

rank correlation 0.077
Pr[rank correlation=0] 0.458

10

% hematite

1

0.1

0.1   1   10   100

% feld_plag_albite

hematite vs. feld_plag_bytownite

100

Number of data 131
Number plotted 131
Number trimmed 32

log10(X Variable): mean 1.405
std. dev. 0.201

log10(Y Variable): mean -0.281
std. dev. 0.134

correlation 0.142
Pr[correlation=0] 0.106

rank correlation 0.230
Pr[rank correlation=0] 0.008

10

% hematite

1

0.1

0.1   1   10   100

% feld_plag_bytownite

Figure 3.33 Scatterplots evaluating bivariate correlation between hematite and the non-sorbing minerals tridymite, hornblende, orthoclase, sanidine, albite, and bytownite.

Figure 3.34 Scatterplots evaluating bivariate correlation between mica and the non-sorbing minerals dolomite, kaolinite, glass, cristobalite, opal, and quartz.

mica vs. tridymite

% mica (y-axis), % tridymite (x-axis)

Number of data 52
Number plotted 52
Number trimmed 111

log10(X Variable): mean 0.082
std. dev. 0.350

log10(Y Variable): mean 0.575
std. dev. 0.154

correlation -0.018
Pr[correlation=0] 0.900

rank correlation 0.052
Pr[rank correlation=0] 0.715

mica vs. hornblende

% mica (y-axis), % hornblende (x-axis)

Number of data 154
Number plotted 154
Number trimmed 9

log10(X Variable): mean -0.323
std. dev. 0.311

log10(Y Variable): mean 0.492
std. dev. 0.217

correlation 0.469
Pr[correlation=0] 0.000

rank correlation 0.511
Pr[rank correlation=0] 0.000

mica vs. feld_Kspar_orthoclase

% mica (y-axis), % feld_Kspar_orthoclase (x-axis)

Number of data 162
Number plotted 162
Number trimmed 1

log10(X Variable): mean 0.825
std. dev. 0.224

log10(Y Variable): mean 0.490
std. dev. 0.214

correlation 0.062
Pr[correlation=0] 0.431

rank correlation 0.103
Pr[rank correlation=0] 0.191

mica vs. feld_Kspar_sanidine

% mica (y-axis), % feld_Kspar_sanidine (x-axis)

Number of data 148
Number plotted 148
Number trimmed 15

log10(X Variable): mean 0.499
std. dev. 0.212

log10(Y Variable): mean 0.483
std. dev. 0.217

correlation -0.115
Pr[correlation=0] 0.164

rank correlation -0.135
Pr[rank correlation=0] 0.103

mica vs. feld_plag_albite

% mica (y-axis), % feld_plag_albite (x-axis)

Number of data 126
Number plotted 126
Number trimmed 37

log10(X Variable): mean 0.516
std. dev. 0.251

log10(Y Variable): mean 0.464
std. dev. 0.223

correlation -0.170
Pr[correlation=0] 0.056

rank correlation -0.191
Pr[rank correlation=0] 0.032

mica vs. feld_plag_bytownite

% mica (y-axis), % feld_plag_bytownite (x-axis)

Number of data 162
Number plotted 162
Number trimmed 1

log10(X Variable): mean 1.337
std. dev. 0.273

log10(Y Variable): mean 0.490
std. dev. 0.214

correlation 0.253
Pr[correlation=0] 0.001

rank correlation 0.428
Pr[rank correlation=0] 0.000

Figure 3.35 Scatterplots evaluating bivariate correlation between mica and the non-sorbing minerals tridymite, hornblende, orthoclase, sanidine, albite, and bytownite.
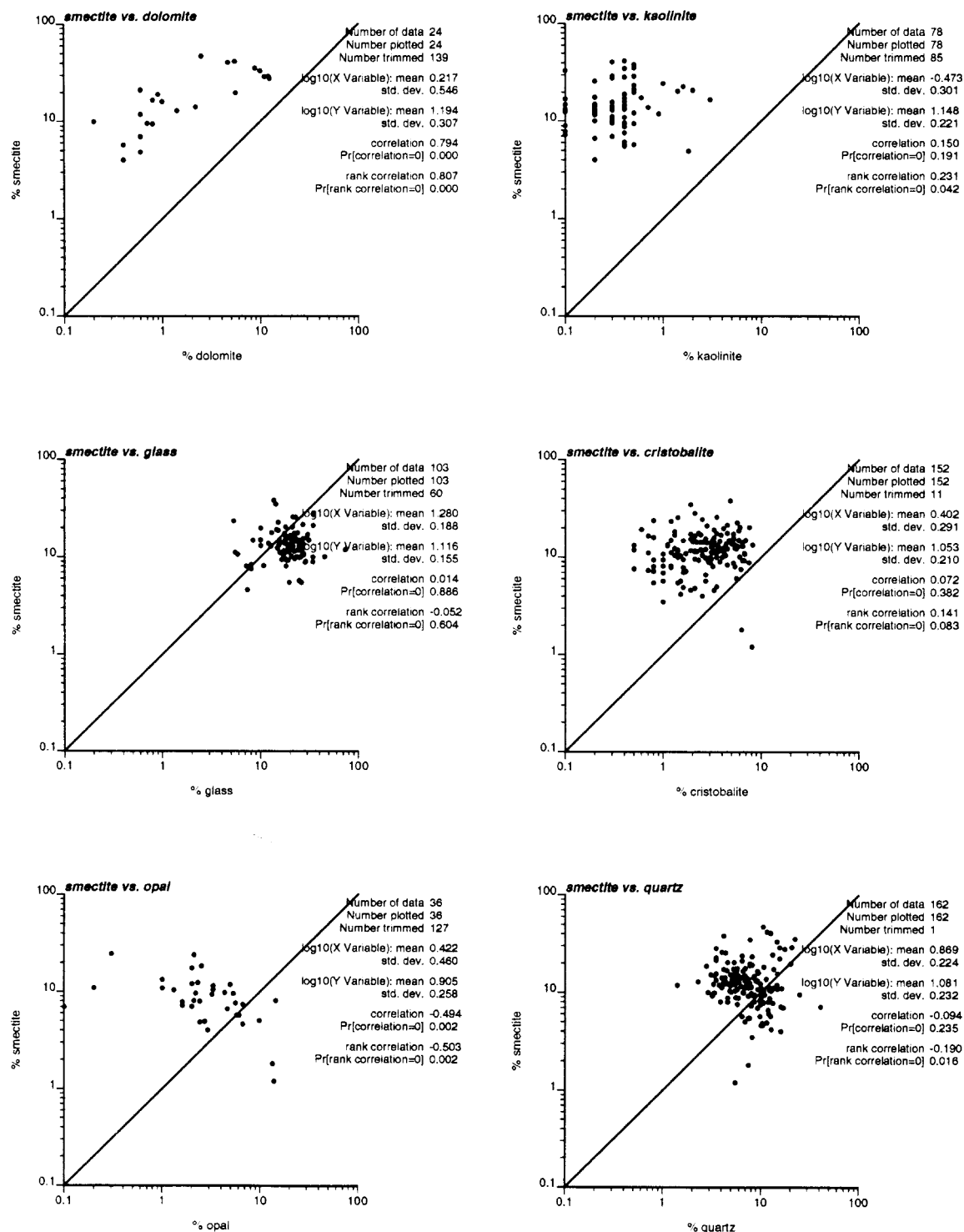
Figure 3.36 Scatterplots evaluating bivariate correlation between smectite and the non-sorbing minerals dolomite, kaolinite, glass, cristobalite, opal, and quartz.

Figure 3.37 Scatterplots evaluating bivariate correlation between smectite and the non-sorbing minerals tridymite, hornblende, orthoclase, sanidine, albite, and bytownite.

zeol_clinoptilolite vs. dolomite

Number of data 23
Number plotted 23
Number trimmed 140

log10(X Variable): mean 0.194
std. dev. 0.546

log10(Y Variable): mean 0.704
std. dev. 0.528

correlation -0.303
Pr[correlation=0] 0.162

rank correlation -0.401
Pr[rank correlation=0] 0.058

% zeol clinoptilolite
% dolomite

zeol_clinoptilolite vs. kaolinite

Number of data 76
Number plotted 76
Number trimmed 87

log10(X Variable): mean -0.485
std. dev. 0.291

log10(Y Variable): mean 0.532
std. dev. 0.577

correlation 0.144
Pr[correlation=0] 0.214

rank correlation 0.198
Pr[rank correlation=0] 0.087

% zeol clinoptilolite
% kaolinite

zeol_clinoptilolite vs. glass

Number of data 100
Number plotted 100
Number trimmed 63

log10(X Variable): mean 1.278
std. dev. 0.178

log10(Y Variable): mean 0.373
std. dev. 0.521

correlation -0.388
Pr[correlation=0] 0.000

rank correlation -0.340
Pr[rank correlation=0] 0.001

% zeol clinoptilolite
% glass

zeol_clinoptilolite vs. cristobalite

Number of data 150
Number plotted 150
Number trimmed 13

log10(X Variable): mean 0.407
std. dev. 0.287

log10(Y Variable): mean 0.680
std. dev. 0.622

correlation -0.449
Pr[correlation=0] 0.000

rank correlation -0.468
Pr[rank correlation=0] 0.000

% zeol_clinoptilolite
% cristobalite

zeol_clinoptilolite vs. opal

Number of data 36
Number plotted 36
Number trimmed 127

log10(X Variable): mean 0.422
std. dev. 0.460

log10(Y Variable): mean 1.369
std. dev. 0.176

correlation -0.072
Pr[correlation=0] 0.677

rank correlation -0.080
Pr[rank correlation=0] 0.643

% zeol clinoptilolite
% opal

zeol_clinoptilolite vs. quartz

Number of data 159
Number plotted 159
Number trimmed 4

log10(X Variable): mean 0.871
std. dev. 0.216

log10(Y Variable): mean 0.676
std. dev. 0.609

correlation 0.492
Pr[correlation=0] 0.000

rank correlation 0.567
Pr[rank correlation=0] 0.000

% zeol_clinoptilolite
% quartz

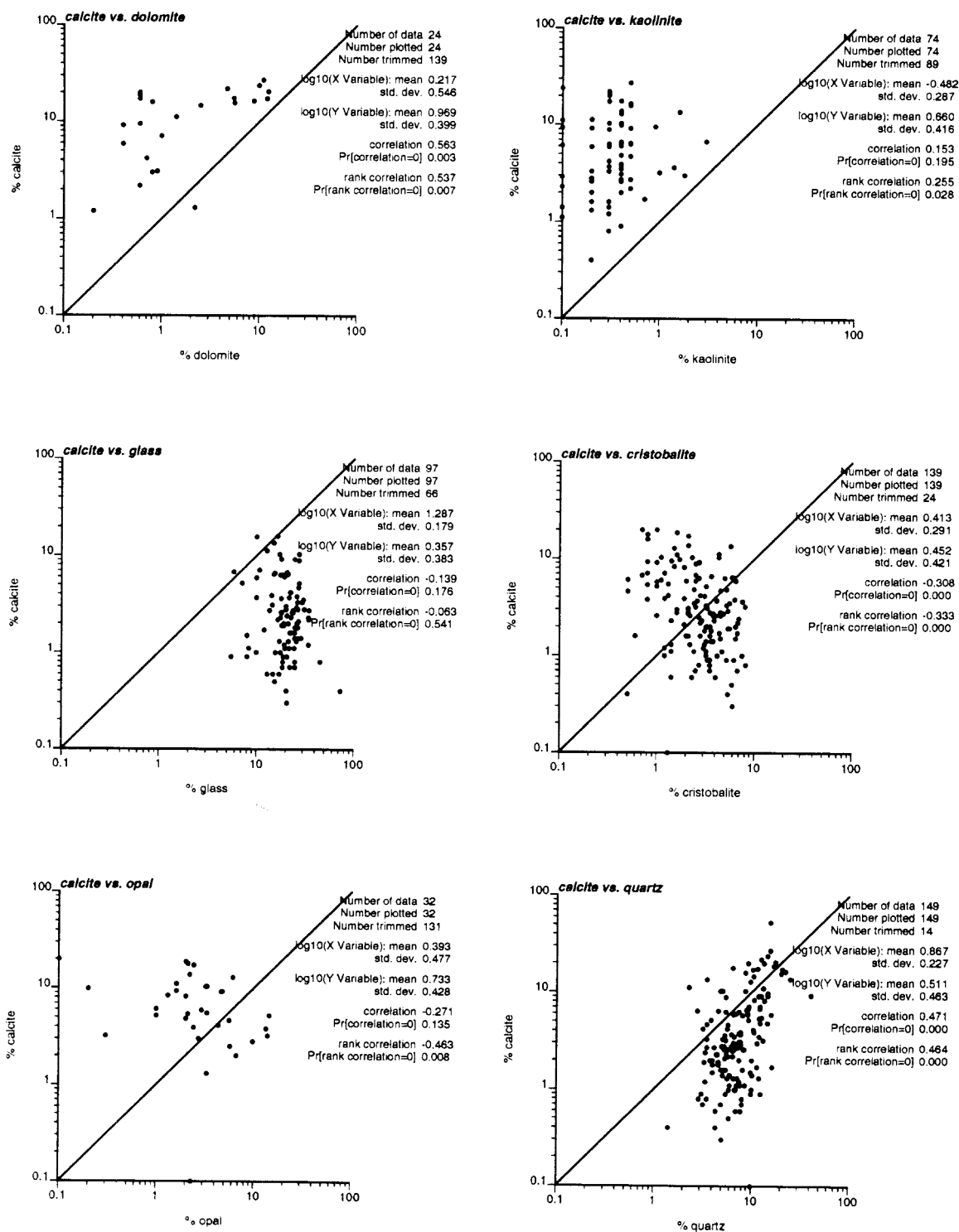Figure 3.38 Scatterplots evaluating bivariate correlation between clinoptilolite and the non-sorbing minerals dolomite, kaolinite, glass, cristobalite, opal, and quartz.
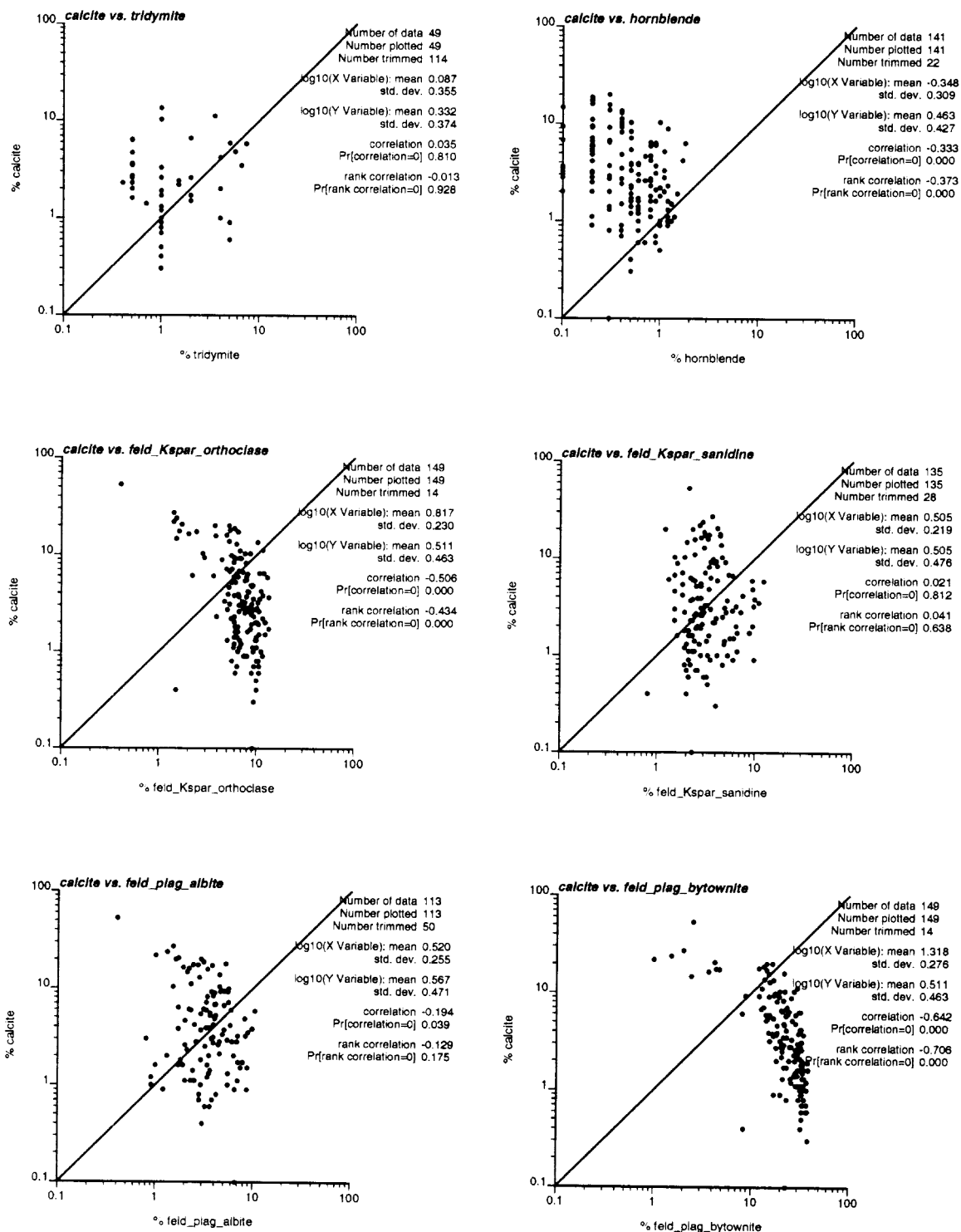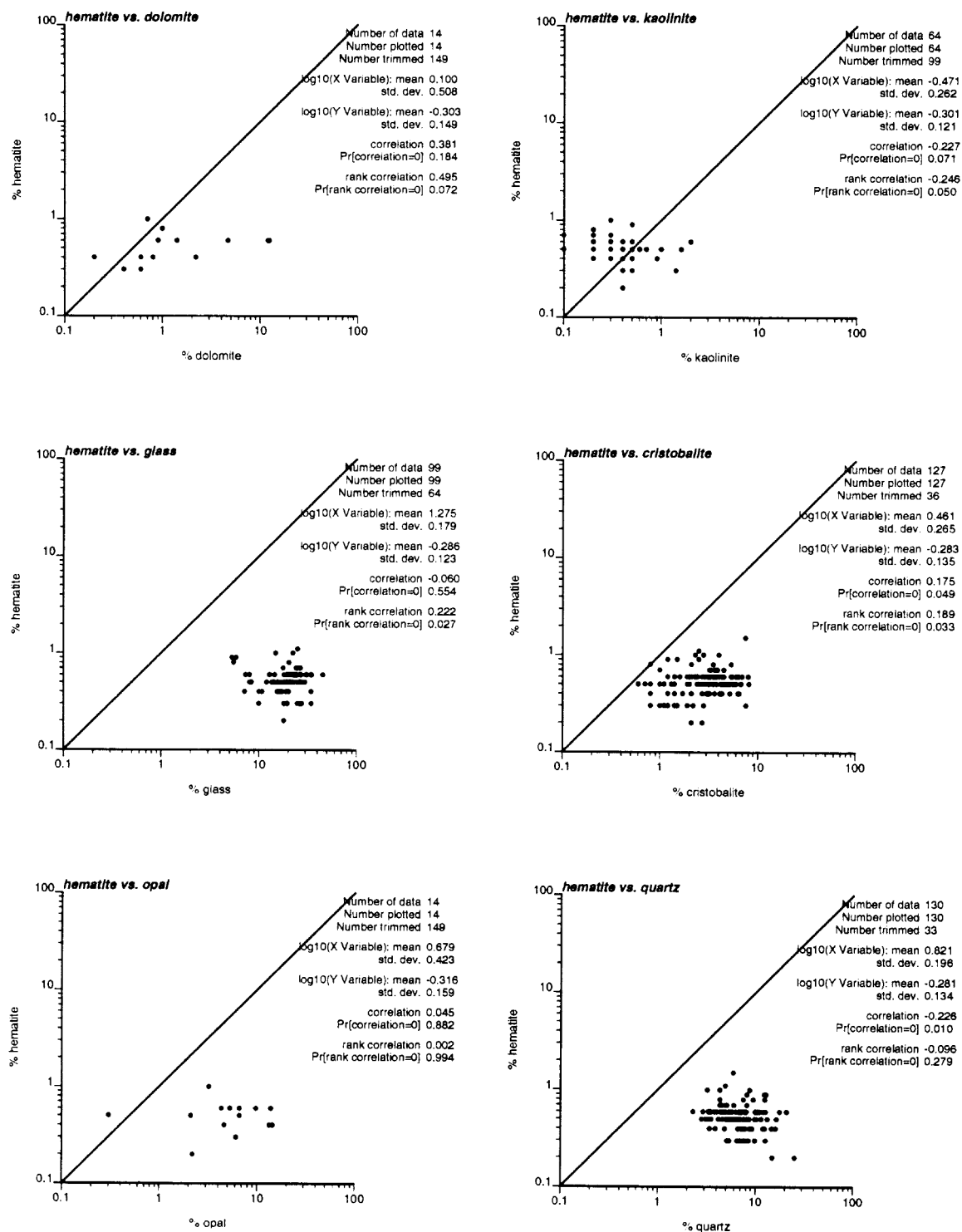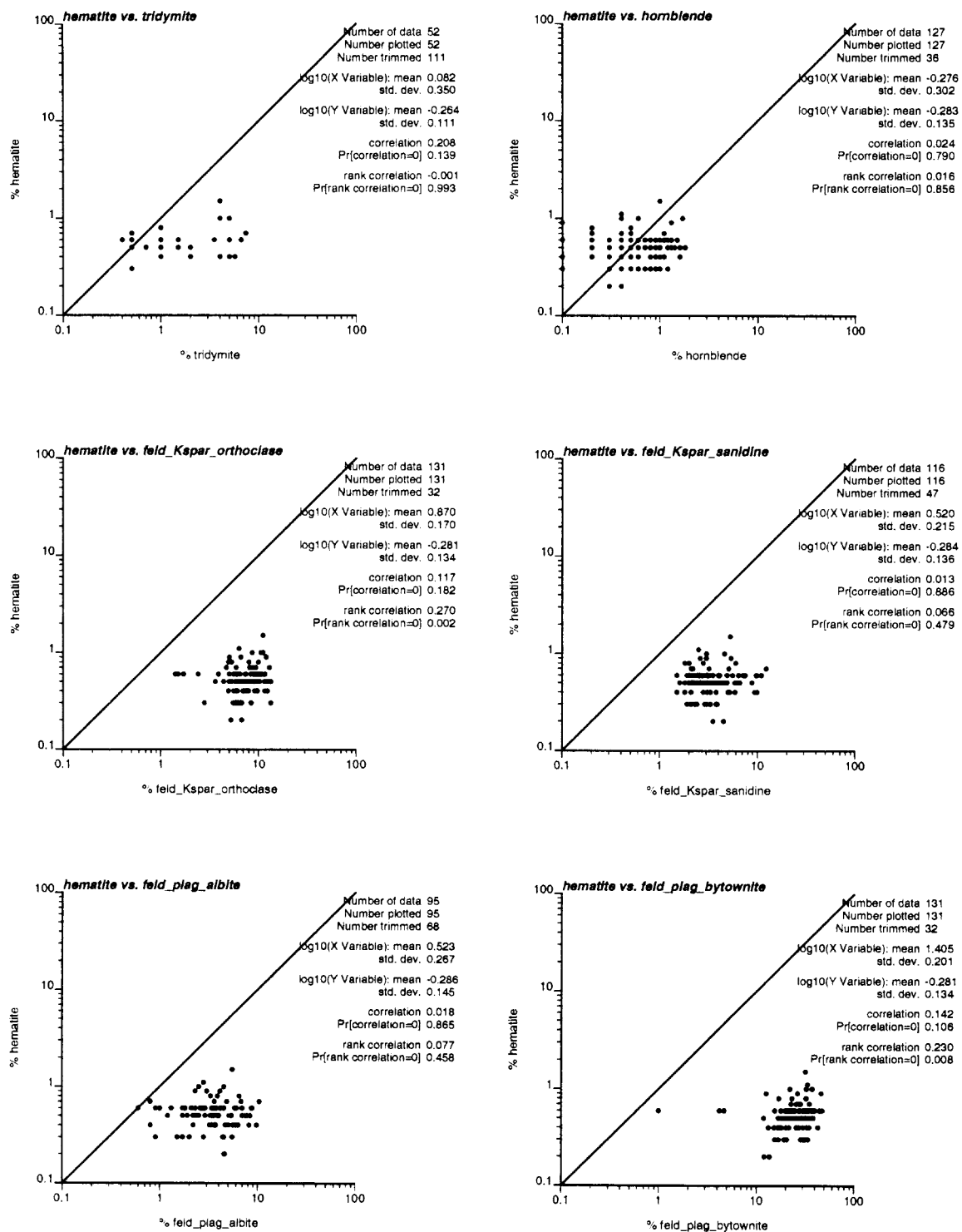
Figure 3.39 Scatterplots evaluating bivariate correlation between clinoptilolite and the non-sorbing minerals tridymite, hornblende, orthoclase, sanidine, albite, and bytownite.
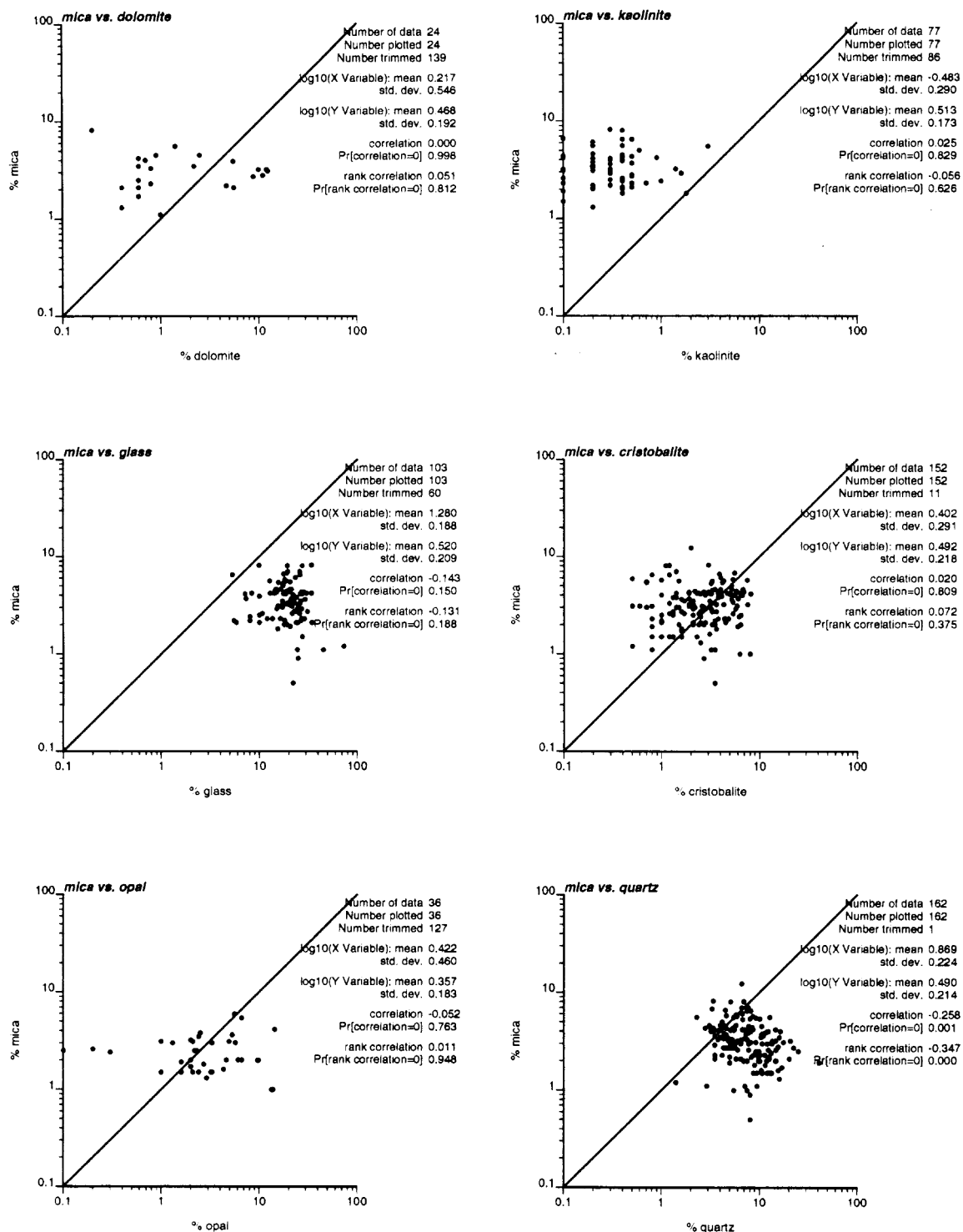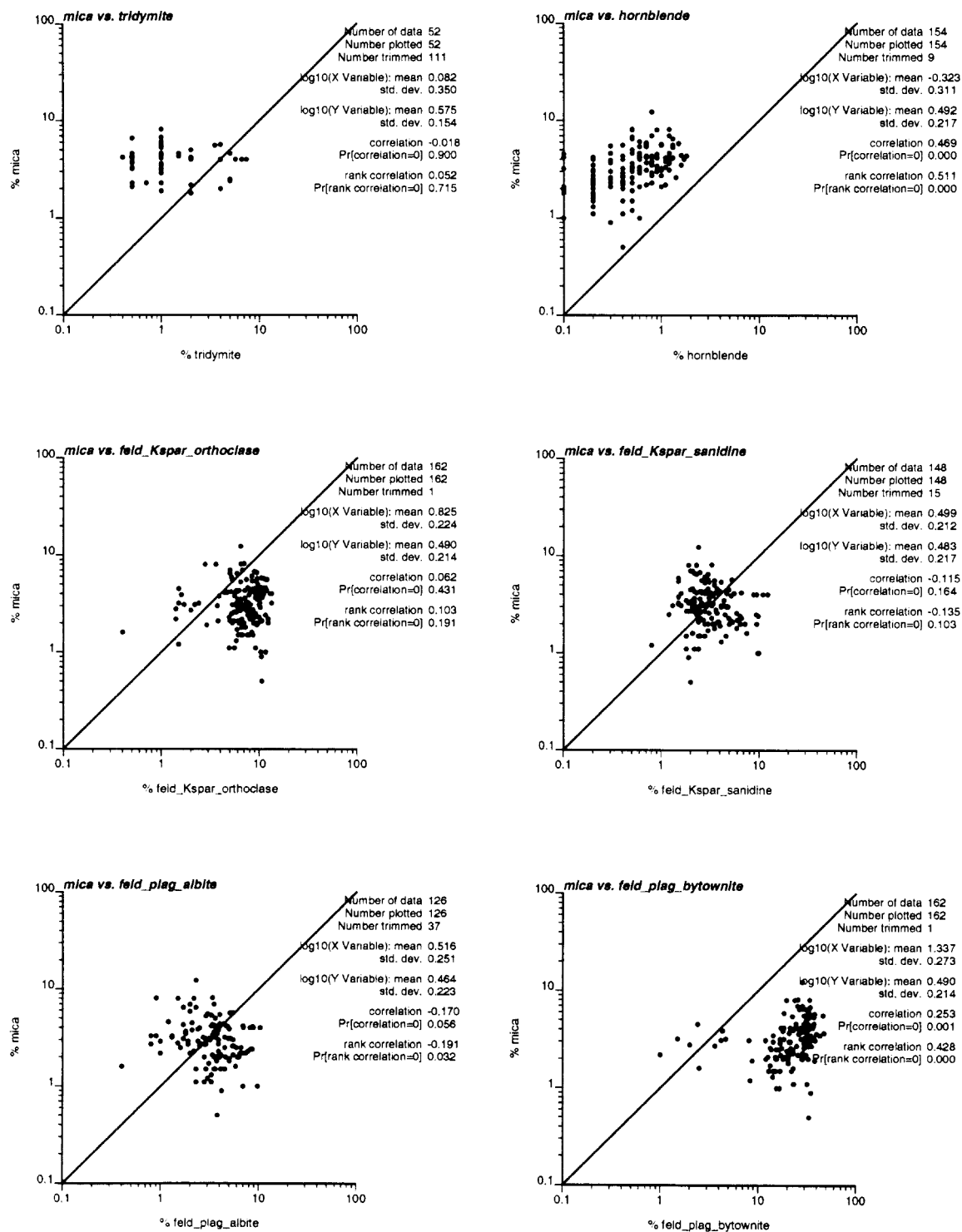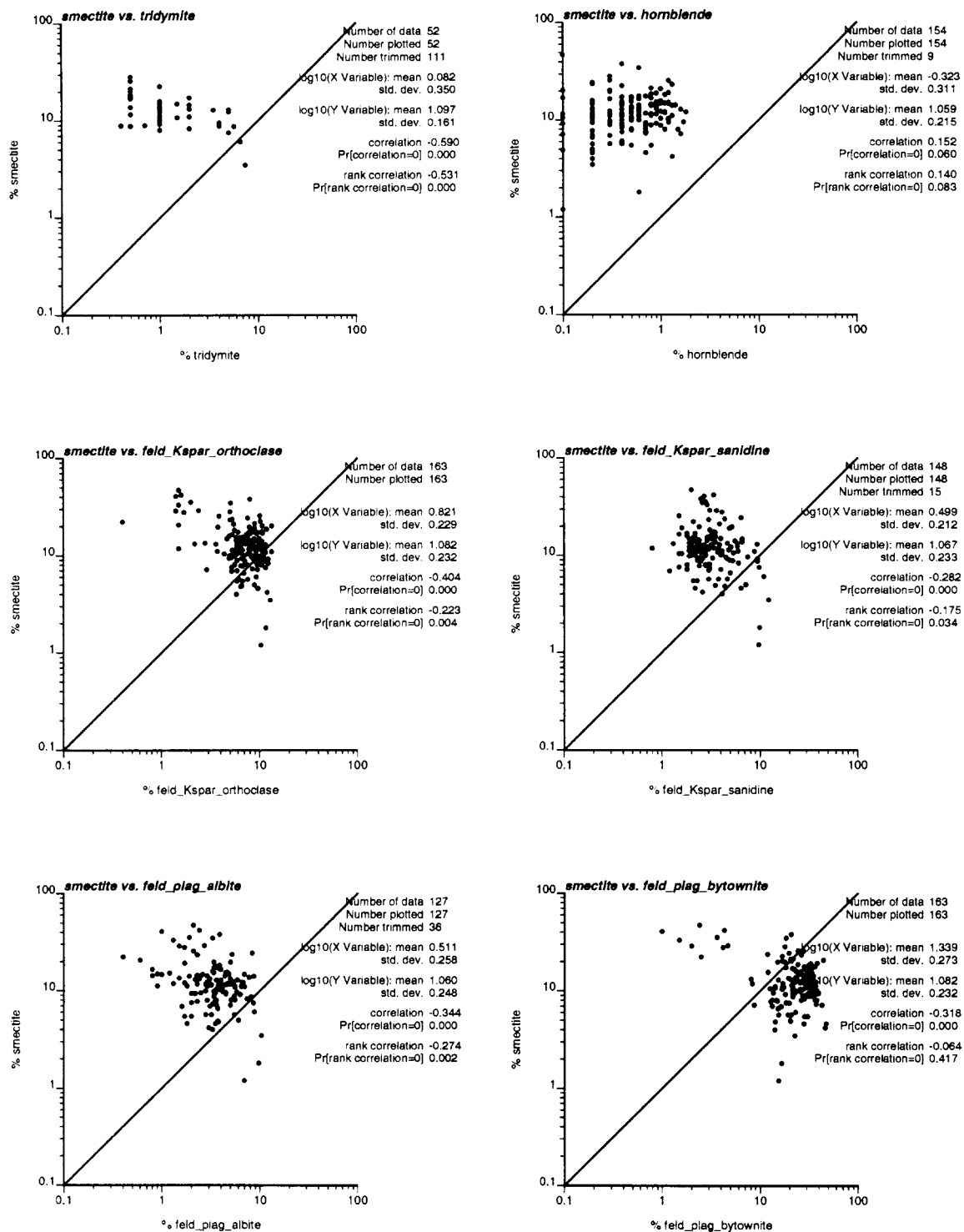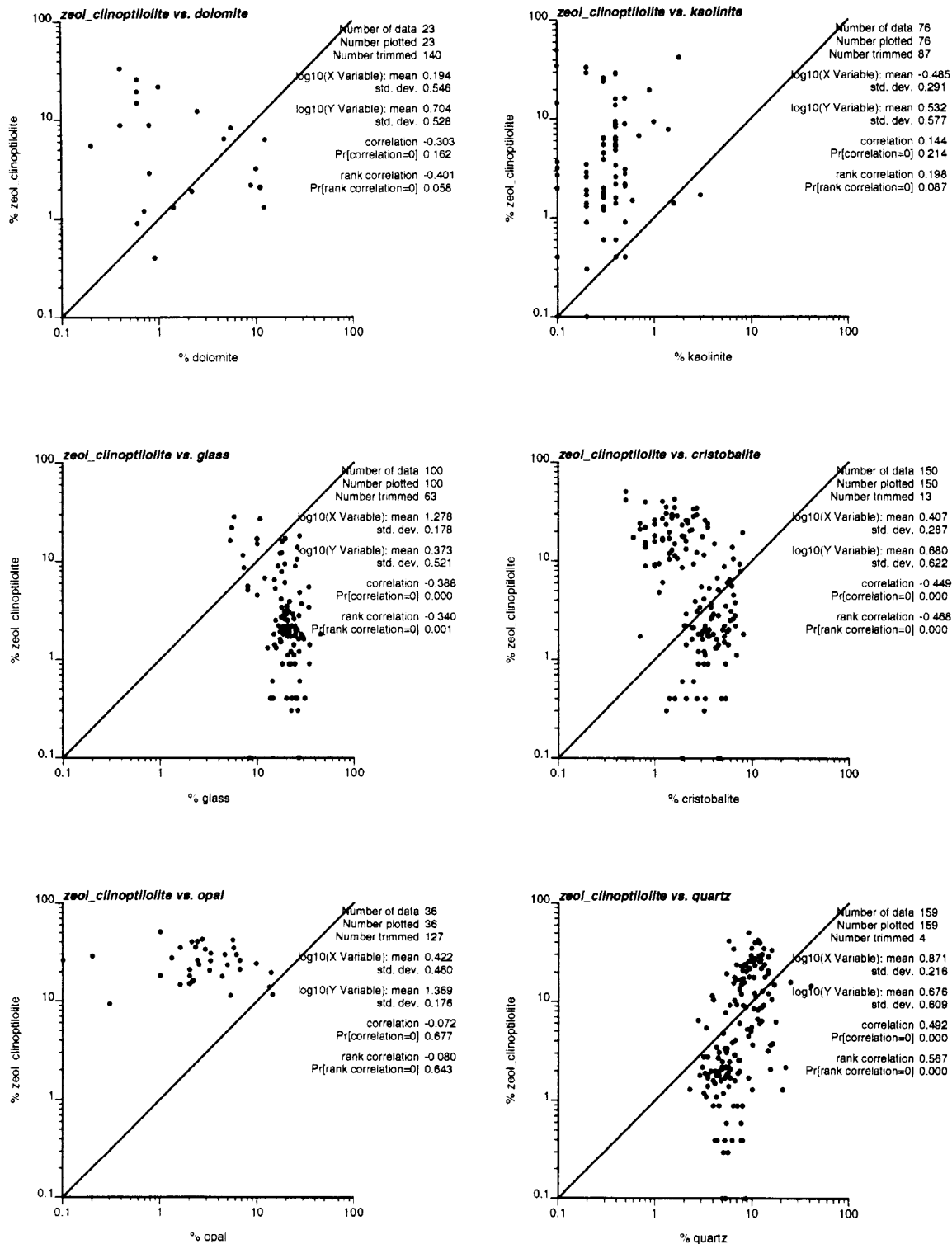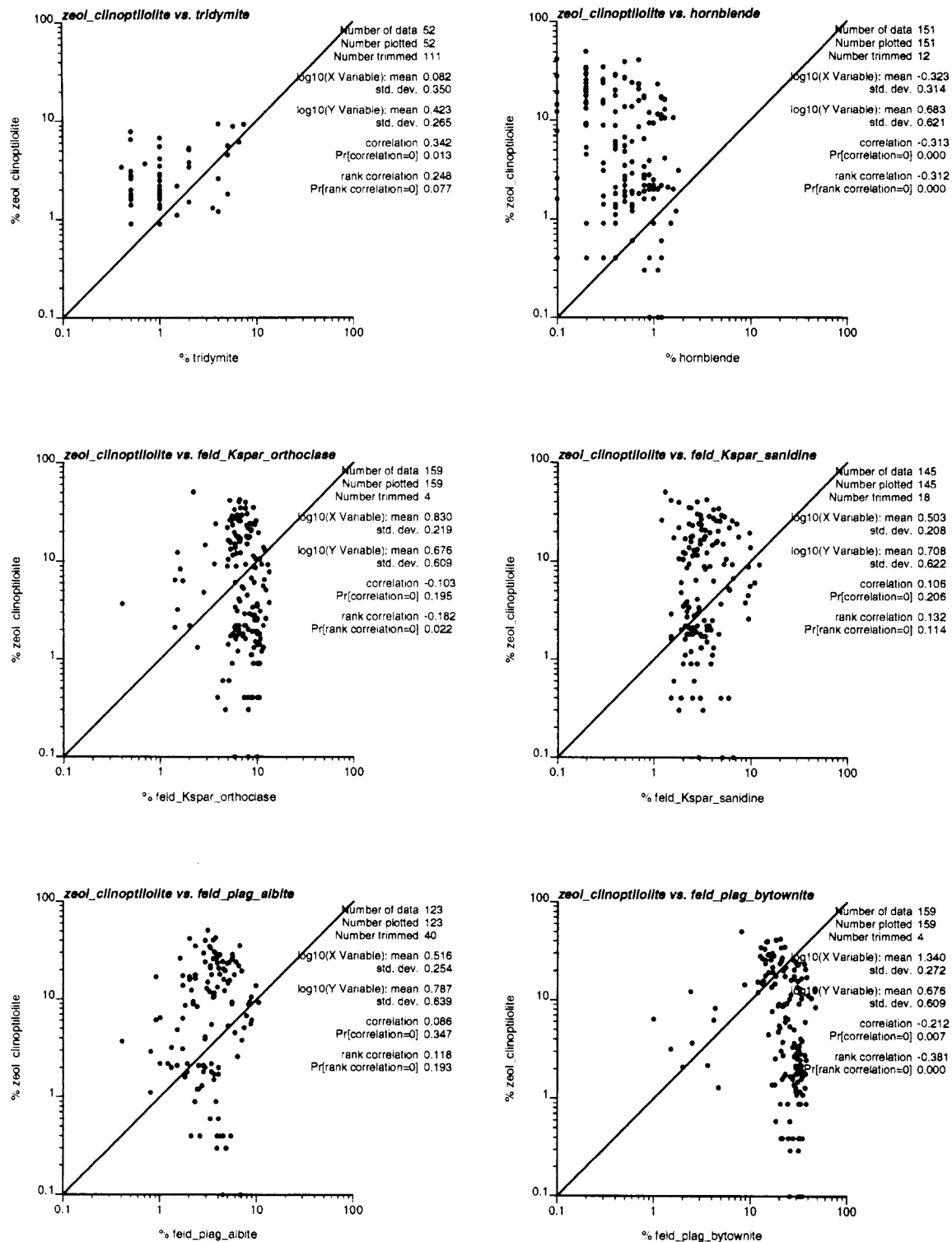
3.5 Comparison of Chemofacies with Alluvial Layering

Based on mineralogic, chemical, and lithologic information, Warren et al. (2002) identified several alluvial layers in ER-5-4 and UE-5n. A description of alluvial layering in Frenchman Flat may provide a suitable framework for developing three-dimensional models of hydraulic and reactive transport properties. To explore this possibility, we compare our interpretations of the zonal mean abundances of sorbing minerals with the interpretations of alluvial layering.

We identify "chemofacies" as vertical intervals or zones of alluvium having similar distributions of zonal mean abundances for all sorbing minerals — calcite, hematite, mica, smectite, and clinoptilolite. Within a chemofacies, the statistical properties of all five mineral abundances appear stationary. Our chemofacies interpretations do not include lithologic interpretations, such as consideration of texture, mode of deposition, or elemental analysis of typically mobile or immobile elements as considered by Warren et al. (2002). Our chemofacies interpretations are strictly concerned with identifying zones of similar distributions of zonal mean abundances of sorbing minerals and, therefore, are bound to differ from the more geologically comprehensive interpretation of alluvial layering.

Another potential source of uncertainty in comparing the chemofacies and alluvial layering interpretations is raised by the analysis of multiple samples or "splits" obtained from the same core. While one split was used to produce XRD data, other splits were used to produce SEM and other data, as described by Warren et al. (2002, Section 3.1.2.3). Despite being located only a few centimeters apart, the data indicate that split samples within the same core may yield significantly different mineral concentrations. Having only a limited number of XRD data for sample splits (1 duplicate and 3 triplicate splits), our geostatistical analysis cannot evaluate small-scale or "microscale" variability at the scale of centimeters or less. Furthermore, since only XRD data were used in the geostatistical analysis, we could not evaluate how different methods of analysis (e.g. SEM data) could affect sorbing mineral abundance results. The geostatistical analysis in Chapter 5 indicates that significant spatial variability typically exists within a scale of about 0.3 m, which is the smallest core sample spacing. Therefore, it would not be surprising if, in actuality, the microscale variability of mineral concentrations in Frenchman Flat alluvium is relevant over scales less than a few centimeters. In future HST or CAU scale modeling, it will be important to recognize the uncertainty in identifying chemofacies or alluvial layers based on analysis of a few or sparse samples. Microscale variability and, possibly, uncertainty in the methods of analysis themselves may cause considerable uncertainty in identifying zones with similar mineral concentrations.

For the purpose of radionuclide transport modeling at HST or CAU scales, it will be important to recognize the potential for differences between interpretations based on alluvial layering and interpretations based on zones with different capacities to attenuate or sorb radionuclides. For example, if an alluvial layer corresponds to a package of alluvial sedimentation, there may be gradations of texture and mineral composition related to the evolution of alluvial deposition over time. Alluvial fans are composite features created by episodic accumulation of sediments. However, alluvial fans do exhibit systematic depositional patterns. Alluvial fans tend to fine outwards and may coarsen or fine upwards. Alluvial fans may consist of different depositional

facies such as sheetflood, debris flow, channel and sieve deposits. Playa deposits also occur in Frenchman Flat. As a result of a depositional hiatus, caliche layers may occur at the top of a package of alluvial sedimentation. Thus, different modes of deposition, various sorting mechanisms, and in situ alteration may complicate the spatial distribution of minerals within an alluvial layer. On the other hand, two different alluvial layers may possess very similar abundances of the sorbing minerals, such that two different alluvial layers could be categorized as the same chemofacies.

Figures 3.40 and 3.41 superpose zonal mean abundances interpreted for ER-5-4 and UE-5n (as shown in Figures 3.21 and 3.22) on the alluvial layering interpretation from Warren et al. (2002). Each mineral possesses a set of different zonal mean abundances, which were interpreted from the depth profiles of mineral abundance (Figures 3.21 to 3.24) and the univariate statistical analyses described in sections 3.1 to section 3.3 and summarized in Tables 3.3 and 3.4. In Figures 3.40 and 3.41, zonal mean abundances for non-sorbing minerals that exhibit significant correlation with at least one sorbing mineral, as indicated by Table 3.10 in section 3.4, are also shown to help identify chemofacies.

In Figure 3.40, the boundaries of alluvial layers for ER-5-4 correspond with many of the abrupt shifts in mean abundances of sorbing minerals. Starting from the top, the vertical interval for layer 1 is not identified in this study because no XRD data were obtained there. A large increase in clinoptilolite abundance distinguishes layers 3, 4 and 5 from layer 2. Lower calcite abundance is evident at the base of layer 5. Layers 6, 7, and 8 exhibit lower clinoptilolite abundance. Smectite abundance appears to increase below the middle of layer 7 down through layers 8 and 9a-c. In layer 9a, clinoptilolite abundance rises slightly, and calcite abundance is very high. Hematite abundance distinctively drops between depths of about 760 and 780 m within layer 9a. With respect to non-sorbing minerals, layer 9a is clearly distinguished from layers 6, 7, and 8 by abrupt decreases in cristobalite, tridymite, hornblende, and orthoclase abundances and increases in albite, dolomite, and quartz. Between depths of 780 to 900 m, layers 9a-c are interfingered, which is evident by large fluctuations in the zonal mean abundances. Layers 10 and 12 appear similar in both sorbing and non-sorbing mineral abundance, with lower smectite and distinctively low clinoptilolite abundance. Layer 11 has similar sorbing mineral abundances to layers 10 and 12, except that clinoptilolite abundance is very high.

Warren et al. (2002) interpreted a similar sequence of alluvial layers in UE-5n to a depth of about 480 m. Figure 3.41 shows zonal mean abundances of sorbing and correlated non-sorbing minerals superposed on the alluvial layers. The alluvial layers are deeper in UE-5n and show some variations in thickness compared to ER-5-4. In UE-5n, layer 4 is either absent or unresolved. The comparison between ER-5-4 and UE-5n, though limited by the limited number and depth range of samples from UE-5n, indicates that the alluvial layers exhibit significant lateral spatial continuity, on the scale of at least hundreds of meters. Additionally, variations in thickness and attitude (e.g., dip and strike of bounding surfaces) of the alluvial layers may need to be considered in both HST and CAU scale models.
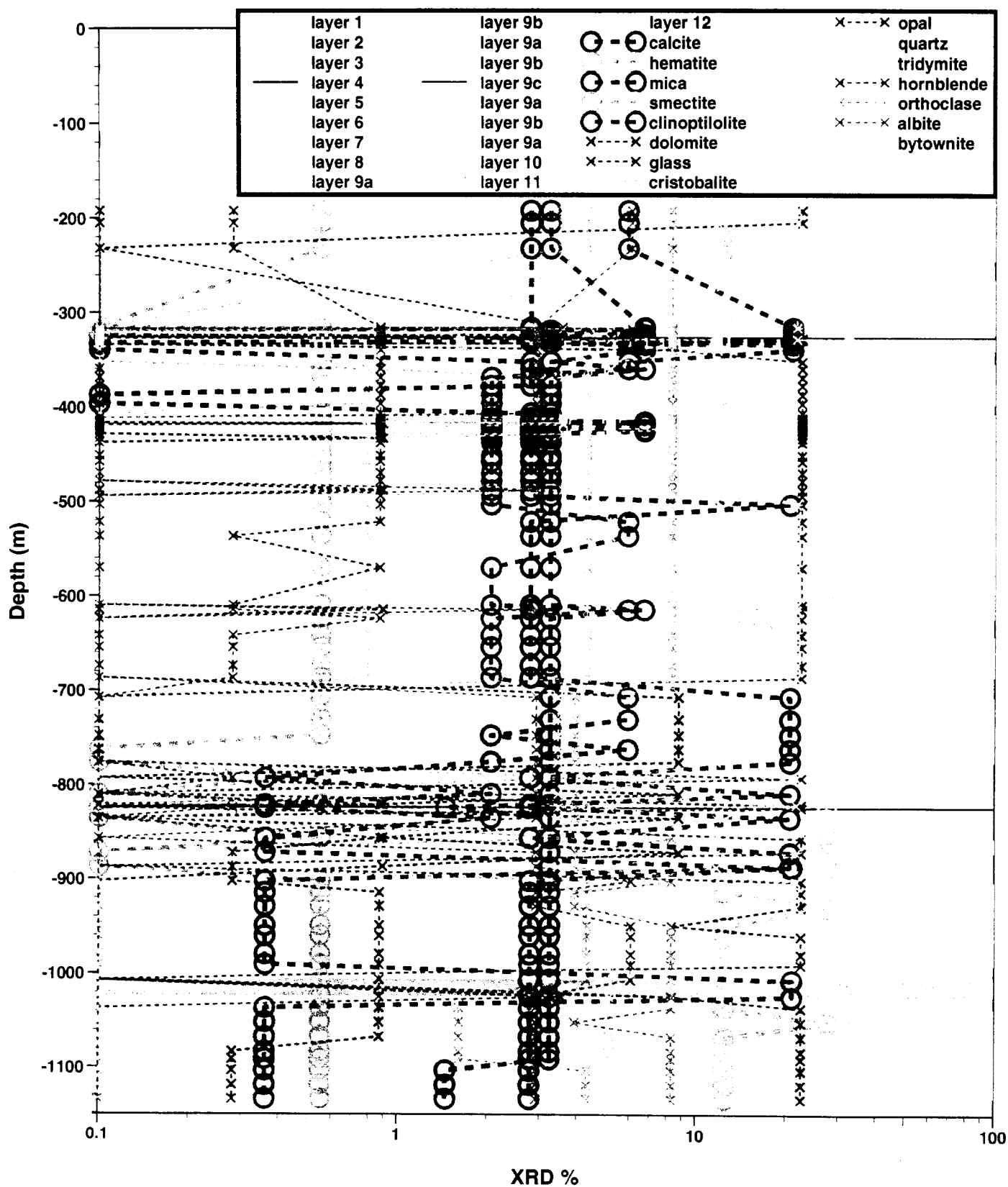
Figure 3.40 Zonal mean abundance of sorbing and correlated non-sorbing minerals in ER-5-4 superposed on alluvial layers proposed in Warren et al. (2002).
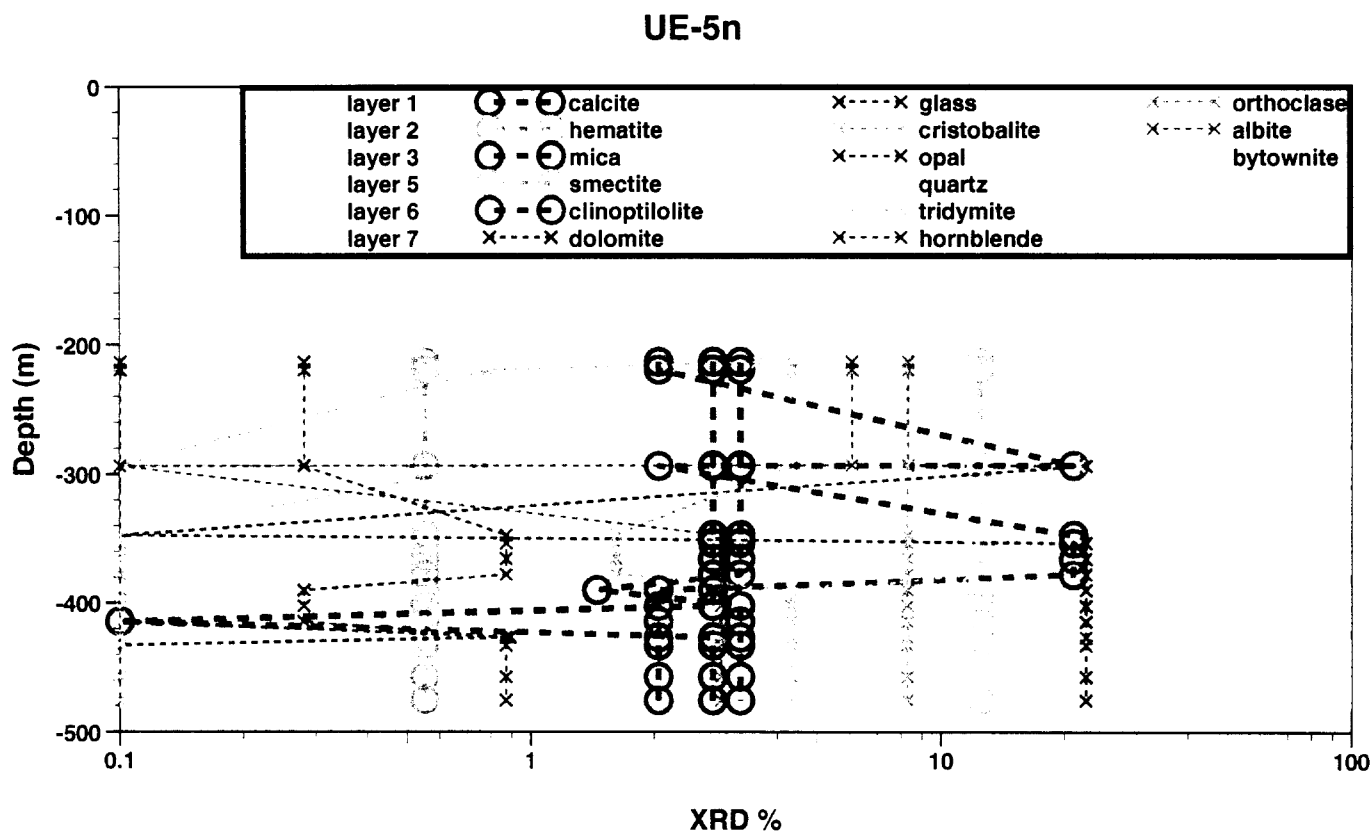
UE-5n

Figure 3.41 Zonal mean abundance of sorbing and correlated non-sorbing minerals in UE-5n superposed on alluvial layers proposed in Warren et al. (2002).

For comparison to the alluvial layering interpretations, Figures 3.42 and 3.43 show our chemofacies interpretations for ER-5-4 and UE-5n. The chemofacies appear as vertical zones with distinctive sets of zonal mean abundances of sorbing minerals. Only the depth profiles of the zonal mean abundances of sorbing minerals are shown because these data distinguish different chemofacies. The legends in both Figures 3.42 and 3.43 provide a depth-ordered profile of the chemofacies. Some chemofacies may repeat at different depth intervals — chemofacies 1 and 2, or example, in ER-5-4.

Table 3.11 summarizes a comparison between the chemofacies interpretations and the alluvial layers identified by Warren et al. (2002). Compared to the alluvial layers, chemofacies 1 corresponds to layers 2 and 6 and the upper portion of layer 7. Chemofacies 2 corresponds to layer 3, and chemofacies 3 corresponds to layer 5. A distinctive chemofacies is not associated with layer 4. Chemofacies 4, distinguished from chemofacies 1 by low calcite, occurs between depths of about 380 to 400 m at the base of layer 6. Chemofacies 5, distinguished by higher smectite relative to chemofacies 1, spans layer 8 and the lower portion of layer 7. Chemofacies 6, distinguished from chemofacies 5 by high calcite, occurs in a thin zone at the top of chemofacies 5 near a depth of 500 m. Chemofacies 6 also corresponds with layer 9a, except between a depth of 760 and 780 m, where chemofacies 7 is distinguished by lack of hematite. Between the depths of 780 to 900 m, a transition zone consisting of a mixture of chemofacies 6, 7, and 8 is apparent, which corresponds to the interfingering of layers 9a, 9b, and 9c. However,

chemofacies 8 continues below a depth 900 m, corresponding to layers 10 and 12, except where another occurrence of chemofacies 2 (having high clinoptilolite abundance) corresponds to layer 11.

Table 3.11 Summary of chemofacies interpretation in ER-5-4, with comparison to alluvial layers identified by Warren et al. (2002).

Chemofacies	Depth Range(s) in ER-5-4	Alluvial Layer(s)	Distinctive Features
1	190-233; 345-380; 400-500	2, 6, 7 (upper)	Lower smectite
2	310-330; 1000-1030	3, 11	High clinoptilolite
3	330-345	5	Like 2, but low calcite
4	380-400	6 (base)	Like 1, but low calcite
5	510-700	7 (lower), 8	Higher smectite
6	500-510; 700-760	5 (top), 9a (upper)	Like 5, but high calcite
7	760-780	9a (lower)	Like 6, but no hematite
6, 7, 8	780-900	9a, 9b, 9c (interfingering)	
8	900-1000; 1030-1132	10, 12	Like 1, but low clinoptilolite

Overall, much of the alluvial layering interpretation of Warren et al. (2002) in ER-5-4 corresponds with our chemofacies interpretations. The differences can be attributed to

- layers that do not appear to have distinctive abundances of sorbing minerals (e.g., layer 4 and layer 8),

- chemofacies that compose sub-units within alluvial layers (e.g., chemofacies 6 within layer 7 and chemofacies 7 within layer 9a),

- layers that have similar sorbing mineral abundances (e.g., layers 10 and 12 or layer 2 and the upper portions of layers 6 and 7), and

- combinations of the above.

The chemofacies interpretation for UE-5n shows a similar depth profile as for ER-5-4. A transition zone between chemofacies 1 and chemofacies 2 may be occurring near depths of 290 to 300 m, but only two XRD data are available in this depth range. Chemofacies 4, which does not correspond directly to an alluvial layer, also appears in UE-5n, indicating that this thin zone of low calcite abundance could be laterally extensive.
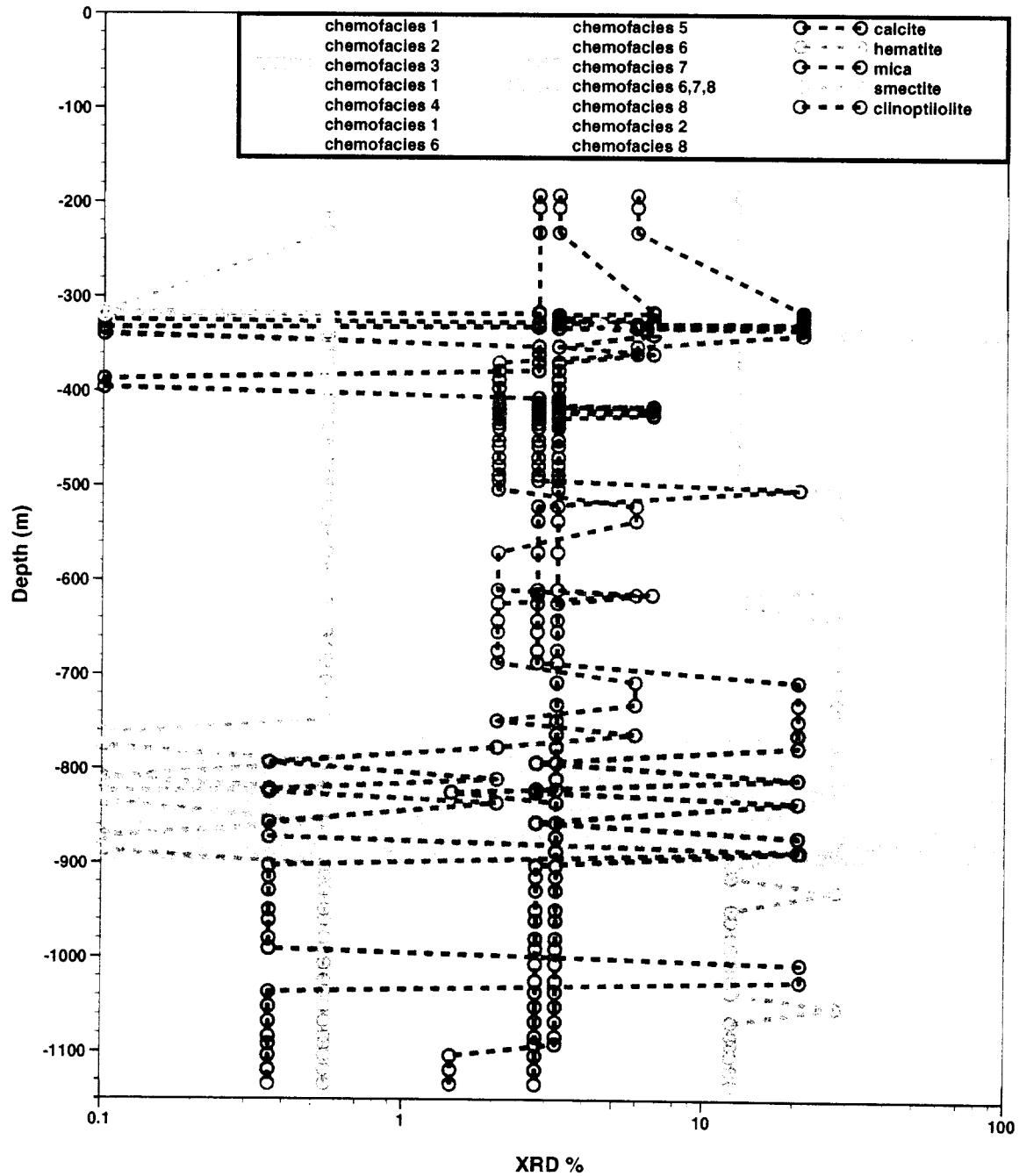
ER-5-4

Figure 3.42 Zonal mean abundance of sorbing minerals in ER-5-4 superposed on distinctive chemofacies zones interpreted in this report.

UE-5n

Figure 3.43 Zonal mean abundance of sorbing minerals in UE-5n superposed on distinctive chemofacies zones interpreted in this report.

The chemofacies interpretations were extended to ER-5-3 and U-11g-1 in northern Frenchman Flat. Of the chemofacies identified in ER-5-4, only chemofacies 1 was found to be applicable to ER-5-3 between depths of about 90 to 200 m. This indicates that portions of the upper alluvium in both central and northern Frenchman flat are very similar with respect to capacity for sorbing radionuclides, but significantly different at greater depths. Between depths of about 200 m to greater than 610 m, clinoptilolite abundance is consistently high in ER-5-3 relative to ER-5-4. Chemofacies 9 is similar to chemofacies 2 in ER-5-4, except that chemofacies 9 exhibits lower mica and smectite abundance. Chemofacies 12 is similar to chemofacies 9 except that it exhibits lower hematite and higher smectite. Chemofacies 10 and 11 show some similarities to chemofacies 7 in ER-5-4, having low hematite and relatively high calcite and clinoptilolite. It is possible that these differences could be attributed to lateral gradations within the sequence of alluvial deposition. Between depths of about 225 and 360 m in ER-5-3, zonal mean abundances of sorbing minerals vary substantially, indicating a transition zone between chemofacies 1, 9, 10, 11, and 12. The three samples from U-11g-1 appear to fall into this transition zone, as indicated in Figure 3.45.

Figure 3.44 Zonal mean abundance of sorbing minerals in ER-5-3 superposed on distinctive chemofacies zones interpreted in this report.

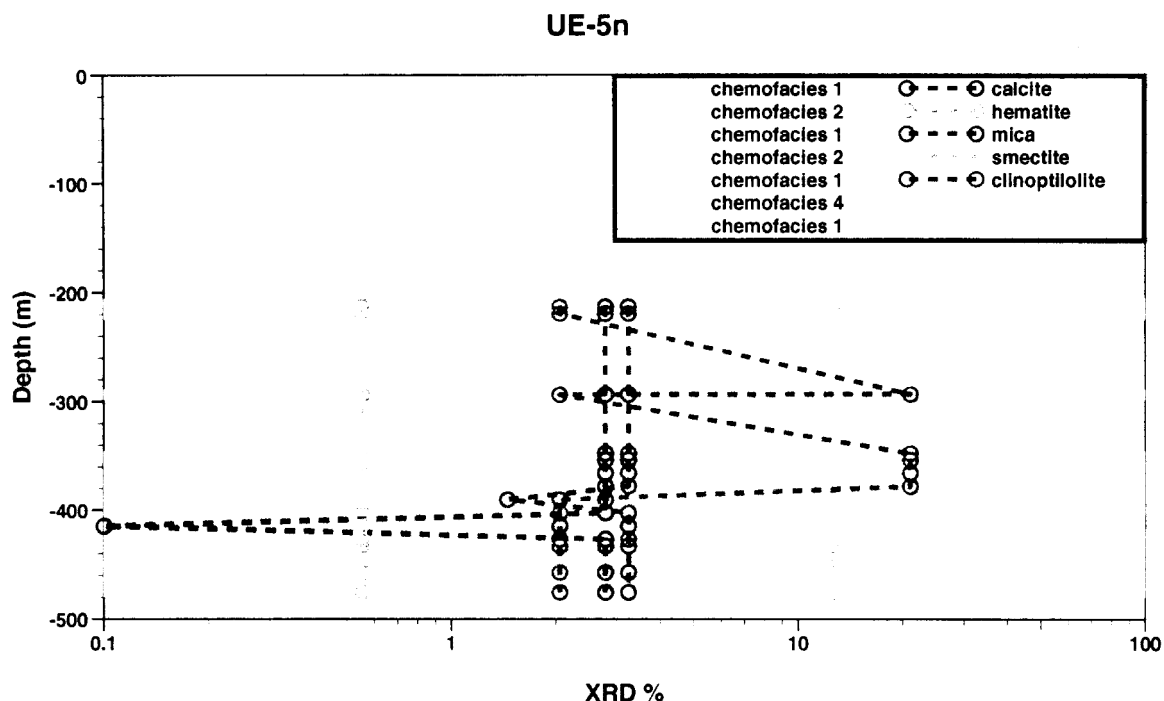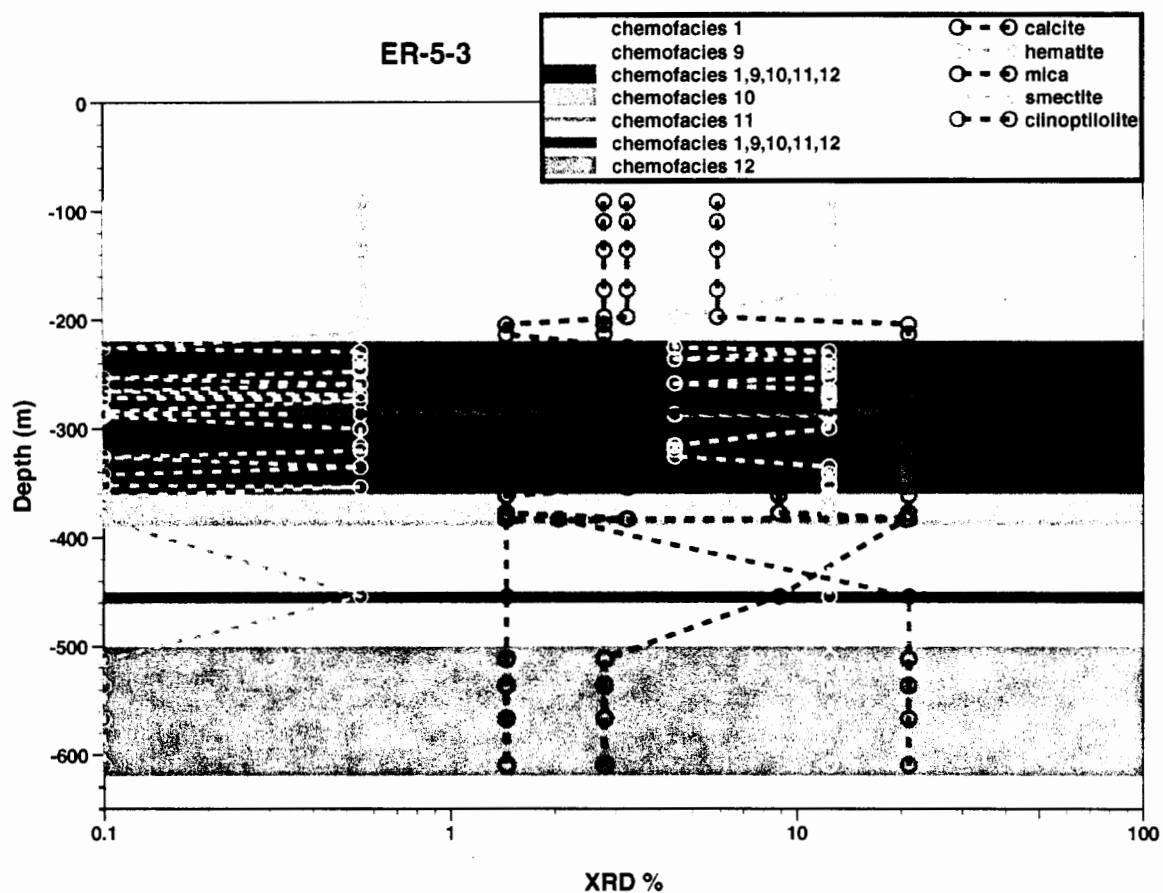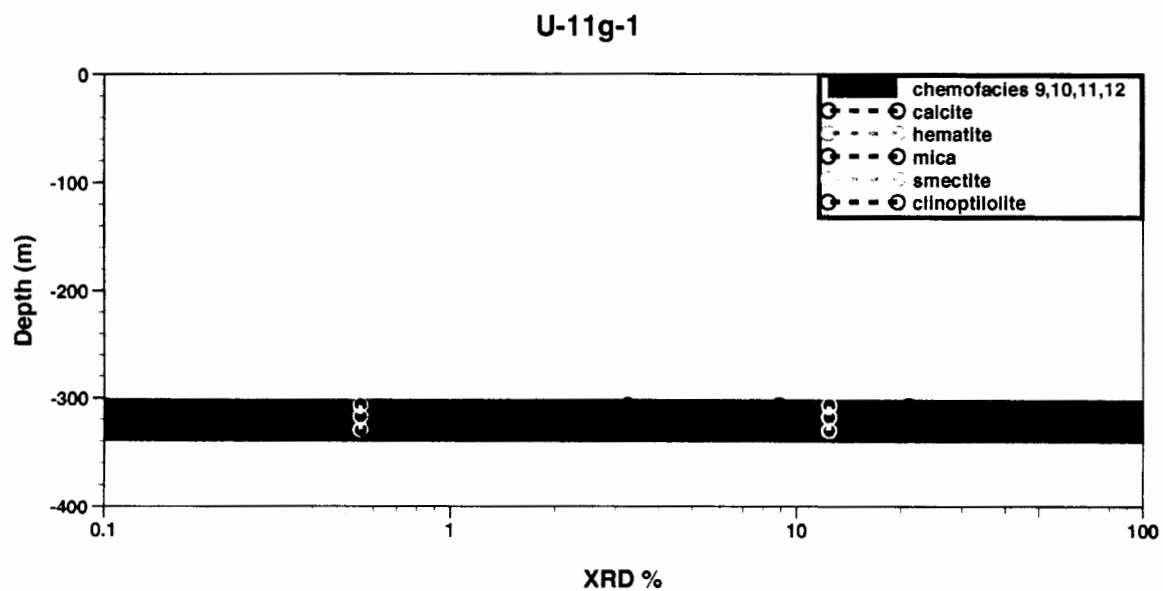Figure 3.45 Zonal mean abundance of sorbing minerals in U-11g-1 superposed on distinctive chemofacies zones interpreted in this report.

In general, the more detailed and comprehensive analysis of Warren et al. (2002) focused on identifying distinct packages of alluvial deposits. Our analysis relied solely on mineralogy data provided by XRD. Our chemofacies interpretations did not consider all geologic data available because its purpose was to interpret geochemical factors affecting radionuclide reactive transport — principally, the abundance of 5 sorbing minerals included in our mechanistic model. While the interpretation of alluvial layers by Warren et al. (2002) is better suited to define provenance and stratigraphy, our statistical analysis of mineral abundance is focused on understanding the role that mineral distributions play on radionuclide sorption. The important conclusions are:

- Interpretations of alluvial layering, as performed by Warren et al. (2002), could provide a useful geometric framework for modeling major spatial variations in the abundances of radionuclide-sorbing minerals.

- Some zones or sub-units within the alluvial layers may need to be distinguished for purposes of reactive transport modeling based on distinctive differences in abundances of sorbing minerals.

- Some alluvial layers may possess effectively the same distribution of zonal mean abundances of sorbing minerals. Unless bulk density and porosity are significantly different, it may be plausible to use the same retardation factors for different alluvial layers of the same chemofacies in CAU or HST scale particle-tracking transport simulations.

- In some sections of the alluvial sequence, complex interfingering of different lithologies occurs, resulting in large fluctuations in abundances of sorbing minerals. These "transition zones" are bound to be heterogeneous in both hydraulic and reactive transport properties. For HST models, it may be essential to consider such heterogeneity if radionuclide transport is expected to occur there.

- In developing CAU scale three-dimensional models, with or without consideration of interpretations of alluvial layers or chemofacies, some consideration for lateral gradations of sorbing mineral abundances should be included.

- The chemofacies interpretations we have made are intended to provide an illustrative example for identifying zones with distinctive abundances of sorbing minerals within the alluvium in Frenchman Flat. Certainly different interpretations of lesser or greater detail could be made.

4 Sorption Modeling and Estimating K_d

Our evaluation of mineral abundance discussed in Chapter 3 provides an overall description of mineralogic heterogeneity in Frenchman Flat alluvium. The mineralogic information can be used to evaluate depositional patterns within alluvium. Moreover, the data may also assist in developing a framework for understanding the lateral and vertical continuity of depositionally and mineralogically distinct zones or layers which may have unique radionuclide transport characteristics. We define the description of zones or layers based on spatial distribution of sorbing mineral abundances as a *chemofacies* approach. Warren et al. (2002) used mineral abundance information along with petrographic and other information to describe alluvial layering. In Section 3.5, we compared the alluvial layer interpretations in ER-5-4 and UE-5n to our interpretations of chemofacies which were based entirely on abundances of radionuclide sorbing minerals.

In this chapter, we evaluate the same mineral abundance data from a radionuclide retardation perspective instead of a mineralogic perspective. The distribution coefficient (K_d) can be used to account for retardation of radionuclide transport in conjunction with either of two conceptual approaches to modeling spatial variability of K_d discussed in Chapters 5 and 6:

- Combine chemofacies and alluvial layering interpretations to define zones with relatively constant mineral abundances and K_d — the chemofacies approach.

- Treat K_d as a random field — the random field approach.

In a reactive transport modeling approach assuming zonal spatial variation of sorbing minerals, either mechanistic or K_d approaches may be used to simulate retardation of radionuclide transport. In this chapter, we discuss the mechanistic approach only as it relates to the calculation of K_ds.

Regardless of its ultimate use, the method used to convert abundances of radionuclide sorbing minerals to K_ds is the same. The discussion of K_d variability in this chapter parallels the mineralogic discussion in Chapter 3; we discuss only univariate and bivariate statistics as a preliminary step to performing variogram analysis of spatial variability of K_d. The results of the variogram analyses in Chapter 5 are applied to generation of random fields of K_d in Chapter 6.

In a recent report, Zavarin (2002) proposed linking radionuclide K_ds used in large-scale CAU models (the K_d approach) to a mechanistic surface complexation/ion exchange radionuclide sorption model (the mechanistic approach).[6] The mechanistic sorption model was developed for near-field hydrologic source term (HST) modeling of reactive transport (most recently used in Pawloski et al., 2001). The mechanistic sorption model accounts for effects such as changing

---

[6] For the link to be valid, the following assumptions need to be made: constant groundwater solution composition, constant temperature, constant pH, constant groundwater redox state, constant mineralogy, and radionuclide concentrations well below concentrations at which non-linear sorption and/or radionuclide precipitation would be expected.

groundwater conditions on radionuclide sorption to mineral surfaces. As such, it provides a robust description of radionuclide sorption. The benefits of linking the large-scale CAU model K_d approach to the mechanistic approach are the following:

- K_ds used in large-scale models would be based on a technically defensible mechanistic sorption model, and

- K_ds used in large-scale models would be directly linked to the mechanistic sorption model used in near-field HST models.

Several recent reports describe the mechanistic sorption model used in near-field HST calculations (Zavarin and Bruton, 2000a; 2000b), employ the mechanistic sorption model in near-field HST calculations (Pawloski et al., 2001), validate the mechanistic sorption model parameters (Zavarin et al., 2002), and describe how one may link K_ds to the mechanistic sorption model (Zavarin, 2002). These topics will not be repeated here but a brief description of the methods used to develop K_ds follows.

4.1 Mechanistic Sorption Model-based K_ds

4.1.1 Radionuclide Species and Radionuclide-Sorbing Minerals

At present, the mechanistic sorption model used in near-field HST calculations includes Am, Ca, Cs, Sr, Eu, Sm, Np, Pu, and U radionuclides[7] and iron oxide, smectite, zeolite, illite, and calcite minerals (Table 4.1). While this database is quite substantial, there are limitations to it. The completeness of the radionuclide list is dependent on the radiologic source term being evaluated. For example, a recent near-field HST modeling report (Pawloski et al., 2001) included the following radionuclides as pertinent to the Pahute Mesa HST: ^{3}H, ^{14}C, ^{36}Cl, ^{39}Ar, ^{41}Ca, ^{59,63}Ni, ^{85}Kr, ^{90}Sr, ^{93}Zr, ^{93,94}Nb, ^{99}Tc, ^{107}Pd, ^{121,126}Sn, ^{129}I, ^{135,137}Cs, ^{151}Sm, ^{150,152,154}Eu, ^{166}Ho, ^{232,233,234,235,236,238}U, ^{237}Np, $^{238,239,.240,241}$Pu, ^{241}Am, and ^{244}Cm. Of those, ^{3}H, ^{14}C, ^{36}Cl, ^{39}Ar, ^{85}Kr, ^{99}Tc, and ^{129}I were modeled as tracers because they were not expected to sorb strongly to any minerals in NTS groundwater. ^{41}Ca, ^{90}Sr, ^{135,137}Cs, ^{151}Sm, ^{150,152,154}Eu, ^{232,233,234,235,236,238}U, ^{237}Np, $^{238,239,.240,241}$Pu, and ^{241}Am sorption was modeled based on the mechanistic sorption model. The behavior of ^{166}Ho, and ^{244}Cm was based on the behavior of Eu since these trivalent cations are expected to have similar chemistry. However, ^{59,63}Ni, ^{93}Zr, ^{93,94}Nb, ^{107}Pd, and ^{121,126}Sn could not be modeled correctly because their behavior was not included in the mechanistic model. These radionuclides are missing from the mechanistic model due to a combination of data limitations and mechanistic sorption model development time constraints. Evaluation of their sorption behavior should be included in future versions of the mechanistic sorption model.

---

[*] Note that radionuclide isotopes of the same element are assumed to behave identically. The mechanistic model does not distinguish between isotopes of a particular element.

An additional missing aspect of the mechanistic sorption model is the absence of manganese oxide radionuclide sorbing minerals. Manganese oxides can be strong radionuclide sorbers (Duff et al., 1999). However, Frenchman Flat alluvium data suggest that manganese oxides are not present in significant abundance (see Warren et al., 2002). While the absence of manganese oxides in the mechanistic sorption model may be an issue for areas of the NTS where manganese oxides are prevalent (i.e. fracture coatings in certain Pahute Mesa locations), it is not a significant issue for Frenchman Flat alluvium.

The aluminosilicate mineralogy of Frenchman Flat alluvium is composed of a large number of heterogeneously distributed minerals and glasses (e.g. K-feldspar, plagioclase, glass, cristobalite, opal, quartz, tridymite, hornblende, kaolinite, zeolite, mica, smectite). However, the mechanistic sorption model accounts for only smectite, mica, and a zeolite (clinoptilolite). While the other aluminosilicate minerals may contribute to radionuclide surface complexation or ion exchange to some degree, it is likely that the aluminosilicate minerals included in our model are the dominant aluminosilicate radionuclide sorbers. For example, the ion exchange capacity of zeolite, mica, and smectite far outweighs the ion exchange capacity of kaolinite (the only other significant ion exchanger in Frenchman Flat alluvium). Furthermore, the very high surface area of smectite is likely to result in its dominance over all other aluminosilicate minerals with respect to surface complexation. This is consistent with our recent measurements of BET surface area of alluvium from UE-5n and U-1a which suggest that the surface area of smectite dominates the total alluvium BET surface area (unpublished data).

Table 4.1 Surface complexation (SC) and ion exchange (IE) reactions included in the mechanistic sorption model.

	Zeolite	Illite/mica	Smectite	Iron oxide	Calcite
Ca	IE	IE	IE	-	SC
Cs	IE	IE	IE	-	
Sr	IE	IE	IE	SC	SC
Am	-	-	SC	SC	SC
Eu	-	-	SC	SC	SC
Sm	-	-	SC[1]	SC[1]	SC
Np	-	-	SC	SC	SC
U	-	-	SC	SC	SC
Pu	-	-	SC	SC	SC

[1] Samarium sorption to smectite and iron oxide was estimated based on analogy to europium because published sorption data were not available.

4.1.2 Radionuclide-Mineral K_ds

In the mechanistic sorption model, radionuclide sorption is a function of the fluid composition, the sorbing mineral properties (cation exchange capacity, surface area, reactive site density), and the surface complexation/ion exchange constants that govern radionuclide sorption affinities. To predict radionuclide sorption, all these factors must be evaluated. The fluid composition for Frenchman Flat alluvium was based on Rose et al. (1997) and additional unpublished LLNL

groundwater analyses from various wells located in Frenchman Flat alluvium (average reported in Table 4.2). Speciation of radionuclides in Frenchman Flat groundwater was accomplished using the GEMBOCHS database (Johnson and Lundeen, 1989) with revisions as noted in Zavarin and Bruton (2000a; 2000b). The sorbing mineral properties were based on published data and our recent model validation experiments performed on Yucca Flat and Frenchman Flat alluvium (Zavarin et al., 2002). These experiments indicated that published surface areas and cation exchange capacities may be too high for certain minerals. The reduced reactive surface areas and cation exchange capacities may relate to mineral accessibility issues which are not accounted for directly in this report. However, the adjustment of surface areas and cation exchange capacities based on validation experiments indirectly (and qualitatively) accounts for the effect of mineral accessibility on radionuclide sorption. The surface complexation/ion exchange constants that govern radionuclide sorption affinities were developed based on non-electrostatic surface complexation and Vanselow ion exchange (Zavarin and Bruton, 2000a; 2000b). Model validation experiments performed on Yucca Flat and Frenchman Flat alluvium (Zavarin et al., 2002) indicated that some ion exchange constant adjustment is necessary to accurately predict radionuclide sorption to these sediments. All adjustments suggested in Zavarin et al. (2002) are included in the calculations presented here. The radionuclide-mineral K_ds based on our mechanistic model are summarized in Table 4.3. For details regarding the process used to calculate these K_ds based on the mechanistic sorption model, see Pawloski et al. (2001) and Zavarin (2002).

Table 4.2 Fluid composition used in mechanistic sorption model.

	Concentration[†]
pH	8.4 ± 0.3[§]
	mg/kg
F^-	1.1 ± 0.3
Na^+	79 ± 26
K^+	6.7 ± 1.0
Mg^{2+}	2.8 ± 1.7
Ca^{2+}	12.0 ± 4.7
Sr^{2+}	-
Cl^-	13.2 ± 3.5
HCO_3^-	190 ± 62
SO_4^{2-}	34.8 ± 8.7
SiO_2	56 ± 21[¶]

[†] Average based on Rose et al. (1997) and additional unpublished LLNL data.

[§] Uncertainty (±1SD) determined from analyses of a number of groundwater samples.

[¶] Data regarding Si was not reported; value of IT (1999) was used.

Table 4.3 K_ds based on the mechanistic sorption model.

	Calcite	Zeolite (clinoptilolite)	Iron Oxide[¶] (hematite)	Mica/illite[¥]	Smectite
			Log (K_d)		
Am	4.30		3.23		4.72
Ca	0.44	3.51		2.33	2.67
Cs		3.47		5.45	2.80
Eu	4.02		2.91		3.92
Np	1.58		1.95		1.23
Pu ($O_2 = 10^{-5}$)[§]	1.20		1.99		1.77
Pu ($O_2 = 10^{-10}$)	1.69		2.48		2.15
Pu ($O_2 = 10^{-15}$)	2.30		3.07		2.60
Sm	4.56		3.08		4.09
Sr	-1.31	3.29	-0.02	2.32	2.27
U	-3.07		1.83		0.79

[§] Pu K_ds determined at three $O_2(g)$ fugacities : 10^{-5}, 10^{-10}, and 10^{-15} bars. The range of $O_2(g)$ fugacities was suggested in Zavarin et al. (2002) to evaluate the effect of Pu redox state on transport.

[¶] Mechanistic sorption model is based on hematite. However, XRD analysis did not distinguish between hematite, goethite, hydrous ferric oxide, magnetite, ilmenite, maghemite, or pseudobrookite iron oxides. We assume in our model that all iron oxides behave similarly.

[¥] Mechanistic sorption model is based on illite. However, XRD analysis did not distinguish between illite and mica. We assume in our model that these two minerals behave similarly.

4.1.3 Radionuclide-Alluvium K_ds

Based on the K_ds in Table 4.3, we can employ the component additivity approach to predict radionuclide K_ds as a function of alluvium mineralogy. The component additivity approach (Zavarin, 2002) relies on the principal that the radionuclide K_d for a particular alluvium mineralogy is simply the sum of individual K_d contributions from the various radionuclide sorbing minerals in the alluvium. Thus, based on the data in Table 4.3, the K_d (mL/g) for each radionuclide under specific mineralogic conditions is defined by:

Am : $K_d = f_{calcite}10^{4.30} + f_{hematite}10^{3.23} + f_{smectite}10^{4.72}$

Ca : $K_d = f_{calcite}10^{0.44} + f_{clinoptilolite}10^{3.51} + f_{mica}10^{2.33} + f_{smectite}10^{2.67}$

Cs : $K_d = f_{clinoptilolite}10^{3.47} + f_{mica}10^{5.45} + f_{smectite}10^{2.80}$

Eu : $K_d = f_{calcite}10^{4.02} + f_{hematite}10^{2.91} + f_{smectite}10^{3.92}$

Np : $K_d = f_{calcite}10^{1.58} + f_{hematite}10^{1.95} + f_{smectite}10^{1.23}$

$Pu(O_2 = 10^{-5})$: $K_d = f_{calcite}10^{1.20} + f_{hematite}10^{1.99} + f_{smectite}10^{1.77}$

$Pu(O_2 = 10^{-10})$: $K_d = f_{calcite}10^{1.69} + f_{hematite}10^{2.48} + f_{smectite}10^{2.15}$

$Pu(O_2 = 10^{-15})$: $K_d = f_{calcite}10^{2.30} + f_{hematite}10^{3.07} + f_{smectite}10^{2.60}$

Sm: $\quad K_d = f_{calcite}10^{4.56} + f_{hematite}10^{3.08} + f_{smectite}10^{4.09}$

Sr: $\quad K_d = f_{calcite}10^{-1.31} + f_{clinoptilolite}10^{3.29} + f_{hematite}10^{-0.02} + f_{mica}10^{2.32} + f_{smectite}10^{2.27}$

U: $\quad K_d = f_{calcite}10^{-3.07} + f_{hematite}10^{1.83} + f_{smectite}10^{0.79}$

where f is the mineral mass fraction in the alluvium.

4.2 Histograms and Lateral Variation of K_d

In Figures 4.1 to 4.11, histograms of K_ds are plotted on a log scale for each radionuclide. Separate histograms are shown for XRD data from all drillholes and for XRD data from drillholes ER-5-4, UE-5n, ER-5-3, and U-11g-1 individually. The log scale (versus linear) is useful because

- it helps span the wide variation in K_d for different radionuclides (over 5 orders of magnitude),

- the K_ds tend to be distributed as log-normal, and

- stochastic models of K_d usually assume a log-normal distribution.

The histograms are useful for examining the variation of K_d in several ways:

- to illustrate the range of K_ds for the radionuclide,

- to illustrate the most frequent K_ds for the radionuclide,

- to examine the shape of the distribution compared to a log-normal (Gaussian) distribution, and

- to examine the possibility of bi-modal or multi-modal distributions.

Drillholes ER-5-4 and UE-5n are situated in central Frenchman Flat, and drillholes ER-5-3 and U-11g-1 are situated in northern Frenchman Flat. Comparison of the histograms for drillholes in different locations is useful for examining how K_d varies (or does not vary) laterally as a result of changes in sorbing mineral abundances.[8] These drillhole locations are sufficiently distant to detect lateral variations or trends in K_d, should they exist in Frenchman Flat. The issue of

---

[8] Note, however, that we have not evaluated whether changes in groundwater chemistry in Northern and Central Frenchman Flat would have an additional effect on radionuclide retardation. In this report, we assume that the groundwater chemistry in all of the Frenchman Flat alluvium is essentially identical. Thus we are evaluating the effects of mineral variability only. Other effects such as groundwater composition changes may further affect K_ds. This is particularly the case when approaching the carbonate aquifer whose groundwater chemistry is believed to be quite different.

laterally varying K_d is of potential concern for Corrective Action Unit (CAU) scale radionuclide transport modeling efforts in Frenchman Flat. If significant lateral variations or trends in K_d exist, CAU scale models may need to provide enough model resolution to account for differences in radionuclide transport properties as a function of alluvium location. If, however, radionuclide retardation is relatively uniform in Frenchman Flat alluvium, spatially heterogeneous radionuclide retardation information may not be necessary to consider at the CAU scale. Heterogeneous lateral K_ds may also be of concern for near-field HST modeling efforts because K_d variability may impact categorization of underground nuclear tests.

To address modeling issues related to K_d for different radionuclides, we first examine the histograms of K_d for radionuclides Am, Ca, Cs, Eu, Np, Pu, Sm, Sr, and U, as shown in Figures 4.1 to 4.11. The main issues of concern are the magnitude and spread of K_ds, which are indicated by the mean and standard deviation statistics. The coefficient of variation, which is the standard deviation divided by the mean, indicates the range of spread in the distribution, where a value of 1.0 or greater indicates a wide spread. All of the histograms of K_d have a coefficient of variation less than 1.0, indicating that the K_ds typically have a relatively narrow range. Other statistics included on the histograms are the minimum and maximum values, lower and upper quartiles (25th and 75th percentiles), and median (50th percentile). A bell-shaped distribution on the log scale indicates a log-normal distribution of K_d. A bi- or multi-modal distribution is indicated by two or more peaks in the frequency distribution. Lateral variation is indicated if the mean values and shapes of the distributions are significantly different for data from different drillhole locations. Table 4.4 summarizes our interpretation of the radionuclide K_d histograms for the XRD data from all drillholes. Our interpretations of distribution shapes are based on visual inspection.

Table 4.4 Summary interpretation of radionuclide K_d histograms.

Radionuclide	Mean (mL/g)	σ (mL/g)	Log-Normal?	Bi-Modal?	Multi-Modal?	Lateral Variation?
Am	8280	4610	Yes	No	No	No
Ca	392	345	No	Yes	No	Yes
Cs	10100	4770	Yes	No	No	Yes
Eu	1700	1100	Yes	No	No	No
Np	4.68	3.14	Yes	No	No	No
Pu(O$_2$=10^{-5})[§]	9.37	4.85	Yes	No	No	No
Pu(O$_2$=10^{-10})	23.4	12.1	Yes	No	No	No
Pu(O$_2$=10^{-15})	70.2	36.2	Yes	No	No	No
Sm	3560	2870	Yes	No	No	No
Sr	225	210	No	Yes	No	Yes
U	1.15	0.49	Yes	No	No	No

[§] Pu K_ds determined at three O$_2$(g) fugacities : 10^{-5}, 10^{-10}, and 10^{-15} bars. The range of O$_2$(g) fugacities was suggested in Zavarin et al. (2002) to evaluate the effect of Pu redox state on transport.

Most of the K_d distributions for different radionuclides, namely Am, Eu, Np, Pu, Sm, and U, appear to be well characterized by a log normal distribution and exhibit no significant lateral variation. For these radionuclides, a stationary stochastic model of K_d variation for Frenchman Flat based on a log-normal distribution may be a valid model assumption.

The exceptional radionuclides are Ca, Cs, and Sr. The retardation of these radionuclides is dominated by ion exchange reactions rather than surface complexation reactions. The dominant ion exchanging minerals include smectite, clinoptilolite, and illite/mica. Both Ca and Sr exhibit a notable bi-modal shape in the histogram for all XRD data. The higher K_ds for Ca and Sr tend to occur in northern Frenchman Flat (in drillholes ER-5-3 and U-11g-1) and the lower values in central Frenchman Flat (in drillholes ER-5-4 and UE-5n). This difference is primarily attributed to differences in zeolite (clinoptilolite) abundance, which tend to be greater in the northern Frenchman Flat drillholes. This is consistent with K_d data listed in Table 4.3, which shows that Ca and Sr have a greater affinity for zeolite (clinoptilolite) than for any other mineral in the model. Therefore, large-scale spatial variation of zeolite is a key issue to consider for Ca and Sr transport modeling in Frenchman Flat. Although the frequency distribution of K_d for Cs appears log-normal at different locations, some lateral variation in the mean K_d is evident. The mean K_d for Cs in the central Frenchman Flat drillholes (ER-5-4 and UE-5n) is about 11,300 mL/g, and the mean K_d for Cs in the northern Frenchman Flat drillholes (ER-5-3 and U-11g-1) is about 7220 mL/g. This difference is attributed to a larger abundance of illite/mica in the central Frenchman Flat drillholes. However, the difference is not large when compared to the range of variation of K_d observed in within either the central and northern Frenchman Flat drillholes.

Figure 4.1 Log-scale histograms of K_d for Am based on XRD data for all drillholes and ER-5-4, UE-5n, ER-5-3, and U-11g-1 individually.

Figure 4.2 Log-scale histograms of K_d for Ca based on XRD data for all drillholes and ER-5-4, UE-5n, ER-5-3, and U-11g-1 individually.

Figure 4.3 Log-scale histograms of K_d for Cs based on XRD data for all drillholes and ER-5-4, UE-5n, ER-5-3, and U-11g-1 individually.

Figure 4.4 Log-scale histograms of K_d for Eu based on XRD data for all drillholes and ER-5-4, UE-5n, ER-5-3, and U-11g-1 individually.

Figure 4.5 Log-scale histograms of K_d for Np based on XRD data for all drillholes and ER-5-4, UE-5n, ER-5-3, and U-11g-1 individually.
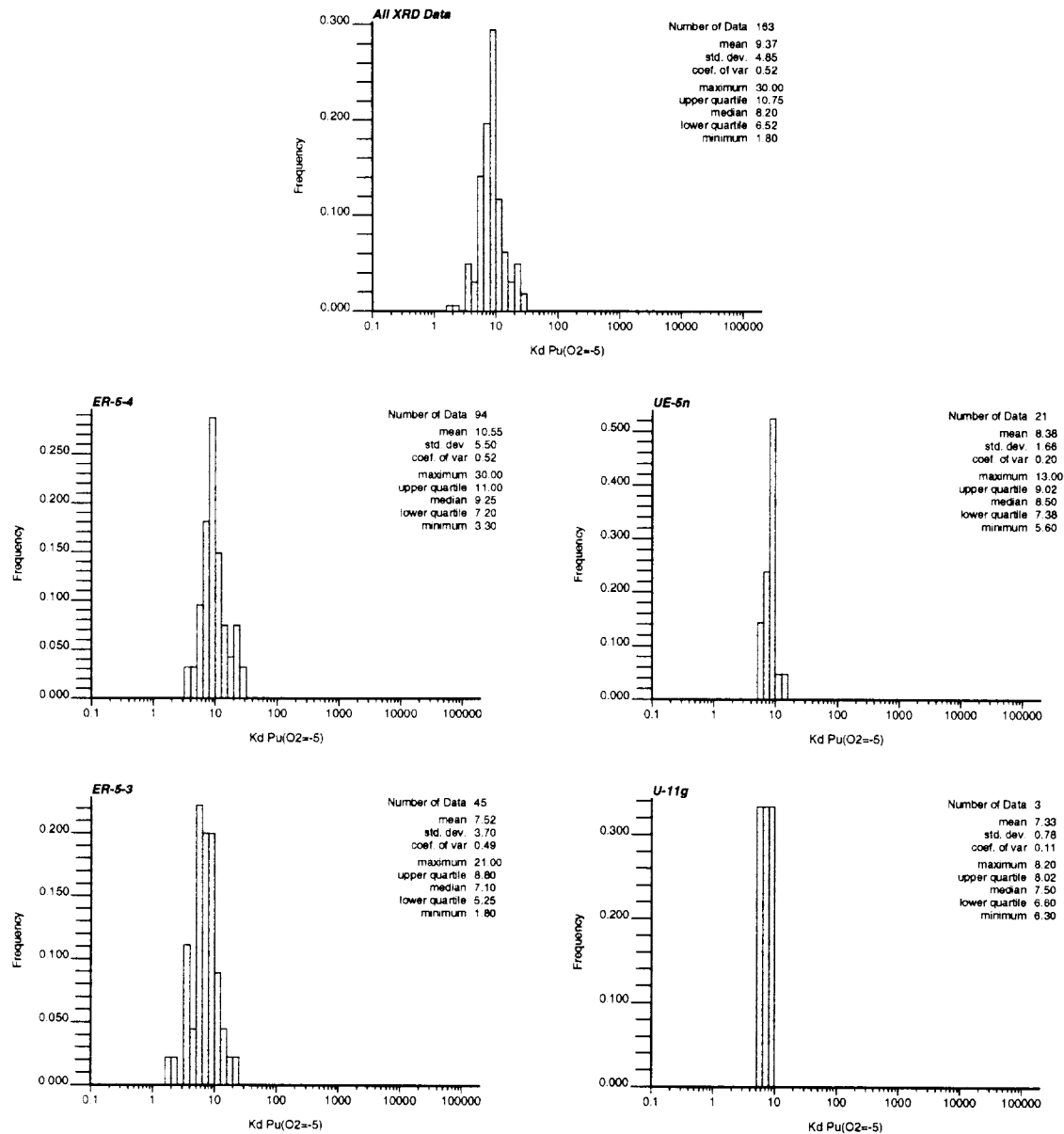
Figure 4.6 Log-scale histograms of K_d for Pu(O2=-5) based on XRD data for all drillholes and ER-5-4, UE-5n, ER-5-3, and U-11g-1 individually.
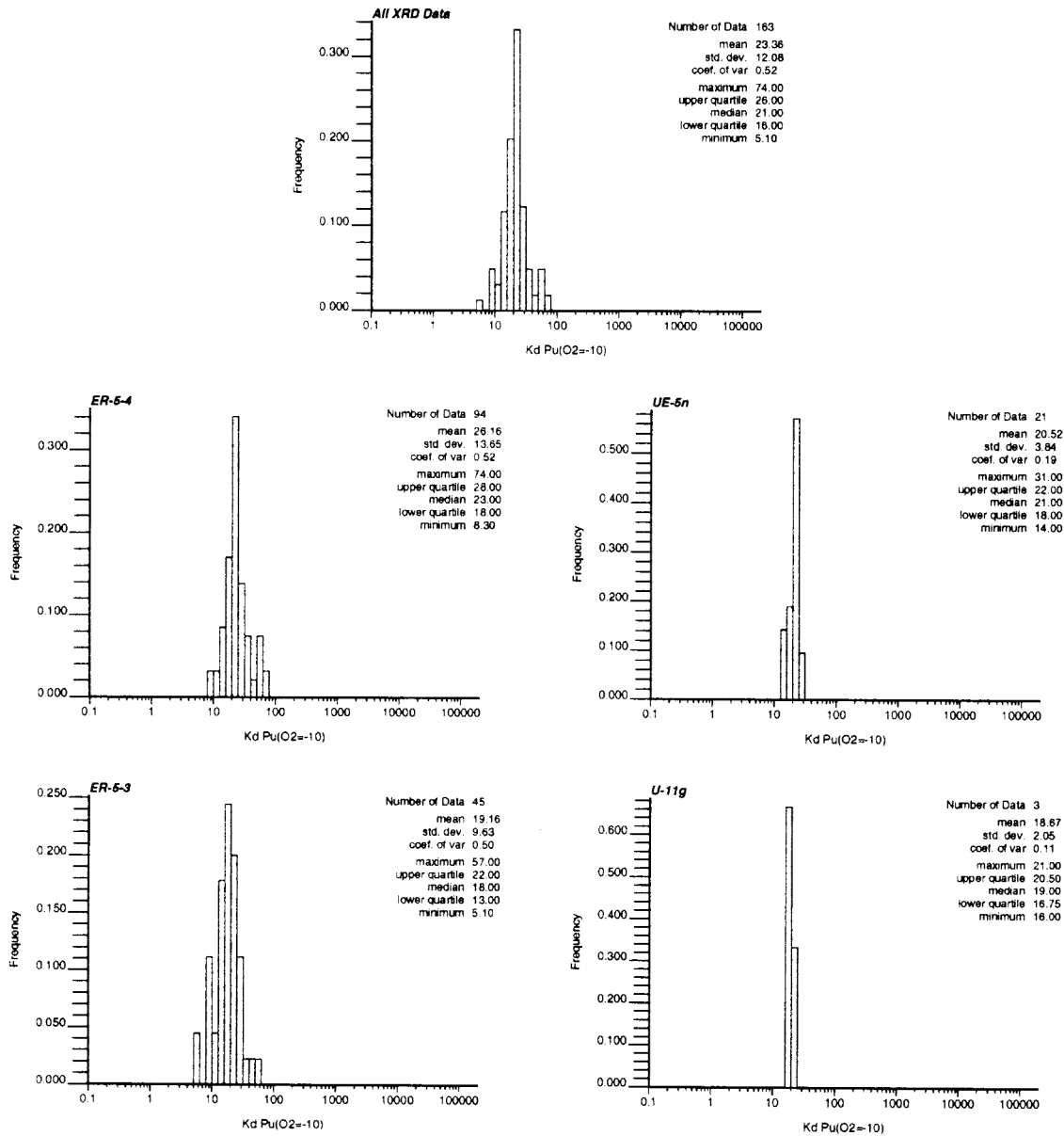
Figure 4.7 Log-scale histograms of K_d for Pu(O2=-10) based on XRD data for all drillholes and ER-5-4, UE-5n, ER-5-3, and U-11g-1 individually.
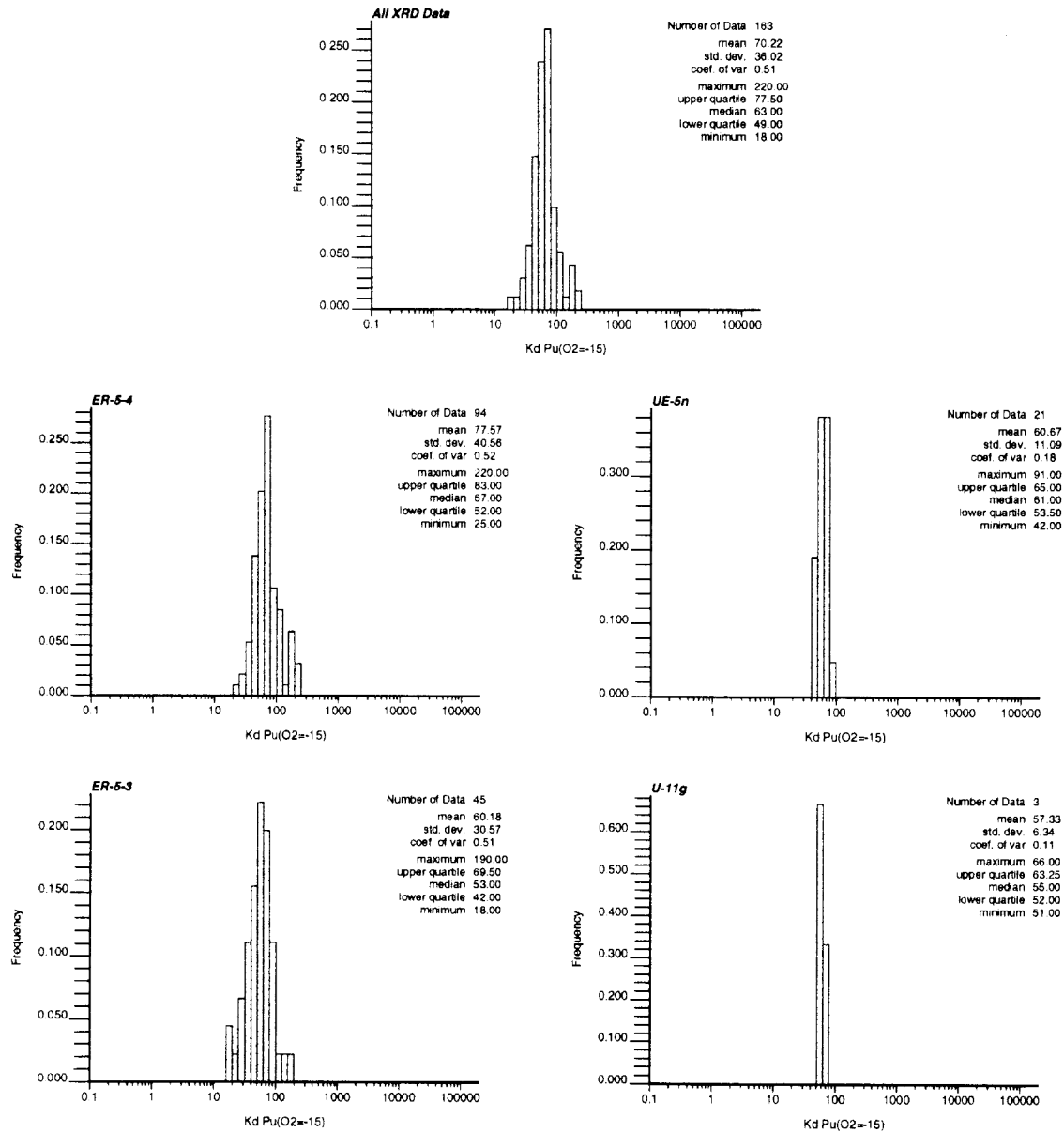
Figure 4.8 Log-scale histograms of K_d for Pu(O2=-15) based on XRD data for all drillholes and ER-5-4, UE-5n, ER-5-3, and U-11g-1 individually.
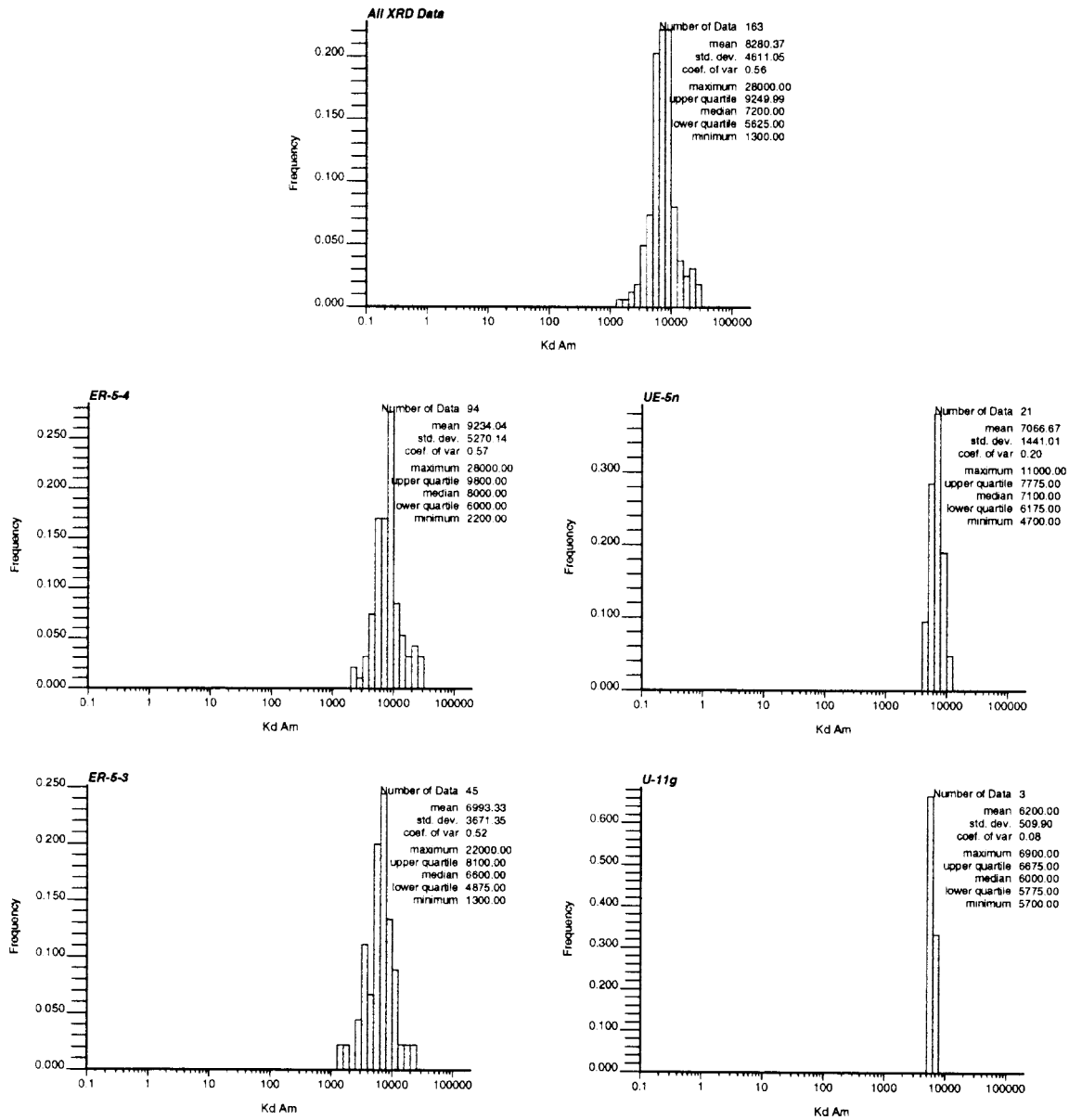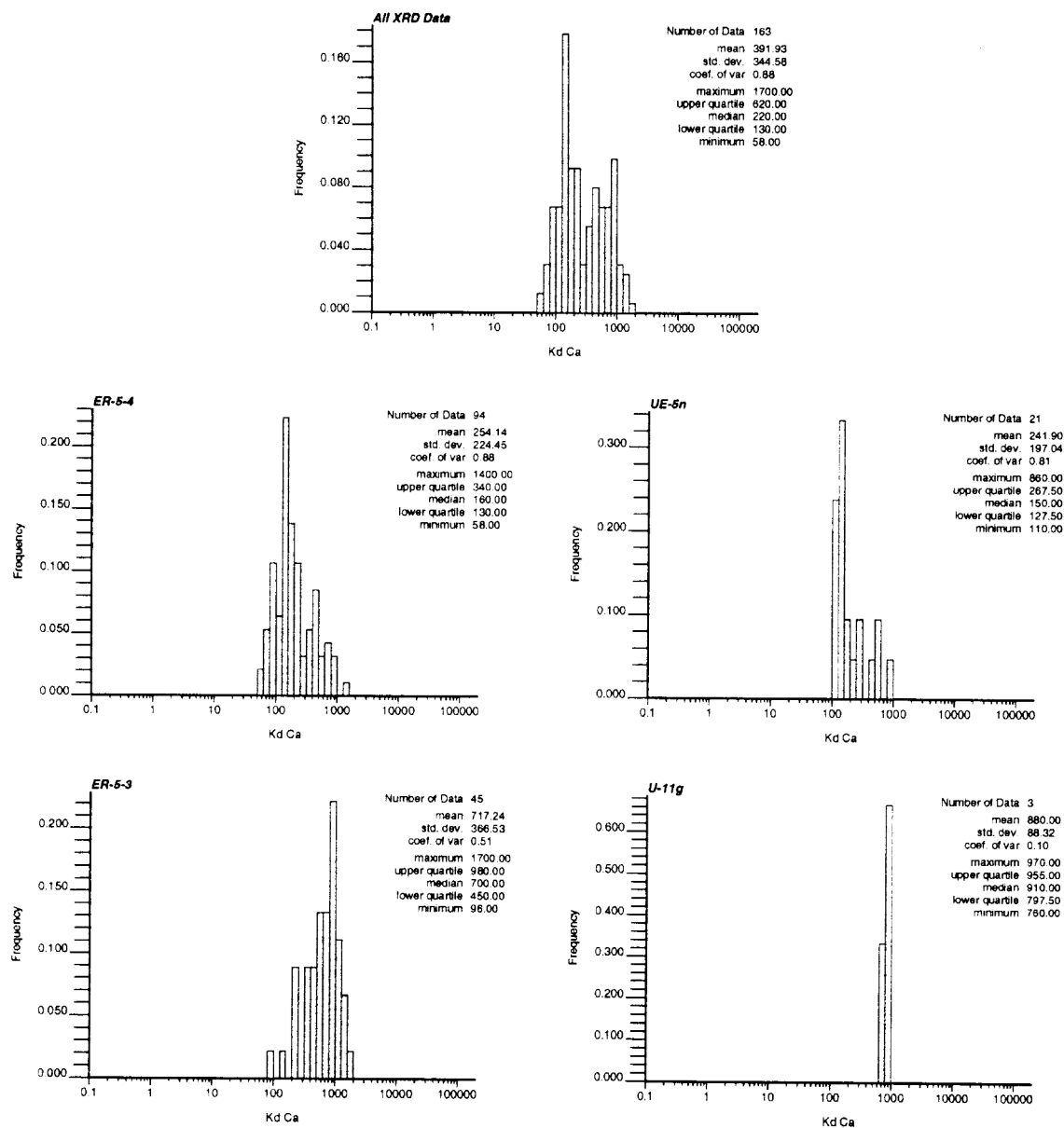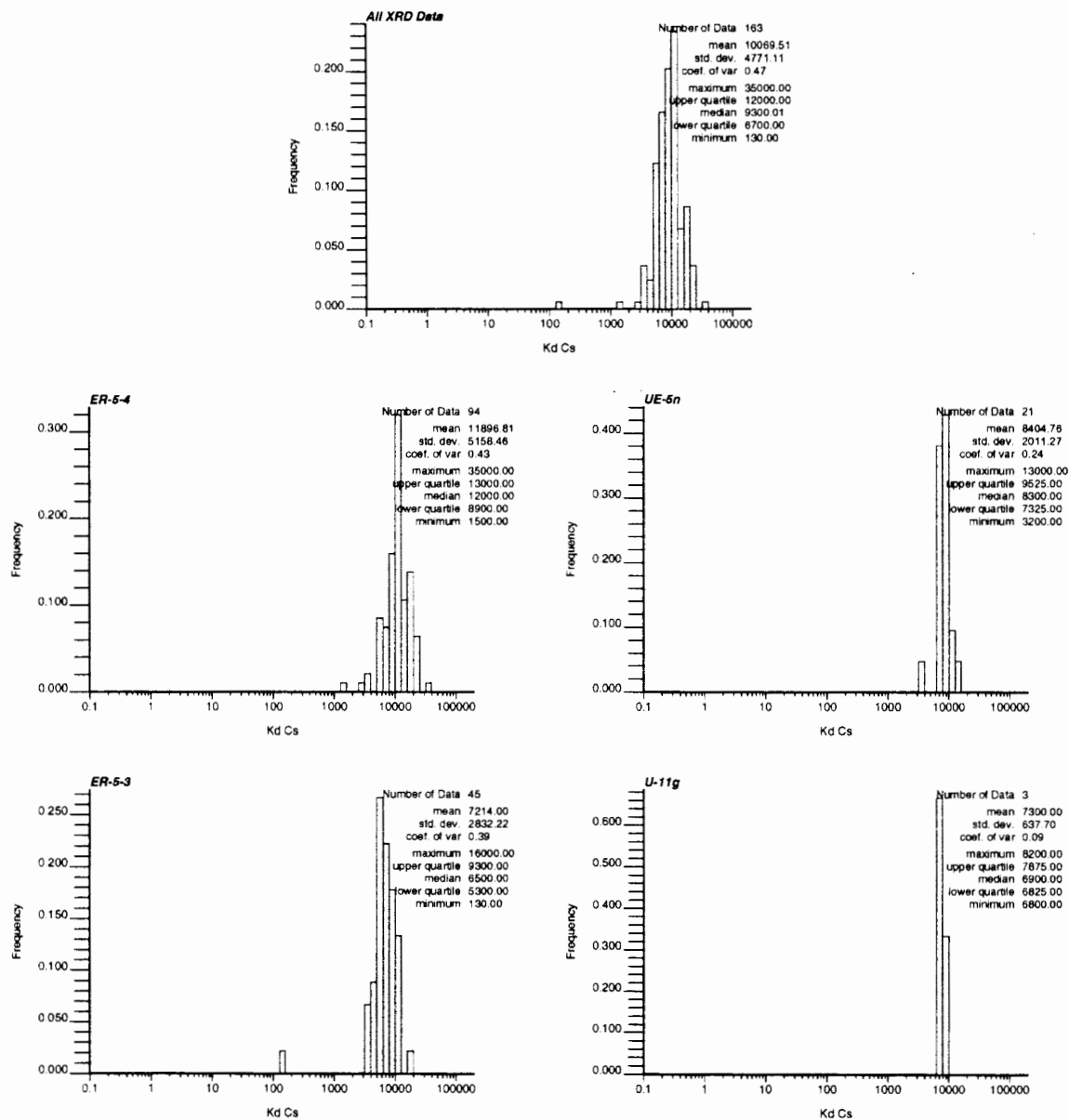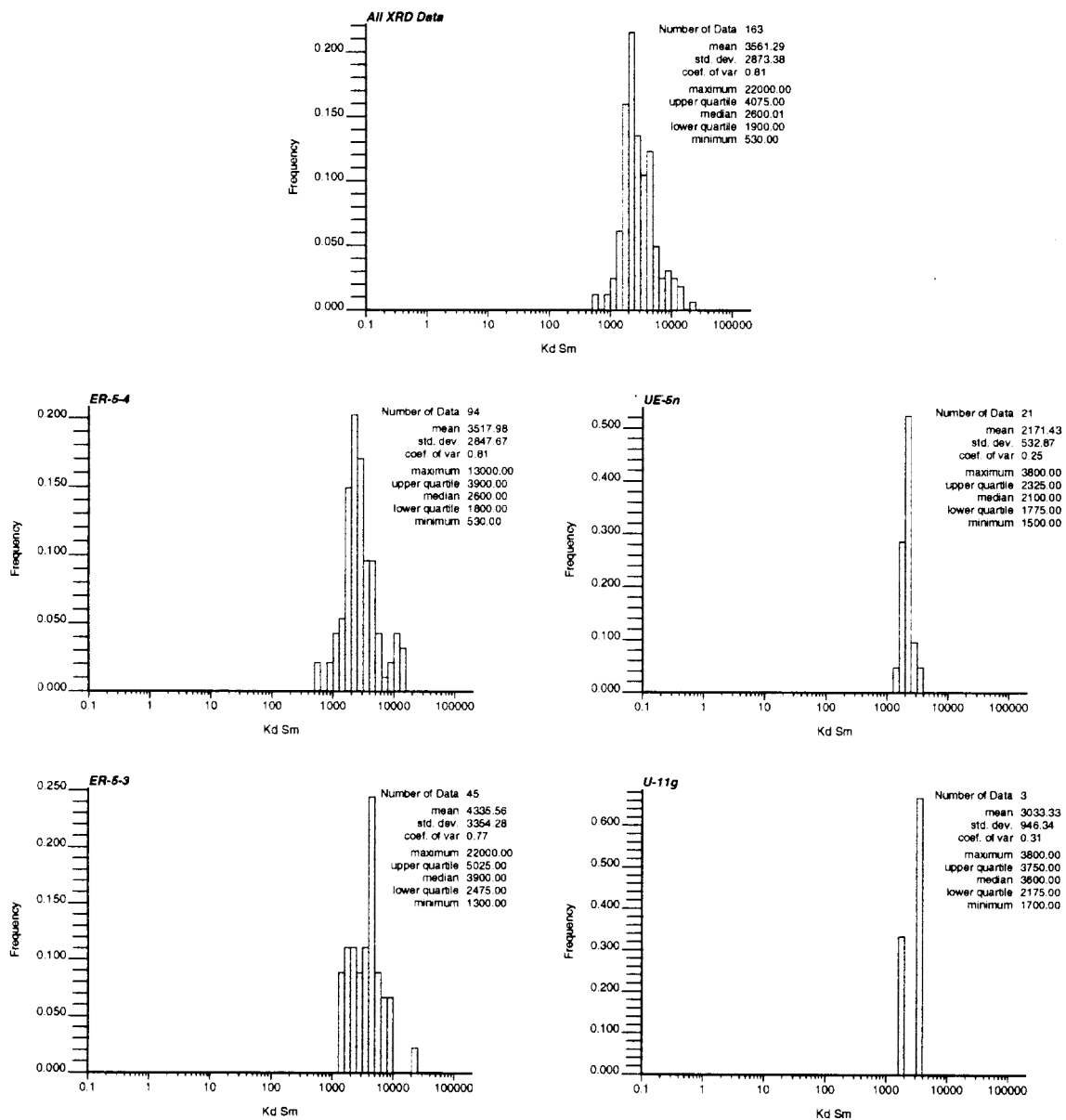
Figure 4.9 Log-scale histograms of K_d for Sm based on XRD data for all drillholes and ER-5-4, UE-5n, ER-5-3, and U-11g-1 individually.
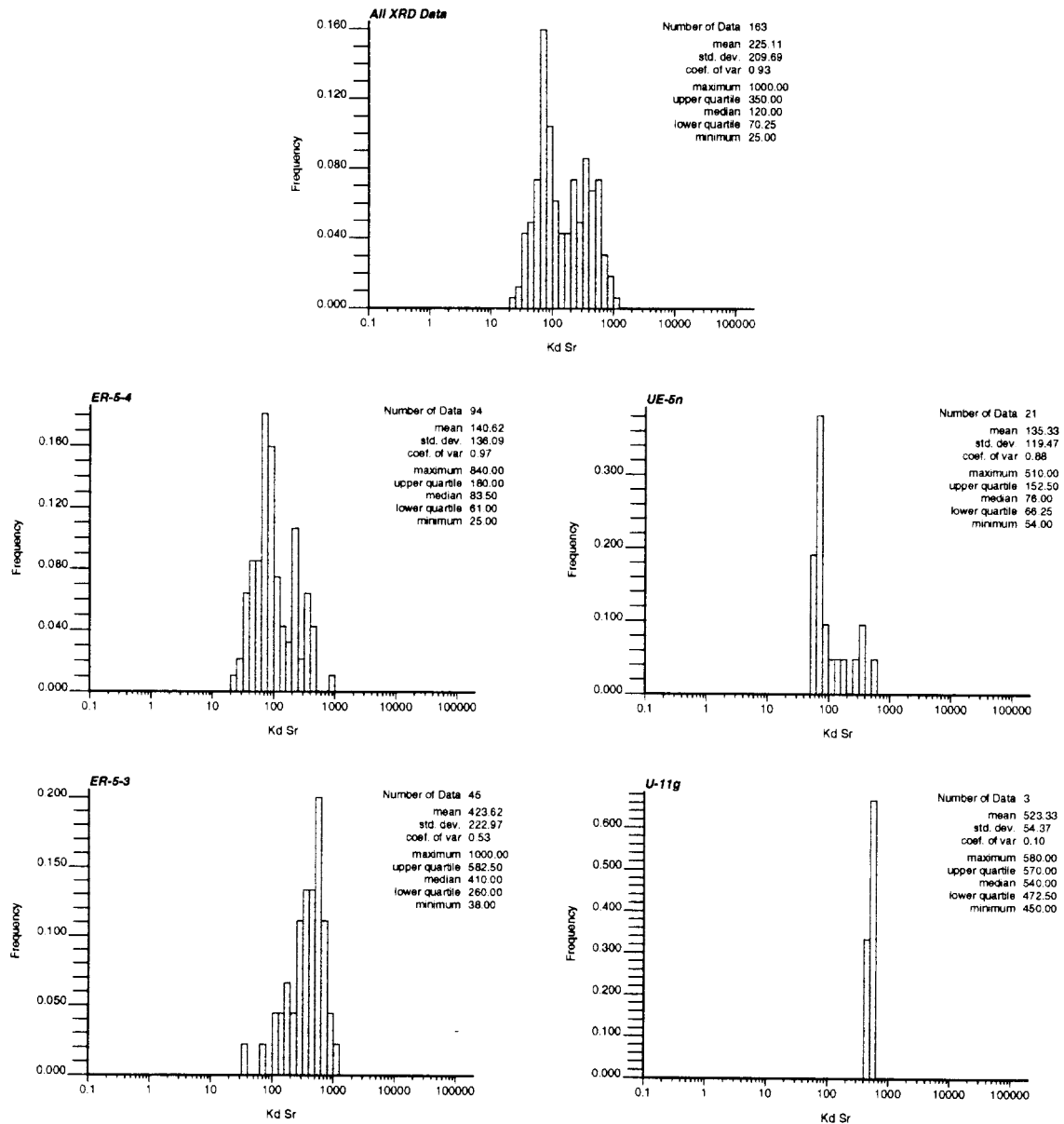
Figure 4.10 Log-scale histograms of K_d for Sr based on XRD data for all drillholes and ER-5-4, UE-5n, ER-5-3, and U-11g-1 individually.

Figure 4.11 Log-scale histograms of K_d for U based on XRD data for all drillholes and ER-5-4, UE-5n, ER-5-3, and U-11g-1 individually.
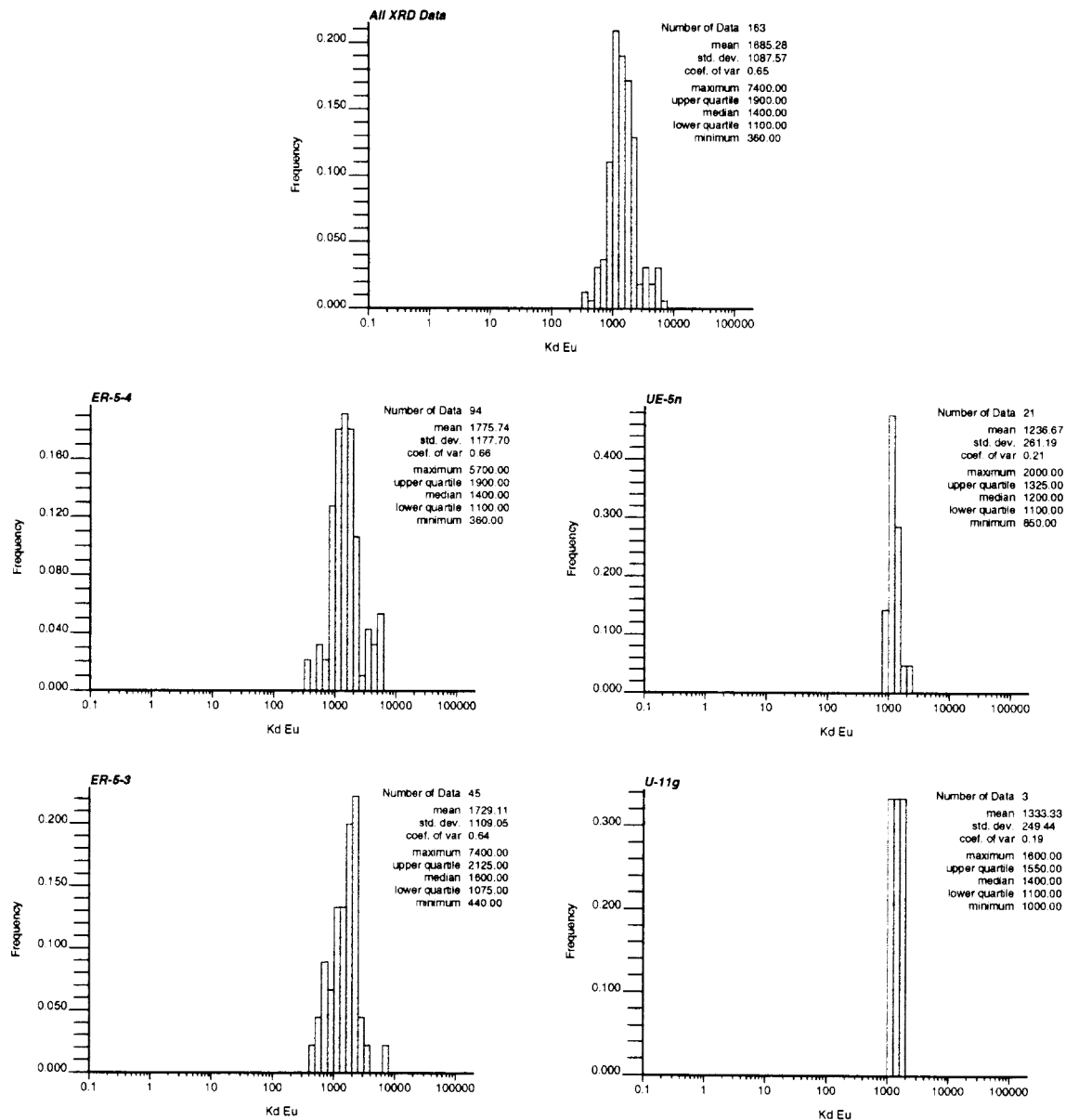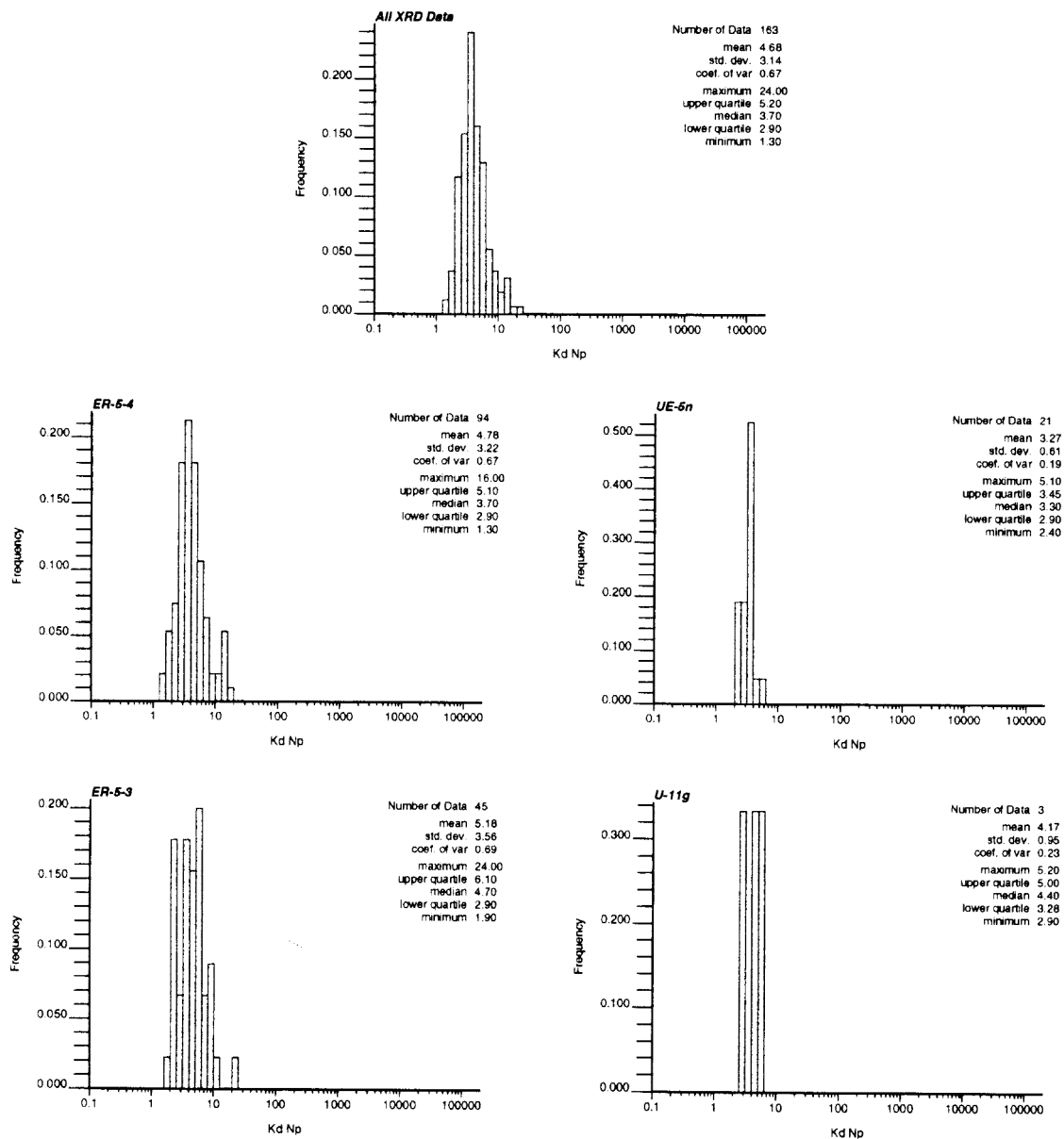
ER-5-3

Number of Data 45
mean 0.80
std. dev. 0.38
coef. of var 0.48
maximum 1.80
upper quartile 1.00
median 0.70
lower quartile 0.49
minimum 0.25

U-11g

Number of Data 3
mean 1.09
std. dev. 0.23
coef. of var 0.21
maximum 1.30
upper quartile 1.27
median 1.20
lower quartile 0.88
minimum 0.77

ER-5-4

Number of Data 94
mean 1.31
std. dev. 0.50
coef. of var 0.38
maximum 2.90
upper quartile 1.50
median 1.20
lower quartile 1.00
minimum 0.47

UE-5n

Number of Data 21
mean 1.16
std. dev. 0.19
coef. of var 0.16
maximum 1.50
upper quartile 1.30
median 1.20
lower quartile 1.08
minimum 0.78

All XRD Data

Number of Data 163
mean 1.15
std. dev. 0.49
coef. of var 0.43
maximum 2.90
upper quartile 1.37
median 1.10
lower quartile 0.82
minimum 0.25

4.3 Vertical K_d Variability

The potential for vertical variability of K_d is of concern for both CAU and HST scale radionuclide transport modeling efforts. Contaminant source location is obviously related to test depth, which both CAU and HST scale models must consider. As indicated from the XRD data, mineralogy can vary significantly with depth, particularly in certain zones (see Chapter 3) or alluvial layers (Warren et al., 2002). To address the long-term issue of potential downward and lateral migration of radionuclides out of Frenchman Flat alluvium toward deeper aquifers, vertical variation of K_d may need to be addressed. Spatial variation of K_d, in general, will tend to produce a dispersive effect on radionuclide transport (Garabedian et al., 1988; Tompson, 1993; Abulaban and Nieber, 2000).

Radionuclides may be transported several hundred meters vertically within several years following an underground nuclear test. Vertical transport has been documented by migration of radionuclides away from the Benham test (Kersting et al., 1999) and downgradient radionuclide sampling and HST modeling of the Cheshire test at Pahute Mesa (Erikson, 1991; Pawloski et al., 2001). This vertical radionuclide transport results from an upward component of groundwater flow. In addition to naturally occurring mechanisms for upward groundwater flow, such as faults, heterogeneity, or geothermal gradients, the underground nuclear test itself may cause vertical groundwater flow through a combination of test-induced effects, such as the collapse chimney, fractured zones, test pressure, and test heat (Pawloski et al., 2001). As shown in Section 4.2, the K_d histograms for mineral abundance data from drillholes ER-5-4, ER-5-3, UE-5n, and U-11g-1 exhibit uni- or bi-modal log-normal distributions. In the following sections, we examine vertical variability of K_d in these drillholes as a function of depth. The K_d data are presented in both log and linear scales to facilitate interpretation of the data. A variogram analysis of vertical spatial variability of K_d is presented in Chapter 5.

4.3.1 Log-Scale Vertical K_d Variability

Figure 4.12 plots K_d for radionuclides on a log scale versus depth. The K_ds are derived by application of the XRD mineral abundance data to the equations given in Section 4.1.3. In addition to illustrating the wide range in magnitude of K_d for different radionuclides, these plots show that K_d generally varies within one order of magnitude for each radionuclide (also indicated by histograms presented in Section 4.3). Some of the larger-scale variations can be traced to zones described in Chapter 3, such as depth intervals in drillhole ER-5-4 with high abundances of clinoptilolite at 310-340 m depth and calcite at 700-780 m depth. K_ds for Ca and Sr, the two radionuclides with pronounced bi-modal K_d distributions, exhibit a strong dependence on the abundance of clinoptilolite. The relatively higher mean value of K_d for Cs in drillhole ER-5-4 compared to ER-5-3 can be attributed to higher mica abundances in the depth range of 320 to 430 m in ER-5-4. K_ds appear to correlate between drillholes ER-5-4 and UE-5n at similar depths, as well as between drillholes ER-5-3 and U-11g-1. This apparently localized lateral correlation is examined more closely in the next section. The spatial distribution of K_ds exhibits a combination of structured and random variability. Because the K_ds are a function of several mineral abundances, spatial variation of K_d over the entire alluvial section appears to behave more as a random field compared to spatial variation of abundance of individual minerals, which is more directly linked to mineralization zones or alluvial layers.
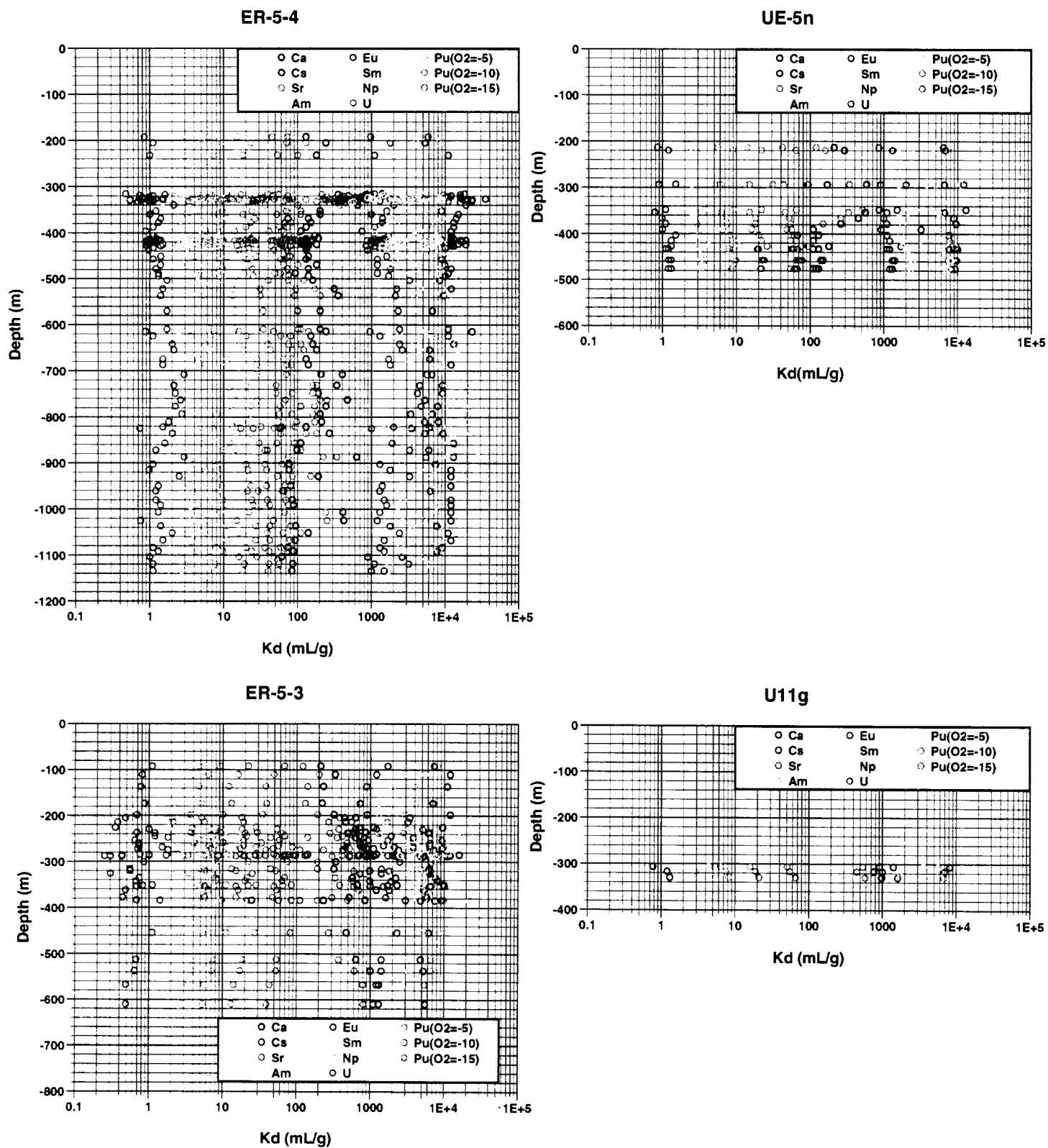
Figure 4.12 K_ds of all radionuclides plotted on log scale versus depth at locations having XRD data for drillholes ER-5-4, UE-5n, ER-5-3, and U-11g-1.

4.3.2 Linear-Scale Vertical K_d Variability

Figures 4.13 to 4.15 plot K_d as a function of depth on a linear scale for different radionuclides, with K_ds from the different drillholes on the same graph. These plots permit close examination of the lateral correlation of K_d between drillholes for different radionuclides. The radionuclide K_ds correlate well between drillholes ER-5-4 and UE-5n in central Frenchman Flat and between drillholes ER-5-3 and U-11g-1 in northern Frenchman Flat. The major variations in K_d with depth can be related to the mineralization zones described in Chapter 3, which are related to the alluvial layers identified by Warren et al. (2002). For example, the high Sr K_ds between 320 and 340 meters in ER-5-4 can be attributed to high clinoptilolite abundance in that zone. Similarly, high Am, Eu, Sm, Np, and Pu K_ds between 700 and 900 meters in ER-5-4 can be attributed to high calcite abundances in that zone. These layers appear to be laterally extensive, but not over the entire extent of Frenchman Flat. The K_d correlations between wells are complicated by the fact that predicted K_ds are a function of a combination of minerals weighted by their respective radionuclide affinities. Correlations between the wells are more easily observed where mineralogy is examined directly (Chapter 3). Since the K_ds are based on the abundance of a combination of minerals, radionuclide K_d variability is buffered to some degree.[9] Regardless, it is important to view these data in the context of radionuclide retardation as this will be principle parameter controlling the transport of radionuclides in the near- and far-fields. Based on these K_d data, it appears likely that vertical K_d variability will affect radionuclide transport for some radionuclides.

It is important to remember that the variability in K_d discussed in this report is based on a component additivity approach that assumes that the affinity of a radionuclide for a mineral surface under the specified average solution conditions does not change. Thus, is assumes that the K_d of Sr with regards to clinoptilolite is identical throughout the Frenchman Flat alluvium. The Sr K_d with respect to the alluvium varies only as a function of the mass fraction of sorbing minerals in the alluvium. We do not account for possible changes in K_d that might result from changes in the accessibility of sorbing minerals. For example, the clinoptilolite in the high zeolite zone (320 to 340 meters in ER-5-4) may be less accessible or behave differently compared to the clinoptilolite in the low zeolite zones. The *predicted* K_ds discussed here are based on the upscaled mechanistic component additivity approach described earlier in this chapter. This approach has a number of limitations that should not be ignored.

The pattern of K_d variability suggests that smaller scale HST models might incorporate vertically zoned variations of K_d based on alluvial layers or chemofacies. As for larger-scale CAU models, consideration of vertically zoned variation of K_d would require additional knowledge or assumptions about the lateral extent of the alluvial layers. Alternatively, spatial variation of K_d might be plausibly considered at the CAU-scale by assuming a stochastic random field based on a log-normal distribution for the radionuclides Am, Eu, Np, Pu, Sm, and U. For Ca and Sr, some

---

[9] Buffering refers to a concept that large variability in, for example, clinoptilolite abundance may not completely dominate K_d variation for Sr because other minerals, such as smectite, will tend to compensate for the large variations in clinoptilolite, resulting in a more uniform K_d.

additional assumptions about large-scale spatial variation of zeolitized zones may need to be considered. Alternatively, the more conservative region of the bi-modal log-normal distribution may be used. For Cs, some additional assumptions about large-scale spatial variation of mica may need to be considered. On the other hand, histogram data suggest that the lateral variations of K_ds for Cs may not be significant compared to the localized variation. These zonal and random field approaches to simulating spatial variation of K_d are further discussed in Chapter 6.

Figure 4.13 K_d for Am, Eu, and Np plotted on linear scale versus depth for ER-5-4, ER-5-3, UE-5n, and U-11g-1.
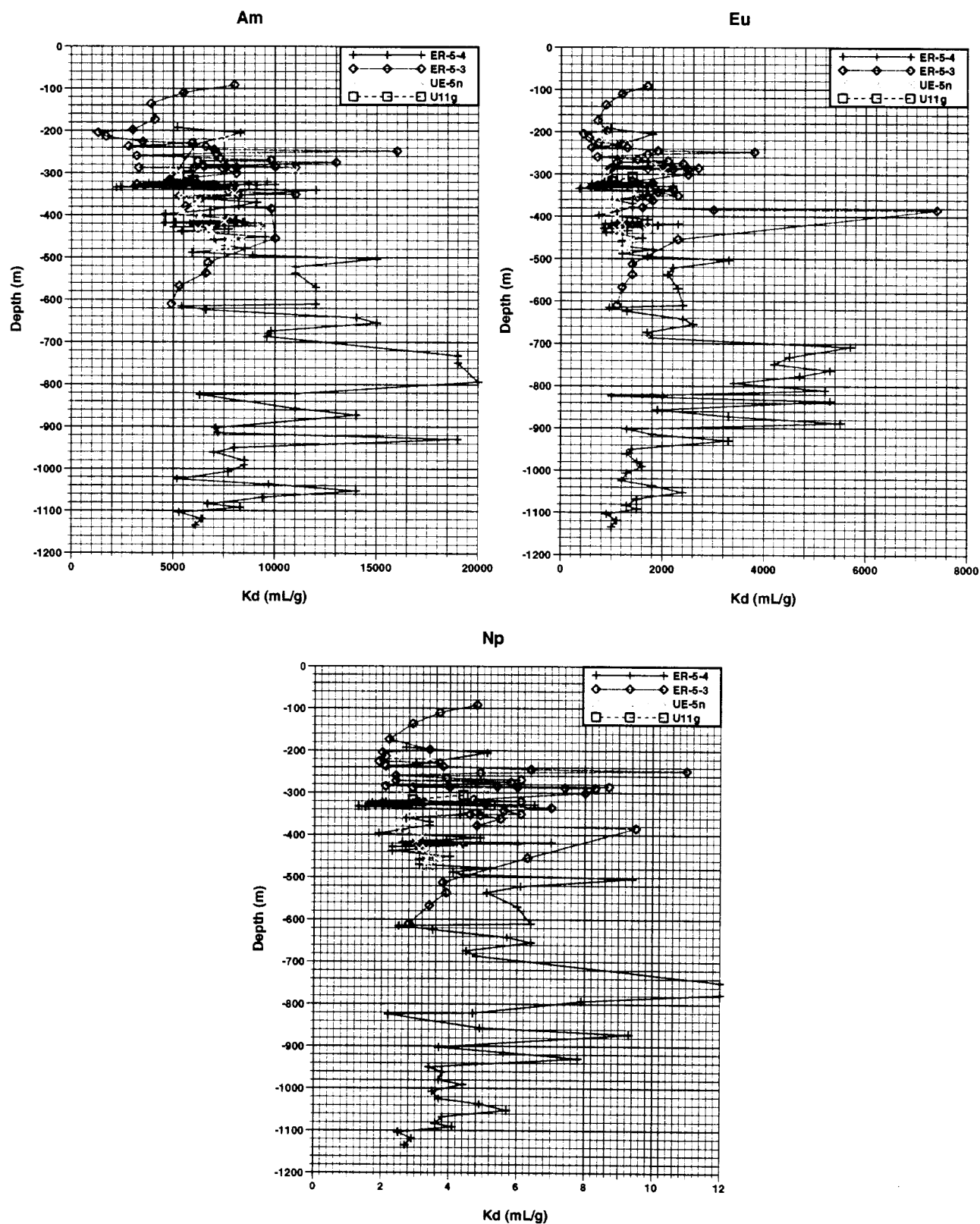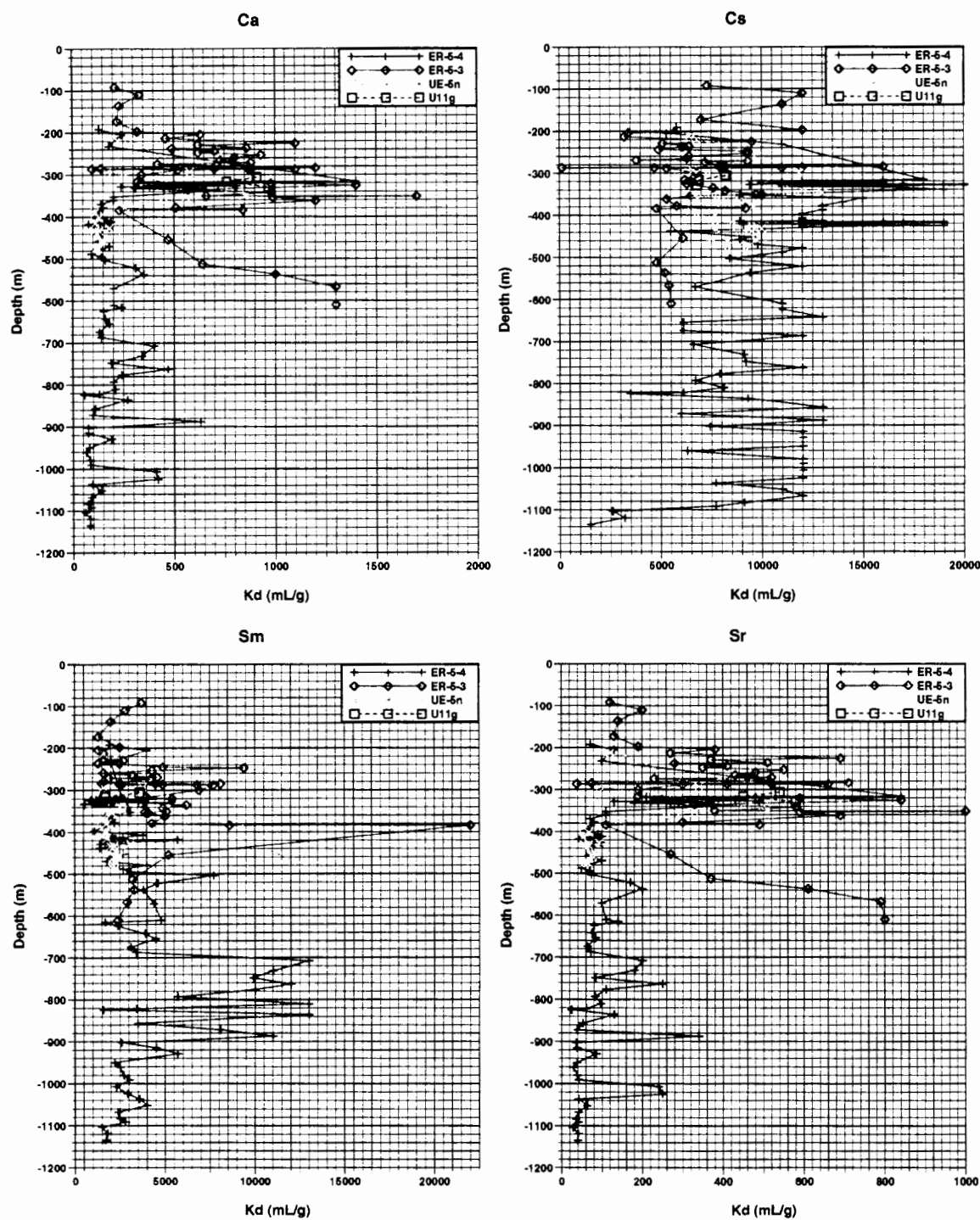
Figure 4.14 K_d for Ca, Cs, Sm, and Sr plotted on linear scale versus depth for ER-5-4, ER-5-3, UE-5n, and U-11g-1.
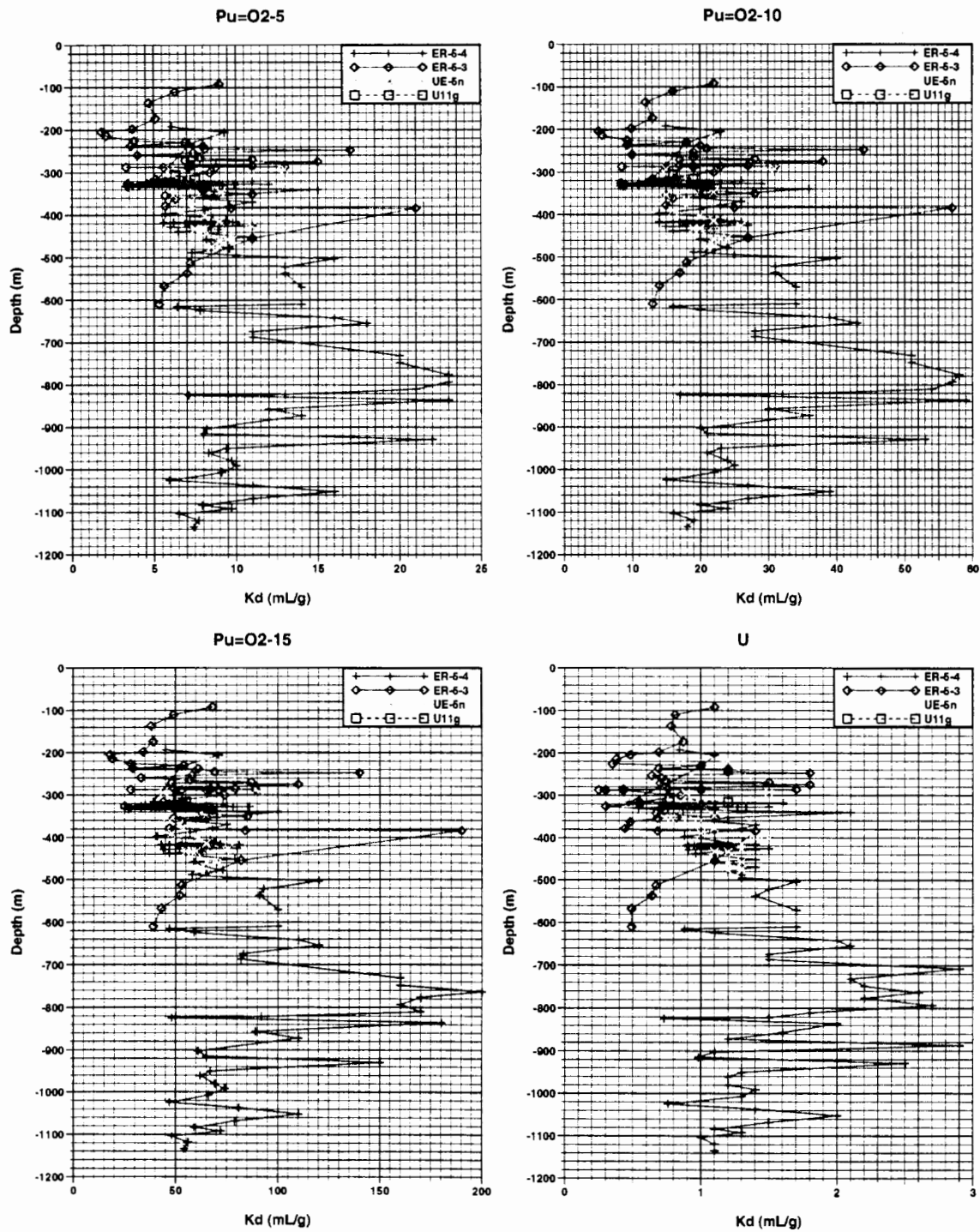
Figure 4.15 K_d for Pu(fugacity $O_2(g) = 10^{-5}$ bars), Pu(fugacity $O_2(g) = 10^{-10}$ bars), Pu(fugacity $O_2(g) = 10^{-15}$ bars), and U plotted on linear scale versus depth for ER-5-4, ER-5-3, UE-5n, and U-11g-1.

5 Variogram Analysis

This chapter applies the geostatistical technique of variogram analysis to quantitatively evaluate spatial variability of mineral abundance and K_d within Frenchman Flat alluvium. In application to the XRD mineral abundance data, "experimental" variograms are computed in the vertical direction for logarithms of mineral fractions within each of the mineralization zones identified in Chapter 3. The variogram analysis indicates that for all minerals except hematite, the spatial variability of mineral abundance within a mineralization zone is mostly attributable to micro-scale variability. The term "micro-scale" variability refers to spatial variability at a scale that is smaller than the minimum data spacing, which ranges from about 0.3 to 3 m depending on the mineral.

In application to the $\log_{10}[K_d]$ values derived in Chapter 4, experimental variograms are computed in the vertical direction for each radionuclide. Variogram models indicate that spatial variation of K_d is attributed in part to micro-scale variability and in part to subregional-scale spatial variability related to mineralization zones or alluvial layers. The term "subregional-scale" refers to spatial variability at scales smaller than the region of interest, which is the northern portion of the Frenchman Flat basin. Lateral variogram models of $\log_{10}[K_d]$ could be inferred by combining vertical variogram parameters with experimental lateral-direction variogram values obtained by comparing data from drillholes ER-5-4 and UE-5n.

5.1 Variogram Theory

Different bivariate statistics (e.g., spatial covariance, spatial correlation, or variogram) can be used to quantitatively characterize spatial variability of a geologic attribute such as mineral abundance or K_d. These statistics are spatially dependent because they are formulated as a function of "lag" or vector separation between data from different locations. In practice, the variogram is usually employed instead of spatial covariance or correlation to allow for consideration of nonstationarity in the mean.

Variogram analysis is most successfully applied in directions were data are aligned so that numerous data pairs exist for a given lag. In most subsurface applications, the vertical direction is most conducive to variogram analysis, given borehole data. Lag spacing is chosen by considering data spacing and number of data pairs per lag. The maximum practical magnitude of the lag is dictated by the spatial extent of the domain or "zone" of interest. Usually, lags with magnitude of ½ or greater the spatial extent of the domain are subject to error. For example, if data are collected in a vertical borehole at 1 m spacing in a 100-m-thick zone with uniform statistical properties, then the variogram analysis could be performed in the vertical direction at 1 m spacing, but variogram values for lags greater than 50 m would likely be subject to error.

5.1.1 Stationarity

As discussed in Chapter 3, the issues of stationarity and normality are crucial to performing a geostatistical analysis of spatial variability. For that reason, this study carefully examined the frequency distributions and zonal variations of mean mineral abundances in Chapter 3. To review, the concept of stationarity in a geostatistical context means that the statistical measures used to characterize the spatial variability of the data are constant, do not depend on location within the region being characterized, and depend only on the lag vector. Usually, only first- and second-order statistics are employed (e.g., mean, covariance, variogram, etc.), with the assumption that the frequency distribution is approximately normal.

If the data are truly second-order stationary (mean and covariance are stationary), either the spatial covariance or variogram will yield effectively the same measure of spatial variability. However, in many earth science applications, the mean of the data may vary smoothly (exhibit a trend). In this case, the variogram, which employs the concept of "intrinsic stationarity" to allow for nonstationarity of the mean, is a more robust measure of spatial variability. Therefore, the variogram, rather than the spatial covariance or correlation, is usually applied to the analysis of spatial variability of geologic attributes.

5.1.2 Variogram Formulation

The variogram (or semivariogram), $\gamma(\mathbf{h})$, is defined by

$$\gamma(\mathbf{h}) = \frac{1}{2} E\left\{ \left[V(\mathbf{x}) - V(\mathbf{x} + \mathbf{h}) \right]^2 \right\}$$

where $V(\mathbf{x})$ is the random variable (e.g., mineral fraction or K_d) at a location $\mathbf{x}$, and $\mathbf{h}$ is the lag (separation vector between data at two different locations). In words, the variogram is the expected value of one-half the squared difference of data values at different locations separated by a vector of variable magnitude and direction. Ideally, as shown in Figure 5.1, the variogram magnitude is zero or small at $\mathbf{h} = 0$ (the "nugget") and rises in magnitude with increasing $\mathbf{h}$ until asymptotically reaching a plateau (the "sill") at a lag beyond which the variogram does not increase much in magnitude (the "range"). The range of spatial correlation is indicated by the variogram "range." The magnitude of the nugget indicates the degree of spatial variability attributed to very small scale or "micro-scale" variability. The sill indicates the magnitude of variability attributed to the total of micro and subregional-scale (within the region of interest) variability. If the data are second-order stationary, the magnitude of the sill will correspond to the variance. If the mean varies with location or a trend exists in the data, the variogram sill may not match the variance of the data at large $\mathbf{h}$.
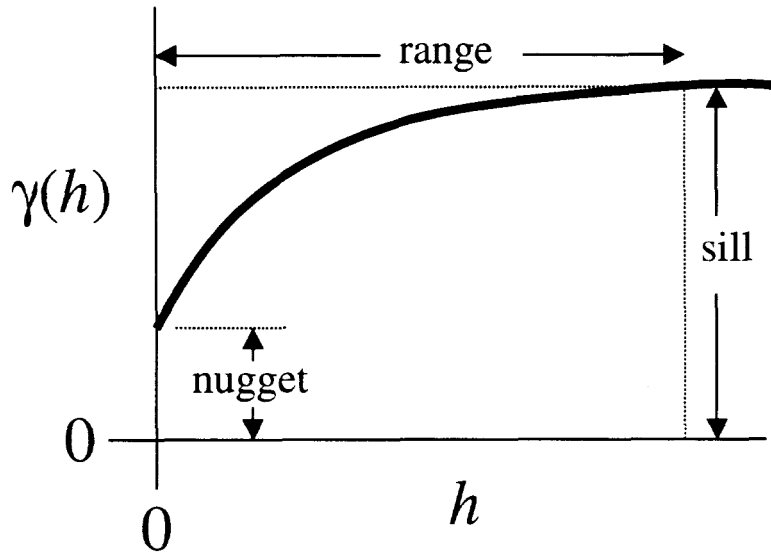
Figure 5.1 Schematic showing variogram attributes: nugget, sill, and range.

5.1.3 Variogram Estimation

In practice, experimental variogram values are usually estimated from

$$\gamma(\mathbf{h}) = \frac{1}{2N(\mathbf{h})} \sum_{i=1}^{N(\mathbf{h})} [v_i(\mathbf{x}) - v_i(\mathbf{x}+\mathbf{h})]^2$$

where

$N(\mathbf{h})$ is the number of data pairs separated by a lag $\mathbf{h}$, and

$v_i(\mathbf{x})$ and $v_i(\mathbf{x}+\mathbf{h})$ is the ith data pair having a separation of $\mathbf{h}$.

An important consideration for obtaining successful variogram estimates is to have enough data pairs for each lag of interest. If the number of data pairs is inadequate, the experimental variogram may appear scattered or noisy. Typically, at least 20 data pairs are needed to yield reasonably accurate variogram value estimates for a single lag.

In most applications, including this study's, the data are not regularly spaced. Therefore, it is necessary to allow for a range of lags to estimate each value of $\gamma(\mathbf{h})$. Usually, each value of $\gamma(\mathbf{h})$ is computed over a range of $\mathbf{h}$, and the average value of $\mathbf{h}$ is used in presentation of the experimental value of $\gamma(\mathbf{h})$. In this study, the ranges of $\mathbf{h}$ were allowed to vary to obtain a minimum number of data pairs. These ranges of $\mathbf{h}$ varied for different mineralization zones because of differences in the amounts of data and spacing of data pairs.

5.2 Application to Mineral Abundances within Mineralization Zones

As discussed above and in Chapter 3, the interpretation and identification of mineralization zones was implemented given the fact that the mineral abundance data exhibit zonal variations with depth. These zonal variations were evident by significant and abrupt shifts in the mean value or variance of mineral abundances. From a geostatistical perspective, these shifts in the mean values of mineral abundances represent a nonstationarity that required sorting of the data into different categories within which intrinsic stationarity could be assumed. Intrinsic stationarity could not be assumed throughout the entire depth because of the abruptness of the changes in mean values and nonstationarity of variance.

Based on geostatistical theory and the analysis of univariate statistics given in Chapter 3, it is reasonable to assume that spatial variation of logarithms of mineral fraction within each mineralization zone can be characterized by a variogram. Because the data were sampled from multiple locations in vertical drillholes, the data provide excellent coverage for examining vertical spatial variability of mineral abundances over scales of meters to hundreds of meters. Implementation of variogram analysis to examine lateral spatial variability of mineral abundances is thwarted by the limited number of drillholes having abundant XRD data as obtained from drillholes ER-5-4, ER-5-3, and UE-5n. Only data from drillholes ER-5-4 and UE-5n provide significant numbers of data for evaluation of lateral continuity of mineral abundances. However, these two drillholes provide information at only one lag vector. Ideally, similar spatial density of mineral abundance data obtained from several closely-spaced (e.g., 0.1 to 2 km) drillholes might be used to quantitatively and directly evaluate lateral spatial variability of mineral abundance.

5.2.1 Vertical Variograms of Log Mineral Abundance

Figures 5.2 to 5.5 show experimental variograms for logarithms (base 10) of mineral abundances within each mineralization zone identified in Chapter 3. The experimental variogram values are shown by symbols, indexed to each zone with zonal mean value of mineral abundance given in percent. The dashed lines on each variogram plot indicate the variance of the logarithm of mineral fraction within each mineralization zone. The variance line provides an indication of a reasonable variogram sill value assuming second-order stationarity. For most mineralization zones, the data variance does indeed provide a plausible variogram sill value. Zones represented by XRD values below the detection limit are indicated by a zone mean value of 0.0. The constant zero values in these zones produce variograms with constant zero values.

For each mineralization zone of each mineral, the experimental variogram values were obtained for lag intervals with a minimum of 40 data pairs. Different minimum numbers of data pairs were attempted on this data set — forty were found to be the minimum number of data pairs needed to adequately reduce scatter in the experimental variogram values. Notice that depending on the mineral and zone, different numbers of experimental variogram values were computed because of the differences in numbers of data pairs. For example, for the mineralization zones of calcite having a mean values of 2.79%, 20.61%, and 8.89%, there are 16, 2, and 3 variogram values, respectively. These differences reflect the fact that the mineralization zone of calcite with a 2.79% mean value is much more abundant than the other zones.

Another important feature in the variograms is that variance of the $\log_{10}$ mineral abundances is often different in the different mineralization zones. For example, the variance of calcite within the zone of 2.79% mean value is about 0.15, whereas the variance is between 0.01 and 0.02 for the other zones with non-zero mean values. Because these variances are computed from the logarithm of the mineral abundances, the variance is scaled relative to the magnitude.
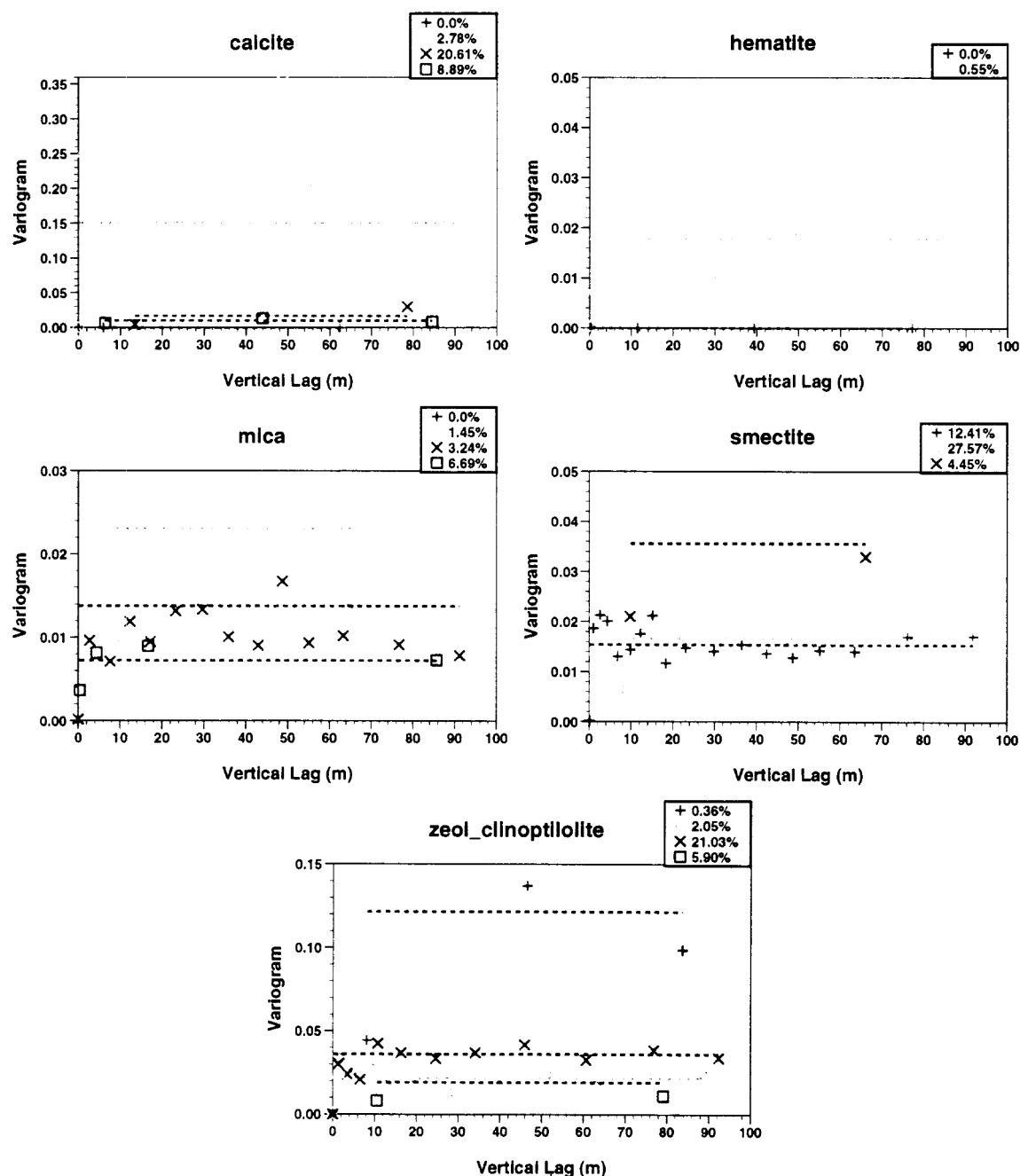
Figure 5.2 Experimental variograms for $\log_{10}$ mineral fraction of calcite, hematite, mica, smectite, and clinoptilolite mineralization zones for XRD data from ER-5-4, UE-5n, ER-5-3 and U-11g-1. Zonal variances are shown by dashed lines for reference.
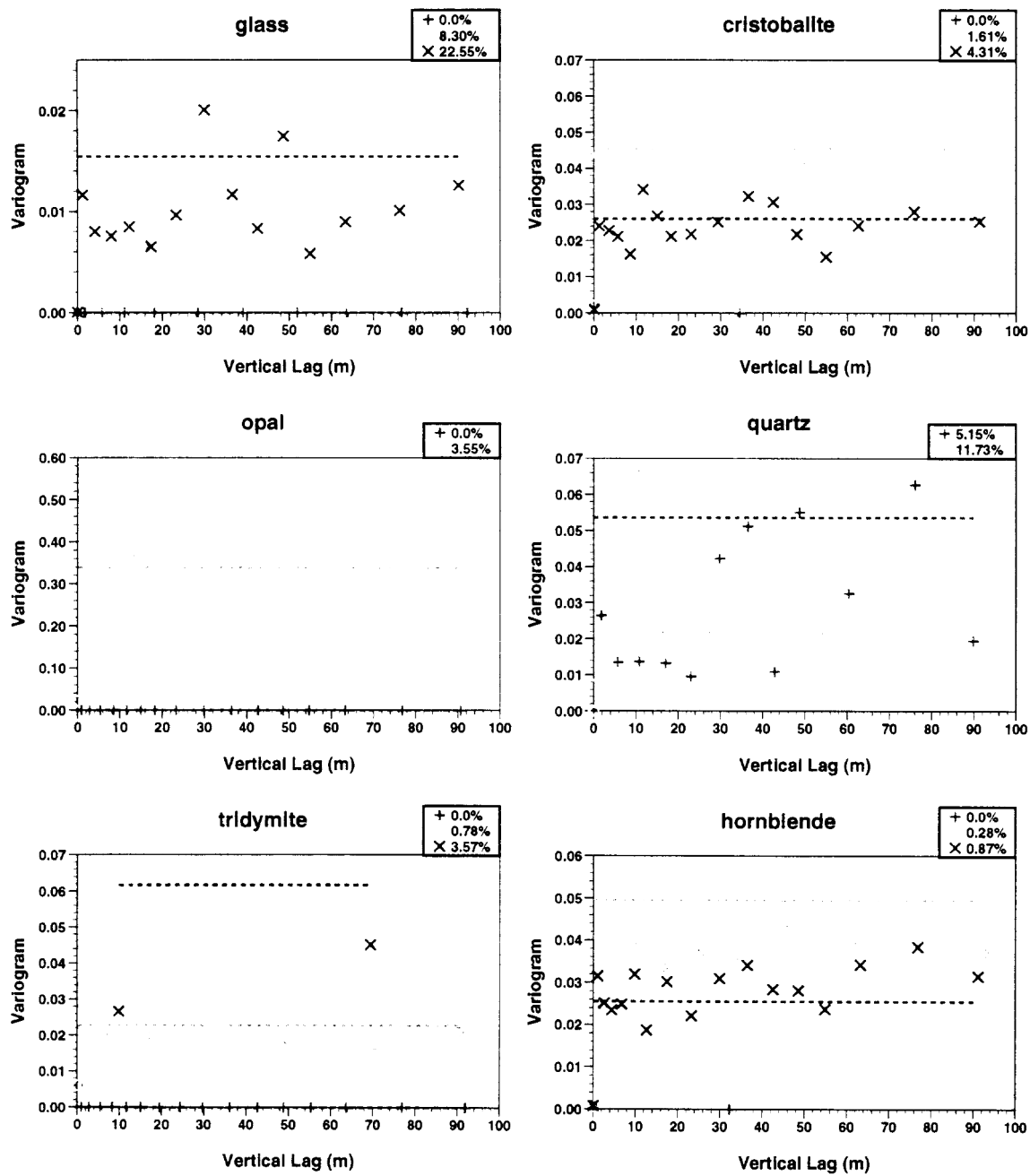
Figure 5.3 Experimental variograms for $\log_{10}$ mineral fraction of glass, cristobalite, opal, quartz, tridymite, and hornblende mineralization zones for XRD data from ER-5-4, UE-5n, ER-5-3 and U-11g-1. Zonal variances are shown by dashed lines for reference.

Figure 5.4 Experimental variograms for $\log_{10}$ mineral fraction of dolomite, kaolinite, analcime, mordenite, and clinopyroxene mineralization zones for XRD data from ER-5-4, UE-5n, ER-5-3 and U-11g-1. Zonal variances are shown by dashed lines for reference.

Figure 5.5 Experimental variograms of $\log_{10}$ mineral fraction in orthoclase, sanidine, albite, bytownite, and anorthite mineralization zones for XRD data from ER-5-4, UE-5n, ER-5-3 and U-11g-1. Zonal variances are shown by dashed lines for reference.
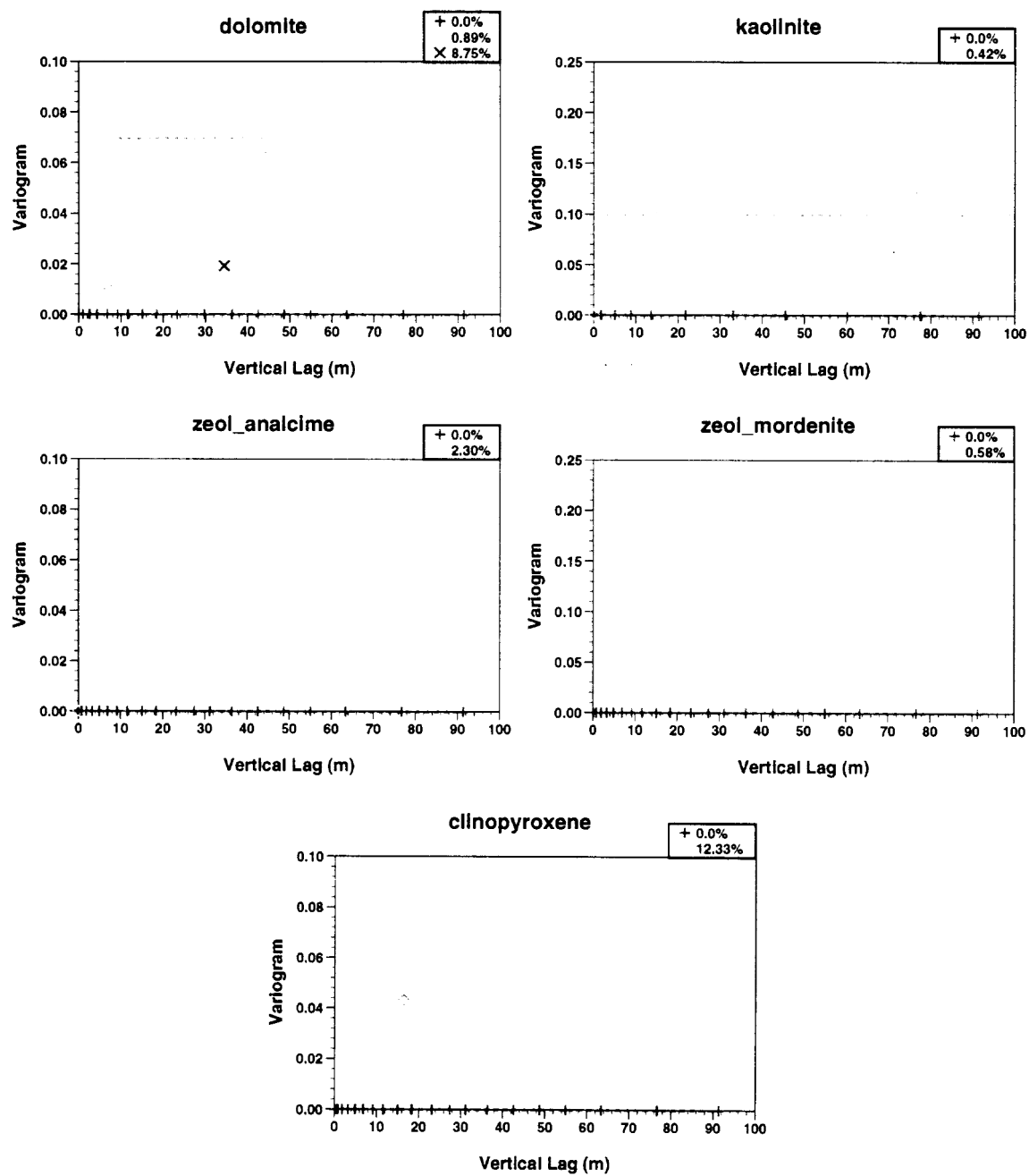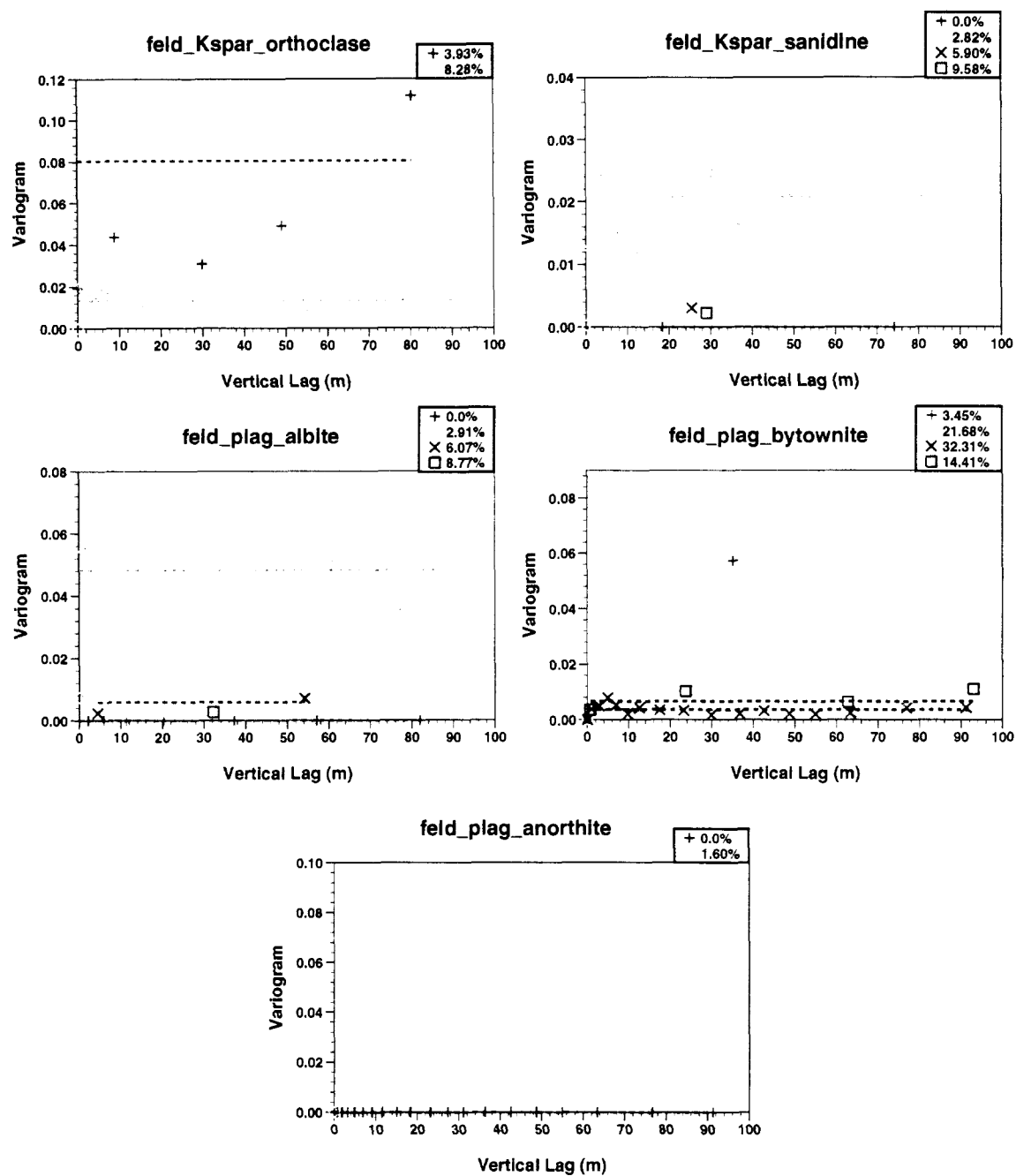
5.2.2 Interpretation

The most important result of the variogram analysis of mineral abundances within the mineralization zones is that, with the exception of hematite-bearing zone, the spatial variation of mineral abundances can be plausibly modeled by a variogram having pure nugget (no spatial correlation). Thus, with the exception of hematite, spatial variation within the mineralization zones for all of the sorbing minerals is essentially random down to scales of less than one meter. The variograms indicate that some non-sorbing minerals such as kaolinite (0.42%) and hornblende (0.28% mean) may exhibit some spatial continuity within zones, however the data are insufficient to confirm this. The major component of spatial variation of the mineral abundance is attributed to different mineralization zones, which are related to different alluvial layers identified by Warren et al. (2002). Therefore, the issue of vertical and lateral spatial variation of mineral abundances, which is of concern to development of CAU and HST scale transport models in Frenchman Flat, may be best addressed by considering the three-dimensional geometry of chemofacies or alluvial layers.

For hematite, vertical spatial variability of $\log_{10}$ hematite abundance within hematite-bearing zones (about 81% of the alluvium sampled) appears to have a correlation range of about 5 m. Figure 5.6 shows a variogram model fit to the experimental variogram values (minimum of 20 data pairs) for the hematite-bearing zone. The variogram model parameters are

- nugget = 0.0

- sill = 0.0178

- range = 5.0 m

- structure = exponential

such that the variogram model is formulated by:

$$\gamma(h_z) = 0.0178 \times \left[1.0 - \exp\left(\frac{-3h_z}{5.0\,\text{m}} \right) \right]$$

where h_z is the lag in the vertical (z) direction. This variogram model could be used to characterize vertical spatial variability of hematite within hematite-bearing zones. However, explicit consideration of vertical spatial variation of hematite within mineralization zones would require numerical grid spacing of 5m or less in the vertical direction.
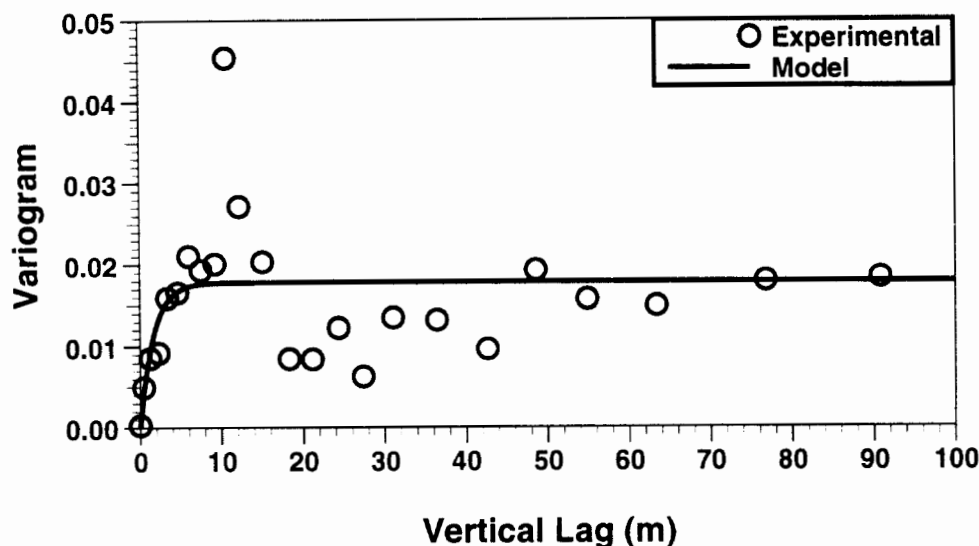
Figure 5.6 Variogram model fit to the experimental variogram in the vertical direction for the $\log_{10}$ fraction of hematite in the hematite-bearing mineralization zone.

5.3 Application to K_d

In the application of variogram analysis to $\log_{10}[K_d]$, the combined effect of spatial variability of mineral abundances within and between mineralization zones is lumped together. Conceivably, K_d could be treated as a random field in CAU or HST scale transport models in Frenchman Flat. This approach might be used to model the spatial distribution of K_d directly as an alternative to modeling the spatial distribution of mineral abundances, then translating the mineral abundances to K_ds. To implement this direct K_d approach, plausible random field models of K_d will need to be developed. Geostatistical simulation approaches, such as sequential Gaussian simulation parameterized by 2- or 3-D variogram models (Deutsch and Journel, 1998), could provide plausible random field models of K_d, as implemented in Chapter 6.

As shown in Chapter 4, the K_ds computed for the radionuclides Cs, Am, Eu, Sm, Np, U, and Pu tend to exhibit a log-normal distribution. The exceptions are Ca and Sr, which exhibit bi-modal distributions of $\log_{10}[K_d]$. The depth profiles generally exhibit little vertical variation in the mean. Some lateral variations in mean K_ds between wells in central and northern Frenchman were evident for the radionuclides Ca, Cs, and Sr. These lateral variations in K_d were attributed to lateral variations in clinoptilolite and mica abundance between central and northern Frenchman Flat. Based on these data, it may be plausible to assume that stationary K_d random field models could be developed for the radionuclides Am, Eu, Sm, Np, U, and Pu for CAU or HST scale transport models in Frenchman Flat. For Ca, Cs, and Sr, some consideration of lateral nonstationarity in mean K_d in Frenchman Flat may need to be integrated into the development of CAU or HST scale transport models. In either case, three-dimensional variogram models could be used to characterize three-dimensional spatial variability of $\log_{10}[K_d]$.

The excellent vertical sampling afforded by the XRD data from drillholes ER-5-4, UE-5n, ER-5-3, and U-11g-1 enables estimation of experimental variograms of $\log_{10}[K_d]$ in the vertical direction. Vertical variogram models for spatial variation of $\log_{10}[K_d]$ can be developed. At this time, quantification of lateral spatial variability remains the major difficulty in development of three-dimensional variogram models for $\log_{10}[K_d]$.

5.3.1 Vertical Variogram Analysis of $\log_{10}[K_d]$

Figure 5.7 shows variogram values of $\log_{10}[K_d]$ computed from the composite of XRD data from drillholes ER-5-4, UE-5n, ER-5-3, and U-11g-1. The experimental values are indicated by symbols, and fitted variogram models are indicated by solid lines of matching color. Different variogram structures are evident for different radionuclides. The sill of each variogram model is matched to the experimental variogram values of 300 m or less. The variogram values at lags greater than 300 m begin to suffer from the "L/2" effect, where data pairs with lags greater than one half of the spatial length of the data set are adversely affected by extreme values.

The vertical variograms of $\log_{10}[K_d]$ for Cs and U appear to lack spatial correlation, evident by experimental variogram values that oscillate near the sill for all lags. Nevertheless, a small degree of spatial continuity is incorporated in the model. The vertical variograms for $\log_{10}[K_d]$ of Am, Eu, Sm, Np, and Pu all show similar structure, with about 30-45% of the spatial variation attributed to micro-scale variability, and the remaining subregional-scale variability attributed to a exponential structure with a range of correlation of about 300 to 400 m. The subregional-scale variability is attributed to different mineralization zones or alluvial layers. The radionuclides Ca and Sr exhibit much larger magnitude of spatial variation dominated by subregional-scale spatial variability of $\log_{10}[K_d]$. The vertical variogram structures for $\log_{10}[K_d]$ of Ca and Sr are largely attributed to variations of clinoptilolite abundance in different mineralization zones. The nugget component all of these variograms is directly related to micro-scale variability within the mineralization zones. Table 5.1 shows the $\log_{10}[K_d]$ vertical variogram model parameters used in Figure 5.7. Certainly other variogram model parameters, including variogram structures such as the spherical function, could be proposed to fit the experimental variograms. The variogram model parameters are given as plausible values to consider in developing stochastic realizations of $\log_{10}[K_d]$. Certainly other model interpretations of the experimental variograms could be made.

Table 5.1 Parameters for vertical variogram models of $\log_{10}[K_d]$ shown in Figure 5.7 for radionuclides Ca, Cs, Sr, Am, Eu, Sm, Np, U, and Pu.

Radionuclide	Nugget	Sill	Range (m)	Vertical Variogram Model Equation
Ca	0.015	0.105	150	$\gamma(h_z) = 0.015 + 0.090\left[1 - \exp\left(-\frac{3h_z}{150\,\text{m}}\right)\right]$
Cs	0.040	0.040	0	$\gamma(h_z) = 0.040$
Sr	0.015	0.12	150	$\gamma(h_z) = 0.015 + 0.105\left[1 - \exp\left(-\frac{3h_z}{150\,\text{m}}\right)\right]$
Am	0.016	0.052	300	$\gamma(h_z) = 0.016 + 0.036\left[1 - \exp\left(-\frac{3h_z}{300\,\text{m}}\right)\right]$
Eu	0.020	0.065	300	$\gamma(h_z) = 0.020 + 0.045\left[1 - \exp\left(-\frac{3h_z}{300\,\text{m}}\right)\right]$
Sm	0.028	0.087	300	$\gamma(h_z) = 0.028 + 0.059\left[1 - \exp\left(-\frac{3h_z}{300\,\text{m}}\right)\right]$
Np	0.020	0.065	400	$\gamma(h_z) = 0.020 + 0.045\left[1 - \exp\left(-\frac{3h_z}{400\,\text{m}}\right)\right]$
U	0.023	0.027	300	$\gamma(h_z) = 0.023 + 0.004\left[1 - \exp\left(-\frac{3h_z}{300\,\text{m}}\right)\right]$
Pu(O_2=-5)	0.018	0.043	300	$\gamma(h_z) = 0.018 + 0.043\left[1 - \exp\left(-\frac{3h_z}{300\,\text{m}}\right)\right]$
Pu(O_2=-10)	0.017	0.042	300	$\gamma(h_z) = 0.017 + 0.042\left[1 - \exp\left(-\frac{3h_z}{300\,\text{m}}\right)\right]$
Pu(O_2=-15)	0.016	0.041	300	$\gamma(h_z) = 0.016 + 0.041\left[1 - \exp\left(-\frac{3h_z}{300\,\text{m}}\right)\right]$

Figure 5.7 Experimental and modeled vertical direction variograms of $\log_{10} [K_d]$ for radionuclides Ca, Cs, Sr, Am, Eu, Sm, Np, U, and Pu based on XRD mineral abundance data from drillholes ER-5-4, UE-5n, ER-5-3, and U-11g-1 in Frenchman Flat.

The issue of the bi-modal $\log_{10}[K_d]$ frequency distributions for Ca and Sr can be addressed by separating the K_ds into two sub-populations — low and high — based on cutoff values of 300 and 200 mL/g for Ca and Sr, respectively. Vertical spatial variability within the low and high K_d zones can be assessed by variogram analysis of the sub-populations of data defined by the cutoff values. Figure 5.8 shows vertical experimental and model variograms of K_d spatial variability of Ca and Sr within the low and high K_d zones. Table 5.2 shows the parameters of the variogram models in Figure 5.8. The sill values are much smaller than for the variogram models of the complete Ca and Sr K_d data because the spatial variability of K_d related to differences between low and high K_d is removed. The variograms for the high K_d zones exhibit a large nugget component of the variogram, indicating that spatial variability of K_d within the high K_d zones for Ca and Sr is dominated by micro-scale variability. The variograms for the low K_d zones exhibit more spatial continuity, indicating that subregional-scale spatial variations of K_d would exist within the low K_d zones.
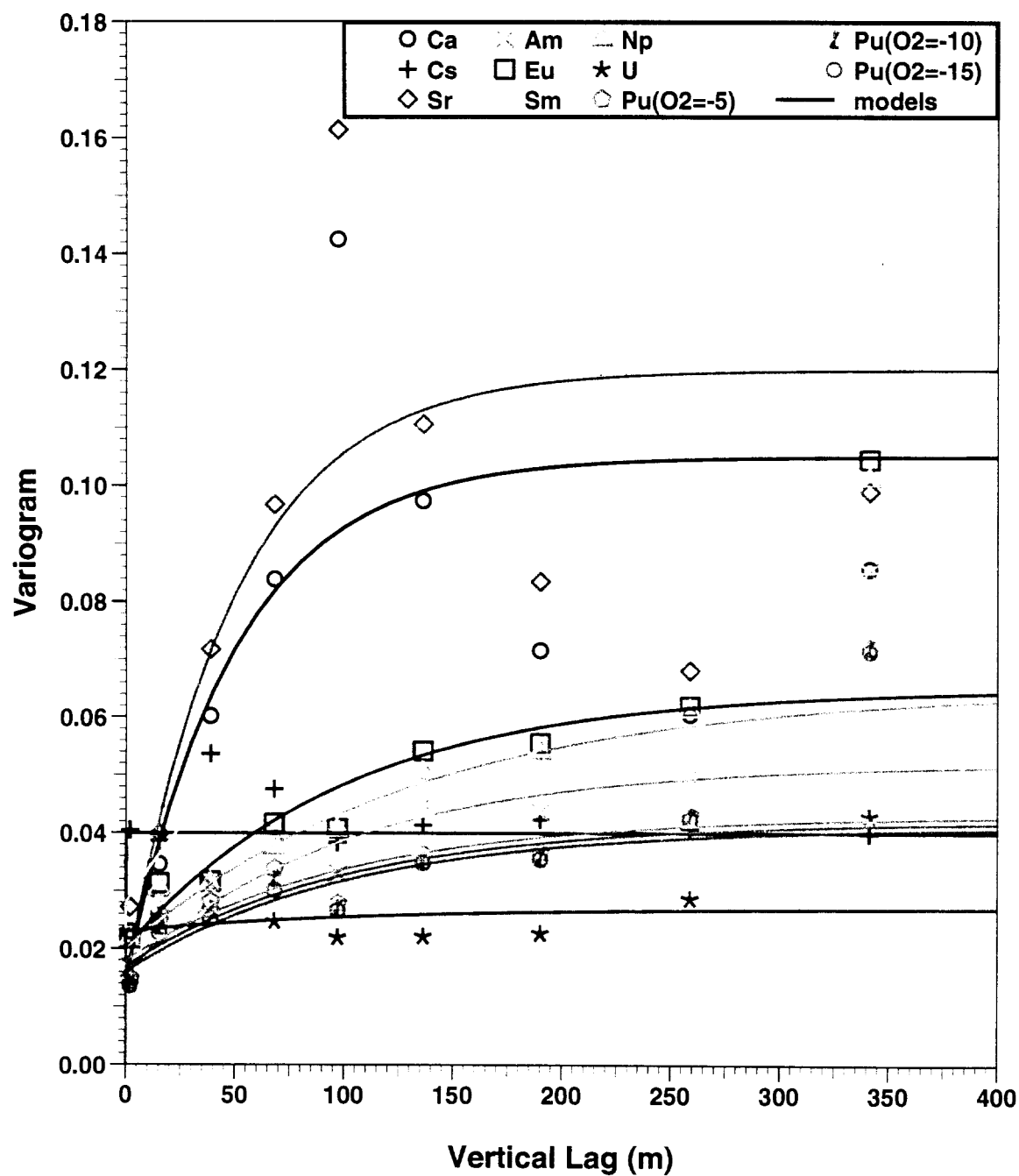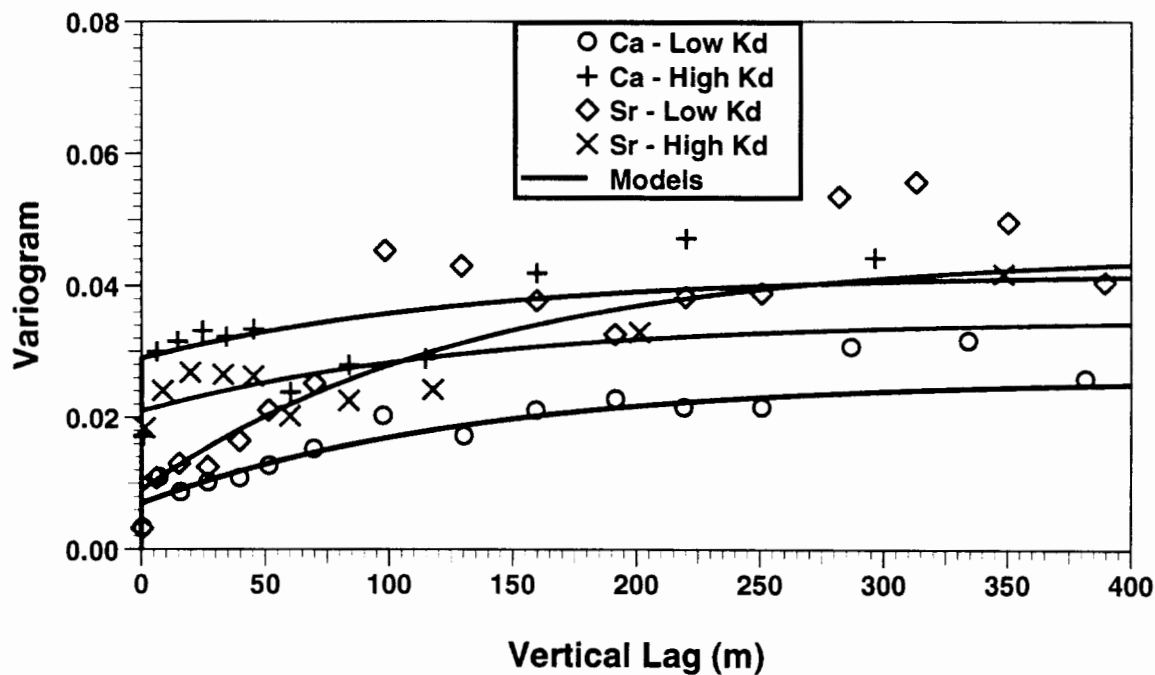

Figure 5.8 Experimental and modeled vertical direction variograms of $\log_{10}[K_d]$ for radionuclides Ca and Sr separated into low and high K_d zones based on 300 and 200 mL/g cutoffs, respectively.

Table 5.2 Parameters for vertical variogram models of $\log_{10}[K_d]$ shown in Figure 5.8 for low and high K_d zones or radionuclides Ca and Sr.

Radionuclide	Nugget	Sill	Range (m)	Vertical Variogram Model Equation
Ca – low K_d	0.007	0.026	400	$\gamma(h_z) = 0.007 + 0.019\left[1 - \exp\left(-\frac{3h_z}{400\,\mathrm{m}}\right)\right]$
Ca – high K_d	0.029	0.042	400	$\gamma(h_z) = 0.029 + 0.042\left[1 - \exp\left(-\frac{3h_z}{400\,\mathrm{m}}\right)\right]$
Sr – low K_d	0.009	0.045	400	$\gamma(h_z) = 0.009 + 0.045\left[1 - \exp\left(-\frac{3h_z}{400\,\mathrm{m}}\right)\right]$
Sr – high K_d	0.021	0.035	400	$\gamma(h_z) = 0.021 + 0.035\left[1 - \exp\left(-\frac{3h_z}{400\,\mathrm{m}}\right)\right]$

5.3.2 Lateral Spatial Variability of $\log_{10}[K_d]$

Three-dimensional stochastic realizations of K_d could be used to examine the effect of spatial variability of K_d on radionuclide transport. Generation of the realizations would require development of three-dimensional variograms of $\log_{10}[K_d]$. The XRD mineral abundance data from drillholes ER-5-4, UE-5n, ER-5-3, and U-11g-1 have provided an excellent foundation for evaluating vertical spatial variability of $\log_{10}[K_d]$. However, the characterization of lateral spatial variability of K_d is more difficult to determine from drillhole data.

In general, it is difficult to directly characterize lateral spatial variability of geologic attributes for several reasons:

- Drillholes are vertical and, thus, preferentially sample the vertical direction.

- Heterogeneity within geologic formations, such as alluvial deposits, is controlled by irregular depositional processes that are difficult to track laterally.

- The "lateral direction" is not necessarily horizontal or parallel to the ground surface.

- If the spatial variability is strongly anisotropic between the lateral and vertical directions, small dip angles compound the difficulty of correlating geologic attributes between drillholes.

Of the XRD data from drillholes ER-5-4, UE-5n, ER-5-3, and U-11g-1, only the data from ER-5-4 and UE-5n offer a possible opportunity to quantitatively analyze lateral spatial variability of K_d, and only for a lag of 477 m (the distance between drillholes ER-5-4 and UE-5n). Between these two drillholes, the mineral abundances do appear to show correlation (see Chapter 3). Although drillhole ER-5-3 has much data, the mineral abundances are clearly different from ER-5-4. Drillhole ER-5-3 appears to be located beyond the lateral range of correlation of $\log_{10}[K_d]$ with respect to drillhole ER-5-4. Drillhole U-11g-1 has only three data, which are inadequate to estimate a variogram value. From visual inspection of depth profiles of $\log_{10}[K_d]$ between drillholes ER-5-4, UE-5n, and ER-5-3 in Figure 4.12, it appears that a reasonable estimate of the range of lateral correlation of $\log_{10}[K_d]$ in Frenchman Flat would be between 477 m and 5585 m (the distances from drillhole ER-5-4 to drillholes UE-5n and

ER-5-3). Certainly other information on the three-dimensional geometry of alluvial layers would be useful for estimating lateral spatial continuity of K_d for those radionuclides that appear sensitive to the spatial distribution of mineralization zones or alluvial layers.

Figure 5.9 shows experimental variogram values for $\log_{10}[K_d]$ for different radionuclides computed for a lateral lag of 477 m from the XRD data from drillholes ER-5-4 and UE-5n. The lag pairs were vertically shifted to account for difference in the depth of the mineralization zone with high clinoptilolite abundance between 310-340 m depth in ER-5-4 and about 340-370 depth in UE-5n. The lateral variogram models shown were constructed by assuming the same nugget and sill values and exponential structure used for the vertical variogram models, but with adjusted range values, as shown in Table 5.3. The range was adjusted so that the variogram models honor the experimental variogram values for all radionuclides but Cs and U, which exhibit mostly micro-scale variability. The fitted range values vary from 1350 to 3900 m, which appears consistent with the appearance of lateral spatial correlation of mineral abundance between drillholes spaced hundreds of meters apart and lack of spatial correlation between drillholes spaced over 5 km apart. Comparison of vertical and lateral range values indicates lateral:vertical anisotropy ratios ranging between 4.5:1 to 13:1. Considering the difficulties in quantifying lateral spatial correlation listed above, these ratios could be greater. The lateral-direction variogram model range parameters for $\log_{10}[K_d]$ for the radionuclides shown in Table 5.3 are uncertain because of the sparse data on lateral continuity of mineral abundance.

Warren et al. (2002) suggest that the Frenchman Flat alluvial basin deposits consist of coalesced fans having three dominant source areas — Rock Valley, Massachussets Mountain, and the Ranger Mountains. Lateral continuity may be easier to track near the source areas and more difficult to track in distal areas where fans are more interfingered. Lateral continuity of $\log_{10}[K_d]$ would not necessarily be isotropic. More lateral continuity could be expected in the downslope direction of the ancient alluvial fan surfaces. In any case, lateral continuity of $\log_{10}[K_d]$ is most likely dominated by the lateral continuity of mineralization zones or alluvial layers. Because the alluvial layers represent different episodes of alluvial fan deposition, some lateral gradation of grain size distribution and mineralogy should be expected.

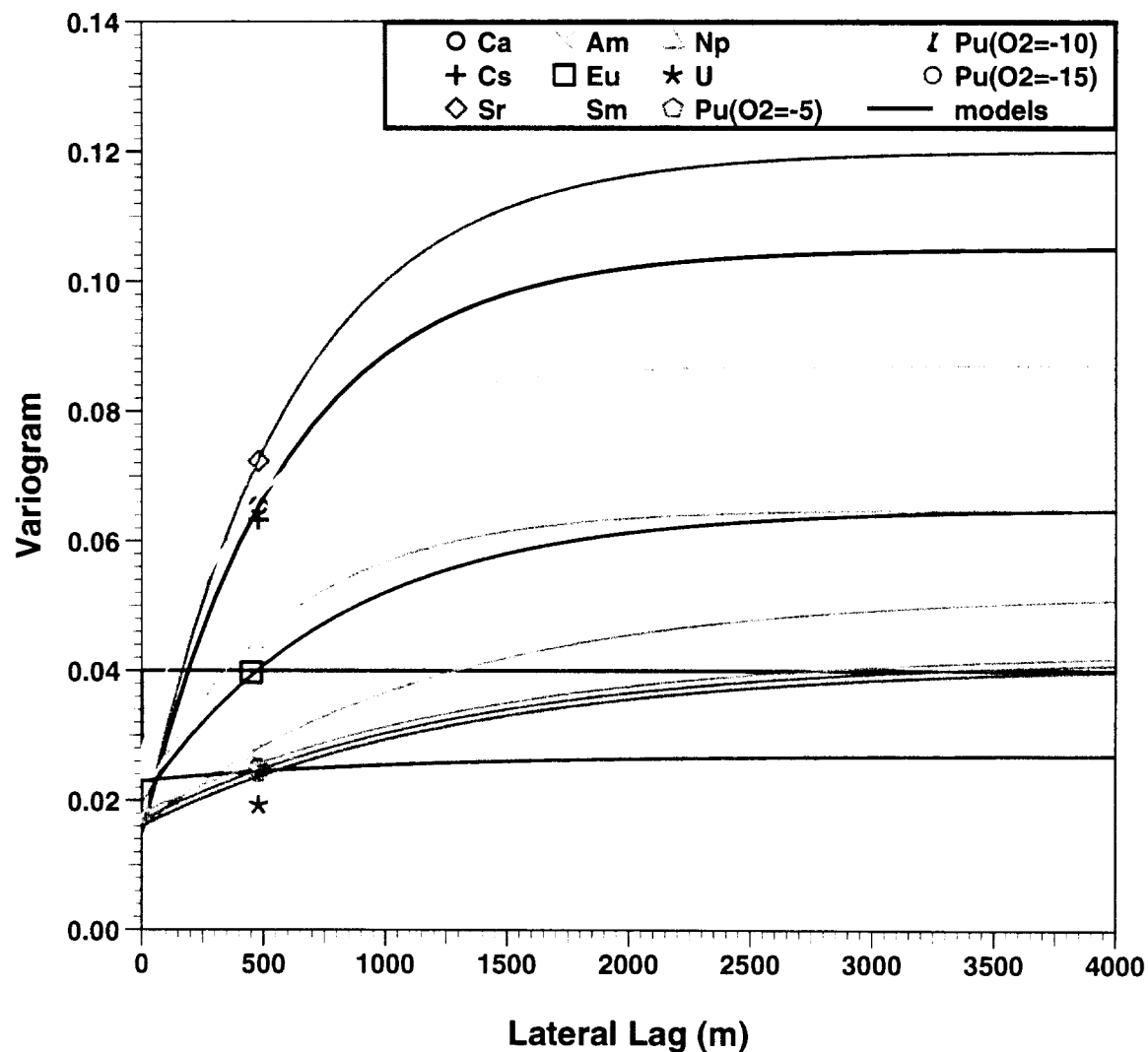Figure 5.9 Experimental and modeled lateral direction variograms of $\log_{10}$ [K_d] for radionuclides Ca, Cs, Sr, Am, Eu, Sm, Np, U, and Pu based on XRD mineral abundance data from drillholes ER-5-4, UE-5n, ER-5-3, and U-11g-1 in Frenchman Flat.

Table 5.3 Parameters for lateral variogram models of $\log_{10}[K_d]$ shown in Figure 5.9 for radionuclides Ca, Cs, Sr, Am, Eu, Sm, Np, U, and Pu.

Radionuclide	Nugget	Sill	Range (m)	Lateral Variogram Model Equation
Ca	0.015	0.105	1750	$\gamma(h_x) = 0.015 + 0.090\left[1 - \exp\left(-\frac{3h_x}{1750\,\mathrm{m}}\right)\right]$
Cs	0.040	0.040	0	$\gamma(h_x) = 0.040$
Sr	0.015	0.12	1800	$\gamma(h_x) = 0.015 + 0.105\left[1 - \exp\left(-\frac{3h_x}{1800\,\mathrm{m}}\right)\right]$
Am	0.016	0.052	3500	$\gamma(h_x) = 0.016 + 0.036\left[1 - \exp\left(-\frac{3h_x}{3500\,\mathrm{m}}\right)\right]$
Eu	0.020	0.065	2400	$\gamma(h_x) = 0.020 + 0.045\left[1 - \exp\left(-\frac{3h_x}{2400\,\mathrm{m}}\right)\right]$
Sm	0.028	0.087	1350	$\gamma(h_x) = 0.028 + 0.059\left[1 - \exp\left(-\frac{3h_x}{1350\,\mathrm{m}}\right)\right]$
Np	0.020	0.065	1750	$\gamma(h_x) = 0.020 + 0.045\left[1 - \exp\left(-\frac{3h_x}{1750\,\mathrm{m}}\right)\right]$
U	0.023	0.027	3000	$\gamma(h_x) = 0.023 + 0.004\left[1 - \exp\left(-\frac{3h_x}{3000\,\mathrm{m}}\right)\right]$
Pu(O$_2$=-5)	0.018	0.043	3900	$\gamma(h_x) = 0.018 + 0.043\left[1 - \exp\left(-\frac{3h_x}{3900\,\mathrm{m}}\right)\right]$
Pu(O$_2$=-10)	0.017	0.042	3900	$\gamma(h_x) = 0.017 + 0.042\left[1 - \exp\left(-\frac{3h_x}{3900\,\mathrm{m}}\right)\right]$
Pu(O$_2$=-15)	0.016	0.041	3900	$\gamma(h_x) = 0.016 + 0.041\left[1 - \exp\left(-\frac{3h_x}{3900\,\mathrm{m}}\right)\right]$

5.3.3 Interpretation

In application to the $\log_{10}[K_d]$ values derived in Chapter 4, vertical and lateral variogram models indicate that spatial variation of K_d is attributed in part to micro-scale variability and in part to subregional-scale spatial variability related to mineralization zones or alluvial layers. For Cs and U, most of the spatial variability is attributed to micro-scale variability. For Am, Eu, Sm, Np, and Pu, about 30-45% of the spatial variability of K_d is related to micro-scale variability. The remaining component of spatial variability has a vertical range of correlation between 200 and 400 m, indicating sensitivity to different mineralization zones or alluvial layers. According to the lateral variogram analysis, the lateral range of correlation of K_d ranges may be between 1350 m and 3900 m for different radionuclides. These ranges are consistent with the observations that mineral abundances appear correlated between the drillhole pairs ER-5-4 and UE-5n and the drillhole pair ER-5-3 and U-11g-1, but not the drillhole pair ER-5-4 and ER-5-3. Ca and Sr exhibit the largest spatial variability, most of which can be attributed to variations in clinoptilolite abundance between different mineralization zones or alluvial layers. Considering

that the histograms of $\log_{10}[K_d]$ for Ca and Sr are bi-modal, unlike the log-normal K_d distributions for other radionuclides, the spatial variability of K_d for Ca and Sr may need to be analyzed by categorizing K_d into high and low values.

5.4 Application of Variogram Models to Reactive Transport Models

Variogram models of mineral abundance and K_d could be applied to reactive transport models in two ways, which are described in further detail in Chapter 6:

- Zones or "layers" having similar mineral abundances could be identified, and a variogram model could be used to characterize the spatial variability of mineral abundance of each sorbing mineral within each zone. The degree of variability of mineral abundance within a zone would depend on the magnitude of the range of correlation relative to the resolution or grid-block size of the transport model. Based on the interpretation of the XRD data in this report, hematite is the only sorbing mineral that exhibits measurable spatial correlation within a zone, so it may be plausible to assume constant K_ds within each layer for most radionuclides. The spatial correlation of hematite might be considered in a reactive transport model with a grid-block size of 5 m or less. The lateral continuity of the zones or layers could be inferred from interpretations of 3-D geometry of the alluvial layers.

- Variogram models of K_d could be used to generate random fields or stochastic "realizations" that explicitly account for spatial variability of K_d throughout the alluvial section (including different mineralization zones or alluvial layers). Estimates of lateral spatial variability could possibly be inferred from variogram analysis of K_ds from closely spaced drillholes. The concept of treating K_d as a spatially correlated random field has been previously applied in hydrology (e.g., Garabedian et al., 1988; Tompson, 1993; Tompson et al., 1996; Miralles-Wilhelm and Gelhar, 1996; Abulaban and Neiber, 2000; Pawloski et al., 2000; Painter et al., 2001).

6 Incorporation of Mineralogic Considerations into Reactive Transport Modeling

The purpose of analyzing mineral abundances in alluvium from drillholes in Frenchman Flat is to characterize the spatial distribution of radionuclide sorbing minerals, which needs to be considered in CAU and HST modeling of radionuclide transport. Two reactive transport modeling approaches have been used to relate radionuclide sorbing mineral abundance to radionuclide retardation:

- The mechanistic approach, where aqueous speciation, combined with surface complexation and ion exchange sorption reactions and sorbing mineral characteristics are explicitly used to evaluate radionuclide retardation, as implemented in the HST transient streamline simulations for the Cheshire test based on the CRUNCH code (Pawloski et al, 2001).[10]

- The K_d approach, where the mechanistic information for each radionuclide-mineral pair under specific aqueous conditions is reduced to a distribution coefficient (K_d). A radionuclide K_d in an alluvium of mixed mineralogy can then be calculated using the component additivity approach (see Chapter 4). This approach was also applied in the HST particle simulations for the Cheshire test (Pawloski et al., 2001).

In regard to addressing *spatial* variability of radionuclide retardation, two plausible approaches are:

- The facies-based approach, where the spatial distribution of radionuclide retardation is defined according to a combination of geologic interpretation in a three-dimensional geometric framework of "alluvial layers" or "chemofacies" to categorize rocks by distinctive mineralogic and lithologic characteristics. Within each rock category or "facies," the hydraulic and reactive transport properties may be considered constant or described by statistical properties. This approach may also require an evaluation of the spatial distribution of sorbing and non-sorbing minerals within each of the mineralization zones, chemofacies, or alluvial layers. If the categorization is solely concerned with the spatial distribution of sorbing minerals, the categories are, in effect, chemofacies, as described in Section 3.5. The mineral distribution parameters within a chemofacies can then be used by either the mechanistic *or* K_d approaches to evaluate retardation for each radionuclide.[11]

---

[10] In HST simulations, dissolution and precipitation reactions were also included in the mechanistic model. These reactions are not discussed in this report.

[11] In the Cheshire HST simulations, the chemofacies approach was used. However, the entire modeling domain was defined as one "layer" (mafic poor Calico Hills lava) and only an evaluation of heterogeneous mineral distribution within this "layer" was necessary.

- The K_d "random field" approach, where the conceptual model for the spatial distribution of radionuclide retardation treats K_d as a collection of random variables positioned in space with spatial correlation defined by a variogram model. This approach requires translating sorbing mineral abundances into K_d for individual radionuclides using the component additivity concept described in Chapter 4. In this approach, K_d distribution information replaces mineral distribution information. The pattern of spatial variability of K_d is described by a random field model with parameters that are specific to each radionuclide.

In both the chemofacies and K_d random field approaches, grid block sizes are finite, requiring assumptions about the effective or "average" mineral abundances and radionuclide retardation over finite volumes. These effective values may depend on grid block size. The analysis of mineral abundance data in this report indicates that spatial dependencies in mineral abundance and K_d do exist within and between zones or "alluvial layers" in Frenchman Flat. These spatial heterogeneities of radionuclide sorbing minerals may need to be considered in both CAU and HST scale models.

If a mechanistic approach is used to predict radionuclide transport, a chemofacies approach is more practical for describing spatial variations of sorbing mineral abundance. This is because the mechanistic approach directly relies on a description of the radionuclide sorbing mineral abundances. Based on the analysis in Chapter 3, the major spatial variations of sorbing mineral abundance are zonal. However, if a K_d approach is used to predict radionuclide retardation, either a chemofacies or a K_d random field approach may be practical. The practicality and applicability of either approach depends on geologic interpretation, model resolution and scale, data availability, and appropriateness to site conditions.

6.1 Scaling Issues

The mineral abundance data from drillholes ER-5-4, UE-5n, and ER-5-3, and U-11g-1 were obtained from core samples, which are much smaller than typical grid block sizes in numerical models. Considering differences in mineral abundance in sidewall splits from sidewall cores and the variogram analysis of Chapter 5, much small or "micro" scale variability is expected. Therefore, some assumptions must be made on scaling data to effective model parameters.

Garabedian et al. (1988) and Gelhar (1993) suggest that the effective retardation coefficient, $\langle R_d \rangle$, is an arithmetic average of local point values. Pawloski et al. (2000) appear to confirm the validity of the relationship in reactive transport simulations of radionuclide transport for the Cambric test.

In transport simulations of Np for alluvium near Yucca Mountain, NTS, Painter et al. (2001) assumed an effective K_d based on the geometric mean of a log-normal K_d distribution. In these Np transport simulations, the effective K_d yielded similar breakthrough behavior (with slightly delayed initial breakthrough) compared to a random field assumption with a log-normal

distribution of K_d. However, the point was made that these modeling results pertained only to Np for the specific statistical model used.

Based on the results of univariate statistical analysis in Chapter 4 and variogram analysis in Chapter 5, chemofacies and random field approaches are described below as plausible means for addressing spatial variability of K_d in Frenchman Flat.

6.2 The Chemofacies Approach

The variogram analysis in application to mineral abundance (Section 5.2) indicated that spatial variation of the abundance of sorbing and non-sorbing minerals within mineralization zones (which partly correspond to alluvial layers as discussed in Section 3.5) was largely attributed to micro-scale variability. Assuming arithmetic averaging of mineral abundance within zones, most of the spatial variation of mineral abundance in Frenchman Flat is attributable to the different mineralization zones or alluvial layers. Therefore, consideration of heterogeneity of sorbing mineral abundance in Frenchman Flat based on a chemofacies approach could be accomplished by including layers or zones with different sorbing mineral abundances. A comparison of the alluvial layering interpretation developed by Warren et al. (2002) and a chemofacies interpretation was described in Section 3.5

An interpretation of the three-dimensional geometry of the alluvial layers in Frenchman Flat could provide a framework for developing a model of spatial variation of sorbing mineral abundances. Based on our chemofacies interpretations, much of the geometric structure of chemofacies is directly associated with the alluvial layers. However, some chemofacies may be recognized as sub-units within the alluvial layers, such as zones with distinctively different abundances of calcite, hematite, and smectite recognized within alluvial layers identified in ER-5-4. Other chemofacies may be composites of alluvial layers that have been distinguished based on textural or chemical differences not examined in this study. Abrupt lateral changes, as observed in differences between ER-5-4 and ER-5-3, may reflect complexity of alluvial fan deposition combined with different source areas. Importantly, some depth intervals, such as between 780 and 900 m depth in ER-5-4, clearly consist of complex interfingerings of lithologies with different mineral abundances, which may need to be explicitly considered in development of high-resolution HST scale models. In application to CAU models, interfingering may need to be accounted for by scaled effective properties. Comparison of chemofacies identified in ER-5-4 and ER-5-3 indicates that some chemofacies might exhibit lateral gradations of sorbing mineral abundances, which may need to be considered in development of either HST or CAU scale models.

6.3 K_d Approach

In the K_d approach to modeling radionuclide transport, the retardation factor, R_d, linearly scales the transport velocity. R_d is related to K_d by

$$R_d = 1 + \frac{(1-n)\rho_s K_d}{n}$$

where n is porosity and ρ_s is solid density of the porous media. Different radionuclides will have different K_d factors that depend on the abundances of sorbing minerals, as shown in Section 4.1.3. The spatial distribution of K_d for each radionuclide was examined based on variogram analyses in Section 5.3.

6.3.1 Zonal Approaches

Log-normal distributions of K_d were evident for the radionuclides Am, Cs, Eu, Np, Pu, Sm, and U (see Section 4.2). For these radionuclides, it is conceivable that Frenchman Flat alluvium could be treated in a large-scale transport model as one zone having an effective K_d based on the arithmetic mean, geometric mean, or another volumetric average. The validity of using a single effective K_d throughout a model domain would largely depend on the scale, location, and desired resolution of the simulations. The use of single effective K_ds could be tested by comparing simulations of transport behavior with or without spatially variable K_d and permeability (e.g., Painter et al., 2001).

For the radionuclides Ca and Sr, the log-transformed frequency distributions of K_d are clearly bi-modal. As indicated in section 4.1.3, K_ds for Ca and Sr strongly depend on clinoptilolite abundance. The log-scale histograms shown in Figures 4.2 and 4.10 indicate that cutoff values of K_d at approximately 300 and 200 mL/g for Ca and Sr, respectively, separate the K_ds into two zones of relatively low K_d and high K_d. These histograms also indicate that high K_d zones for Ca and Sr are prevalent in northern Frenchman Flat — as evident in ER-5-3 and U-11g-1 — and low K_d zones for Ca and Sr are prevalent in southern Frenchman Flat — as evident in ER-5-4 and UE-5n. Therefore, the spatial distribution of K_d throughout Frenchman Flat largely depends on the spatial locations of these relatively high and low K_d zones.

To illustrate this concept, the mineral abundance data in ER-5-3 and ER-5-4 were categorized into low and high K_d based on 300 and 200 mL/g cutoffs for Ca and Sr. Categorical geostatistical models were developed to characterize the vertical spatial variation of the low and high K_d zones for both Ca and Sr using two-dimensional Markov chains (Carle and Fogg, 1997). For a two-category Markov chain model, the only parameters needed are the proportions and mean lengths in the vertical and lateral directions for one of the two categories (the high K_d category was chosen). The proportions were taken from the composite of the ER-5-4, UE-5n, ER-5-3, and U-11g-1 mineral abundance data. The vertical mean lengths were inferred from vertical transition probability measurements (Carle and Fogg, 1996). The lateral mean lengths were estimated at 2000 m, based on strong correlation of mineral abundances in ER-5-4 and UE-5n (477 m apart) and lack of correlation between ER-5-4 and ER-5-3 (5585 m apart). Geostatistical realizations of the low and high zones could then be generated based on the Markov chain model. Figure 6.1 shows realizations of low K_d and high K_d zones for Ca and Sr between ER-5-4 and ER-5-3. The data from ER-5-4 and ER-5-3 are used to condition the realizations. These realizations yield a geologically plausible model of zonal variations of K_d within Frenchman Flat with patterns of heterogeneity related to different episodes of alluvial fan deposition.
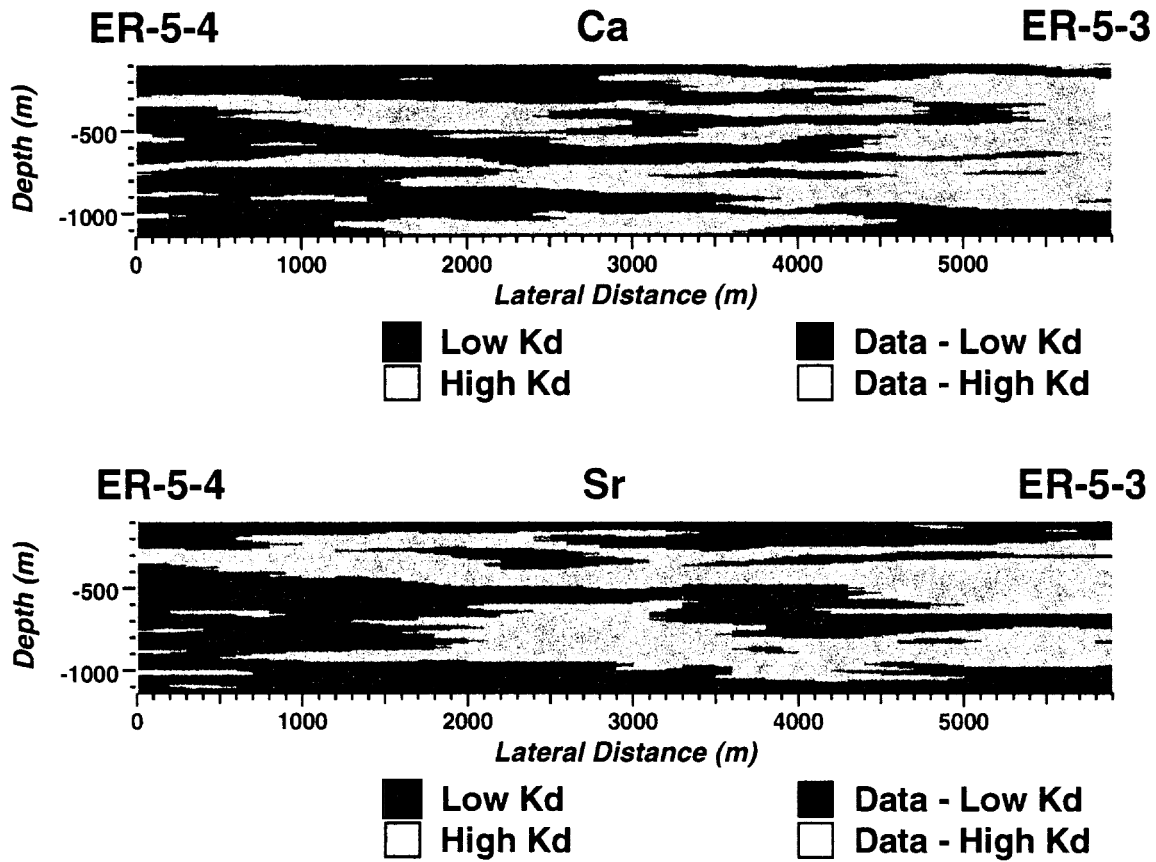
Figure 6.1 Categorical realizations of "low K_d" and "high K_d" zones for Ca and Sr. Conditioning of realizations with data from drillholes ER-5-4 and ER-5-3 is indicated by black (low K_d) and white (high K_d).

6.3.2 Gaussian Random Field Approaches

The Gaussian random field is the most common stochastic conceptual model for considering spatial variation of K_d for reactive transport modeling in hydrology (Garabedian et al., 1988; Tompson (1993); Tompson et al. (1996); Miralles-Wilhelm and Gelhar, 1996; Abulaban and Neiber, 2000; Pawloski et al., 2000; Painter et al., 2001). In particular, a log-normal distribution and exponentially decaying spatial covariance of K_d is typically assumed. In some cases, a negative cross-correlation with permeability is assumed.

In Section 5.3, a combination of nugget and exponential variogram model structures were found to provide plausible fits to the experimental vertical variograms of K_d for all radionuclides. Assuming second-order stationarity, these variogram models can be directly converted to exponentially decaying spatial covariance models. The nugget structure is attributed to micro-scale variability that may either be explicitly included in the random field model or folded into the average or effective K_ds.

To illustrate the random field approach, realizations of K_d for each radionuclide were generated using the code "sgsim" from the Geostatistical Software Library (Deutsch and Journel, 1998) based on the variogram models developed in Section 5.3. Single realizations of $\log_{10}[K_d]$ for each radionuclide are shown in Figures 6.2 and 6.3. These realizations extend 1500 m vertically and 15 km laterally, reflecting possible spatial distributions of K_d over a large cross-sectional area of Frenchman Flat. The differences in the spatial structure of K_d for different radionuclides are attributed to differences in variogram model structure. For example, Am shows spatially correlated regions of relatively low or high K_d, whereas Cs shows only random variation. The variogram model for Am has pronounced spatial correlation, whereas the variogram model for Cs is pure nugget without spatial correlation, which yields only small-scale variability.

As discussed earlier, the frequency distributions for Ca and Sr were bi-modal and thus do not conform to the Gaussian random field conceptual model. The realizations shown in Figures 6.2 and 6.3 for Ca and Sr were nonetheless constructed under the assumption of a Gaussian random field. The spatial variation of K_d in these realizations exhibits the largest variations in magnitude compared to other radionuclides, reflecting the high sill parameters of the fitted variogram models. A problem with using a Gaussian random field model for Ca and Sr is that the realizations produce a normal distribution of $\log_{10}[K_d]$ values, which will contain an excess of intermediate values instead of two modes of low K_d and high K_d.
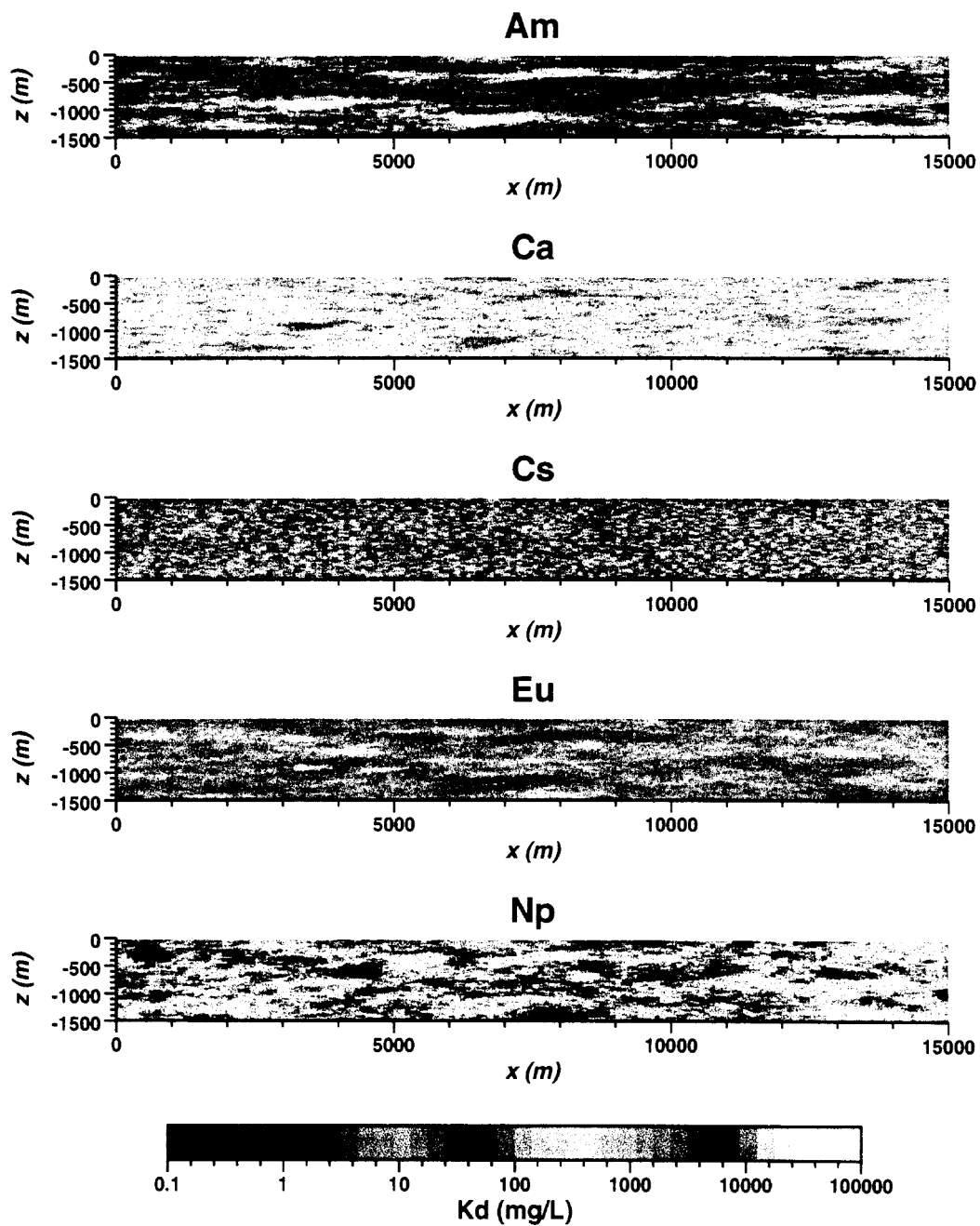
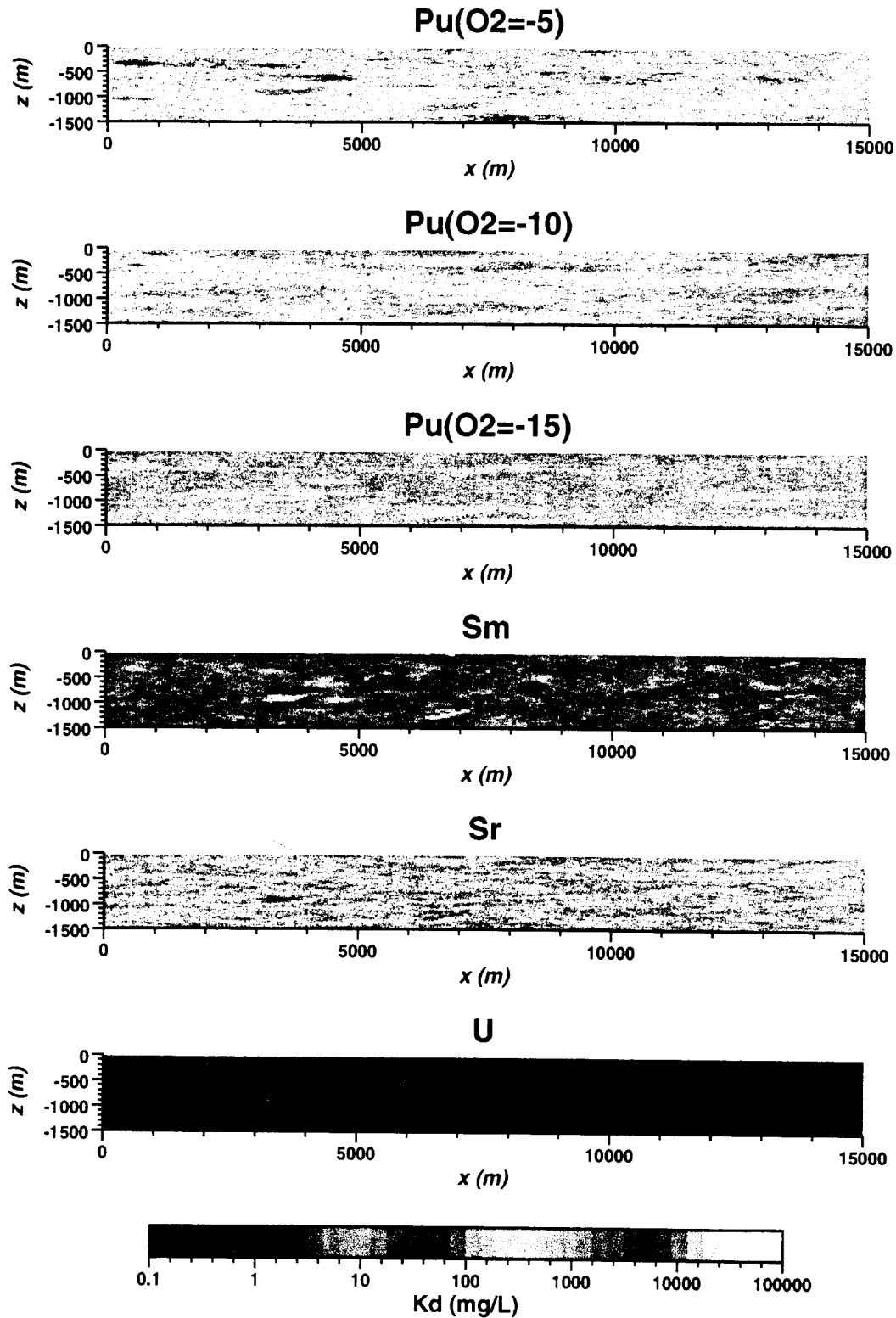Figure 6.2 Gaussian random field realizations of spatial variability of K_d for Am, Ca, Cs, Eu, and Np.

Figure 6.3 Gaussian random field realizations of spatial variability of K_d for Pu(O2=-5), Pu(O2=-10), Pu(O2=-15), Sm, Sr, and U.

6.3.3 Hybrid Approaches

Alternatively, zonal and Gaussian random field geostatistical approaches can be combined to address the bi-modal K_d distributions evident for Ca and Sr. Gaussian random fields can be used to conceptualize spatial variation of K_d within the low and high K_d zones. Figure 6.4 shows realizations of K_d of Ca and Sr with Gaussian random field spatial variation within the low K_d and high K_d zones. The Gaussian random fields are based on the variogram models for spatial variation of K_d for Ca and Sr within low K_d and high K_d zones shown in Figure 5.8. The zonal random fields shown in Figure 6.1 can be used as templates for choosing K_ds from either the realization for low or high K_d zones. Figure 6.5 illustrates the result of a combination of the zonal and Gaussian random field approaches. The resulting realizations reflect three scales of spatial variability: micro, zonal, and within-zone.
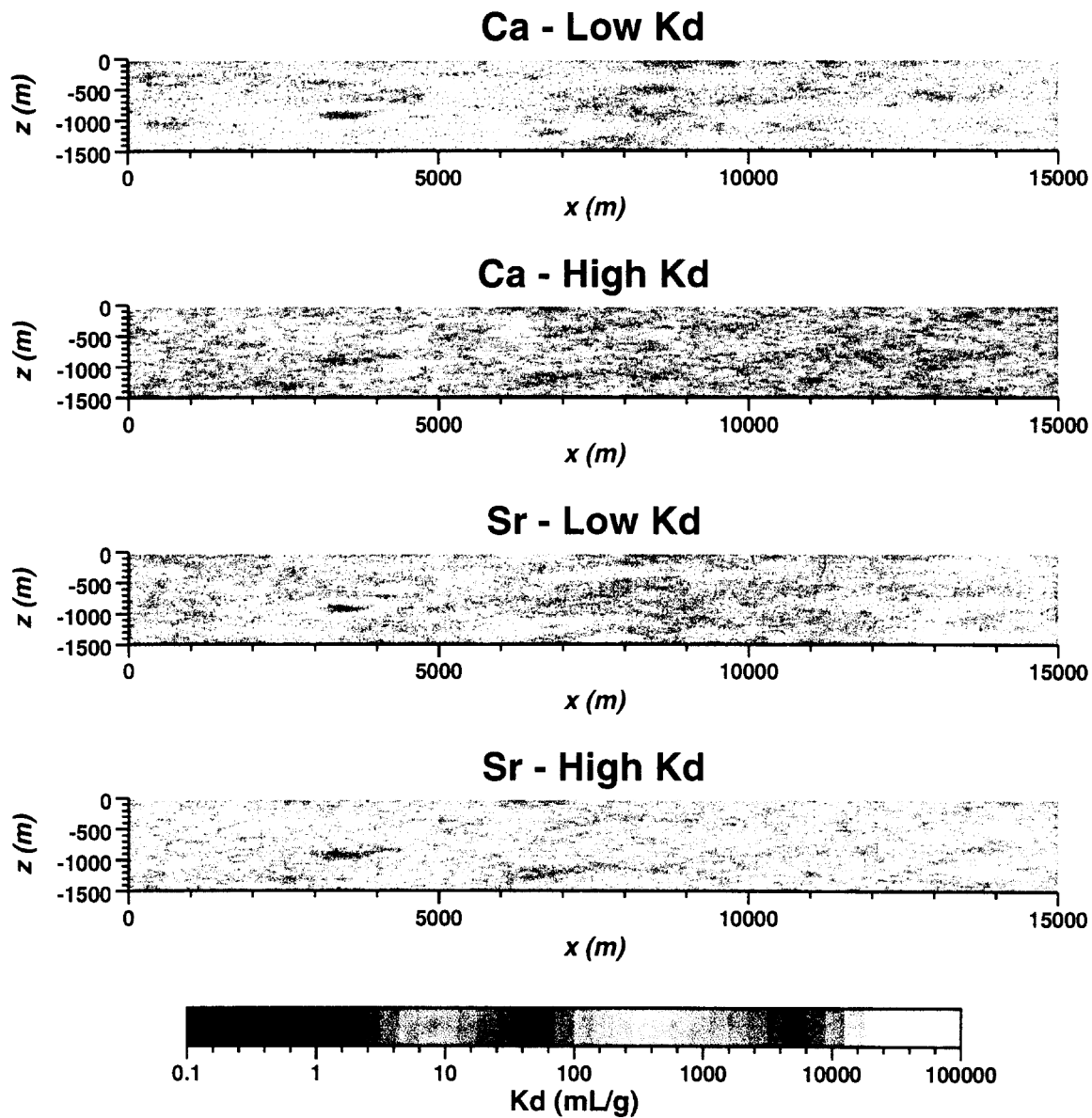
Figure 6.4 Gaussian random field realizations of spatial variability of K_d for Ca and Sr within low K_d and high K_d zones.
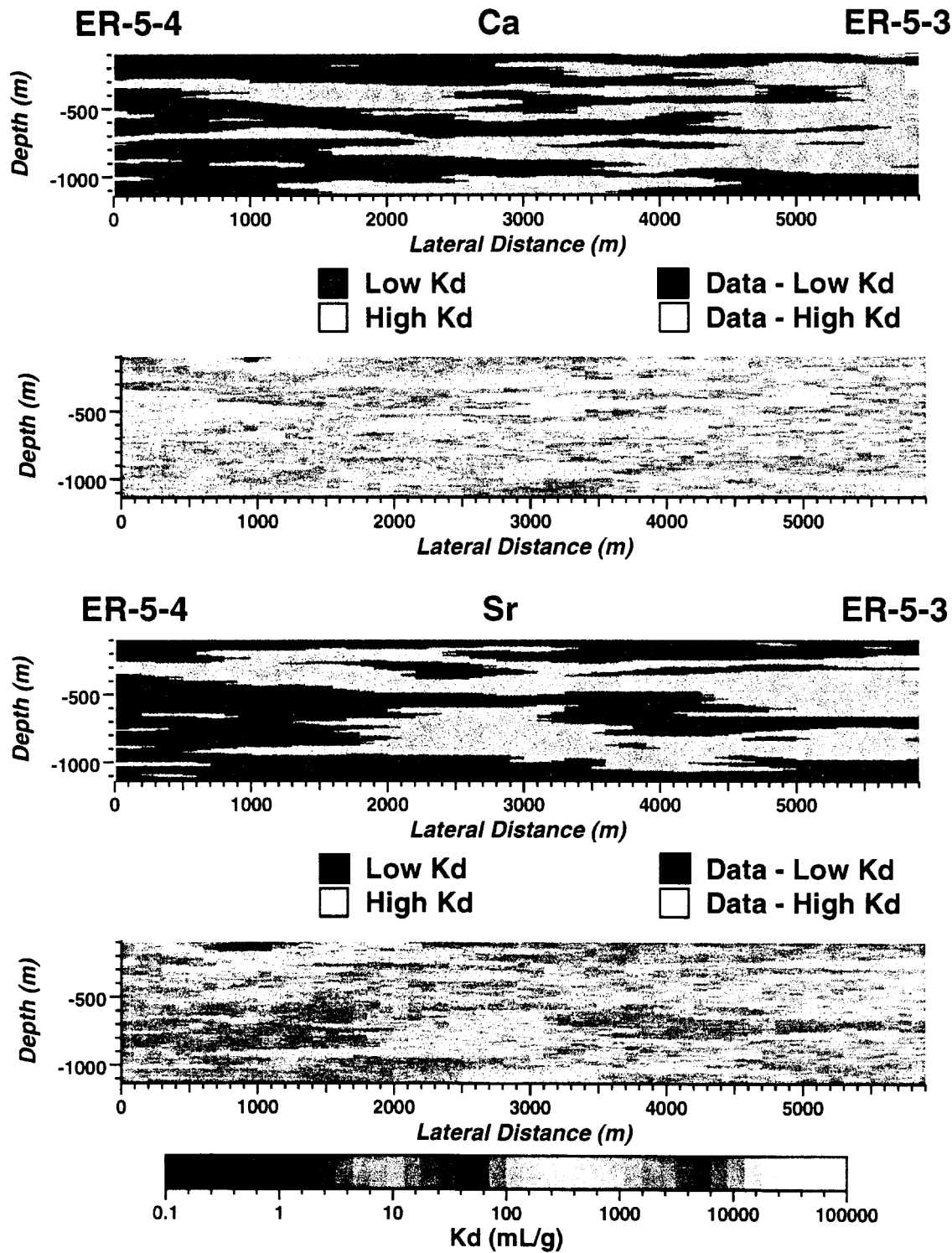
Figure 6.5 Realizations of spatial variability of K_d for Ca and Sr generated by combining both zonal and Gaussian random field geostatistical models. The zonal realizations (in grayshade) are shown above the K_d realizations (in color).

6.3.4 Application to CAU Models

Grid block size for CAU models will certainly be too large to consider the high-resolution spatial variation of K_d shown in Figures 6.2 to 6.5. Single effective K_ds could be plausibly assumed in CAU models for radionuclides that exhibit mostly micro-scale spatial variability — Cs and U, in particular.

For other radionuclides that exhibit significant spatial variability, measurable spatial correlation, and log normal distributions — Am, Eu, Np, Pu, Sm — several approaches could be considered:

- Assume effective K_ds based on arithmetic or geometric mean values.

- Assume arithmetic scale averaging of K_d and generate Gaussian random field models at larger grid block sizes. However, if the grid block size is larger than the range of correlation, this approach will have no effect compared to assuming a single effective value.

- Derive effective K_ds from numerical modeling experiments having high-resolution spatial variation of K_d. Note that such experiments would need to address the issue of spatial cross-correlation of K_d with permeability.

- Assume that spatial variations of K_d are primarily related to chemofacies or alluvial layers with distinctive mineral abundances as identified, for example, in Section 3.5 or by Warren et al. (2002). Base K_ds on average mineral abundances for the chemofacies or alluvial layers. This approach would require development of a three-dimensional model of the alluvial layers and important chemofacies within Frenchman Flat.

For radionuclides that exhibit strong dependence on clinoptilolite abundance — Ca and Sr, in particular — CAU scale models in Frenchman Flat will need to consider location dependent K_ds. The difference in average K_d between the low K_d and high K_d zones is about a factor of five for both Ca and Sr. For these magnitudes of K_d, retardation coefficients are nearly proportional to K_d, producing an approximate factor of 5 difference in the retardation coefficients. Such zonal variations in K_d for Ca and Sr could be also be addressed in several ways:

- Using a three-dimensional model of the alluvial layers in Frenchman Flat (chemofacies approach).

- Apply a categorical geostatistical approach as illustrated in Figure 6.1, but at a coarser scale in three dimensions.

- Interpolate K_ds for Ca and Sr throughout Frenchman Flat to account for large-scale trends, such as generally higher K_ds in northern Frenchman Flat relative to central Frenchman Flat.

6.3.5 Application to HST Models

Grid block sizes for HST-scale models are much smaller than for CAU-scale models — as small as 2 m for HST modeling of the Cambric test in Frenchman Flat (Pawloski et al., 2000). Therefore, HST models can certainly resolve the subregional-scale spatial variation of K_d evident from the mineral abundance data examined in this report.

HST models can be expected to extend to several hundred meters in the vertical direction. Therefore, a HST model will usually span several chemofacies or alluvial layers. Several distinctive layers were in fact recognized in HST modeling of the Cambric test based on permeability data and lithologic descriptions (Pawloski et al., 2000). The examination of mineral abundance data in this report certainly suggests that interpretations of chemofacies and alluvial layers can account for much of the spatial variation of K_d.

Given that the spatial variation of K_d for several radionuclides is expected to primarily relate to different chemofacies or alluvial layers, HST models should attempt to identify and incorporate zonal or layered heterogeneity of K_d. Smaller-scale heterogeneity of K_d expected within the zones or layers may be plausibly accounted for by effective K_ds for each zone or layer. The examination of mineral abundances within zones in Chapter 3 indicated that spatial variability within zones is mostly related to micro-scale variability with correlation ranges of 1 m or less. The one exception was for hematite, which exhibited a vertical spatial correlation of about 5 m. However, this small-scale spatial variation of hematite may not have much impact to HST modeling. Hematite abundances are relatively low, and recent flow-through data have suggested that the effective influence of iron oxides in radionuclide retardation may be quite small (Zavarin et al., 2002).

Another consideration for HST models is that some of the alluvial layers appear to be situated in "transition zones" as described in Chapter 3. The transition zones can be attributed to portions of the alluvial sequence where alluvial deposits of different lithologies or source areas are interfingered. The transition zones could provide regions of most intense heterogeneity of both hydraulic and chemical properties.

Alternatively, if the chemofacies or alluvial layers cannot be identified, the Gaussian random field or hybrid zonal/random field approaches described in sections 6.2.4 and 6.2.5 could be applied to the HST models. The vertical variogram model parameters given in Tables 5.1, 5.2, and 5.3 could be applied at different model resolutions. Lateral variogram models parameters are more uncertain, but plausible correlation ranges would range between about 1000 to 5000 m. Given the strong sensitivity of Ca and Sr K_d to clinoptilolite abundance, the models of spatial variability for K_d of Ca and Sr would need to be customized to different locations in Frenchman Flat. Alternatively, a trend in K_ds could be added to the Gaussian random field values.

7 Conclusions

The overall goal of this study is to understand and characterize the spatial variation of sorbing minerals in Frenchman Flat alluvium using geostatistical techniques, with consideration for the potential impact on reactive transport of radionuclides. To achieve this goal requires an effort to ensure that plausible geostatistical models are used to characterize the spatial variation of minerals. The models must also be plausible from a geological perspective. Spatial variation of mineral abundance is caused not only by random processes but also by ordered geologic processes such as alluvial fan progradation, provenance, and in-situ alteration. Much of the spatial variation of sorbing mineral abundances is attributable to different "chemofacies" within which zonal mean abundances are relatively uniform. The chemofacies are, in large part, associated with the alluvial layers interpreted by Warren et al. (2002).

The preliminary data analysis in Chapter 3 using depth profiles of mineral abundance, histograms, and probability plots revealed that mineral abundances typically exhibit micro-scale variability superposed on large-scale variability that occurs in zones with relatively constant mean mineral abundances. From a transport modeling perspective, the micro-scale variability, which occurs at scales of 1 m or less, can be practically addressed by use of effective properties. The larger-scale variability — referred to as "mineralization zones" — should be considered in HST models and may need to be addressed in CAU scale models for certain radionuclides. The sorbing minerals calcite, clinoptilolite, and hematite exhibit some zones where abundances are below detection limits. Mica and smectite appear to be ubiquitous.

Comparison of depth profiles of mineral abundance between drillholes ER-5-4, ER-5-3, UE-5n, U-11g-1 indicates that mineralization zones are laterally continuous over scales greater than about 500 m and less than about 5000 m. Variations in thickness and attitude (e.g., dip and strike of bounding surfaces) of mineralizations zones or alluvial layers are uncertain. The major differences in sorbing mineral abundances in northern Frenchman Flat compared to central Frenchman Flat are:

- Clinoptilolite is more abundant.

- Mica is slightly less abundant at greater depth.

- Hematite is not present below a depth of 460 m.

- Calcite exhibits more extensive zones of high abundance.

- Smectite abundance is slightly lower at greater depths.

Based on groupings of mineralization zones, nine chemofacies were interpreted in ER-5-4. The differences between chemofacies and alluvial layers are attributed to:

- Some alluvial layers have distinctive abundances of non-sorbing minerals, but not sorbing minerals.

- Some chemofacies are subunits within an alluvial layer.

- Different alluvial layers with similar distributions of zonal mean abundances of sorbing minerals are interpreted as the same chemofacies.

Nonetheless, the interpretation of alluvial layering by Warren et al. (2002) provides a useful geometric framework for modeling spatial variations of mineral abundance. Some zones exhibit complex interfingering of chemofacies. These transition zones also exhibit variations in lithology or source area (Warren et al., 2002) and, thus, are expected to be highly heterogeneous in both geochemical and hydraulic properties. Because the data examined in this study are located in central and northern Frenchman Flat, more consideration of southern alluvial source areas would be needed for basin-wide models.

In an analysis of correlation between abundances of different minerals, several conclusions could be made:

- Within the sorbing minerals, clinoptilolite shows significant correlation with calcite (positive) and smectite (negative).

- Hematite shows no correlation with any other sorbing or non-sorbing minerals.

- All non-sorbing minerals except for kaolinite and sanidine show significant correlation with at least one sorbing mineral.

- The negative correlation between calcite and bytownite suggests that calcite may have formed as a result of weathering of the Ca-rich plagioclase.

Considering that both CAU and HST scale models may employ K_ds to simulate retardation of radionuclide transport, the XRD mineral abundances were also evaluated from a K_d perspective. In Chapter 4, K_d for Am, Ca, Cs, Eu, Np, Pu (at different oxygen fugacities), Sm, Sr, and U, is linked to mineral abundance by the component additivity approach (Zavarin, 2002). Using this approach, K_d can be geostatistically evaluated as a random variable that directly relates to radionuclide retardation parameters for particle tracking models. The following are conclusions on K_d variation in Frenchman Flat:

- K_d frequency distributions for Am, Eu, Np, Pu, Sm, and U appear to be log normal and exhibit no significant vertical or lateral variation.

- Compared to mineral abundance, spatial variation of K_d throughout Frenchman Flat is less zonal and appears to behave more like a spatially correlated random field, except for Ca and Sr.

- K_d frequency distributions for Ca and Sr appear to be bi-modal and strongly dependent on clinoptilolite abundance, which varies significantly vertically and laterally. Large-scale heterogeneity of zeolite is a key issue for CAU and HST scale modeling of radionuclide transport.

- HST models may need to incorporate zonal variations of K_d based on alluvial layers or chemofacies.

Chapter 5 applies the geostatistical technique of variogram analysis to quantitatively evaluate spatial variability of mineral abundance and K_d within Frenchman Flat alluvium. In application to mineral abundances within mineralization zones, the variogram analyses conclude:

- With the exception of hematite, the spatial variation of mineral abundance within mineralization zones is essentially random and has no spatial correlation.

- The major component of spatial variation of mineral abundance is attributed to different mineralization zones.

In application to K_d, the following conclusions can be made:

- Spatial variation of K_d for Cs and U is essentially random with little or no spatial correlation.

- Approximately 30-45% of spatial variation of K_d for Am, Eu, Sm, Np, and Pu is attributed to micro-scale variability, and the remainder is attributed to subregional variability associated with mineralization zones or alluvial layers.

- The 163 data were adequate for development of vertical variogram models.

- Lateral variogram models could be developed by analyzing data from ER-5-4 and UE-5n for one lag of 477 m and assuming the same nugget and sill values as used in the vertical variogram models.

- Comparison of vertical and lateral variogram range values indicates lateral:vertical anisotropy ratios ranging between 4.5:1 and 13:1. Considering the difficulties in quantifying lateral spatial correlation, the ratios could be greater.

- Spatial variability of K_d for Ca and Sr is much greater than for other radionuclides because of the strong dependency on clinoptilolite abundance.

Chapter 6 applies the overall geostatistical analysis of spatial variability conducted in Chapters 3-5 to development of models of spatial variability of mineral abundance. The chemofacies approach is recommended for addressing spatial variability directly from sorbing mineral abundance, such as in application of a mechanistic reactive transport model. Using the component additivity approach, the chemofacies approach could also be applied to development

of effective K_ds for different radionuclides. The chemofacies approach could be integrated with three-dimensional interpretations of alluvial layer geometry to develop realistic models of spatial variation of mineral abundance or K_d within Frenchman Flat alluvium. A K_d random field approach is also suggested for simulation of subregional scale spatial variability of K_d within Frenchman Flat alluvium for Am, Eu, Sm, Np, and Pu. For Cs and U, it is conceivable that a single effective value of K_d could be assumed throughout most of Frenchman Flat. The variogram models for K_d developed in Chapter 5 can be applied to generation of stochastic realizations of K_d based on Gaussian random fields. For Ca and Sr, a hybrid stochastic simulation approach that combines categorical and Gaussian random field approaches is demonstrated to show how the bi-modality and lateral variation of the frequency distribution of K_d could be considered in simulation. Spatial variability within transition zones of interfingered lithologies presents the most complex situation of heterogeneity in both geochemical and hydraulic properties. Therefore, in high-resolution simulation of reactive transport of radionuclides, such as HST modeling, it will be important to determine if transition zones are present within the model domain.

Based on the experience of this study's work in analyzing spatial variability of sorbing mineral abundances and K_d, the effort to obtain core samples and apply XRD analysis to obtain high quality data with detailed spatial coverage has been rewarding. The manner in which sorbing minerals vary in the vertical direction within the Frenchman Flat is now confidently understood. Some uncertainty remains in identifying the actual scale of "microscale" variability of mineral concentrations, which appears to occur at scales less than 0.3 m for most minerals. Smaller scales of variability could be effectively evaluated by identification of mineral concentrations in "split" samples using the same method of analysis on many (e.g., 20+) core. Some uncertainty also remains as a result of applying only XRD data to our geostatistical analysis. Incorporation of SEM and petrographic data could provide greater confidence in the geostatistical model of sorbing mineral abundance. Some insights have been gained on lateral spatial variability, but considerable uncertainty remains on characterizing three-dimensional spatial variation. Nonetheless, the scant lateral correlation analysis that could be made from the data is encouraging in that plausible interpretations could be made, suggesting that future data collection would be useful for further constraining uncertainty in reactive transport simulations.

8 References

Abulaban, A, and J.L. Nieber (2000), "Modeling the Effects of Nonlinear Equilibrium Sorption on the Transport of Solute Plumes in Saturated Heterogeneous Porous Media," *Advances in Water Resources* **23**(8), 893-905

Carle, S. F., and G. E. Fogg (1996), "Transition Probability-based Indicator Geostatistics," *Mathematical Geology* 28, 453-476.

Carle, S. F., and G. E. Fogg (1997), "Modeling Spatial Variability with one- and Multidimensional Continuous-Lag Markov Chains," *Mathematical Geology* 29, 891-918.

Deutsch, C. V., and A. G. Journel (1998), *Geostatistical Software Library and User's Guide*, Oxford University Press, New York, 369 p.

Duff M. C., Hunter D. B., Triay I. R., Bertsch P. M., Reed D. T., Sutton S. R., Shea-Mccarthy G., Kitten J., Eng P., Chipera S. J., and Vaniman D. T. (1999) Mineral associations and average oxidation states of sorbed Pu on tuff. *Environmental Science & Technology* 33(13), 2163-2169.

Erikson S. J. (1991) Report of Drilling and Radionuclide Migration Investigations at UE20n#1, Pahute Mesa, Nevada Test Site, DOE/NV/10384-35, Desert Research Institute, University of Nevada System.

Garabedian, S. P., Gelhar, L. W., and Celia, M. A. (1988), *Large-scale Dispersive Transport in Aquifers: Field Experiments and Reactive Transport Theory*, Massachusetts Institute of Technology, Cambridge, MA, Parsons Laboratory Report 315.

IT Corporation. (1999) Underground Test Area Project, Corrective Action Unit 98: Frenchman Flat. Volume 2: Groundwater Data Documentation Package. IT Corporation.

Johnson J. W. and Lundeen S. R. (1997) GEMBOCHS thermodynamic datafiles for use with the EQ3/6 modeling package. Lawrence Livermore National Laboratory.

Kersting A. B., Efurd D. W., Finnegan D. L., Rokop D. J., Smith D. K., and Thompson J. L. (1999) Migration of plutonium in ground water at the Nevada Test Site. *Nature* **397**(6714), 56-59.

Miralles-Wilhelm, F., and L. W. Gelhar (1996), "Stochastic Analysis of Sorption Macrokinetics in Heterogeneous Aquifers," *Water Resources Research*, **32**(6) 1541-1549.

Painter, S, V. Cvetkovic, and D. R. Turner (2001), "Effect of Heterogeneity on Radionuclide Retardation in the Alluvial Aquifer Near Yucca Mountain, Nevada," *Ground Water*, **39**(3), 326-338.

Pawloski, G. A., A. F. B. Tompson, C. J. Bruton, and M. Zavarin Eds. (2000), *Evaluation of the Hydrologic Source Term from Underground Nuclear Tests in Frenchman Flat at the Nevada Test Site (U)*, Contributors: W. L. Bourcier, C. J. Bruton, S. F. Carle, B. K. Esser, A. B. Kersting, R. M. Maxwell, G. A. Pawloski, J. A. Rard, D. E. Shumaker, D. K. Smith, A. F. B. Tompson, and M. Zavarin, UCRL-ID-138007, Lawrence Livermore National Laboratory, CA.

Pawloski G. A., Tompson A. F. B., and Carle S. F., eds. (2001) *Evaluation of the Hydrologic Source Term for Underground Nuclear Tests on Pahute Mesa and the Nevada Test Site: The Cheshire Test*, Contributors: W.L. Bourcier, C.J. Bruton, S.F. Carle, J.I. Daniels, R.M. Maxwell, G.A. Pawloski, D.S. Shumaker, D.K. Smith, A.F.B. Tompson, and M. Zavarin. UCRL-ID-147023. Lawrence Livermore National Laboratory, Livermore, California.

Rose T. P., Kenneally, J.M., Smith, D.K., Davisson, M.L., Hudson, G.B., and Rego, J.H. (1997), Chemical and Isotopic Data for Groundwater in Southern Nevada. Lawrence Livermore National Laboratory, UCRL-ID-128000, Livermore, California.

Tompson, A. F. B. (1993), "Numerical Simulation of Chemical Migration in Physically and Chemically Heterogeneous Porous Media," *Water Resources Research*, **29**(11), 3709-3726.

Tompson, A. F. B, A. L. Schafer, and R. W. Smith (1996), "Impacts of Physical and Chemical Heterogeneity on Co-contaminant Transport in a Sandy Porous Medium," *Water Resources Research*, **32**(4), 801-818.

Warren R. G., Benedict F. C., Jr., Rose T. P., Smith D. K., Chipera S. J., Kluk E. C., and Raven K. M. (2002) Alluvial Layering and Distribution of Reactive Phases within Drill Holes ER5/4 and UE5n of Frenchman Flat. LA-UR-02-6206, Los Alamos National Laboratory, Los Alamos, New Mexico.

Zavarin M. and Bruton C. J. (2000a) A Non-Electrostatic Surface Complexation Approach to Modeling Radionuclide Migration at the Nevada Test Site: Aluminosilicates. UCRL-ID-141840 DR, Lawrence Livermore National Laboratory, Livermore, California.

Zavarin M. and Bruton C. J. (2000b) A Non-Electrostatic Surface Complexation Approach to Modeling Radionuclide Migration at the Nevada Test Site: Iron Oxides and Calcite. UCRL-ID-141841 DR, Lawrence Livermore National Laboratory, Livermore, California.

Zavarin M. (2002) Upscaling Radionuclide Retardation — Linking Mechanistic Surface Complexation and Ion Exchange Model to a Linear Kd Approach. Report to UGTA project, Lawrence Livermore National Laboratory, Livermore, California.

Zavarin M., Roberts S. K., Rose T. P., and Phinney D. L. (2002) Validating Mechanistic Sorption Model Parameters and Processes for Reactive Transport in Alluvium. UCRL-ID-149728, Lawrence Livermore National Laboratory, Livermore, California.